

*A Silvia,  
ed a tutte quelle persone che hanno creduto in me e che mi vogliono bene.  
...  
"Brick walls are there for a reason: they let us prove how badly we want things."  
Randy Pausch*



UNIVERSITY OF PADOVA

DEPARTMENT OF ELECTRICAL ENGINEERING  
Padova, Italy

MASTER'S THESIS

**DESIGN OF A  
PERMANENT MAGNET SYNCHRONOUS MOTOR  
ACCORDING TO  
FREEDOMCAR SPECIFICATIONS**

Supervisor: Ch.mo Prof. NICOLA BIANCHI

Co-supervisor: Dipl.-Ing. WOJECIECH CHLEBOSZ

Dr.-Ing. GRZEGORZ OMBACH

*Brose Fahrzeugteile GmbH & Co. Kommanditgesellschaft*

Student: ENRICO CARRARO

Academic year

2011 - 2012



## Contents

<b>ABSTRACT</b>	<b>v</b>
<b>INTRODUCTION</b>	<b>vii</b>
<b>1 FREEDOMCAR</b>	<b>1</b>
1.1 Introduction . . . . .	1
1.2 Electric motors requirements . . . . .	3
1.3 State of art of the research: important issue . . . . .	6
1.3.1 Efficiency at partial load (20% rated torque) for wide speed range $10 \div 100\%$ maximum speed $> 95\%$ . . . . .	6
1.3.2 Line-to-line back $EMF$ at max speed $< 600V_{peak}$ . . . . .	7
<b>2 PRELIMINARY ANALYSIS</b>	<b>11</b>
2.1 Motor configuration: $IPM$ , $SPM$ . . . . .	11
2.1.1 Flux weakening ( $FW$ ) capability . . . . .	11
2.1.2 Anisotropy level . . . . .	15
2.1.3 $PMs$ collocation . . . . .	16
2.1.4 Conclusions . . . . .	16
2.2 Number of poles and slots, winding topology . . . . .	16
2.2.1 Influence of number of poles . . . . .	16
2.2.2 Influence of number of slots / number of poles combination	17
2.2.3 Winding topology: $FSCW$ , $ISDW$ . . . . .	20
2.2.4 Conclusions . . . . .	22

<b>3</b>	<b>ANALYTICAL SYNTHESIS</b>	<b>25</b>
3.1	"SPM equivalent motor" . . . . .	25
3.2	Design procedure . . . . .	29
3.2.1	Machine general data . . . . .	30
3.2.2	Design temperature . . . . .	31
3.2.3	PM characteristics and max flux density no load - load drop	31
3.2.4	Main geometry of the machine . . . . .	32
3.2.5	Number of conductors . . . . .	33
3.2.6	Slot sizing . . . . .	33
3.2.7	Yoke sizing . . . . .	36
3.2.8	Rotor sizing . . . . .	36
3.2.9	Masses and volumes . . . . .	37
3.3	Definition of the starting design . . . . .	39
3.4	Winding disposition . . . . .	42
<b>4</b>	<b>FINITE ELEMENT ANALYSIS</b>	<b>45</b>
4.1	Model settings . . . . .	46
4.2	Tuning the models . . . . .	48
4.2.1	Round shape analysis . . . . .	48
4.2.2	Final design . . . . .	57
4.3	No load simulation . . . . .	63
4.4	Load simulation . . . . .	69
4.5	Overload simulation and demagnetization check . . . . .	75
4.6	Current parametric simulation . . . . .	82
4.6.1	d/q-axis flux linkages . . . . .	83
4.6.2	Current space vector trajectory . . . . .	85
4.6.3	Torque . . . . .	91
4.6.4	Torque ripple . . . . .	95
4.6.5	Phase current and phase voltage . . . . .	96
4.7	Losses simulation . . . . .	101
4.7.1	Copper losses . . . . .	102
4.7.2	Iron and PMs eddy current losses . . . . .	103
4.7.3	Efficiency vs. speed . . . . .	108
4.8	Comparison to a conventional rotor . . . . .	111
4.8.1	Load simulation . . . . .	111

---

4.8.2	Current parametric simulation . . . . .	112
4.8.3	Torque ripple . . . . .	112
4.8.4	Iron, <i>PMs</i> eddy current losses and electrical efficiency . . .	116
<b>5</b>	<b>CONCLUSIONS</b>	<b>121</b>
<b>6</b>	<b>ADDENDUM</b>	<b>125</b>
6.1	Iron datasheet: ThyssenKrupp® M235-35A . . . . .	126
6.2	NdFeB <i>PM</i> datasheet: Neomax® NMX-36EH . . . . .	134
6.3	Conductors datasheet: <i>CEI-UNEL</i> 01723-72 . . . . .	137
6.4	Program codes . . . . .	138
	<b>Bibliography</b>	<b>141</b>





## ABSTRACT

Electric mobility is becoming in recent years a growing reality due to increase of the demand and cost of oil and the environmental impact of conventional *ICE* (Internal Combustion Engine). This phenomena is becoming relevant in the western countries, that are usually large consumer but also also heavily dependent on foreign imports, especially for the transport sector: in the USA were born public-private cooperative research programs, the last called *FreedomCAR*, aimed at developing high efficiency and cost competitive technologies for electrification of private transport in which electric motors are the key devices. This research provide the description of the design of an high performance *IPM* (Interior Permanent Magnets) electric motor, according to the latest *FreedomCAR 2020* targets, using an unconventional rotor with round shape polar islands; two different *PMs* configuration were considered, I-shape (radial magnetization) and V-shape. Both the machine are equipped with the same stator and a *FSCW* (Fractional Slot Concentrated Winding).

The design procedure was started from a preliminary analysis, used in order to define the main characteristics of the machine while, an analytical synthesis, had led us to define the main geometry dimensions. The tuning and detailed analysis of the machines was performed using *FEA* (Finite Element Analysis), with particular interest to the final evaluation of losses and efficiency.

The report shows the feasibility of this kind the machines, especially concerning the efficiency, that represent the most difficult constraint to achieve, and highlights also the benefits for using this unique rotor design.



## INTRODUCTION

In the last years, with the increase of the energy demand, especially with the emergence of the Asian economies (e.g. China, India) the problem of the energy supplies, energy efficiencies and pollution is becoming more and more important and critical.

At 2008 transport, are worldwide responsible of about 27% of the total final energy consumption and we expected an annual increase of 1.4% between 2008 and 2035. Analyzing the projections for each economic area, it's noted that, due to a fast-paced improvement of the economic conditions leading to an increase of personal and freight transports demand, a growth is more sustained in the non-*OECD* country, by 2.6% per year, compared with 0.3% per year projected for the *OECD* nations. Besides, for both economic areas, this increasing demand for personal travel is a primary factor underlying projected increases in energy demand in this field. [1]

Transports is the primary user of oil and in 2015 is expected that this consume

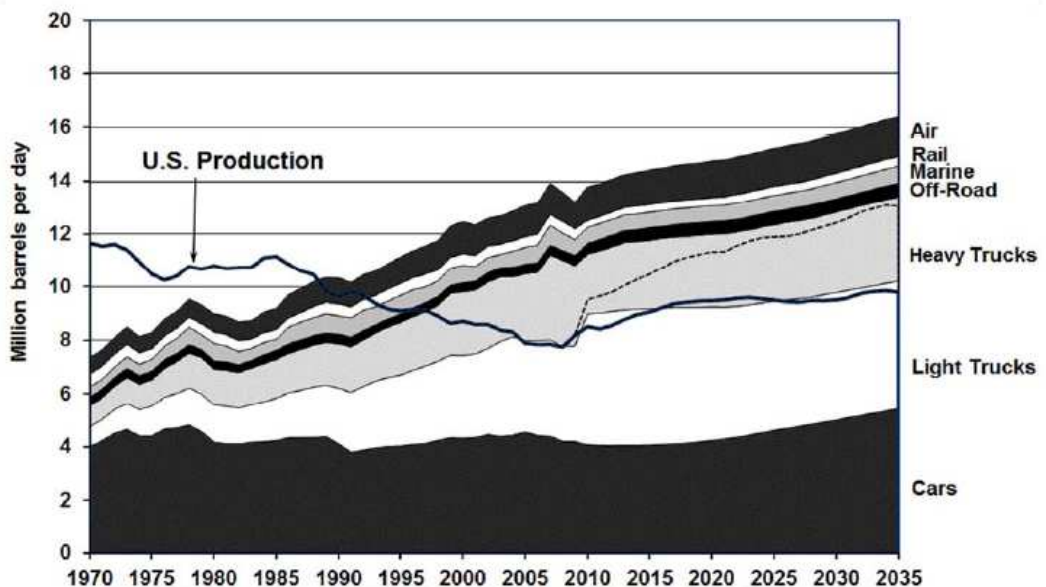


Figure 1: US oil production, consumption by transports field.

Table 1: Comparison of the efficiency between traction technologies (note: the *EV* are battery powered and for conventional vehicle the tank-to-wheel efficiency comes from a weighted average between gasoline and diesel vehicle) [20]

<i>ICE</i> vehicle	<i>EV</i>
Oil raffination efficiency $\sim 90\%$	Thermoelectric generation efficiency $\sim 46\%$
Electric transmission efficiency $\sim 93\%$	Oil transmission efficiency $\sim 98\%$
Tank-to-wheel efficiency $\sim 22\%$	Tank-to-wheel efficiency $\sim 80\%$
Well-to-wheel efficiency $\sim 18\%$	Well-to-wheel efficiency $\sim 34\%$

will achieve about the 55% [19] of the total oil consumed in the world. In developing countries, the transports sector also shows the fastest projected growth in petroleum consumption, promising to rise nearly to the level of non transports energy use by 2020. Most of the largest petroleum consuming nations aren't the most important petroleum-producing countries: this issue become critical in many countries, especially in *USA*, because it's the largest consumer of transportation energy among the *OECD*: at 2015 *US* transports sector is estimated to contribute for about 70% of the total *US* oil consumption, approximately 55% greater than the total oil produced internally, making this country total dependent to the importation from abroad. [18]

Another fundamental issue is the efficiency of the propulsion system: electric propulsion is always in advantage on conventional. Considering the oil as the same primary energy source, the average tank-to-wheel efficiency of Electric Vehicles (*EV*) is almost the double of the corresponding *ICE* value, about 34% vs. 18%, because of the high efficiency that can be achieved with electric motor [20]. For these reason a development in the transport and fuel technology can only have very positive effect in terms of reduction of the global consumption of energy and pollution.

Since 1990s in *US* were born some joint research programs between *US DoE* (Department of Energy) and private companies in order to study and develop a new generation of automotive technology especially oriented, in long terms, to a complete electrification of the road transport systems ad substitution of the oil with "clean" primary energy sources, like hydrogen. The last initiative, called *FreedomCAR*, defines a set of high performance specifications for electric motors for traction especially concerning the efficiency, speed and weight. As will be detailed shown in the first chapter, previous studies suggest that is possible to achieve most of the these requirements, although some of them seem very difficult to get.

The present research aim to investigate some *PM* synchronous motors solutions optimized for the achievement of the aforementioned specifications. Most part of this work was carried out at the Research & Development Department (*DVE*) of Brose Fahrzeugteile GmbH & Co. Kommanditgesellschaft, Würzburg, Germany: this is the headquarters of the electric motors business division of the german multinational automotive company Brose. This facility is the largest production

and design center for electric motors ( $PM$  synchronous and direct current motors), in particular *HVAC* blowers, cooling fan modules, window regulator motors, seatbelt retractor motors, electric power steering motors, *ABS* (Antilock Braking System) motors and drive train actuators. Its most important customers include Behr, Bosch, *BMW*, Continental, Delphi, *TRW*, Valeo, Visteon, Volkswagen and ZF-Lenksysteme.

The present work is organized as follows: after an introductory chapter in which are presented the key point of the *FreedomCAR* program and discussed their relative requested motor specifications also with reference to previous works, the report proceeds in 3 mains parts.

The first describe the preliminary choices used to define the general motor configuration in terms of  $PM$  disposition (surface or internal), number of poles and slots and so winding topology.

The second shows the analytical synthesis procedure that led to define the starting geometry of the machine, estimating the weight and size: the procedure was implemented using MathWorks Matlab®.

The last part explain the Finite Element Analysis (*FEA*) of the motor: starting from an analysis of the rotor shape, this procedure led us to get the final design candidates and analyze in detail the electric and mechanical performances in order to check and achieve the requested specifications. This work was performed using Ansoft Maxwell® while MathWorks Matlab® was used to postprocess the numerical results.

The unique aspect of the design chosen is the rotor shape of the polar islands: in fact wasn't chosen a conventional circular rotor shape but a round shape design (in this case a simple arc of a circumference) in correspondence of polar expansion. This the most used rotor shape in Brose *IPM* synchronous motor for low power (till some chilowatts), low speed (till max speed about  $3000-5000rpm$ ) ranges automotive application, especially power steering, *AMT* (Automated Manual Transmission) [4], *ABS* and *ESP* (Electronic Stability Control). With this work this particular design was extended in the traction field, with high power ( $30/55kW$ ) and speed (max speed  $140000rpm$ ) ranges, getting interesting results.

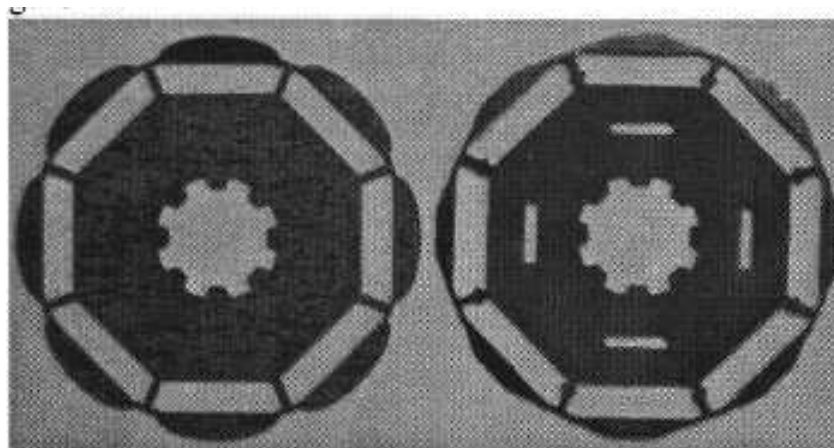


Figure 2: Examples of rotor laminations for round shape design. [4]



# CHAPTER 1

## FREEDOMCAR

### 1.1. Introduction

Established at the beginning of 2002, *FreedomCAR* (term derived from the words "Freedom" and "Cooperative Automotive Research") is a *US* cooperative research program between the *US* Department of Energy (*DoE*) and the main *US* car manufacture companies, regrouped in a consortium, *USCAR* (United States Council for Automotive Research), composed of Chrysler Group *LLC*, Ford Motor Company and General Motors Company. In 2005 and 2009 respectively, this partnership expanded to include 5 energy companies (*BP* America, Chevron Corporation, ConocoPhillips, ExxonMobil and Shell Hydrogen *LLC*) and 2 electric utilities (*DTE* Energy, Southern California Edison). [5]

This new partnership replaces the previous initiative, called *Partnership for a New Generation of Vehicles*, that ran from 1993 till 2001. During the current year (2012) this program will be substituted again with a new initiative called *US Drive* maintaining the same structure and objectives of the previous. [5]

The main long term objective of the *FreedomCAR* program is the development of vehicles and fuel technology that aims to a clean and sustainable energy future, that is address to: [5]

- develop the power and hydrogen storage technologies to enable mass production of affordable Fuel Cell Electric Vehicles (*FCEV*);
- develop the electric propulsion systems applicable to both fuel cell and internal/combustion hybrid electric vehicles (e.g. electric motors, power electronics);
- develop electrical energy storage systems (e.g. batteries, supercapacitors);

- develop innovative combustion and emission control systems for internal combustion engines using a variety of fuels like diesel, hydrogen and renewable sources and investigating innovative concepts such as homogeneous charge compression ignition systems, variable compression ratio, in-cylinder exhaust gas recirculation, etc.;
- develop lightweight structural materials;
- coordinate with public and private entities supporting technology development in order to build a national production and refueling system necessary for the viability of *FCEV*;
- develop the scientific basis for codes and standards to support the hydrogen infrastructure;
- develop a common and standardized component technologies for a wide range of passenger vehicles.

The program is arranged in the following research teams: [7]- [8]

- **Vehicle Technical Teams (*USCAR - DoE*)**
  - Advanced Combustion & Emissions Control.
  - Electrical and Electronics.
  - Electrochemical Energy Storage.
  - Fuel Cells.
  - Materials.
  - Vehicle Systems Analysis.
- **Energy Technical Teams (energy companies - *DoE*)**
  - Fuel Pathway Integration.
  - Hydrogen Delivery.
  - Hydrogen Production.
- **Joint Technical Teams (*USCAR - energy and utility companies - DoE*)**
  - Codes and Standards.
  - Onboard Hydrogen Storage.
  - Grid Interaction.



Table 1.1: Technical targets for *ETS*. [9]

<b>Edition</b>	2015	2020
Maximum speed [ <i>rpm</i> ]	10000	14000
Rated power/max power [ <i>kW</i> ]	55/30	55/30
Specific power [ <i>kW/kg</i> ]	>1.2	> 1.4
Power density [ <i>kW/ℓ</i> ]	> 3.5	> 4
Efficiency (10 ÷ 100% max speed, 20% rated torque) [%]	> 93	> 94
Cost [\$/ <i>kW</i> ]	< 12	< 8

## 1.2. Electric motors requirements

During these years *FreedomCAR* program defines a sets of technical targets for the Electric Traction System (*ETS*, inclusive of the inverter and motor unit), for the year 2015 and 2020 as reported in tab. 1.1. Although the technical targets have been established at the system level, was made an estimation of the electric motor and power electronics performances in order to achieve that specifications. Electric motors are key devices in and the desirable characteristics for traction application can be summarized as follows: [10]

- high torque and power density in order to reduce mass and volumes;
- wide *CPSR* (Constant Power Speed Range) ranging from 3 – 5 times the base speed. The *CPSR* is define as the speed range over the base speed in which rated power can be maintained [11];
- high efficiency over wide speed and torque ranges;
- low torque ripple for reduced noise and vibration;
- intermittent maximum torque capability, extending to nearly twice the rated torque for short durations (usually 15 – 20s);
- high torque for starting and low speed operation for acceleration combined with high power for high speed cruising;
- low cost.

The last release, *FreedomCAR 2020*, aims to develop an electric motor with a rated power of 30*kW*, maximum power 55*kW* (for a limited services 18s): both these values should be developed at rated voltage 325*V DC* leading to important consequence on choice of the appropriate current spatial trajectory, as described in chap. 4. A requested minimum efficiency of 95% in a wide range speed, from the base speed 2800*rpm* to the maximum speed 14000*rpm* (10000*rpm* till

2015 edition [16]) and a low cost of production lower than 275\$ in quantities of 100000s.

According to tab. 1.3 , important constraints are relate to keeping the motor mass under  $35kg$  (power/mass ratio higher than  $1.6kW/kg$ ) and motor volume under  $9.7\ell$  (power/volume ratio higher than  $5.7kW/\ell$ ), the torque ripple doesn't exceed at any speed 5% and the line to line back  $EMF$  is lower than  $600V$  peak in case of inverter failure at maximum speed ( $UCG$ , UnControlled Generator operation) [12] during which the current no longer support the fluxweakening of the motor, leading to a great increase of the  $EMF$  and so the  $DC$  bus voltage, value that can compromising especially the seal of the condensators pack. The machines will be liquid cooled with a coolant inlet temperature of  $105^{\circ}C$ .

The request mechanical characteristic is typical for traction application: from 0 to base speed operation mode is with available constant torque while for higher speed the available torque decrease till the maximum speed. In this last area one important feature requested is a  $30kW$  constant power produced, with a  $CPSR$  equal to 5 : 1. Therefore, ideally, the torque should reduce itself according to an hyperbolic law.

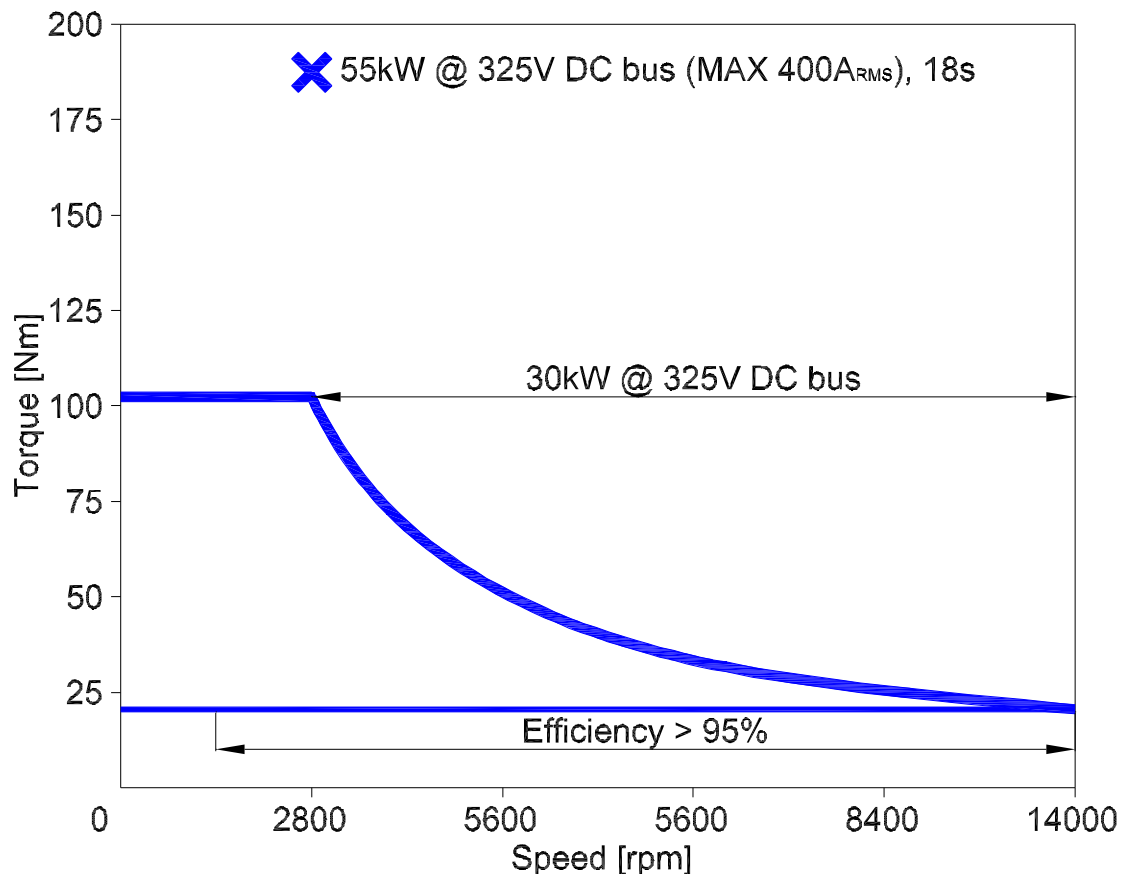


Figure 1.1: *FreedomCAR* 2020 target available torque vs. speed.

Table 1.2: *FreedomCAR* 2020 specifications [10]

Specifications	Target	Conditions
Max speed	14000rpm	
Continuous output power	30kW	- 20 ÷ 100% max speed - rated voltage
Peak output power	55kW	- limited service, 18s - 20% max speed - rated voltage
Efficiency	> 95%	- 10 ÷ 100% max speed - 20% rated torque
Torque ripple	< 5% peak torque	- 0 ÷ 100% max speed
DC bus operating voltage	200 ÷ 450V 325V rated	
Max phase current	400A <sub>RMS</sub>	
Characteristic current	< 400A <sub>RMS</sub>	
Line-to-line back <i>EMF</i>	< 600V <sub>peak</sub>	- max speed
Max isolation impedance	1MΩ	
Mass	< 35kg	- with frame
Volume	≤ 9.7ℓ	- with frame
Ambient operating temperature	−40 ÷ 140°C	- outside housing
Coolant inlet temperature	105°C	
Max coolant flow rate	10ℓ/min	
Max pressure drop	13.79kPa	
Max coolant inlet pressure	137.8kPa	
Unit cost	≤ 275\$	- in quantities of 100000

### 1.3. State of art of the research: important issue

In the last years some authors (Reddy, El-Refaie, Huh, Tangudu, Jahns, Bohn, McClear) investigate the design of an electric motor in order to aim *FreedomCAR* targets: their research, oriented both on Interior Permanent Magnet (*IPM*) and Surface Permanent Magnet (*SPM*) design, suggest that it's possible to meet most of these requirements, although two specifications seems very difficult to achieve.

#### 1.3.1. Efficiency at partial load (20% rated torque) for wide speed range 10 ÷ 100% maximum speed > 95%

Because of the high requested maximum speed of the machine, 14000rpm, the rotor losses caused by the space *MMF* harmonic contents aren't negligible [8] and this lead to reduction of the efficiency at high speeds. Comparing to the iron, due to the low resistivity (about 1/3 for a typical *NdFeB*) and absence of lamination, the *PM* eddy current losses prove to be very high (till about 2kW), the main losses component at high speed, and this suggest that a segmentation is mandatory (axial, circumferential or both). However this doesn't seem enough to achieve an electrical efficiency, and more so a total efficiency higher than 95%; none of the previous *FreedomCAR* designs (see [10] - [12] - [13] - [14]) are be able to achieve this important target.

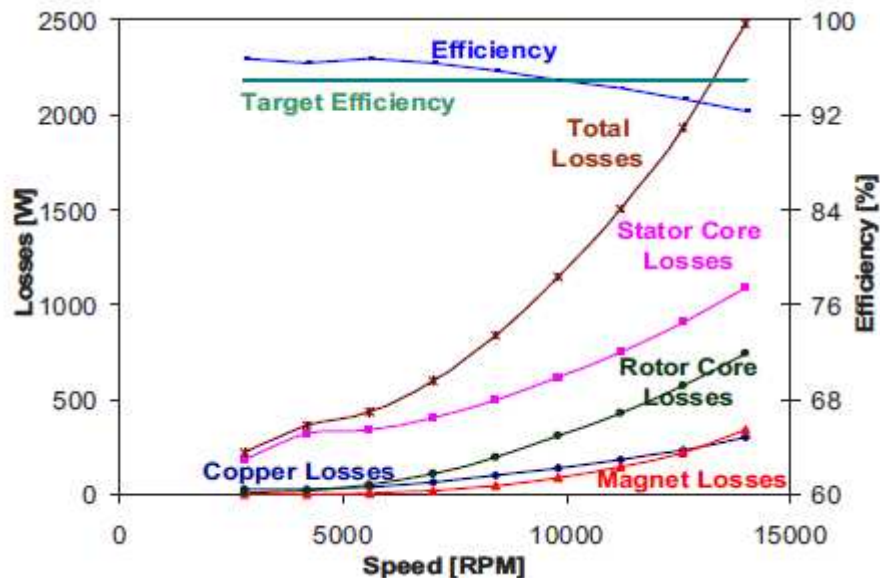


Figure 1.2: 2011 J.K. Tangudu *et al FreedomCAR* design: predicted machine losses for wide speed operation under partial load (20% rated torque) conditions. [14]

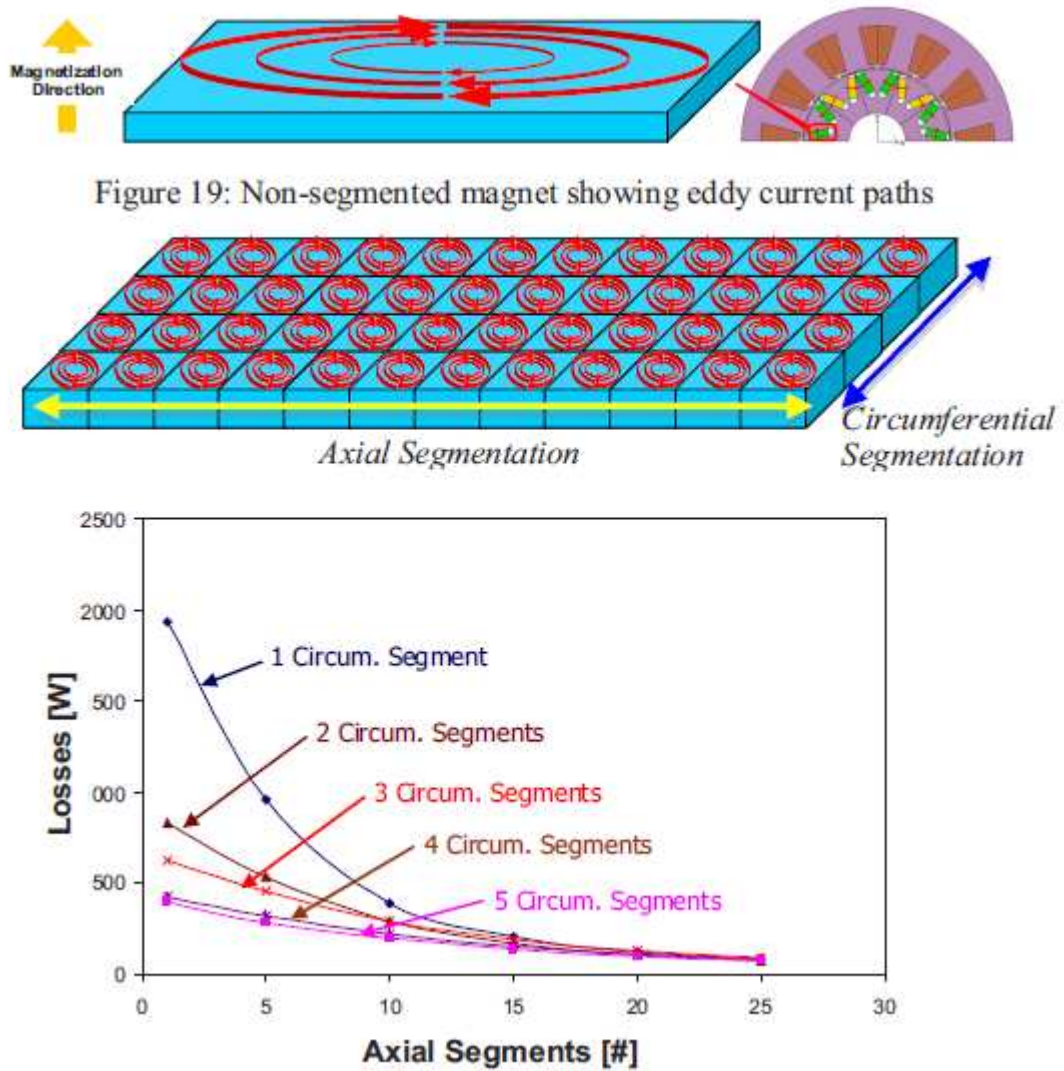


Figure 1.3: 2011 J.K. Tangudu *et al FreedomCAR* design: predicted *PM* eddy current losses in function of axial and circumferential segments at maximum speed. [14]

### 1.3.2. Line-to-line back *EMF* at max speed $< 600V_{peak}$

From the d/q reference frame voltage equation, in no load operation,

$$\begin{cases} E_d = 0 \\ E_q = 2 \cdot \pi \cdot \frac{n}{60} \cdot p \cdot \Lambda_{PM} \end{cases} \quad (1.1)$$

where:

$E_d$  is the d-axis phase voltage;

$E_q$  is the q-axis phase voltage;

$p$  is the number of pole pairs;

Table 1.3: *aaa*

$p$	[-]	2	3	4	5	6
$\Lambda_{PM}$	[ $mWb_{peak}$ ]	<118.0	< 78.6	< 59.0	< 47.2	< 39.3

$n$  is the speed;

$\Lambda_{PM}$  is the  $PM$  flux linkage;

The back  $EMF$  is,

$$E_0 = E_q = 2 \cdot \pi \cdot \frac{n}{60} \cdot p \cdot \Lambda_{PM} \quad (1.2)$$

Assuming a Y connection, the line-to-line back  $EMF$   $V_0$  is,

$$V_0 = \sqrt{3} \cdot 2 \cdot \pi \cdot \frac{n}{60} \cdot p \cdot \Lambda_{PM} \quad (1.3)$$

Explaining the flux linkage, we get,

$$\Lambda_{PM} \leq \frac{60 \cdot V_0}{\sqrt{3} \cdot 2 \cdot \pi \cdot n \cdot p} \quad (1.4)$$

In order to achieve the  $600V_{peak}$  @  $14000rpm$  limit, is possible to estimate  $\Lambda_{PM}$  as follows,

$$\Lambda_{PM} \leq \frac{60 \cdot 600}{\sqrt{3} \cdot 2 \cdot \pi \cdot 14000 \cdot p} = \frac{0.236}{p} \quad (1.5)$$

But an envisage reduction of this flux linkage lead also to a degradation of the torque countervailable only with an increase of the current to obtain the same torque: this issue is clearly evident in previous research in which none of the motor designs (see [10] - [12] - [13] - [14]) are be able to achieve this voltage target. In fact it can be shown that, neglecting the reluctance torque component, if present (this is especially true as higher the level of saturation or in  $SPM$  machines), we can express the  $PM$  flux linkage as follows,

$$\Lambda_{PM} = \frac{2}{3} \cdot \frac{T}{p \cdot \sqrt{2} \cdot I} \quad (1.6)$$

where:

$T$  is the torque;

$I$  is the stator current;

Substituting in eq. 1.3, considering as working conditions the maximum speed and torque ( $n_{MAX} = 14000rpm$ ,  $T_{MAX} \cong 188Nm$ ), we get the hyperbolic relationship between the minimum required current and and line-to-line back  $EMF$ ,

$$I = \frac{1}{\sqrt{2}} \cdot \frac{\sqrt{3} \cdot 4 \cdot \pi \cdot n_{MAX} \cdot T_{MAX}}{3 \cdot 60 \cdot V_0}; \quad (1.7)$$

As reported from fig. 1.4, in which are highlighted the upper limits for current ( $400A_{RMS}$ ) and line-to-line back  $EMF$  ( $600V_{peak}$ ) the design area is very narrow explaining the difficulty for getting this target. However this specification, in the original edition, can be exceeded if system requirements are met, suggesting that additional protective provisions have been implemented to prevent excessive  $DC$  link voltage under fault operation. [16]

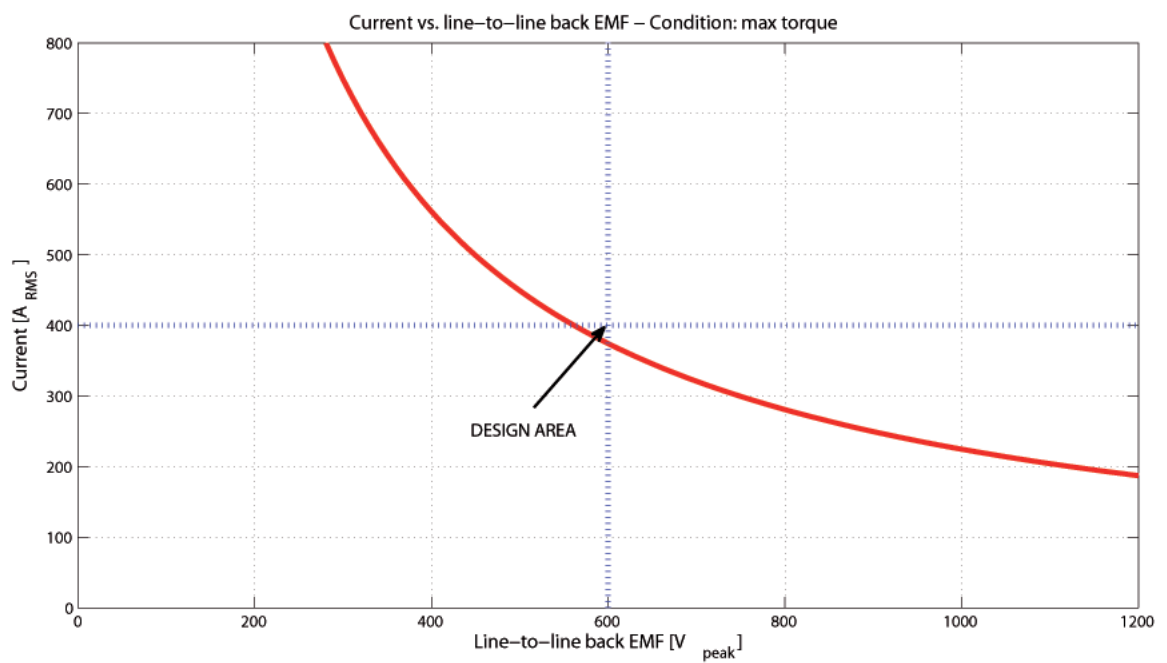


Figure 1.4: Theoretical minimum current rating vs. line-to-line back  $EMF$





## PRELIMINARY ANALYSIS

The preliminary analysis has the objective to explore the possible best configurations of the *PM* machines, that will be subsequently studied and developed using analytical synthesis and tuned and optimized by *FEA*. This is an important phase because the final performance are strictly relate to these fundamental choices. The guidelines are summarized as follows.

- Motor configuration: *IPM*, *SPM*.
- Number of poles and slots, winding topology

### 2.1. Motor configuration: *IPM*, *SPM*

The key factors that we have considered are listed below.

#### 2.1.1. Flux weakening (*FW*) capability

The *FW* capability defines the width of the speed range over the base speed in which the d-axis current is gradually increase in negative sense, reducing in this way the d-axis flux linkage, ensuring the maintenance of the rated voltage limit: if is required a wide speed range, like for our application, the motor must show an high *FW* area. Let's consider the d/q-reference frame voltage equations in steady state operation, for a generic *IPM* motor, assuming magnetically linear.

$$\begin{cases} E_d = R \cdot I_d - \Omega_{me} \cdot L_q \cdot I_q \\ E_q = R \cdot I_q + \Omega_{me} \cdot (\Lambda_{PM} + L_d \cdot I_d) \end{cases} \quad (2.1)$$

where:

$R$  is the phase resistance;

$I_d$  is the d-axis current;

$I_q$  is the q-axis current;

$\Omega_{me}$  is the electrical speed;

$L_d$  is the d-axis synchronous inductance;

$L_q$  is the q-axis synchronous inductance;

For a *SPM* machine the inductances are equal to one another, so  $L_d = L_q = L$ .

The working area is defined by intersection between current limit and voltage limit regions, represented by the following equations,

$$\begin{cases} I^2 = I_d^2 + I_q^2 \leq I_n^2 \\ E^2 = E_d^2 + E_q^2 \leq E_n^2 \end{cases} \quad (2.2)$$

where:

$I_n$  is the rated current;

$E_n$  is the rated phase voltage.

The first relation define the current limit and it's the equation of a circumference with center in the origin in the d/q-plane with radius equal to the rated current. The second equation represent the voltage limit and can be expressed, by substitution from eq. 2.1 as follows,

$$(R \cdot I_d - \Omega_{me} \cdot L_q \cdot I_q)^2 + (R \cdot I_q + \Omega_{me} \cdot (\Lambda_{PM} + L_d \cdot I_d))^2 \leq E_n^2 \quad (2.3)$$

Neglecting the resistive drop voltage, we get,

$$\Omega_{me}^2 \cdot L_q^2 \cdot I_q^2 + \Omega_{me}^2 \cdot (\Lambda_{PM} + L_d \cdot I_d)^2 \leq E_n^2 \quad (2.4)$$

$\Rightarrow$

$$L_q^2 \cdot I_q^2 + (\Lambda_{PM} + L_d \cdot I_d)^2 \leq \frac{E_n^2}{\Omega_{me}^2} \quad (2.5)$$

$\Rightarrow$

$$\frac{L_q^2}{L_d^2} \cdot I_q^2 + \left( \frac{\Lambda_{PM}}{L_d} + I_d \right)^2 \leq \frac{E_n^2}{\Omega_{me}^2 \cdot L_d^2} \quad (2.6)$$

The previous relation describe the equation of ellipse in in d/q-plane with center in  $C(-I_{ch}, 0)$ ;  $I_{ch}$  is called characteristic current and proves to be equal to,

$$I_{ch} = \frac{\Lambda_{PM}}{L_d} \quad (2.7)$$

It's important to note that for *SPM* motors, the ellipse voltage limit degenerates to a circumference and  $C$  is its center. As the machines is, in general, not magnetically linear, the characteristic current is equivalent to the d-axis current in which the d-axis flux linkage is equal to zero.  $I_{ch}$  is an important parameter because its value define the power trend and speed performance of the machine. We have three possible cases:

1.  $I_{ch} > I_n$ , the voltage limit ellipse center is located outside of current limit circumference: it follows that the machine exhibit a short *FW* area because there is an electrical speed limit achieved in point F ( $-I_n, 0$ ) (fig. 2.1a). The motor works in constant available torque in *MTPA* (Maximum Torque per Ampère) locus, operating in point B till base speed (region 1) and after going in *FW* along the current limit circumference till maximum speed (region 2), with a decreasing available torque (fig. 2.2).
2.  $I_{ch} < I_n$ , the voltage limit ellipse center is located inside of the current limit circumference: it follows that the machine exhibit a wide *FW* area because there isn't an electrical speed limit (there is only a mechanical limit) (fig. 2.1b). As the previous case, the machine operate in constant available torque in *MTPA* locus, working in point B till base speed (region 1) and after going in *FW* along the current limit circumference till point F (region 2), in which intersects the *MTPV* (Maximum Torque per Voltage) with a decreasing available torque, achieving the center of the ellipse at theoretical infinite speed (region 3) (fig. 2.3).
3.  $I_{ch} = I_n$ , the voltage limit ellipse center is located exactly in the current limit circumference: this is a particular case of the previous. The machine exhibit in fact a wide *FW* area because there is no electrical speed limit; this is the best way to reach the *CPSR* (Costant Power Speed Range) operation mode.

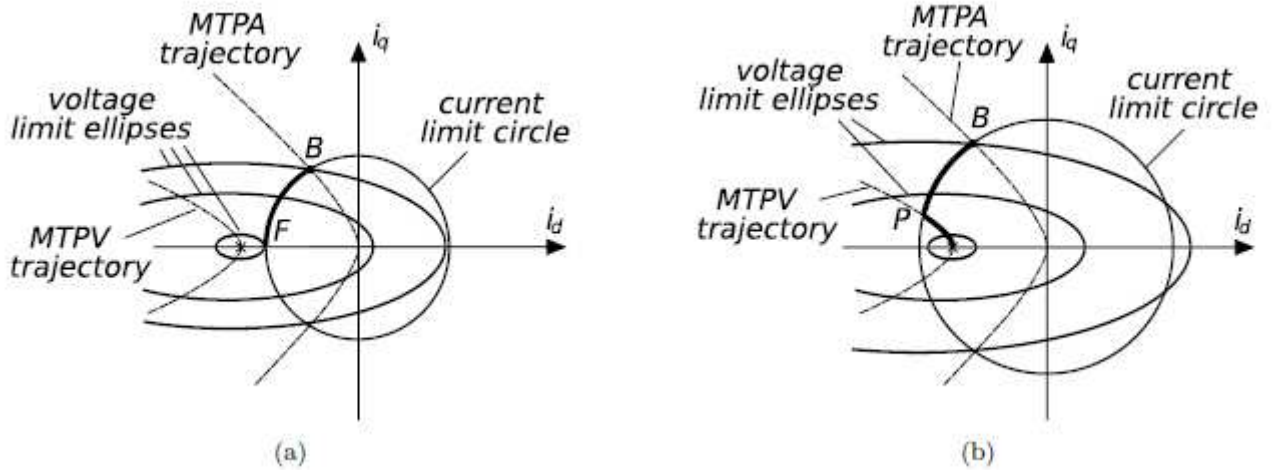


Figure 2.1: Current spatial vector trajectory: (a)  $I_{ch} > I_n$ , (b)  $I_{ch} < I_n$ . [19]

*IPM* synchronous motor are often know to be, in general, ideal candidates for *FW* and *CPSR* applications. In fact, for *SPM* machine, due to the magnets mounted on the rotor surface and the bandage necessary to ensure resistance to centrifugal stresses, the reluctance path is higher than an equivalent *IPM* synchronous motor, so the synchronous inductance prove to be usually lower than d-axis synchronous inductance, leading to an higher characteristic current, often higher of the rated

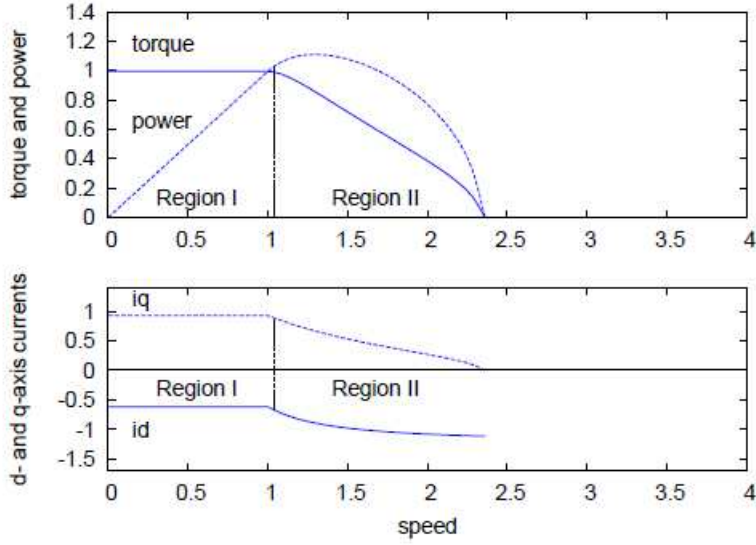


Figure 2.2: Torque/current vs. speed for  $I_{ch} > I_n$  case. [19]

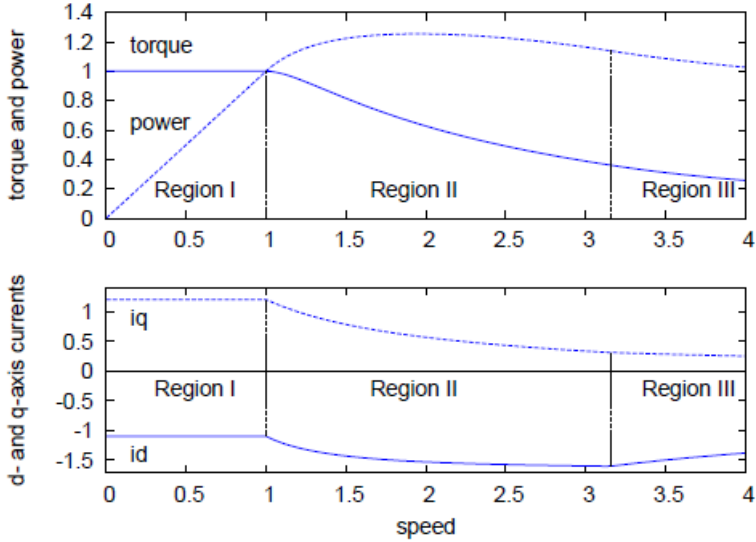


Figure 2.3: Torque/current vs. speed for  $I_{ch} < I_n$  case. [19]

current. For this reason *SPM* machine usually fall in case 1, with a torque-speed curve not suitable to our traction application.

We can evaluate the optimal characteristic current, as described in the last case; assuming a linear modulation of the source inverter the rated phase voltage is,

$$E_n = \frac{V_{DC}}{\sqrt{3} \cdot \sqrt{2}} \cong 132V_{RMS} \quad (2.8)$$

As a result, the estimated rated current absorbed by the machine when it develop the rated power  $P_n = 30kW$  at rated DC bus voltage  $V_{DC} = 325V$ , assuming a

power factor  $\cos \varphi = 0.9$  and efficiency  $\eta = 0.95$ , is,

$$I_n \cong \frac{P_n}{3 \cdot \frac{V_{DC}}{\sqrt{3} \cdot \sqrt{2}} \cdot \cos \varphi \cdot \eta = 0.95} = \frac{30 \cdot 10^3}{3 \cdot \frac{325}{\sqrt{3} \cdot \sqrt{2}} \cdot 0.9 \cdot 0.95} \cong 88 A_{RMS} \quad (2.9)$$

Designing our motor to achieve  $I_{ch}$  close to  $I_n \cong 88 A_{RMS}$  gives us the basis for achieving excellent *FW* performance.

### 2.1.2. Anisotropy level

The anisotropy level of a synchronous motor is quantified by the saliency ratio  $\xi$ , defined as follows,

$$\xi = \frac{L_q}{L_d} \quad (2.10)$$

For an *IPM* machine is higher than 1 while equal to 1 for *SPM*. This ratio has got a great influence on the torque developed by the machine expressed by,

$$T = \underbrace{\frac{3}{2} \cdot p \cdot \Lambda_{PM} \cdot I_q}_{T_{cyl}} + \underbrace{\frac{3}{2} \cdot p \cdot (L_d - L_q) \cdot I_d \cdot I_q}_{T_{rel}} \quad (2.11)$$

Where:

$T_{cyl}$  is the cylindrical torque, caused by the interaction between the *PM* flux linkage and q-axis current. It's the only component of the torque in *SPM* machine.

$T_{rel}$  is the reluctance torque and depends by the anisotropy level of the motor. It can be expressed as follows,

$$T_{rel} = \frac{3}{2} \cdot p \cdot (1 - \xi) \cdot L_d \cdot I_d \cdot I_q \quad (2.12)$$

Comparing to the *SPM* machines, in *IPM* motors both  $I_d$  and  $I_q$  current are "active components" for the torque, and this allows to reduce the flux linkage  $\Lambda_{PM}$  or, in other hands, permits to decrease the magnitude of the current needed for a given torque. This aspect is more evidenced when the machines works in *FW*: in a *SPM* motor is necessary to impose a d-axis current that doesn't contribute to the torque and it's generally a drawback for this kind of motor because of related copper losses: however, in this last kind of machines, it's possible to reduce *PM* flux linkage, but this leads to a degradation of the torque performances.

Reducing *PM* flux linkage allow to reduce also the back *EMF*, usually lower than the value in a *SPM* motors for given torque, and decrease the mass of the *PMs*: this last feature is becoming very desirable in the last years with the arise of the cost of magnet materials. Besides, a reduction of *PM* flux linkage causes the diminution of the characteristic current, making easier the achieving of a *CPSR* mode ( $I_{ch} \cong I_n$ ).

Finally, *IPM* machines can exhibit an higher torque/mass and so power/mass ratio.

Is immediate to realize that the previous argumentations are the more true than

the higher is the anisotropy of the machines and in this case we usually call this machines as *IPMPMASR* (*PM Assisted Synchronous Reluctance*): the saliency ratio is influenced by many factors, that will be illustrated hereafter, slots-poles combination and *PMs* distribution inside the rotor.

### 2.1.3. *PMs* collocation

In *IPM* machines magnets are inside the iron and they're shielded by the rotor steel that represents a preferable path for the armature reaction flux: for these reason, it's possible to employ thinner *PMs* and reduce their masses and impact on the total costs of the machine. Besides, it's possible to employ conventional straight *PMs* while *SPM* machines are usually characterized by a round shape with a consequent increase of their cost of production.

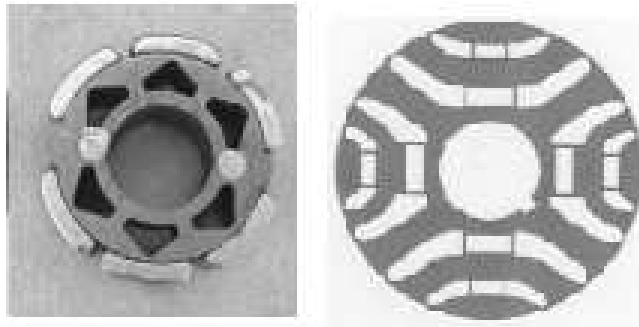


Figure 2.4: An example of *SPM* and *IPM* rotor. [17]

### 2.1.4. Conclusions

I consider for my design the *IPM* topology: I study a simple I-shape, radial magnetization with only one flux barrier per pole and a V-shape design.

## 2.2. Number of poles and slots, winding topology

### 2.2.1. Influence of number of poles

The number of poles has got effects on the machine performance and motor dimension and this is of particular importance for attaining *FreedomCAR* specifications. The main quantities relate to it are:

#### 1. Frequency

The frequency  $f$  of the source quantities, as is know, is directly proportional to the number of poles pairs  $p$  by the speed of the machine.

$$f = \frac{p \cdot n}{60} \quad (2.13)$$

The iron losses  $P_{Fe}$  can be expressed by the equation,

$$P_{Fe} = \underbrace{k_{hys} \cdot f \cdot \widehat{B}^2}_{P_{hys}} + \underbrace{k_{ec} \cdot f^2 \cdot \widehat{B}^2}_{P_{ec}} \quad (2.14)$$

Where:

$k_{hys}$  and  $k_{ec}$  are the hysteresis and eddy current coefficients respectively;  
 $\widehat{B}$  is the flux density (peak value).

Since the requested max speed is very high ( $n_{MAX} = 14000rpm$ ) and so the iron losses, is convenient to keep the frequency and hence the number of poles as low as possible.

## 2. Induced reaction

As will be shown in chapter 3, the induced reaction  $\Delta B$  is proportional to,

$$\Delta B \propto \frac{1}{2 \cdot p \cdot h_{PM}} \quad (2.15)$$

Where  $h_{PM}$  is the *PM* height.

Consequently, in this case, an increase of number of poles produces benefits because being the induced reaction bound by the type of the used *PM*, is possible to reduce the *PM* height and so the amount and cost of the required magnets.

## 3. Flux per pole

The flux per pole  $\phi$  influence the yoke dimension. In fact it's relate to the back iron flux  $\phi_{bi}$  as follows,

$$\phi_{bi} \propto h_{bi} = \frac{1}{2} \cdot \phi \propto \frac{1}{2 \cdot p} \quad (2.16)$$

So an increase of number of poles allows to reduce the back iron height and saving on the amount of the stator iron.

It can therefore be stated that, if on the one hand the reduction of number of poles can reduce the losses, on the other hand this leads to an increase of geometrical dimensions and weight of the machine. But, because the efficiency seems the most problematic arguments in *FreedomCAR* motors while the dimensions constraints aren't, I decide to give priority to a reduction of number of poles.

### 2.2.2. Influence of number of slots / number of poles combination

Motor performance, like torque, losses, strongly depends not only by the number of poles but also by the combination with the number of slots  $Q$  chosen. In this paragraph we discuss about the main quantities relate to them, as follows.

#### 1. Winding factor

The winding factor  $k_w$  ( $\leq 1$ ) is an important index of the quality of the

selected winding. In fact, as will be shown in the next chapter, it influences the electric loading  $\widehat{K}_s$  and so the developed torque  $T$ , as explained by the following relationship,

$$\widehat{K}_s \propto k_w \cdot I \quad (2.17)$$

$\Rightarrow$

$$T \propto \widehat{K}_s \quad (2.18)$$

Good windings, with  $k_w \cong 1$  has got the best electromagnetic use because the phase current  $I$  totally contribute to the developed torque. Low winding factor machines need to compensate the consequent lower torque with an increase of the current and this leads to higher copper losses. In order to deeply understand this aspect we make a comparison between two different winding factor machines: the first, as reference, has got  $k_w = 1$ , while the second, for e.g.  $k_w = 0.866$ : this means that for having the same torque with the same geometrical and number of poles machine, the lower winding factor machine require a current about 15.5% higher, with copper losses as much as 33.4% higher than the reference machine.

## 2. Rotor losses

As evidenced in the previous chapter, rotor losses due to iron losses and eddy current losses, in *FreedomCAR* designs prove to be very high as a consequence of the high speed required.

Because of the slots hasn't got a continue and sinusoidal distribution along the stator circumference the *MMF* (Magneto Motive Force) hasn't got a sinusoidal spatial distribution, with harmonic and subharmonic contents: this *MMF* harmonics are asynchronous with the rotor field (only the main harmonic is synchronous) and hence its iron is invested to a variable magnetic field, and consequently is source of of hysteresis and eddy current losses.

As described in [17], between these harmonics the most important are called slots harmonic because they are characterized by the same winding factor of the main harmonic  $p - th$ , and so important cause of rotor losses. The slot harmonic order  $h_{sh}$  follows the relation,

$$h_{sh} = k \cdot Q \pm p \quad (2.19)$$

Where  $k = 0, 1, 2, \dots$

The frequency  $f_h$  induced in the rotor can be expressed by the following equation [18],

$$f_h = f \cdot \left( sgn - \frac{h}{p} \right) \quad (2.20)$$

Where *sgn* is a sign function and indicates the rotation direction of the  $h - th$  harmonic: when is equal to 1 it rotates in the same direction of the rotor while it's  $-1$  when the harmonic rotate in the opposite direction.

The harmonic contents strongly depends by the winding topology: an index



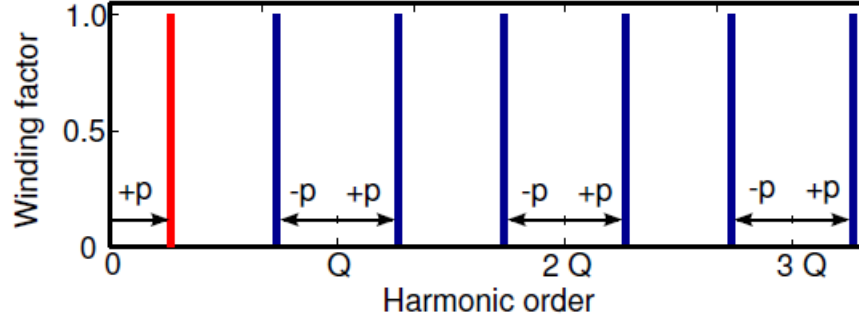


Figure 2.5: An example of slot harmonic orders. [17]

that define this aspect is the coil throw  $y_q$ , given by the follow equation rounded to the lower integer (min value, 1),

$$y_q = \text{fix} \left( \frac{Q}{2 \cdot p} \right) \quad (2.21)$$

When:

- $y_q > 1$ , the winding is a conventional *ISDW* (Integral Slot Distributed Winding);
- $y_q = 1$ , the winding is a *FSCW* (Fractional Slot Concentrated Winding) in which there aren't overlapped coils or, in other words, coils are wounded around a single tooth. [17]

It's show that this ratio ultimately has got great influence on the rotor losses (see [22] for a detailed evaluation of a rotor losses index), as described, for a 3-phase machine in fig 2.6. We can evidence some minima for a single and double layer winding; moving away from these lines, the rotor losses always increase as explained by the white arrows. We can find:

- a global minima in  $Q/2 \cdot p = 3$  ( $y_q = 3$  that means it's achieved only with a *ISDW*);
- first local minima in  $Q/2 \cdot p = 2.5$  ( $y_q > 2$ ), for a double layer winding only: it's achieved again only with a *ISDW*;
- second local minima in  $Q/2 \cdot p = 1.5$  ( $y_q = 1$ ), for both single and double layer winding that is in this case a *FSCW*;
- third local minima in  $Q/2 \cdot p = 1$ , ( $y_q = 1$ ), for a single layer and *FSCW*.

### 3. Cogging torque

The cogging torque  $T_{cog}$  is generated by the variation of the permanence in the airgap [20]. It is relate to the cogging torque index  $I_{cog}$  equal to Lowest Common Multiple between number of slots and poles,

$$I_{cog} = LCM(Q, 2 \cdot p) \quad (2.22)$$

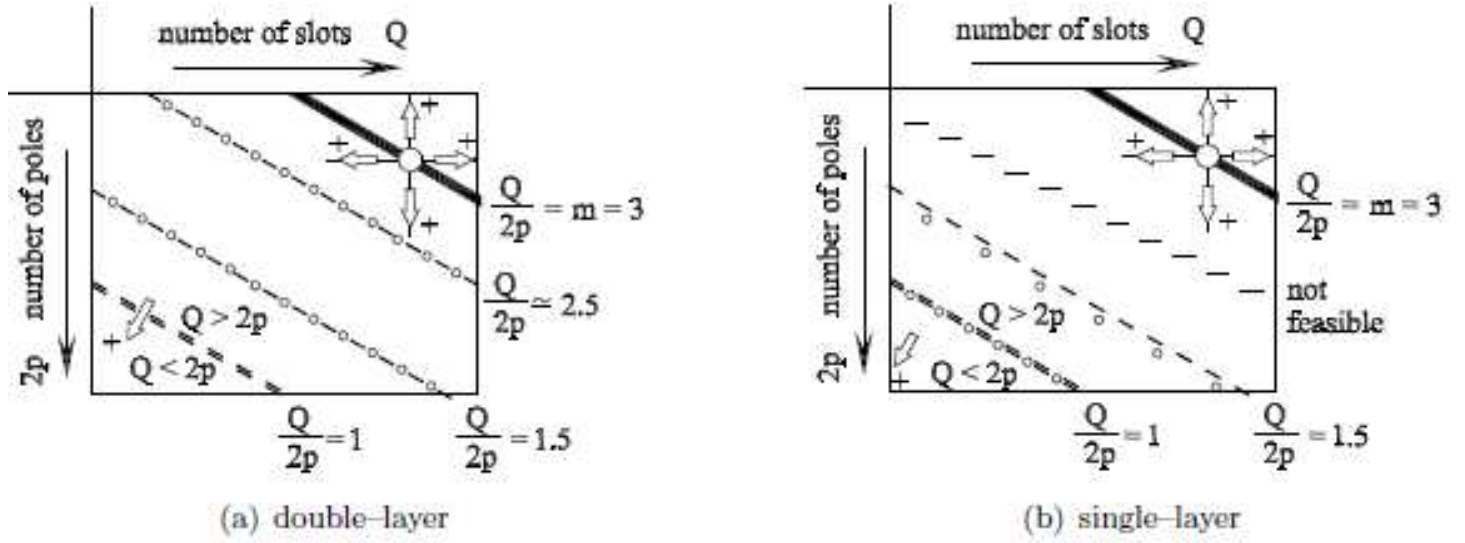


Figure 2.6: Rotor losses trends and minima in function of number of slots and poles. [18]

This parameter should be as high as possible: in fact the harmonic frequency relate to this *LCM* represent the fundamental of the cogging torque frequency, consequently choosing a suitable combination  $Q/2 \cdot p$  that makes high it, means a low value of its magnitude. [21]

It's important to underline that low cogging torque don't means always a low torque ripple. [20]

#### 4. Radial force

The radial forces on the machine depends by its symmetry. This is evaluated by and index,  $I_{rf}$  that is the the Great Common Divisor between number of slots and poles, as follows,

$$I_{rf} = GCD(Q, 2 \cdot p) \quad (2.23)$$

This value should be, for a low radial force, an even number [21].

#### 2.2.3. Winding topology: *FSCW*, *ISDW*

The theoretical number of slots per pole and phase  $q$  for having a *FSCW* can be calculate as follows: from the coil throw  $y_q$ ,

$$y_q < 2 \quad (2.24)$$

$\Rightarrow$

$$\frac{Q}{2 \cdot p} < 2 \quad (2.25)$$

$\Rightarrow$

$$3 \cdot q < 2 \quad (2.26)$$

⇒

$$q < \frac{2}{3} \Rightarrow q < 0.67 \quad (2.27)$$

Comparing to *ISDW*, *FSCW* has got the follows advantages.

1. **Higher fill factor**, especially building the machine with a segmented stator (values in the order of  $k_{fill} = 0.55$  [15]).
2. **Lower end winding length** [19] because each phase is made up coils wrapped around the teeth: so the copper mass and hence the Joule losses are reduced with an higher efficiency for having the same torque. Another consequence is a lower total length given by the sum between the stack length and the total end winding thickness [22], as illustrated in fig. 2.7.

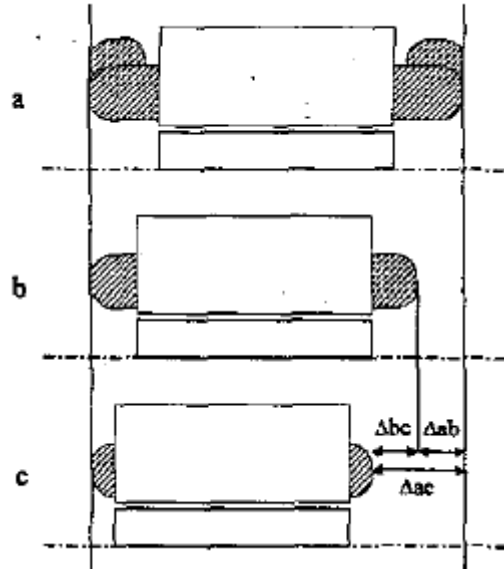


Figure 2.7: Comparison of machines with (a) distributed winding and (b) concentrated, single layer (c) double layer winding. [22]

3. The two previous arguments lead to an **higher power density ad manufacturing simplicity**.
4. The **cogging torque and usually the torque ripple are lower** because it's easy to have an higher  $LCM(Q, 2 \cdot p)$  (in fact  $Q \rightarrow 2 \cdot p$ ).
5. **Higher synchronous inductance**: that means a lower characteristic current that makes the motor more suitable for traction application (wide *FW* area); this make, for the first time, *SPM* motors suitable for *FreedomCAR* speed range [21]: in fact some authors (see [13] - [16]) use with success, for their projects, this kind of motor. Besides, the short circuit current is limited in the event of fault, important when the application required a fault tolerant behavior [19].

6. This last specification is increased by a **perfect electrical separation between phases when using single layer winding**. [19]

But, on the other hands, the disadvantages respect to *ISDW*, can be summarized in the follows points.

1. **Higher *MMF* spatial harmonic content**: as mentioned in the previous paragraph this produces higher rotor losses, iron saturation, *PM* stress and unbalanced torque. [19]
2. **Saliency ratio is generally lower** [23]: *FSCW* motors doesn't exhibit high reluctance torque so, for having the same current and torque performance, is necessary to increase the *PM* flux linkage and hence elevating the back *EMF* at max speed. Analysis [24] suggest the highest saliency ratios are achieved with  $q \geq 0.33$ : in fact when it's less than 0.33 the slot pitch exceeds one full pole pitch, resulting in heavy filtering of the magnetic permanence difference between d and q axis. The highest is reached with  $q = 0.5$  and with double layer configuration.
3. The **winding factor, in some cases, is low** [19], that means a lower torque density [17]. It's shown that high winding factor  $k_w \geq 0.866$  is achieved when  $q = 0.25 \div 0.5$  [24].

*FSCW* is the preferred winding for Brose electric motors, often used with segmented stator.

#### 2.2.4. Conclusions

I choose for my design a *FSCW*, double layer (three phase, Y connection). In order to evaluate the best  $Q/(2 \cdot p)$ , I study all the possible combination, considering the previous arguments, summarized as follows:

1. reduce as much as possible the number of poles  $2 \cdot p$ ;
2. high winding factor  $k_w$ , that means  $q = 0.25 \div 0.5$ , or in other words,  $Q = (0.75 \div 1.5) \cdot 2 \cdot p$ ;
3. keep the saliency ratio as high as possible, choosing  $q > 0.33$ , that means  $Q \geq 2 \cdot p$ ;
4. the previous two points restrict the slots / poles configuration to  $Q = (1 \div 1.5) \cdot 2 \cdot p$ ;
5. reduce as much as possible the rotor losses choosing an appropriate  $Q/2 \cdot$  equal or however close to 1.5;
6. high cogging torque index  $I_{cog}$ ;
7. the radial force index  $I_{rf}$  should be even.

Table 2.1: Possible *FSCW* slots / poles combination.

$2 \cdot p$	$Q$	$q$	$k_{w,1}$	$Q/(2 \cdot p)$	$I_{cog}$	$I_{rf}$
4 (max 467Hz)	6	0.5	0.866	1.5	12	2
6 (max 700Hz)	9	0.5	0.866	1.5	18	3
8 (max 933Hz)	9	0.38	0.945	1.13	72	1
	12	0.5	0.866	1.5	24	4
10 (max 1167Hz)	12	0.4	0.933	1.2	60	2
	15	0.5	0.866	1.5	30	5
12 (max 1400Hz)	18	0.5	0.866	1.5	36	6
14 (max 1633Hz)	15	0.36	0.951	1.07	210	1
	18	0.5	0.902	1.28	126	2
	21	0.5	0.866	1.5	42	7

The winding factor  $k_w$  is given by,

$$k_w = k_d \cdot k_p \quad (2.28)$$

Where:

$k_d$  is the distributed factor;

$k_p$  is the pitch factor;

The distributed factor  $k_d$  is equal to the ratio between the geometrical and arithmetic sum of the *EMF* slots phasors of the same phase. According to the theory of star of slot [17], for *FSCW*, the main harmonic it's given by the follow relationship,

$$\begin{cases} k_d = \frac{\sin\left(\frac{q_{ph} \cdot \alpha_{ph}}{4}\right)}{q_{ph} \cdot \sin\left(\frac{\alpha_{ph}}{2}\right)} \rightarrow q_{ph} = \text{even} \\ k_d = \frac{\sin\left(\frac{q_{ph} \cdot \alpha_{ph}}{4}\right)}{q_{ph} \cdot \sin\left(\frac{\alpha_{ph}}{2}\right)} \rightarrow q_{ph} = \text{odd} \end{cases} \quad (2.29)$$

Where:

$q_{ph} = Q/(3 \cdot t)$  is the number of spokes per phase of the star of slots;  $t = GDC(Q, p)$  is the machine periodicity, or in other words, the number of phasors for the same spoke;

$\alpha_{ph} = (2 \cdot \pi)/(Q/t)$  is the angle between two spokes;

The pitch factor  $k_p$  is given by,

$$k_p = \sin \frac{2 \cdot \pi p \cdot y_q}{2 \cdot Q} \quad (2.30)$$

Analyzing tab. 2.1 we note that there isn't a combination the achieve all the stated objectives simultaneously: machines with the best rotor losses index (1.5)

present low winding factor, and this can lead to a reduction of efficiency; viceversa, high winding factor motors usually don't have good rotor losses performances. Besides, concerning the cogging torque index there is only two configurations, the 15/14 and 18/14, with an exceptional value. A good candidate combination seems to be this last one, but as the problem of the iron losses, in which the stator is, anyway, the main component (more than proportional to the frequency), is very important to keep the number of poles as low as possible. Consequently I choose the 12/10 configuration.

## ANALYTICAL SYNTHESIS

The objective of this chapter is to evaluate the main geometry of the machine, slots and windings dimension, masses and volumes in order to define the starting machine design that will be subsequently analyzed, tuned and optimized using *FEA*.

## 3.1. "SPM equivalent motor"

The analytical procedure that will be showed hereafter allows to evaluate the main dimensions of an equivalent *SPM* machine: the conclusion are however valid for an *IPM* topology. Let's consider a transversal section of the machine, as showed in fig. 3.1. We can transform it in an equivalent machine with an equivalent airgap  $g''$  defined through the Carter coefficient  $k_{Carter}$  that takes into account the non-constancy of the airgap due the slots (defined by a conformal transformation) and the saturation coefficient  $k_{sat}$  that takes into account the not infinite value of the iron permeability and hence the presence of a magnetic voltage drop along iron paths.

$$g'' = k_{Carter} \cdot k_{sat} \cdot g \quad (3.1)$$

in which,

$$k_{Carter} = \frac{p_s}{p_s + g - \frac{3}{4} \cdot w_{so}} \quad (3.2)$$

$$k_{sat} = \frac{\Sigma(H \cdot l)}{\Sigma(H \cdot l)_{airgap}} \quad (3.3)$$

Where:

$p_s$  is the slot pitch;

$w_{so}$  is the slot opening width;

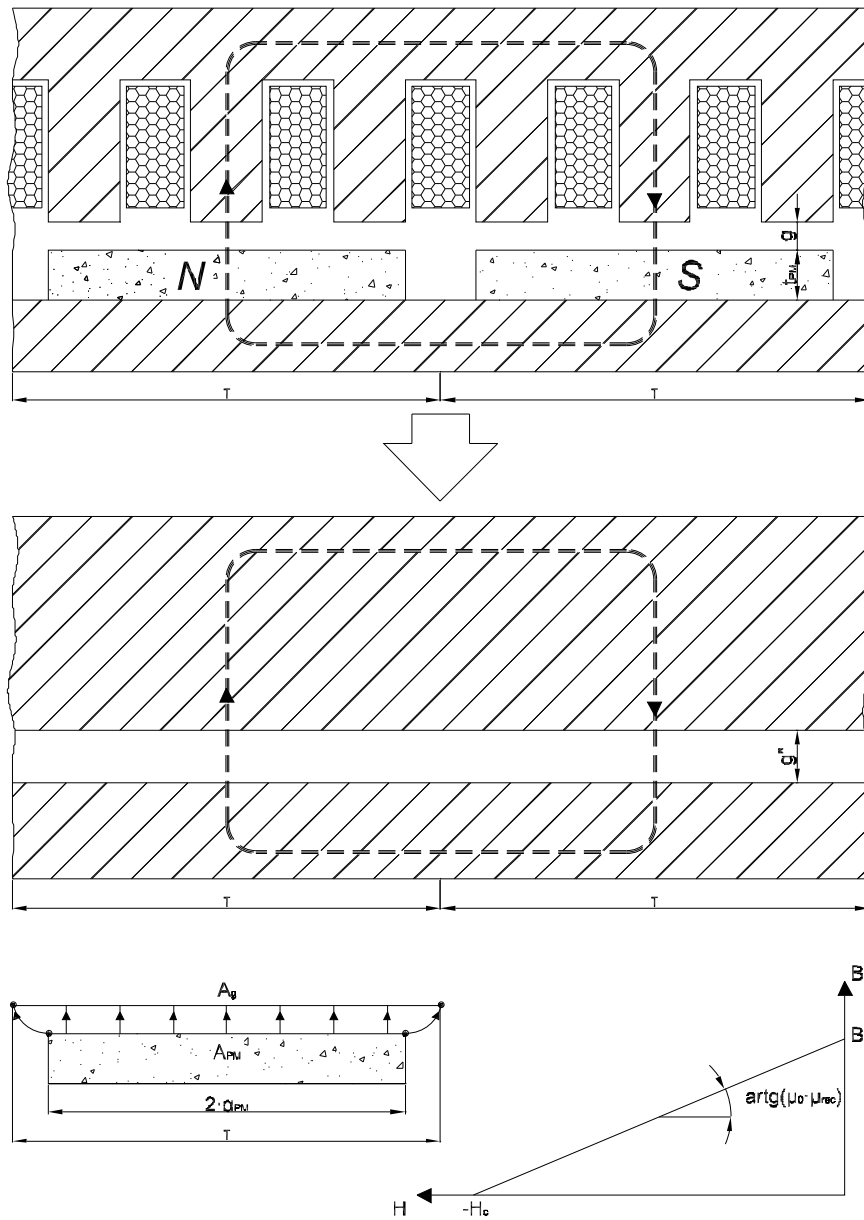


Figure 3.1: Circulation along a section of the machine.

$\Sigma(H \cdot l)$  is the total magnetic voltage drop along the circulation path;  
 $\Sigma(H \cdot l)_{airgap}$  is the airgap magnetic voltage drop along the circulation path.  
 In conclusion, we consider the following assumption:

- the iron core permeability is infinite ( $\mu_{Fe} = \infty$ );
- the PM magnetization characteristics is linear;
- the flux density along the pole semipitch  $\tau$  is constant, it's square wave along the airgap.



Let's define the belly flop factor  $k_\sigma$ , as follows,

$$k_\sigma = \frac{A_{PM}}{A_g} \quad (3.4)$$

where:  $A_g$  is the pole airgap surface;

$A_{PM}$  is the is the pole PM surface.

In no load operation, we can write the follow system of equations,

$$\begin{cases} B_{g0} \cdot A_g = B_{PM} \cdot A_{PM} \\ H_{g0} \cdot g'' + H_{PM0} \cdot h_{PM} = 0 \\ B_{g0} = \mu_0 \cdot H_{g0} \\ B_{PM0} = B_r + \mu_0 \cdot \mu_{rec} \cdot H_{PM0} \end{cases} \quad (3.5)$$

where:

$B_{g0}$  is the no load airgap flux density;

$B_{PM}$  is the no load PM flux density;

$B_r$  is the remanence flux density;

$H_{g0}$  is the no load airgap magnetic field;

$H_{PM0}$  is the no load PM magnetic field;

$\mu_0 = 4 \cdot \pi \cdot 10^{-7} H/m$  is the vacuum/air permeability;

$\mu_{rec}$  is the recoil permeability;

$h_{PM}$  is the  $PM$  height.

Through simple substitutions, starting from the II equation, we arrive at the expression of the no load flux density,

$$B_{g0} = \frac{k_\sigma \cdot B_r}{1 + \frac{k_\sigma \cdot \mu_{rec} \cdot g''}{h_{PM}}} \quad (3.6)$$

In load operation, we evaluate the contribution of the induced reaction produced by the stator current. Let's consider the electric loading  $\widehat{K}_s$  as function of a generic fixed reference angle  $\theta_s$ , as showed in fig. 3.2.

$$\widehat{K}_s(\theta_s) = \widehat{K}_s \cdot \cos(\theta_s - \alpha_s) = \frac{3 \cdot k_w \cdot N_s \sqrt{2} \cdot I}{\pi \cdot D} \cdot \cos(\theta_s - \alpha_s) \quad (3.7)$$

where:

$N_s$  is the number of conductors per phase, series configuration;

$D$  is the airgap diameter;

Performing the Ampère circulation along the indicated path (that represent the worst condition in terms of induced reaction), we obtain the  $MMF$ ,

$$\oint H \cdot dl = I_{linkage} \Rightarrow 2 \cdot (H_g \cdot g'' + H_{PM} \cdot h_{PM}) = \frac{2}{\pi} \cdot \widehat{K}_s \cdot \frac{\pi \cdot D}{2 \cdot p} \quad (3.8)$$

$$\Rightarrow (H_g \cdot g'' + H_{PM} \cdot h_{PM}) = \widehat{K}_s \cdot \frac{D}{2 \cdot p} \quad (3.9)$$

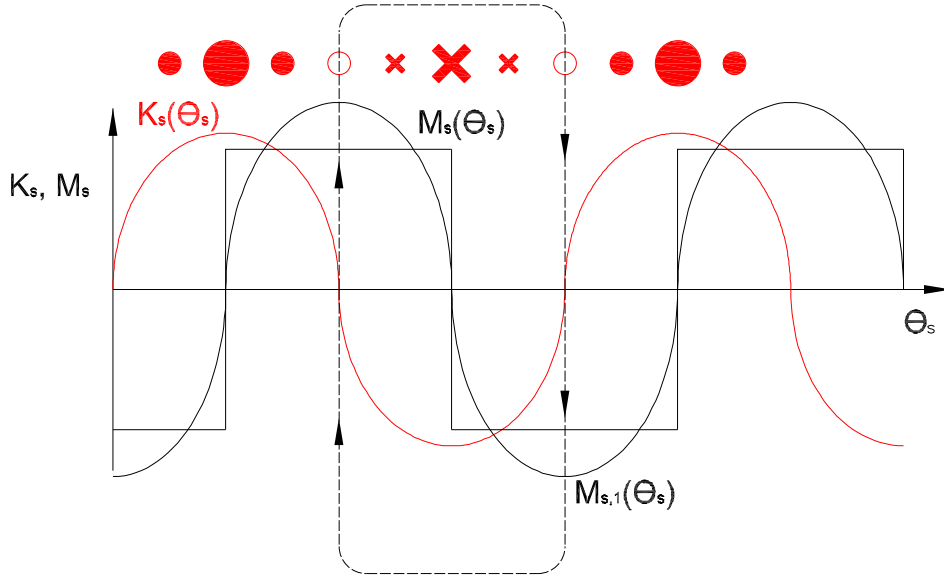


Figure 3.2: Rotor losses trends and minima in function of number of slots and poles.

The system of equation change as follows,

$$\begin{cases} B_g \cdot A_g = B_{PM} \cdot A_{PM} \\ H_g \cdot g'' + H_{PM} \cdot h_{PM} = \frac{\hat{K}_s \cdot D}{2 \cdot p} \\ B_g = \mu_0 \cdot H_g \\ B_{PM} = B_r + \mu_0 \cdot \mu_{rec} \cdot H_{PM} \end{cases} \quad (3.10)$$

Similarly, we get, after some simple step starting from the II equation, the relationship of the load airgap flux density,

$$B_g = \underbrace{\frac{k_\sigma \cdot B_r}{1 + \frac{k_\sigma \cdot \mu_{rec} \cdot g''}{h_{PM}}}}_{B_{g0}} + \mu_0 \cdot \underbrace{\frac{\hat{K}_s \cdot D}{2 \cdot p \left( g'' + \frac{h_{PM}}{k_\sigma \cdot \mu_{rec}} \right)}}_{\Delta B} \quad (3.11)$$

The second term  $\Delta B$  is the induced reaction: it's produce a deformation of the airgap flux density that may lead to a saturation of the iron core, in particular in correspondence of the teeth, but especially it may lead the  $PMs$  to work under the knee flux density, with an irreversible demagnetization of the magnet. Assuming that each  $PM$  cover a full pole semipitch ( $2 \cdot \alpha_{PMe} = 180^\circ$ ), we evaluate the peak value of the fundamental of the airgap flux density, as follows,  $\hat{B}_{g0,1}$ , as follows,

$$\hat{B}_{g0,1} = \frac{4}{\pi} \cdot B_{g0} \quad (3.12)$$

Consequently, the peak value of the fundamentals of  $PM$  flux  $\Phi_1$  and flux linkage  $\Lambda_{PM}$  are,

$$\Phi_1 = \frac{4}{\pi} \cdot B_{g0} \cdot \frac{D \cdot L}{p} \quad (3.13)$$

$$\Lambda_{PM} = k_w \cdot \frac{N_s}{2} \cdot \widehat{\Phi} = k_w \cdot \frac{N_s}{2} \cdot \widehat{B}_{g0,1} \cdot \frac{D \cdot L}{p} \quad (3.14)$$

where:

$L$  is the stack length;

Hence, the no load phase  $EMF$  (fundamental,  $RMS$  value)  $E$ , is,

$$E = \frac{1}{\sqrt{2}} \cdot \Omega_{me} \cdot \widehat{\Lambda}_1 = 2 \cdot \sqrt{2} \cdot k_w \cdot f \cdot N_s \cdot B_{g0} \cdot \frac{D \cdot L}{p} \quad (3.15)$$

where:

$\Omega_{me} = 2 \cdot \pi \cdot f$  is the electrical speed. We evaluate now the torque developed by the machine, computing the force acting on the rotor  $F$ , determined by the iteration between the airgap flux density (we consider, for simplicity, the no load flux density  $B_{g0}$ ) and the stator current, as follows,

$$F(\theta_s) = -B_{g0}(\theta_s) \cdot K_s(\theta_s) = -\widehat{B}_{g0,1} \cdot \cos(\theta_s - \alpha_m) \cdot \widehat{K}_s \cdot \cos(\theta_s - \alpha_s) \quad (3.16)$$

Through appropriate mathematical calculations, we get the follow equation,

$$F(\theta_s) = -\frac{1}{2} \cdot \widehat{B}_{g0,1} \cdot \widehat{K}_s (\cos(2 \cdot \theta_s - \alpha_m - \alpha_s) + \cos(\alpha_s - \alpha_m)) \quad (3.17)$$

For evaluating the torque, we compute the average force along the rotor circumference ( $\theta_s = 0 \div 2 \cdot \pi$ ),

$$\langle F \rangle = \frac{1}{2 \cdot \pi} \int F(\theta_s) \cdot d(\theta_s) = -\frac{1}{2} \cdot \widehat{B}_{g0,1} \cdot \widehat{K}_s \cdot \cos(\alpha_s - \alpha_m) \quad (3.18)$$

This force achieve the maximum value when the electric loading and flux density distribution are in phase, that is when angle  $\alpha_m = \alpha_s$  (that means, in d-q reference frame, when the motor is feeded with only q-axis current). Under this assumption the developed torque  $T$  is,

$$T = \frac{1}{4} \cdot \pi \cdot \widehat{K}_s \cdot B_{g0,1} \cdot D^2 \cdot L = \widehat{K}_s \cdot B_{g0} \cdot D^2 \cdot L \quad (3.19)$$

## 3.2. Design procedure

In this paragraph is presented the mathematical procedure for the analytical synthesis of the motor and that has been implemented in Matlab®.

### 3.2.1. Machine general data

According to *FreedomCAR* specifications, let's calculate the e evaluate the electric and mechanical quantities needed for the synthesis of the motor, as follows,

- Base speed in [rad/s],  $\Omega_B$

$$\Omega_B = \frac{2 \cdot \pi \cdot n_B}{60} \quad (3.20)$$

Where  $n_B$  is the base speed in [rpm].

- Max speed in [rad/s],  $\Omega_{MAX}$

$$\Omega_{MAX} = \frac{2 \cdot \pi \cdot n_{MAX}}{60} \quad (3.21)$$

Where  $n_{MAX}$  is the max speed in [rpm].

- Base frequency,  $f_B$

$$f_B = \frac{\Omega_B \cdot p}{2 \cdot \pi} \quad (3.22)$$

- Max frequency,  $f_{MAX}$

$$f_{MAX} = \frac{\Omega_{MAX} \cdot p}{2 \cdot \pi} \quad (3.23)$$

- Rated torque,  $T_n$

$$T_n = \frac{P_n}{\Omega_B} \quad (3.24)$$

Where  $P_n$  is the rated power.

- Rated phase voltage,  $E_n$

$$E_n = \frac{V_{DCMIN}}{\sqrt{2} \cdot \sqrt{3}} \quad (3.25)$$

Where  $V_{DCMIN}$  is the *DC* bus min voltage: because of the motor must produce the max power at rated voltage and base speed, but a the same speed it must develop the also the rated power, I design the motor with the lowest permissible *DC* bus voltage (200V).

### 3.2.2. Design temperature

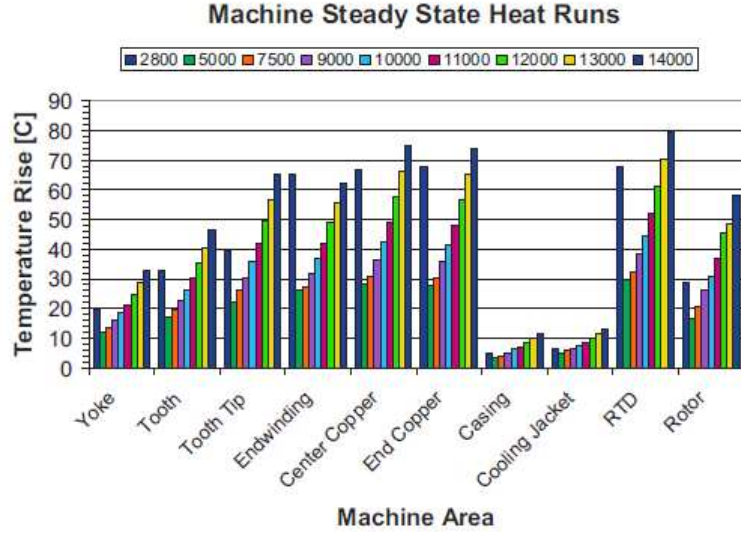


Figure 3.3: Measured temperature rises in various location in 2011 P. B. Reddy *et al IPM FSCW FreedomCAR* design. The reference temperature is the coolant temperature of  $105^{\circ}\text{C}$ . [10]

In order to define the design temperature of the machine, both for magnets and copper, we can refer to a thermal analysis conducted on a *FreedomCAR* design, as illustrated in fig. 3.3: with a coolant temperature of  $105^{\circ}\text{C}$ , the copper achieve approximately  $175^{\circ}\text{C}$ - $185^{\circ}\text{C}$ , while rotor, and so magnets, reach  $165^{\circ}\text{C}$ , in the worst operating condition of the machine, at maximum speed. Consequently I choose for my design a prudential value of  $T = 180^{\circ}\text{C}$ .

### 3.2.3. PM characteristics and max flux density no load - load drop

The chosen magnets are a medium type, high strength, sintered NdFeB magnets by Neomax, signed NMX-36EH, with the follows data:

- Remanence flux density,  $B_r = 1T @ 180^{\circ}\text{C}$ .
- Knee flux density,  $B_{knee} = 0.15T$  ( $0.25T$  prudential)  $@ 180^{\circ}\text{C}$ .
- Recoil permeability,  $\mu_{rec} = 1.05$
- Density,  $\gamma_{PM} = 7600\text{kg}/\text{m}^3$
- Resistivity,  $\rho_{PM} = 1.3\mu\Omega \cdot m$

Being usually the no load airgap flux density  $B_{g0} \cong B_{m0} \cong 0.75 \cdot B_r$ , we calculate the permissible flux density no load-load drop  $\Delta B_{knee}$  in the magnet, as follows,

$$\Delta B_{MAX} = B_{g0} - B_{knee} \quad (3.26)$$

Assuming a safe factor  $k_{safe} = 2 \div 3$ , the permissible flux density drop  $\Delta B$  is derated to,

$$\Delta B = \frac{\Delta B_{MAX}}{k_{safe}} \quad (3.27)$$

Assuming a Carter factor  $k_{Carter} = 1.1$  and a saturation factor  $k_{sat} = 1.2$ , from eq. 3.1 we evaluate the equivalent airgap  $g''$ ; explicit the eq. 3.6 in terms of  $PM$  tickness  $h_{PM}$  (of an  $SPM$  equivalent machine), we get, assuming a belly flop factor  $k_\sigma = 0.85$ ,

$$h_{PM} = k_\sigma \cdot g'' \cdot \mu_{rec} \cdot \frac{1}{k_\sigma \cdot \frac{B_r}{B_{g0}} - 1} \quad (3.28)$$

### 3.2.4. Main geometry of the machine

In order to evaluate the main geometry of the machine we insert eq. 3.19 and the second term of eq. 3.11 in a system, as follows,

$$\begin{cases} \widehat{K}_s \cdot B_{g0} \cdot D^2 \cdot L \\ \Delta B = \mu_0 \cdot \frac{\widehat{K}_s \cdot D}{2 \cdot p \left( g'' + \frac{h_{PM}}{k_\sigma \cdot \mu_{rec}} \right)} \end{cases} \quad (3.29)$$

$\Rightarrow$

$$\begin{cases} T_n = \widehat{K}_s \cdot B_{g0} \cdot D^2 \cdot L \\ \widehat{K}_s \cdot D = \frac{\Delta B \cdot 2 \cdot p \left( g'' + \frac{h_{PM}}{k_\sigma \cdot \mu_{rec}} \right)}{\mu_0} = a \end{cases} \quad (3.30)$$

In the previous system the unknown variables are the electric loading  $\widehat{K}_s$ , the airgap diameter  $D$ , and the stack length  $L$ . In order to solve the system, we have four possible ways, as follows,

1. Set the stack length  $L$ , as a result,

$$\begin{cases} D = \frac{T_n}{B_{g0} \cdot L \cdot a} \\ \widehat{K}_s = \frac{a}{D} \end{cases} \quad (3.31)$$

2. Set the airgap diameter  $D$ , as a result,

$$\begin{cases} \widehat{K}_s = \frac{a}{D} \\ L = \frac{T_n}{\widehat{K}_s \cdot B_{g0} \cdot D^2} \end{cases} \quad (3.32)$$

3. Set the stack length / airgap diameter ratio  $L/D$ , as a result,

$$\begin{cases} D = \sqrt{\frac{T_n}{B_{g0} \cdot L/D \cdot a}} \\ L = L/D \cdot D \widehat{K}_s = \frac{a}{D} \end{cases} \quad (3.33)$$

4. Set the stack length  $L$  and the airgap diameter  $D$ , checking the value of the resultant electric loading  $\widehat{K}_s$ , as follows,

$$\widehat{K}_s = \frac{T_n}{B_{g0} \cdot D^2 \cdot L} \leq \frac{a}{D} \quad (3.34)$$

The slot pitch  $p_s$ , is,

$$p_s = \frac{\pi \cdot D}{Q} \quad (3.35)$$

Let's evaluate the effective length of the iron core  $L_{Fe}$ , assuming a stacking factor  $k_{st} = 0.95$ ,

$$L_{Fe} = k_{st} \cdot L \quad (3.36)$$

Assuming the total flux of the tooth pitch is confined in the tooth (considering a flux density  $B_t = 1.8T$ ), applying the equality of flows, the tooth width  $w_t$  is,

$$w_t = p_s \cdot \frac{B_{g0} + \Delta B}{B_t} \cdot \frac{L}{L_{Fe}} \quad (3.37)$$

### 3.2.5. Number of conductors

The number of conductors per phase, series configuration  $N_s$  from eq. 3.15, are, assuming a drop voltage of 5%,

$$N_s = \text{round} \left( \frac{0.95 \cdot E_n \cdot p}{2 \cdot \sqrt{2} \cdot k_w \cdot f_B \cdot B_{g0} \cdot D \cdot L} \right) \quad (3.38)$$

The number of conductors per slot, series configuration  $n_{cs}$ , is,

$$n_{cs} = \frac{3 \cdot N_s}{Q} \quad (3.39)$$

Having to use a double layer winding, the previous value must be even, so it's necessary to round to the the lower even number. Besides. we decide to use all the coils in series, so the effective number of conductors per each slot  $n_c = n_{cs}$ .

### 3.2.6. Slot sizing

The slot current  $\widehat{I}_s$ , is,

$$\widehat{I}_s = \frac{p_s \cdot \widehat{K}_s}{k_w} \quad (3.40)$$

Setting a current density  $J = 6A/mm^2$ , and a fill factor  $k_{fill} = 0.45$ , the slot area  $S_s$  is,

$$S_s = \frac{I_s}{\sqrt{2} \cdot J \cdot K_{fill}} \quad (3.41)$$

The conductor area, series configuration  $S_{Ceq}$  (that is equal to the effective conductor area  $S_C$  being all the coils in series), is

$$S_{ceq} = S_C = \frac{k_{fill} \cdot S_s}{n_{cs}} \quad (3.42)$$

The conductor diameter  $d_C$  is,

$$d_c = 2 \cdot \sqrt{\frac{S_c}{\pi}} \quad (3.43)$$

The motor is feeded at high frequency so it's important to choose an appropriate conductor diameter in order to reduce the losses due to skin effect: the min skin depth  $\delta_{MIN}$  in the worst operating conditions at max frequency of  $f_{MAX} = 1167Hz$ , is evaluated as follows (we prudentially consider the highest copper conductivity, at ambient temperature  $\sigma_{Cu} = 58 \cdot 10^6 S/m$ ),

$$\delta_{MIN} = \sqrt{\frac{1}{\pi \cdot \mu_0 \cdot f_{MAX} \cdot \sigma_{Cu}}} = \sqrt{\frac{1}{\pi \cdot 4 \cdot \pi \cdot 10^{-7} \cdot 1167 \cdot 58 \cdot 10^6}} = 1.93mm \quad (3.44)$$

At a depth of  $\delta_{MIN}$  the current density is about the 37% of the current on the surface, so, in order to get a current density as much as possible smooth, from the standardized conductor table CEI-UNEL 01723-72, I make the conductor with  $n_w$  insulated wires of copper diameter  $d_{CCOM} = 1mm$  and effective diameter (inclusive of insulation enamel)  $d_{CextCOM} = 1.093mm$ .

$$n_w = round\left(\frac{4 \cdot S_C}{\pi \cdot d_{cCOM}^2}\right) \quad (3.45)$$

The commercial conductor area equal to the equivalent commercial conductor area, series configuration  $S_{CCOM} = S_{CeqCOM}$ , is,

$$S_{cCOM} = n_w \cdot \left(\frac{\pi \cdot d_{cCOM}^2}{4}\right) \quad (3.46)$$

The effective commercial conductor area (inclusive of insulation enamel) equal to the equivalent effective commercial conductor area, series configuration  $S_{CextCOM} = S_{CeqextCOM}$ , is,

$$S_{cextCOM} = n_w \cdot \left(\frac{\pi \cdot d_{cextCOM}^2}{4}\right) \quad (3.47)$$

Let's evaluate the mains dimensions of the slots, assuming a trapezoidal shape as illustrated in fig. 3.4. It follows that the slot area  $S_s$  is equal to,

$$S_s = \frac{h_s}{2} \cdot \left(\frac{\pi \cdot D}{Q} - w_t + \frac{\pi \cdot (D + h_s)}{Q} - w_t\right) \quad (3.48)$$

Through simple mathematical calculations we arrive at the following quadratic equation in the unknown variable slot height  $h_s$ ,

$$h_s^2 + b \cdot h_s + c = 0 \quad (3.49)$$



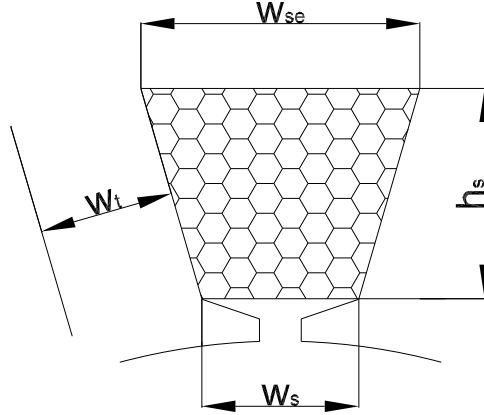


Figure 3.4: Modeling of the slot by trapeze.

Where:

$$b = D - \frac{w_t \cdot Q}{\pi} \quad (3.50)$$

$$c = -\frac{S_s \cdot Q}{\pi} \quad (3.51)$$

It follows that the slot height  $h_s$  is,

$$h_s = \frac{-b + \sqrt{b^2 - 4 \cdot c}}{2} \quad (3.52)$$

Considering the real dimension of the slots (slot open height  $h_{so}$ , slot wedge height  $h_{wed}$ ), we increase appropriately of 10% this last evaluated dimension.

The slot width  $w_s$  is,

$$w_s = p_s - w_t \quad (3.53)$$

The slot end width  $w_{se}$  is,

$$w_{se} = p_s + \frac{2\pi h_s}{Q} - w_t \quad (3.54)$$

The slot open width  $w_{so}$  is relate to the conductors diameter, usually we choose a value  $2 \div 3$  times larger than the conductor diameter  $d_{cCOM}$  in order to easily insert it in the slot. We consider,

$$w_{so} = 2.5 \cdot d_{cCOM} \quad (3.55)$$

The effective fill factor (that consider the insulation enamel),  $k_{fill}$ , is,

$$k_{fill} = \frac{n_{cs} \cdot S_{ceqatCOM}}{S_s} \quad (3.56)$$

The phase current  $I$  equal to the conductor current  $I_C$ , being the coils in series, is,

$$I = I_C = J \cdot S_{CeqCOM} \quad (3.57)$$

The effective electric loading  $\widehat{K}_s$ , is,

$$\widehat{K}_s = \frac{3 \cdot k_w \cdot N_s \cdot \sqrt{2} \cdot I}{\pi \cdot D} \quad (3.58)$$

The effective slot current  $\widehat{I}_s$  is given by,

$$\widehat{I}_s = n_c \cdot I_c \cdot \sqrt{2} \quad (3.59)$$

### 3.2.7. Yoke sizing

Let's evaluate the back iron height  $h_{bi}$  from the back iron flux  $\phi_{bi}$  equal to,

$$\phi_{bi} = \frac{1}{2} \cdot \phi = \frac{1}{2} \cdot B_{g0} \cdot \frac{\pi \cdot D}{2 \cdot p} \cdot L \cdot \frac{2 \cdot \alpha_{PMe}}{180} \quad (3.60)$$

Assuming the  $PM$  electrical angle equal to  $150^\circ$ .

Finally we get the back iron height, assuming a back iron flux density  $B_{bi} = 1.6T$ , it follows that,

$$h_{bi} = \frac{\phi_{bi}}{B_{bi} \cdot L_{Fe}} \quad (3.61)$$

The stator outer diameter  $D_e$  is,

$$D_e = D + 2 \cdot (h_s + h_{bi}) \quad (3.62)$$

### 3.2.8. Rotor sizing

The analytical procedure here presented doesn't provide any kind of information about flux barrier dimension,  $PM$  width. This optimization phase will be executed by  $FEA$  in the next chapter. Anyway, it's possible to estimate the  $PM$  flux linkage, useful for a rough evaluation of the back  $EMF$  line-to-line voltage  $V_0$ , as follows,

$$\Lambda_{PM} = k_w \cdot \frac{N_s}{2} \cdot \frac{4}{\pi} \cdot B_{g0} \cdot \frac{D \cdot L}{p} \quad (3.63)$$

From eq. 1.3,

$$\widehat{V}_0 = \sqrt{3} \cdot 2\pi \cdot f_{MAX} \cdot \Lambda_{PM} \quad (3.64)$$

### 3.2.9. Masses and volumes

Let's estimate the end winding length  $L_{ew}$ , by the following equation,

$$L_{ew} = \pi \cdot \frac{\frac{w_s}{2} + w_t}{2} \quad (3.65)$$

Where  $\frac{w_s}{2} + w_t$  is the average end winding diameter (for double layer winding).

The conductor length  $L_c$  is

$$L_c = L + L_{ew} \quad (3.66)$$

Considering the copper density  $\gamma_{Cu} = 8900\text{kg}/\text{m}^3$ , the copper mass  $G_{Cu}$  is,

$$G_{Cu} = \gamma_{Cu} \cdot n_{cs} \cdot Q \cdot S_{ceqCOM} \cdot L_c \quad (3.67)$$

Concerning the iron, we decide to use an high quality, not oriented steel, by ThyssenKrupp, signed M235-35A, with a conventional density  $\gamma_{Fe} = 7600\text{kg}/\text{m}^3$ . The teeth mass  $G_{Fet}$  and the back iron mass  $G_{bi}$  are,

$$G_{Fet} = \gamma_{Fe} \cdot Q \cdot w_t \cdot h_s \cdot L_{Fe} \quad (3.68)$$

$$G_{Febi} = \gamma_{Fe} \cdot \pi (D_e \cdot h_{bi} - h_{bi}^2) \cdot L_{Fe} \quad (3.69)$$

It follows the total stator iron mass  $G_{Fes}$  is,

$$G_{Fes} = G_{Fet} + G_{bi} \quad (3.70)$$

Assuming prudentially that the rotor hasn't got flux barrier in correspondence of the *PMs*, the rotor iron mass  $G_{Fer}$ , is,

$$G_{Fer} = \gamma_{Fe} \cdot \frac{\pi}{4} \cdot (D_r^2 - D_{ri}^2) \cdot L_{Fe} \quad (3.71)$$

Where  $D_{ri}$  is the motor hollow shaft diameter.

Thus, the total iron mass  $G_{Fe}$  is,

$$G_{Fe} = G_{Fes} + G_{Fer} \quad (3.72)$$

Finally, the total motor mass  $G$  is,

$$G = G_{Fe} + G_{Cu} \quad (3.73)$$

The volume of overall dimensions  $V$ , is,

$$V = \frac{\pi}{4} \cdot D_e \cdot L \quad (3.74)$$

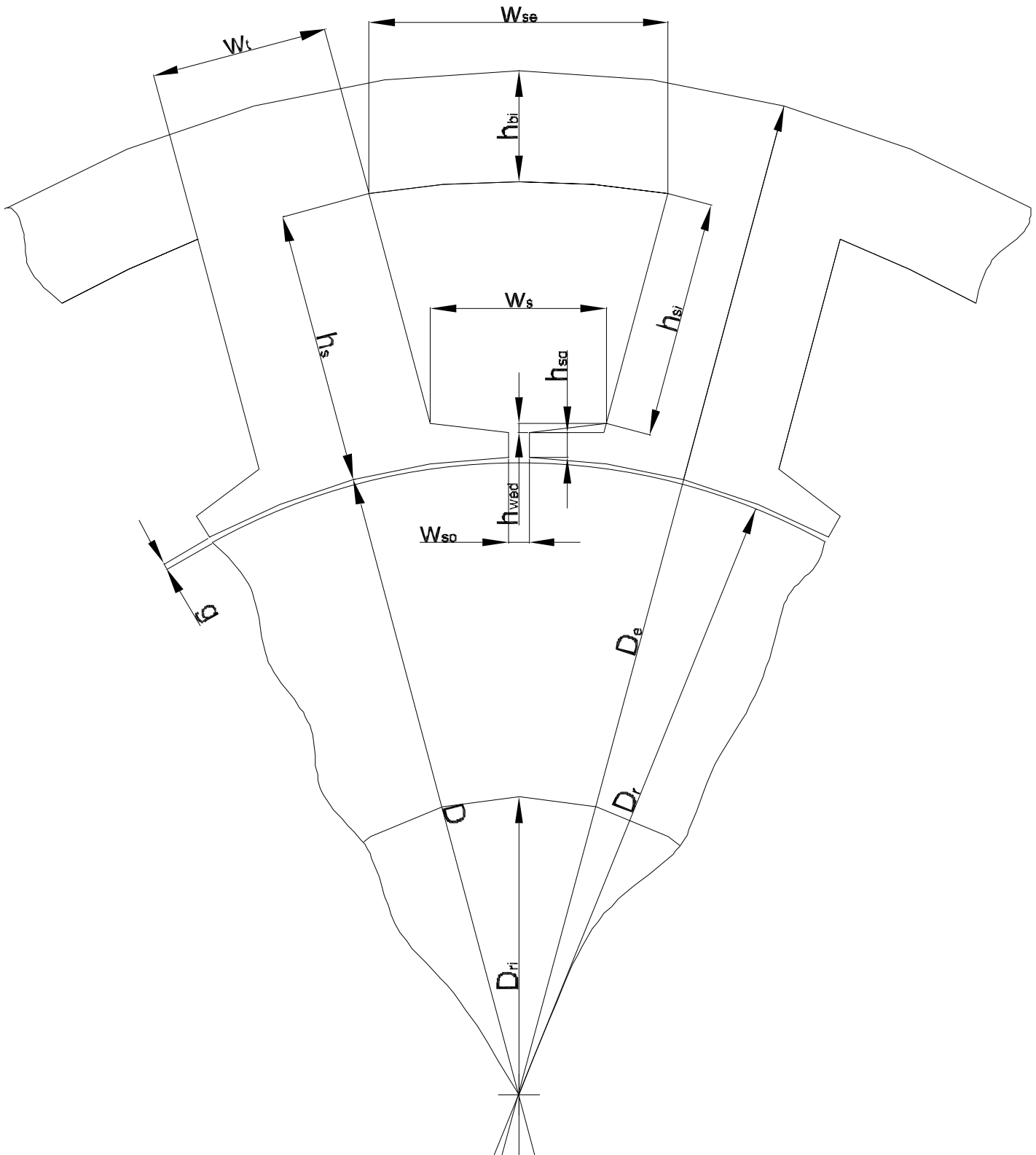


Figure 3.5: Mains dimensions of the motor.

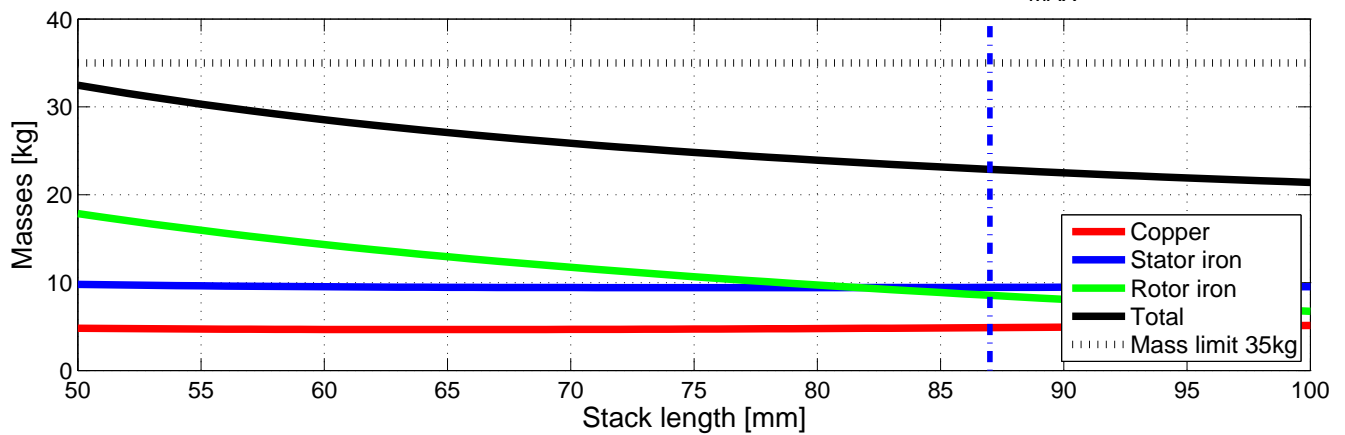
### 3.3. Definition of the starting design

In order to study the masses trends, and define the starting design, we perform a parametric computation, changing the stack length  $L = 50 \div 100\text{mm}$  as illustrated in fig. 3.6.

According to some *FreedomCAR* papers (see, for e.g., [14]) I set the shaft diameter  $D_{ri} = 70\text{mm}$ , the masses, inclusive of all machine parameters (not shown here) are evaluated as consequences, using the previous design procedure.

As you can see, stack length  $L$  and airgap diameter  $D$  follow an hyperbolic

Masses vs. stack length – Condition: induced reaction constant,  $\Delta B = 0.17\text{T}$  ( $\Delta B_{\text{MAX}} = 0.5\text{T}$ , safe factor 3)



Airgap diameter vs. stack length – Condition: induced reaction constant,  $\Delta B = 0.17\text{T}$  ( $\Delta B_{\text{MAX}} = 0.5\text{T}$ , safe factor 3)

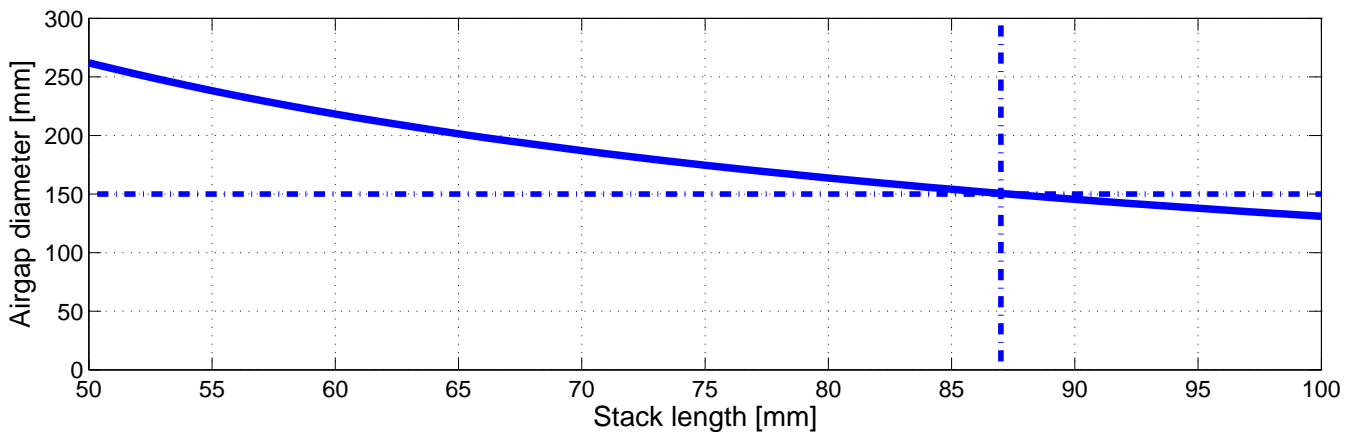


Figure 3.6:

relationship, and this can be easily prove in the eqs. 3.32, 3.33.

We select, in order to make comparison to other *FreedomCAR* motors, the follow configuration: we set the airgap diameter to  $D = 150\text{mm}$ , consequently the resultant stack length is  $L = 87\text{mm}$  and the estimated total mass is lower than  $25\text{kg}$ . It's important to note that the total mass should be inclusive of the motor frame that we can't evaluate herein, so the previous choice is prudential.

The resultant machine parameters that comes from analytical synthesis are reported in tab. 3.1.

Table 3.1: Geometrical and electrical parameter of the starting design.

Quantity	Symbol	Value
Rated power	$P_n$	$30kW$
Rated torque	$T_n$	$102.31Nm$
Rated $DC$ bus voltage	$V_{DCn}$	$200V$
Rated $AC$ phase voltage	$E_n$	$81.65V$
Base speed	$n_B$	$2800rpm$
Number of slots	$Q$	12
Number of poles	$2 \cdot p$	10
Number of slots per poles and per phase	$q$	0.4
Winding factor (main harmonic)	$k_w$	0.933
Airgap height	$g$	$0.7mm$
Remanence flux density	$B_r$	$1T$
No load airgap $PM$ flux density	$B_{g0}$	$0.75T$
Recoil permeability	$\mu_{rec}$	1.05
Belly flop factor	$k_\sigma$	0.85
Safe factor	$k_{safe}$	3
Iron density	$\gamma_{Fe}$	$7600kg/m^3$
Stacking factor	$k_{st}$	0.95
Tooth flux density	$B_t$	$1.8T$
Back iron flux density	$B_t$	$1.6T$
Current density	$J$	$6A/mm^2$
Fill factor	$k_{fill}$	0.45
Copper density	$\gamma_{Cu}$	$8900kg/m^3$

Airgap diameter	$D$	150mm
Stack length	$L$	87.31mm $\rightarrow$ 87mm
Stator outer diameter	$D_e$	234.21mm $\rightarrow$ 241mm
Rotor diameter	$D_r$	148.6mm
Shaft diameter	$D_{ri}$	70mm
PM height	$h_{PM}$	6.19mm $\rightarrow$ 5mm
Slot pitch	$p_s$	39.27mm
Slot width	$w_s$	18.22mm $\rightarrow$ 20.74mm
Slot end width	$w_{se}$	35.21mm $\rightarrow$ 35.29mm
Slot opening width	$w_{so}$	2.5mm
Slot height	$h_s$	32.46mm $\rightarrow$ 32.5mm
Slot inner height	$h_{si}$	– $\rightarrow$ 27.77mm
Slot opening height	$h_{so}$	– $\rightarrow$ 2.5mm
Slot height / slot width ratio	$h_s/w_s$	1.78
Slot area	$S_s$	765.48mm <sup>2</sup> $\rightarrow$ 780.58mm <sup>2</sup>
Tooth width	$w_t$	21.05mm $\rightarrow$ 21mm
Back iron height	$h_{bi}$	9.65mm $\rightarrow$ 13mm
# of conduc. per phase, series config.	$N_s$	64
# of conduc. per each slot, series config.	$n_{cs}$	16
# of conduc. per each slot	$n_c$	16
Conductor area, series config.	$S_{ceq}$	21.21mm <sup>2</sup>
Conductor area	$S_c$	21.21mm <sup>2</sup>
# of wires per each conductor	$n_w$	27
Wire diameter	$d_{cCOM}$	1mm

Wire diameter inclusive of enamel	$d_{cextCOM}$	1.093mm
Conductor configuration	$n_w \times d_{cCOM}$	$27 \times 1mm$
Effective fill factor	$k_{fill}$	0.53
Slot current	$\hat{I}_s$	$2878.99A_{peak}$
Electric loading	$\hat{K}_s$	$68.40kA_{peak}/m$
Phase current	$I$	$127.23A_{RMS}$
Conductor current	$I_c$	$127.23A_{RMS}$
$PM$ flux linkage	$\Lambda_{PM}$	$74.68mWb_{peak}$
Back $EMF$ line-to-line voltage @ 14000rpm	$V_0$	$948.13V_{peak}$
Copper mass	$G_{Cu}$	4.88kg
Teeth iron mass	$G_{Fet}$	5.17kg
Back iron mass	$G_{Febi}$	4.29kg
Stator iron mass	$G_{Fes}$	9.46kg
Rotor iron mass	$G_{Fer}$	8.51kg
Total iron mass	$G_{Fe}$	17.97kg
Total mass	$G$	22.85kg
Total volume	$V$	3.76ℓ

### 3.4. Winding disposition

In order to define the allocation of the coils and the current direction, we refer to the previous mentioned theory of star of slot. Each slot  $EMF$  correspond to a phasor so, for our 12/10 machine, we have 12 phasors: two consecutive phasors are shifted by an electric slot angle  $\alpha_{se}$  equal to,

$$\alpha_{se} = p \cdot \frac{360}{Q} = 5 \cdot \frac{360}{12} = 150^\circ \quad (3.75)$$

Each spoke is made of  $t$  phasors equal to,

$$t = MCD(Q, p) = MCD(12, 5) = 1 \quad (3.76)$$



The number of spokes are  $Q/t = 12/1 = 12$ . The resultant star of slots is represented in fig. 3.7: each phase assumes the spokes with the minimum phase displacement; for this reason, we define an angular sectors of  $60^\circ$ , so the spokes included in, belong to the the first phase, first layer. In the same way, shifting the sector of  $120^\circ$  and  $240^\circ$  we evaluate the spokes belonging to the second and third phase, first layer. Concerning the second layer, it's allocate at the slots distance  $y_q = 1$ .

In conclusion we get:

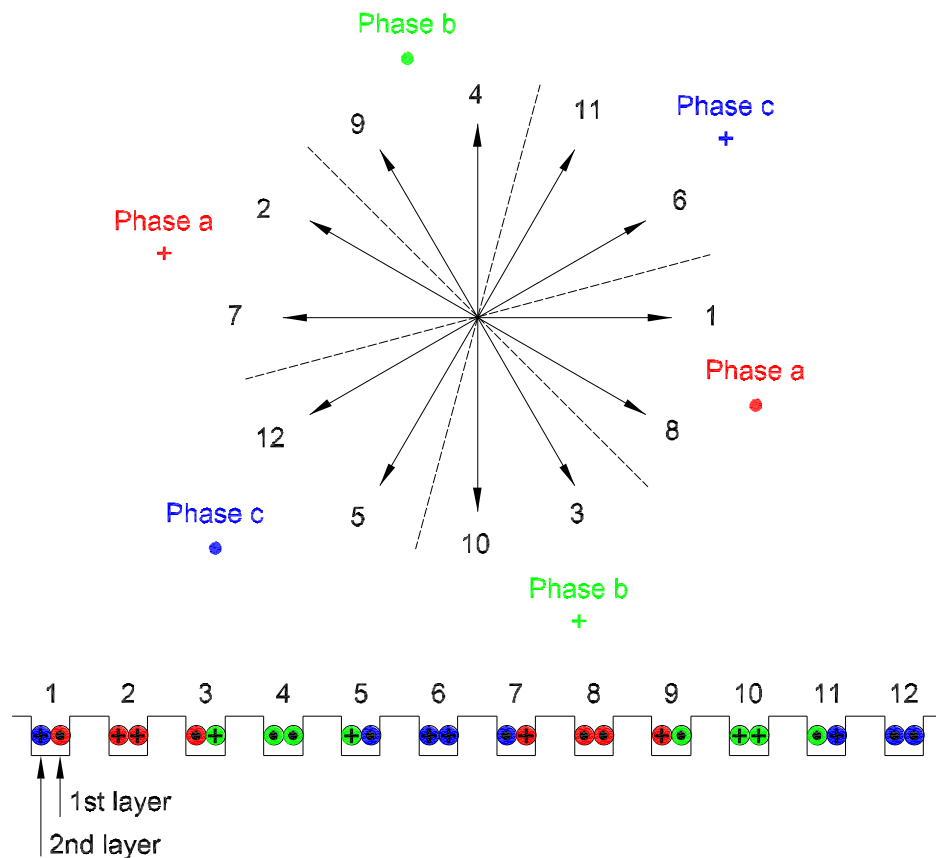


Figure 3.7: Star of slots and winding disposition.

- **First layer**

Phase a: 1, 8 (●); 2, 7 (+);

Phase b: 4, 9 (●); 3, 10 (+);

Phase c: 5, 12 (●); 6, 11 (+);

- **Second layer**

Phase a: 2, 9 (+); 3, 8 (●);

Phase b: 5, 10 (+); 4, 11 (●);

Phase c: 6, 1 (+); 7, 12 (●);



## FINITE ELEMENT ANALYSIS

The aim of this chapter is to tune the machine and analyze it, computing the electrical and magnetic parameters, working in d/q reference frame. The used *FEA* software is Ansoft Maxwell® and the adopted formulation is transient. Being the symmetry along the axial direction of the motor, a 2D problem is sufficient to study the machine. The problem is set for having, as input, the d/q-axis current in [ $A_{RMS}$ ] and speed in [rpm] while output, the torque, phase a/b/c flux linkage transformed in d/q-axis flux linkage and losses.

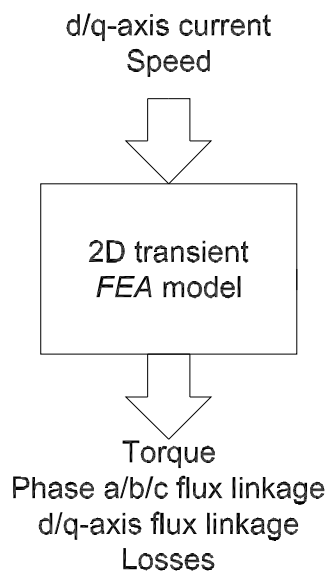


Figure 4.1: Main inputs and outputs of the model.

### 4.1. Model settings

The machine is feeded by a balanced three phase currents,  $i_a$ ,  $i_b$ ,  $i_c$ , as follows,

$$\begin{cases} i_a = \sqrt{2} \cdot I \cdot \cos(\Omega_{me} \cdot t + \alpha_{ie}) \\ i_b = \sqrt{2} \cdot I \cdot \cos(\Omega_{me} \cdot t - \frac{2}{3} \cdot \pi + \alpha_{ie}) \\ i_c = \sqrt{2} \cdot I \cdot \cos(\Omega_{me} \cdot t + \frac{2}{3} \cdot \pi + \alpha_{ie}) \end{cases} \quad (4.1)$$

Where:

$I = \sqrt{I_d^2 + I_q^2}$  is the phase current (*RMS* value):  $I_d$ ,  $I_q$  are respectevly the d/q-axis current (*RMS* value);

$\Omega_{me} = 2 \cdot \pi \cdot f$  is the electrical speed; the frequency  $f$  is given by eq. 2.13;

$t$  is the time;

$\alpha_{ie} = \arctan(I_q/I_d)$  is the phase angle of the system. This relationship is true if the motors has been previously "rephased", in order to match the d-axis to the phase-a magnetization axis in  $t = 0$ .

The transformation between the a/b/c three phase system and d/q system is so

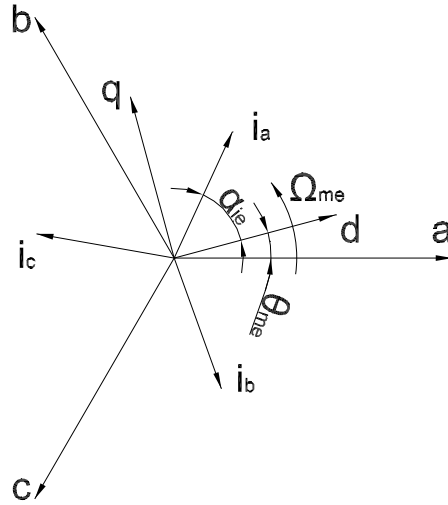


Figure 4.2: d/q-axis and fixed reference frame.

called "not orthogonal" transformation that preserve the magnitude of current and voltage but doesn't maintain power. The transformation matrix  $T_{dq/abc}$  is,

$$T_{abc/dq} = \frac{2}{3} \cdot \begin{bmatrix} \cos \theta_{me} & \cos (\theta_{me} - \frac{2}{3} \cdot \pi) & \cos (\theta_{me} + \frac{2}{3} \cdot \pi) \\ -\sin \theta_{me} & -\sin (\theta_{me} - \frac{2}{3} \cdot \pi) & -\sin (\theta_{me} + \frac{2}{3} \cdot \pi) \end{bmatrix} \quad (4.2)$$

Where  $\theta_{me} = \Omega_{me} \cdot t$  is the angular position (electrical), or in other words, the displacement between the synchronous reference frame and the fixed reference frame.

The *FEA* settings adopted for the model are summarized in tab. 4.1.

Table 4.1: *FEA* settings

<b>Geometry</b>	<b>Physics</b>	<b>Mesh</b>
Airgap Flux barrier	Vacuum	Restricted max length $1.5mm$
Copper	Copper - Conductivity @ $180^{\circ}C$ $34.44MS/m$ - Relative permeability $0.999991$	Restricted max length $4mm$
M235-35A	Magnetically non linear - Relative permeability BH curve (see Addendum) - Hysteresis coefficient $0.0274855$ - Eddy current coefficient $4.16816 \cdot 10^{-5}$ - Density $7600kg/m^3$	Restricted max length $3mm$
NdFeB	Magnetically linear - Conductivity $769231S/m$ - Relative permeability $1.05$ - Remanence flux density $1T$ - Coercivity magnetic field $-757880A/m$ - Density $7600kg/m^3$	Restricted max length $1.5mm$
Shaft	Steel stainless - Relative permeability $1$	Restricted max length $8mm$

## 4.2. Tuning the models

This paragraph describe the procedure used to evaluate the final design of the machines that achieves *FreedomCAR* targets. The first part has the objective of studying the round shape of polar islands, in order to find the best solution; the second part illustrate the way used to reach the final design.

### 4.2.1. Round shape analysis

Round shape design of polar islands is a technique in order to achieve a different airgap flux density distribution, in order to achieve a better shape of the *EMF* and a reduction of cogging torque [21]. There are many different geometry that can be used, as reported for e.g. in fig. 4.3.

We consider, for our machine, a simple round shape design, equivalent to an



Figure 4.3: Different round shape design: from the left, conventional, sinusoidal, semi-block shape. [21]

arc of circumference, characterized by an electrical span angle fixed to  $\beta_e = 150^\circ$ . Let's define the height of this round shape  $\Delta_r$ , as follows,

$$\Delta_r = \frac{D_r - D_{rq}}{2} \quad (4.3)$$

Where  $D_{rq}$  is the interpolar rotor diameter.

We design the I-shape and V-shape rotor as illustrated in fig. 4.5 with main

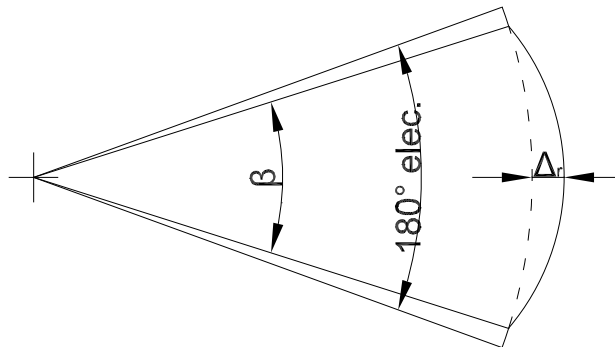


Figure 4.4: Dimensions of polar island.

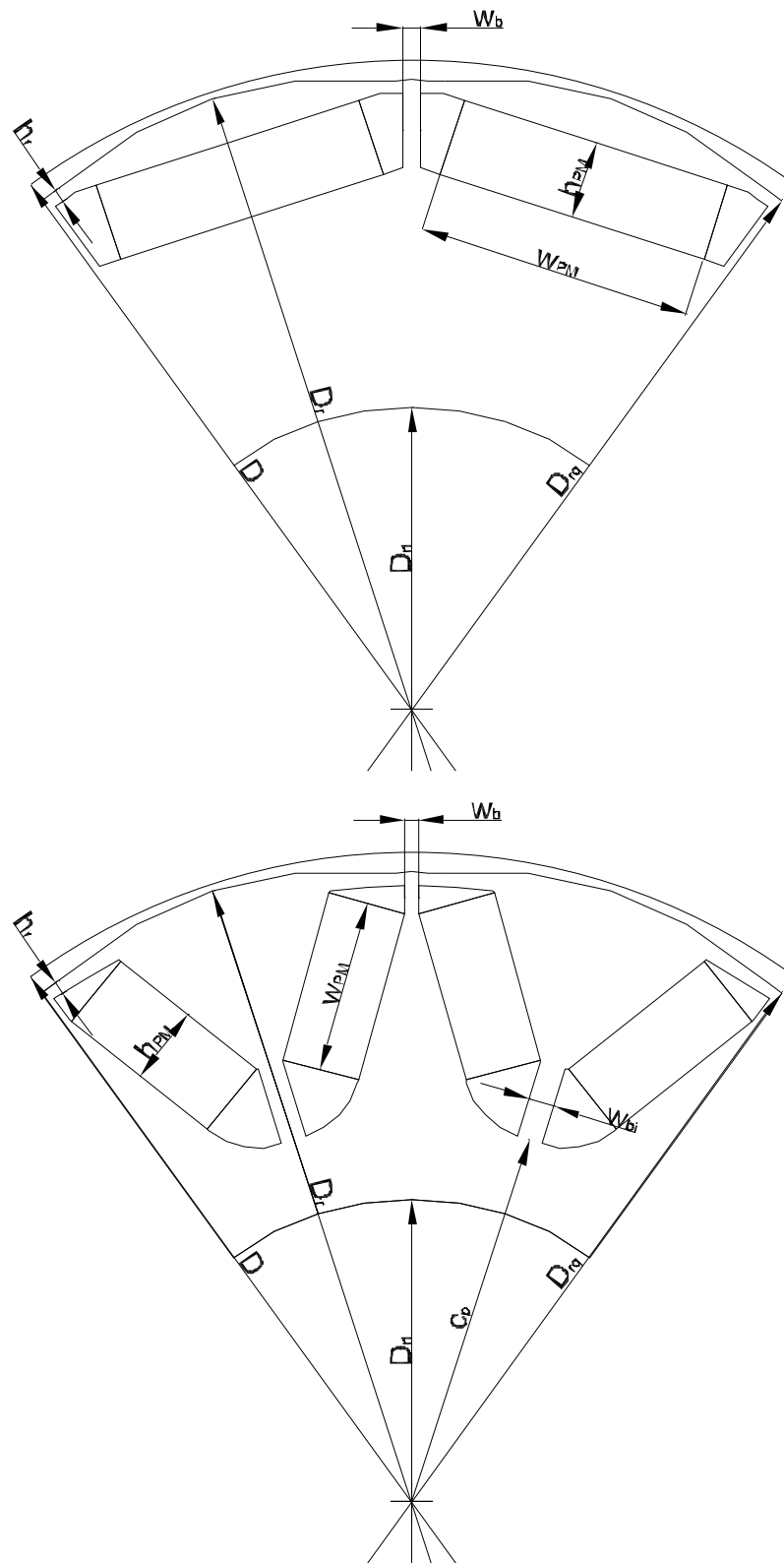


Figure 4.5: Main dimensions of rotor.

Table 4.2: Rotor starting design

Quantity	Symbol	I-shape	V-shape
<i>PM</i> height	$h_{PM}$	5mm	
<i>PM</i> width	$w_{PM}$	35mm	24mm
Bridge width	$w_b$	1.5mm	
Bridge inner width	$w_{bi}$	–	3mm
Rib height	$h_r$	1mm	1.5mm
Center post radius	$c_p$	–	45mm

dimensions reported in tab. 4.5.

Bridge and rib dimension are set to value that should be ensure the mechanical strength in order to survive to peak centrifugal stress during high speed operation: we understand immediately the importance of performing a detailed structural analysis that doesn't that hasn't been here, although we have referred to similar *FreedomCAR* design, in particular [7] in which are reported some *FEA* mechanical stress results.

For our round shape analysis we refer only to the I-shape design and extend the same resultant rotor configuration on the V-shape.

Let's perform the follow parametric simulation changing the round shape height  $\Delta_r = 0 \div 3$ , with step of 0.5mm, evaluating the normal airgap flux density, flux linkages, and torque performing a *FFT* (Fast Fourier Transform) implemented in Matlab®, in order to optimize the round shape height. For graphics clarity we have represented only mininum, medium, and maximum value of the previous range although the computation was made for the entire round shape height variation.

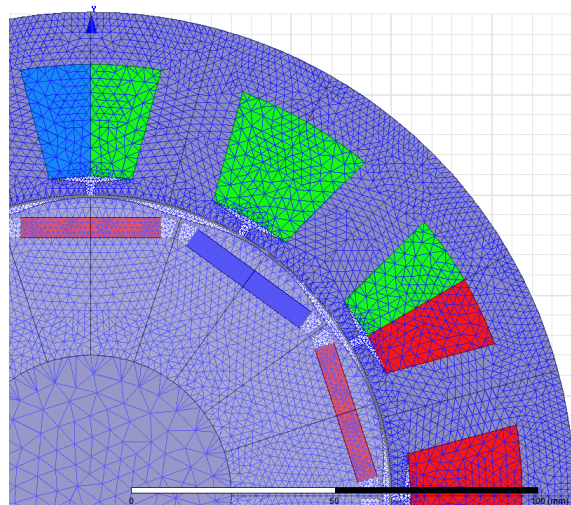


Figure 4.6: Mesh details for I-shape design.



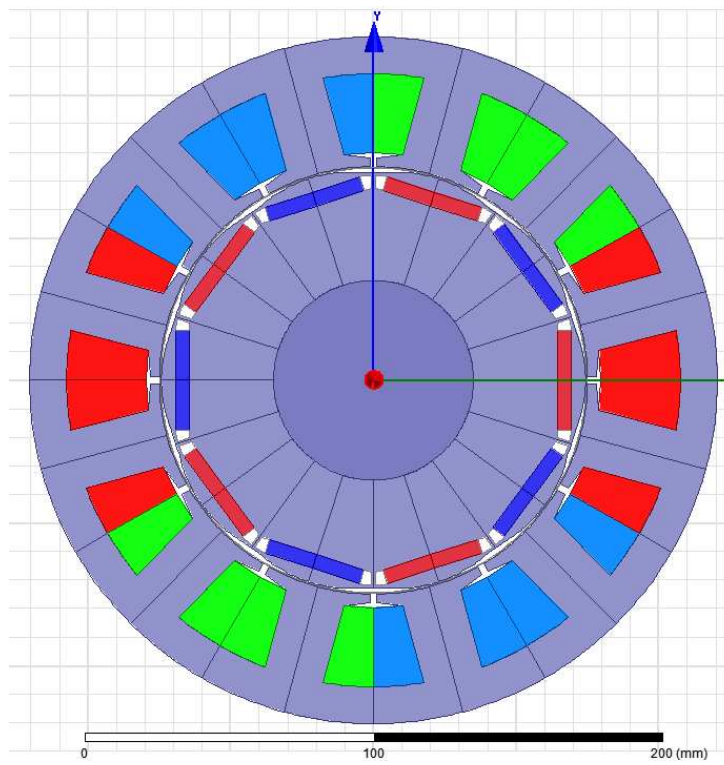


Figure 4.7: I-shape starting design.

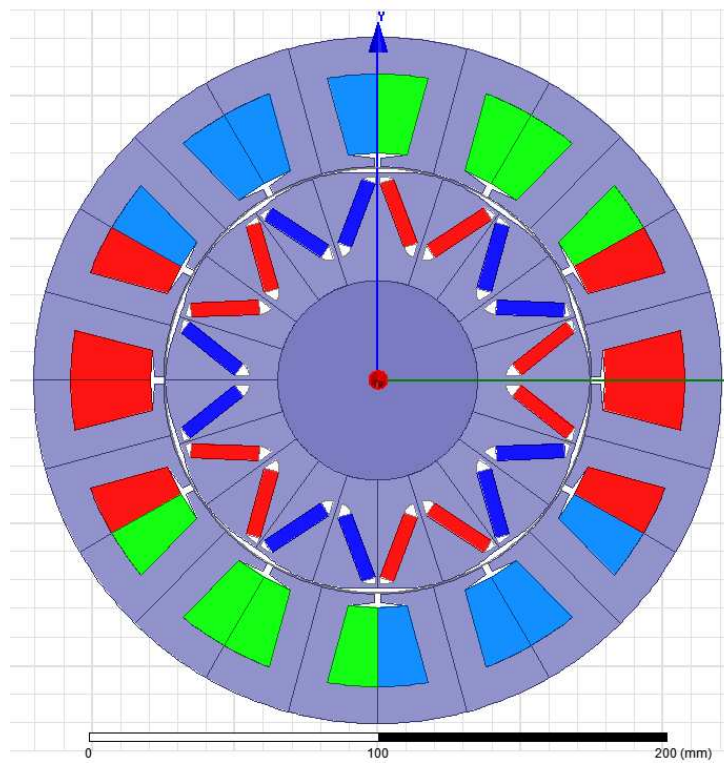


Figure 4.8: V-shape starting design.

- No load simulation

Phase current  $I = 0A_{RMS}$ .

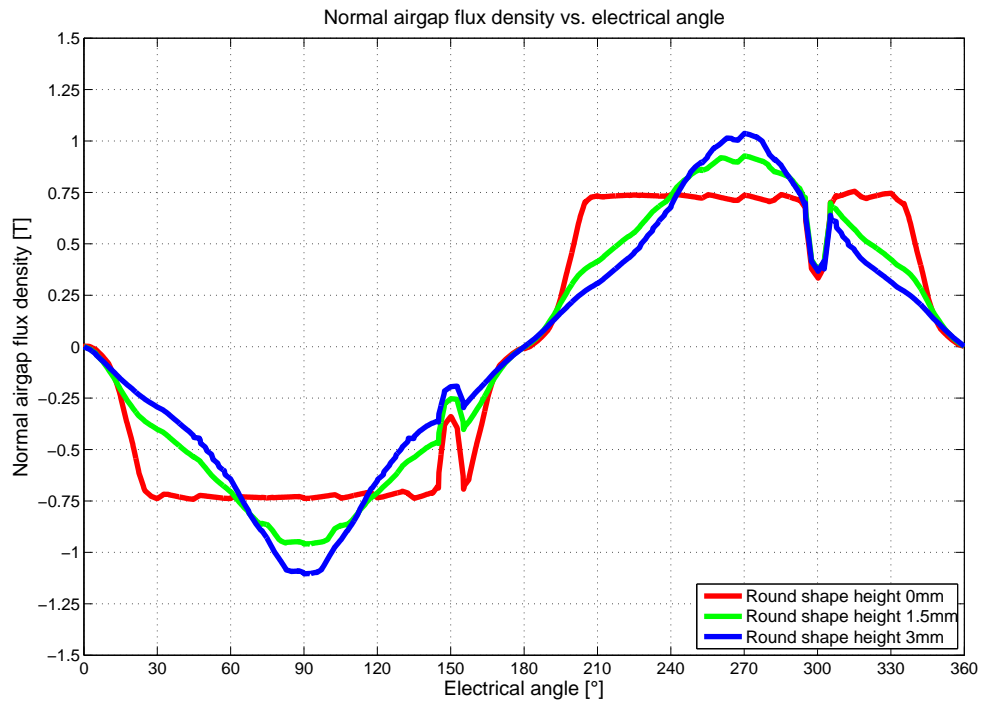


Figure 4.9:

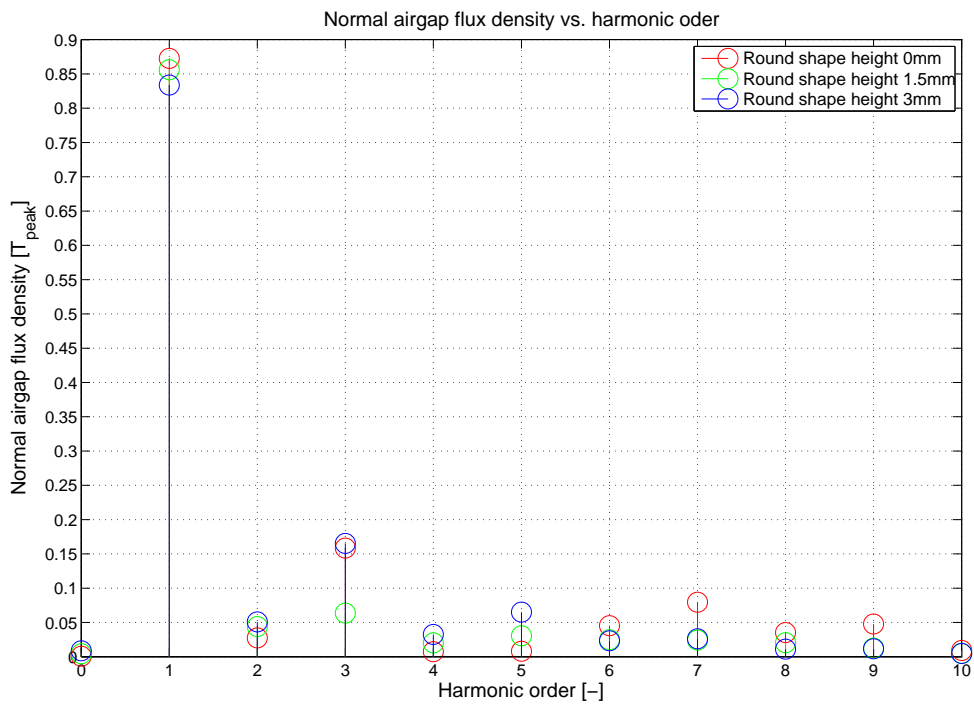


Figure 4.10:

Analyzing the *FFT* of fig. 4.10, according to a square wave distribution, we find the main harmonic contents of odd order, following the relationship,

$$h = 2 \cdot k \pm 1, k = 1, 2, 3... \quad (4.4)$$

The even order harmonics comes from the irregular shape of flux density especially due to slot opening. As we can see, increasing round shape height, we get a general reduction of main harmonics: ideally, the trend would change from a square wave ( $\Delta_r = 0mm$ , magnitude decrement according to  $1/h$ ) to triangular wave ( $\Delta_r \gg 0mm$ , magnitude decrement according to  $1/h^2$ ) moving through a sinusoidal wave. With  $\Delta_r = 1.5mm$ , we achieve a great reduction of more than 50% of the 3rd harmonic, while the fundamental is maintained substantially constant.

According to analytical synthesis, is interesting to notice that, with conventional round, the maximum value of the airgap flux density  $B_{g0} \approx 0.70 - 0.75T$ , highlighting the good validity of the method used.

Let's evaluate the flux linkage and induced *EMF*, as follows.

Concerning to induced *EMF*, comparing to conventional rotor, the effects

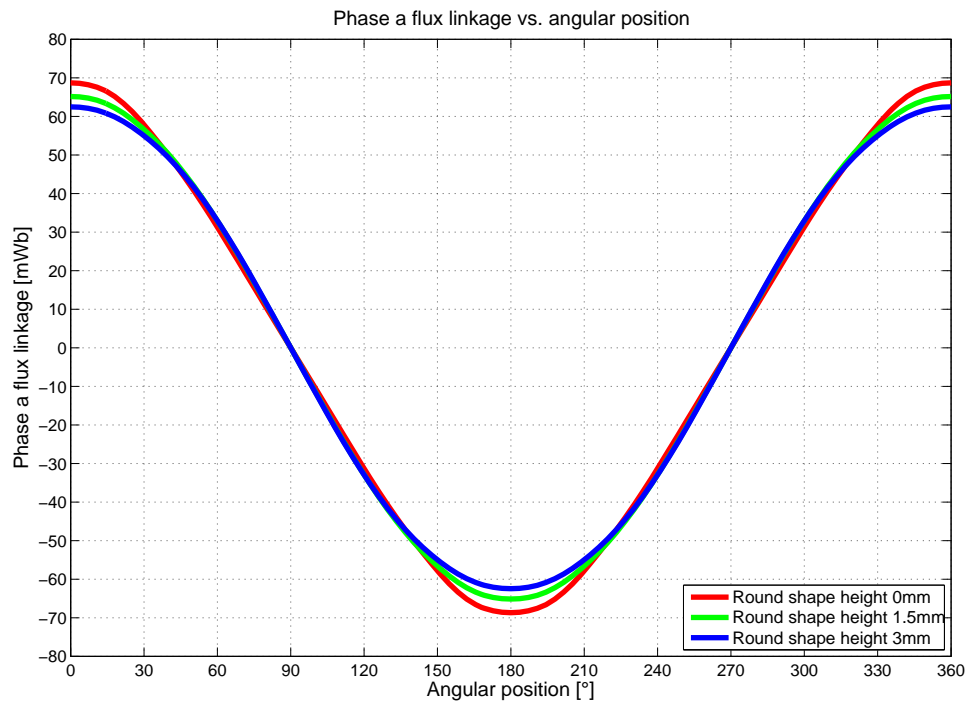


Figure 4.11:

of the round shape design are similarly evident, with a great reduction of the 4th harmonic.

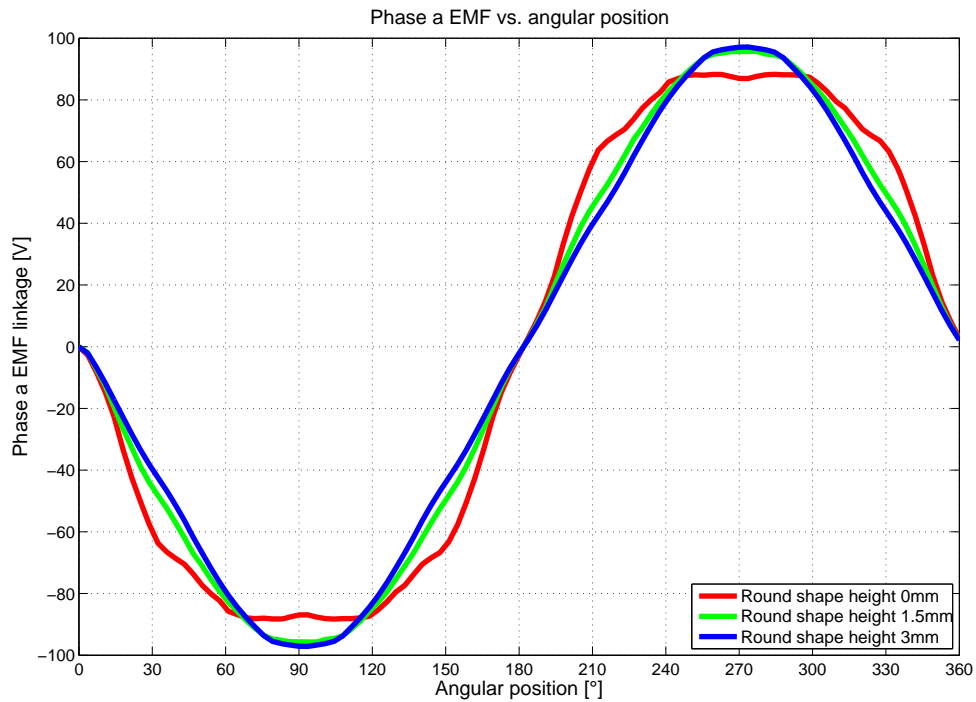


Figure 4.12:

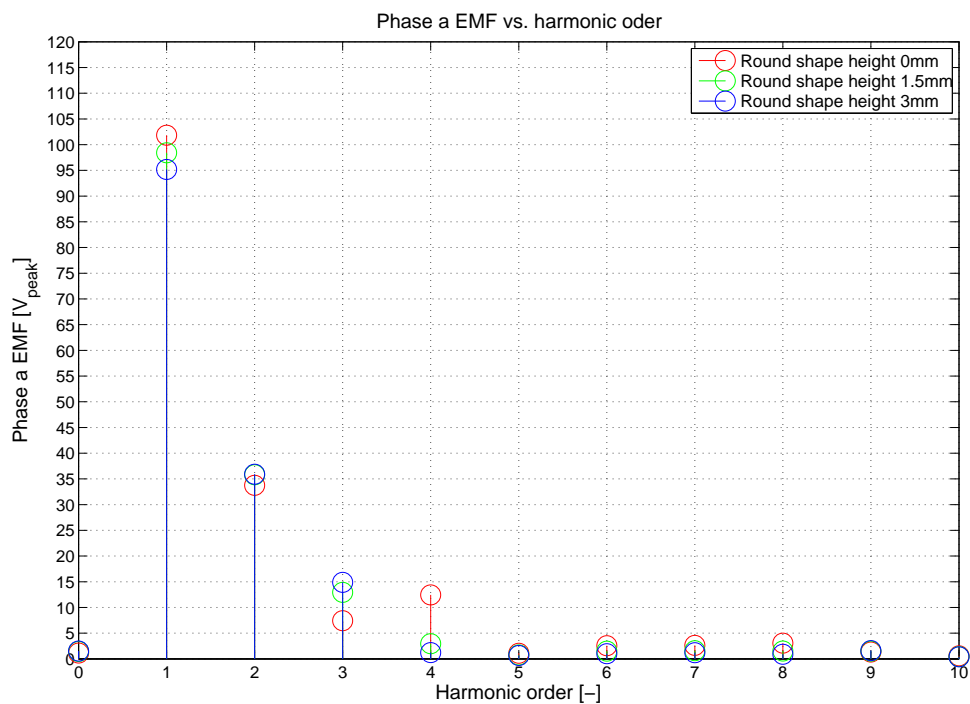


Figure 4.13:

The cogging torque trend is the most interesting results of round shape design: the increase of round shape height till  $3\text{mm}$  leads to a reduction of the magnitude of  $-96\%$ . As highlighted in tab. 4.5 the relationship isn't linear with the height, but tends to saturate by  $\Delta_r = 1.5\text{mm}$  onwards.

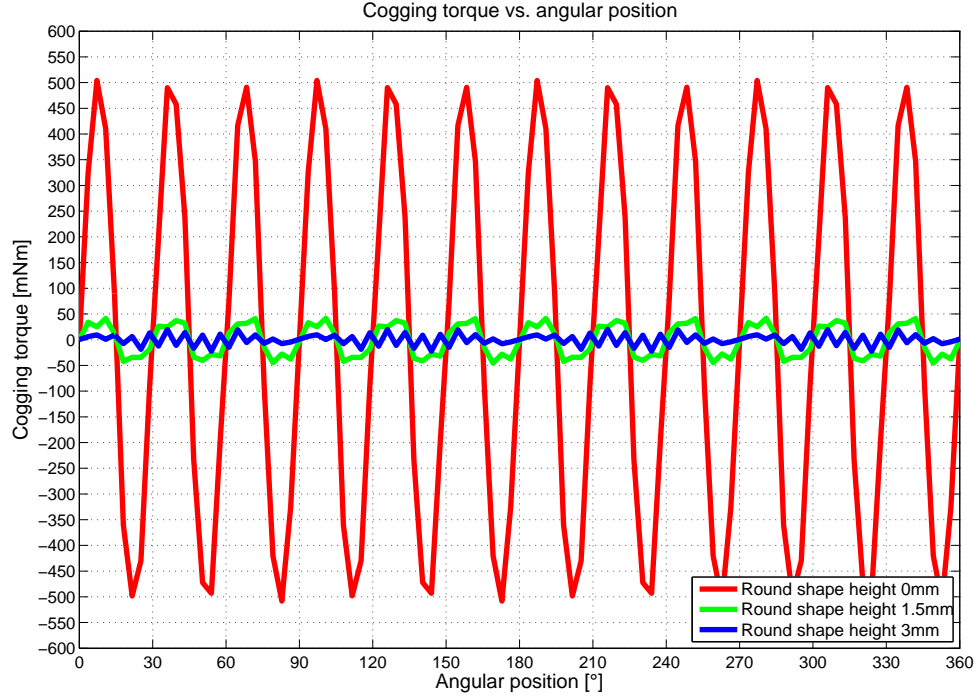


Figure 4.14:

Table 4.3: Cogging torque variation

Round shape height [mm]	0	0.5	1	1.5	2	2.5	3
Cogging torque [ $mNm_{peak}$ ]	504.3	202.2	86.6	41.6	31.9	39.7	20.1
Variation [%]	0	-59.9	-82.8	-92.0	-93.7	-92.1	-96.0

- **Load simulation**

Phase current  $I \cong 130A_{RMS}$ , phase  $\alpha_{ie} \cong 100^\circ$ ; the value chosen for the current phase is typical for *IPM* motors and it's an estimation in order to work in *MTPA* locus.

Although an eventual *FFT* analysis doesn't give any kind of interesting information due to deformed trend of *EMF*, we however notice a more regular and "sinusoidal" shape, increasing round shape height.

Similarly to no load simulation, the torque ripple result shows a reduction slightly smaller than cogging torque variation, being about  $-72\%$ , with a peak of  $-76\%$  at round shape height  $\Delta_r = 2mm$ . The expected drawback is a significantly reduction of torque developed, about  $-12\%$ , due to increase of equivalent airgap: that means, respect to a conventional rotor, we need, for the same torque, a current proportionally higher, or we have to increase the length and/or diameter of the machine. Besides, we can notice that the phase current of  $130A_{RMS}$ , approximately equal to the value achieved from analytical synthesis, it's not sufficient, for this design, to reach the rated torque.

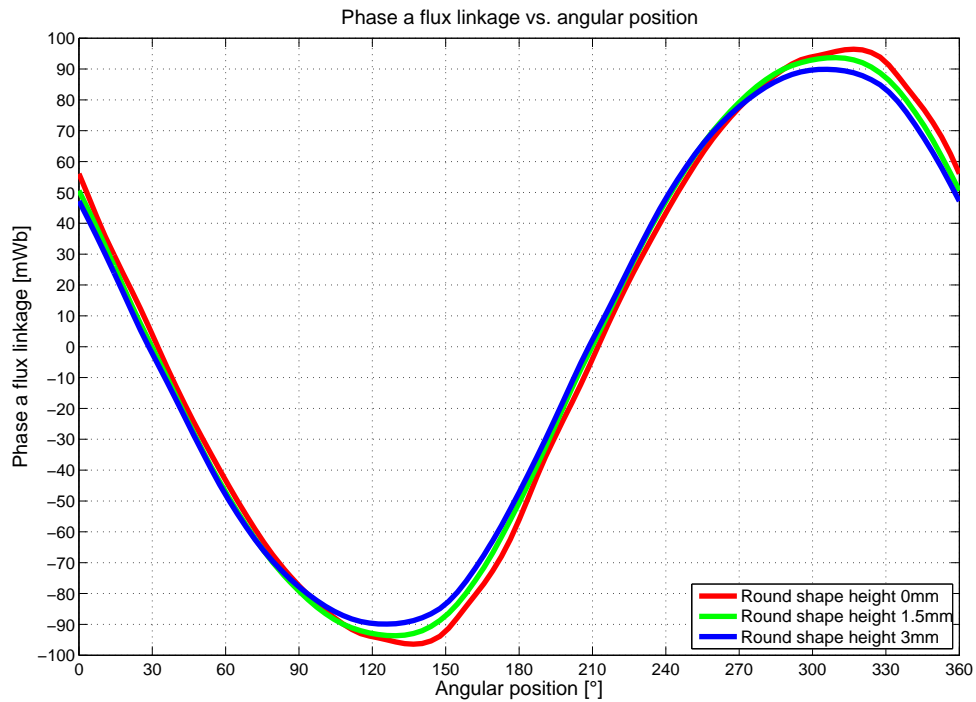


Figure 4.15:

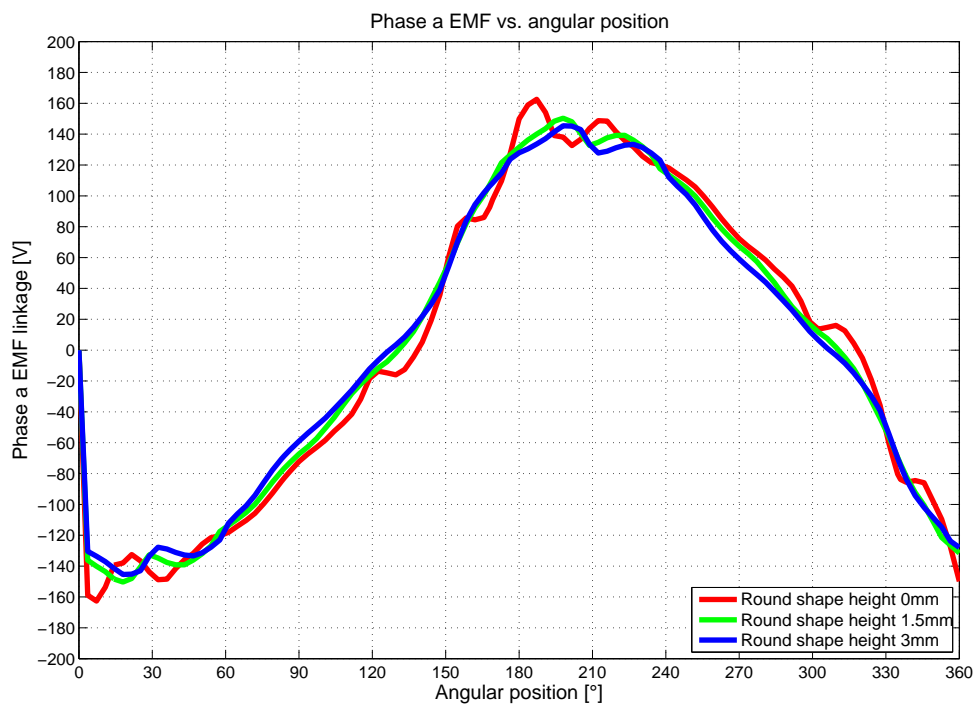


Figure 4.16:

All the previous arguments suggest us to choose an intermediate value for round shape height,  $\Delta_r = 1.5\text{mm}$ , in order to achieve benefits for the reduction of of harmonic contents of no load air gap flux density and induced *EMF*, cogging torque and torque ripple without influence over the loss of torque.

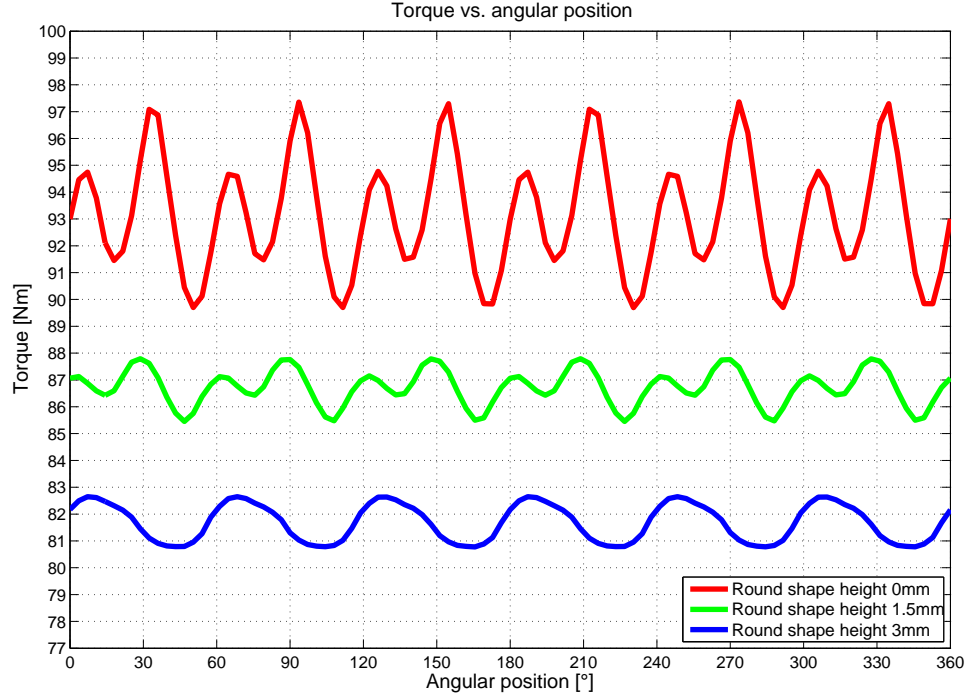


Figure 4.17:

Table 4.4: Torque and torque ripple variation

Round shape height [mm]	0	0.5	1	1.5	2	2.5	3
Torque (mean value) [Nm]	93.1	90.8	88.7	86.7	84.9	83.3	81.7
Variation [%]	0	-2.5	-4.8	-6.8	-8.8	-10.6	-12.3
Torque ripple [%]	8.2	5.9	4.0	2.7	1.9	2.0	2.3
Variation [%]	0	-28.7	-51.2	-67.3	-76.0	-75.5	-72.2

#### 4.2.2. Final design

For reaching the final designs, I changed predominantly the size of the *PMs*, evaluating the maximum capability of the machines: we fed them with the maximum permissible phase current  $I \cong 400A_{RMS}$ , phase  $\alpha_{ie} \cong 100^\circ$  (for the reason mentioned in the previous paragraph), in order to get and check the following points:

1. Maximum torque  $T_{MAX} \cong 188Nm$ .
2. Rated DC bus voltage  $V_{DCn} \cong 325V$ , that means a rated phase voltage  $E_n \cong 132V_{RMS}$ : it's evaluated at base speed  $n_B = 2800rpm$ .
3. Demagnetization check, for preventing the irreversible demagnetization of magnets, achieved when the *PM* flux density become lower than knee value, prudentially chosen equal to  $B_{knee} = 0.25T$ .

Table 4.5: Rotor final design.

Quantity	Symbol	I-shape	V-shape
<i>PM</i> height	$h_{PM}$	9mm	
<i>PM</i> width	$w_{PM}$	32mm	20mm
Bridge width	$w_b$	2mm	1.5mm
Bridge inner width	$w_{bi}$	–	3mm
Rib height	$h_r$	1.5mm	
Center post radius	$c_p$	–	44mm

Subsequent attempts were made in order to reach the final designs: for simplicity we show, in detail, the analysis as for the firsts designs reported in fig. 4.7, 4.8. The following attempts use the same method.

In order to check the results, the torque was evaluated in two ways:

- using the virtual work principles, it's the default setting of the software, and it's called  $T_{Maxwell}$ ;
- using the d/q-axis flux linkage and current and it's called  $T_{dq}$ , according to the relationship,

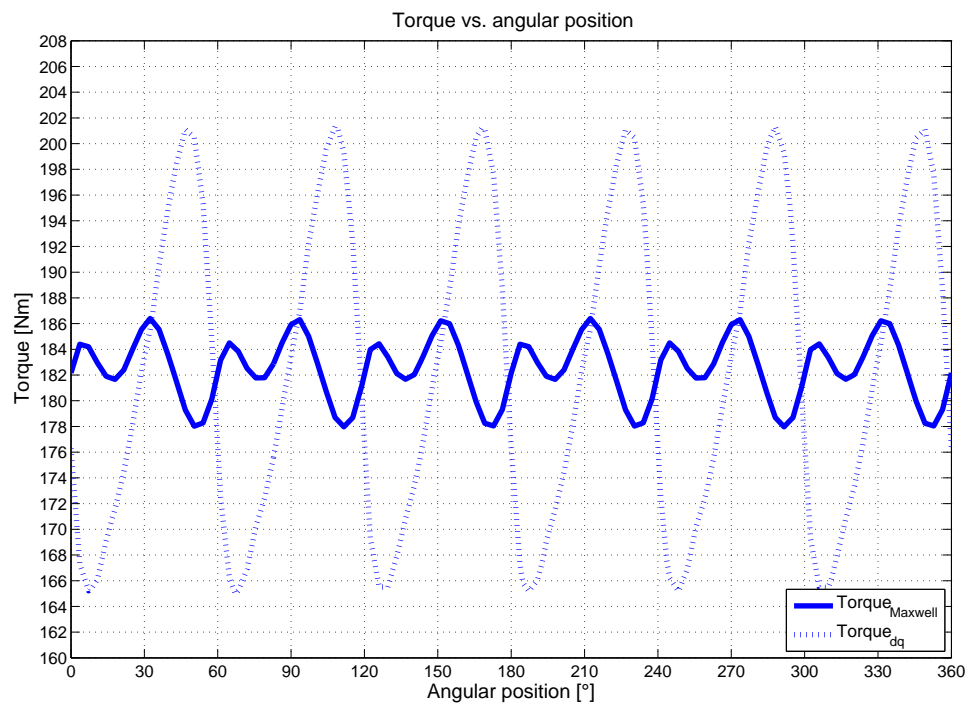
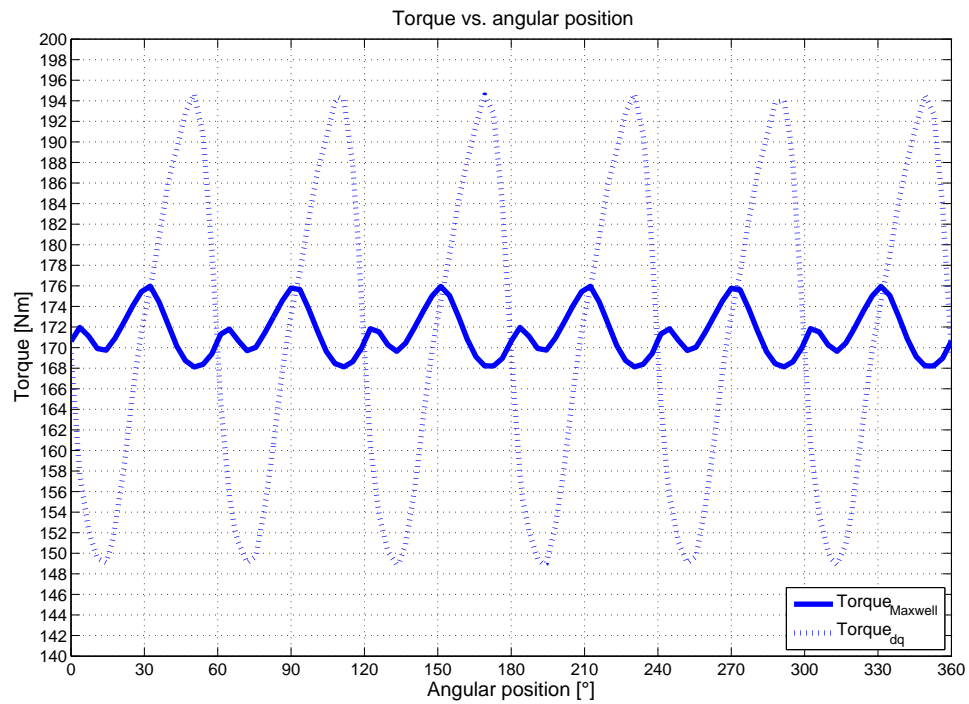
$$T_{dq} = \frac{3}{2} \cdot p \cdot (\lambda_d \cdot I_q - \lambda_q \cdot I_d) \quad (4.5)$$

The mean value of the previous torque must be the same.

As reported in fig. 4.18, 4.19, both the designs don't reach the maximum torque target. Note the phase resistance  $R = 11.9m\Omega$ , base speed  $n_B = 2800rpm$ , and d-q/axis flux linkage, using the eq. ??, and the second of ??, we calculate the phase voltage  $E \cong 136V_{RMS}$  for I-shape and  $E \cong 140V_{RMS}$  for V-shape, higher than the requested  $132V_{RMS}$ . In this operating condition, there are some *PMs* that work under the knee point, as illustrated in fig. ?? and ??: the I-shape prove to be more susceptible to demagnetization due the lower iron shield while V-shape flux density map show some local critical areas.

The method used to fit to the specifics was been to increase *PMs* height  $h_{PM}$  and reduce their width  $w_{PM}$  in order to reduce the *PM* flux linkage, and so the voltage, increasing however the torque and the magnetic strength due to the increase of their height. Consequently, the bridges dimensions are increased in order to ensure the mechanical strength to the centrifugal stress: for both designs, especially for V-shape, I made reference to the mechanical results of the structural *FEA*, performed on a similar *FreedomCAR* motor, described in paper [7].



Figure 4.18: I-shape, mean torque  $182.5Nm$ .Figure 4.19: V-shape, mean torque  $171.4Nm$ .

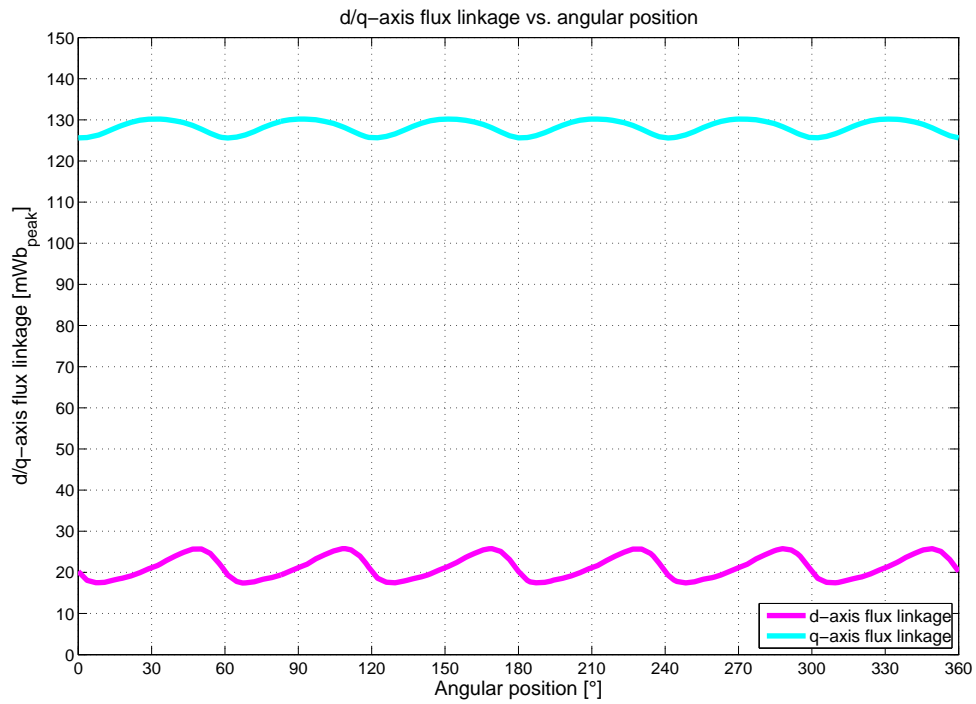


Figure 4.20: I-shape, mean d-axis flux linkage  $21.2mWb_{peak}$ , mean q-axis flux linkage  $128.2mWb_{peak}$

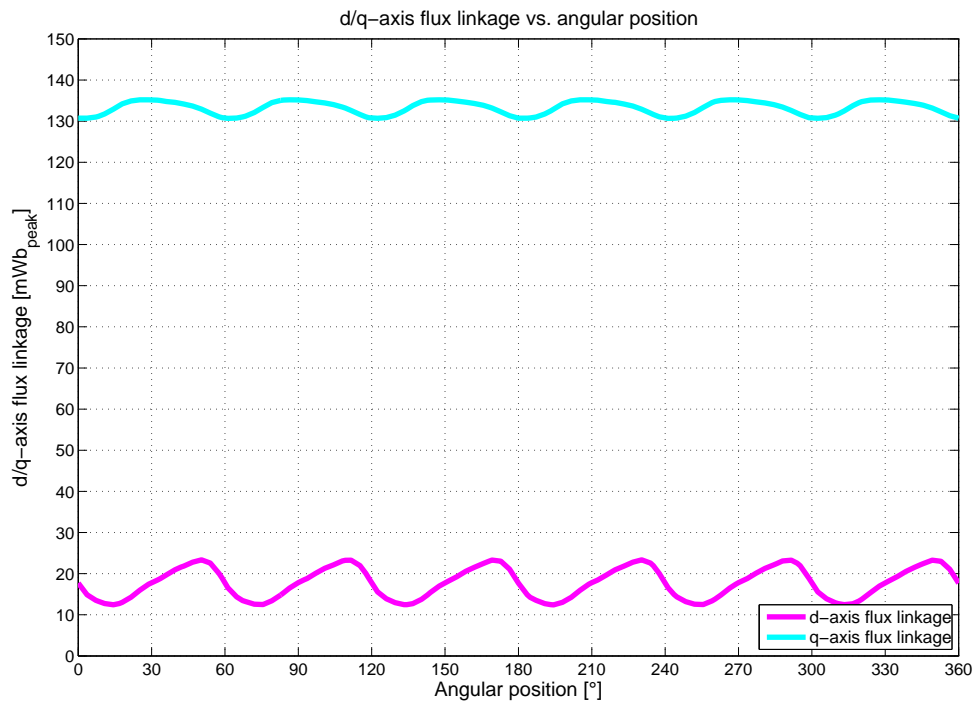


Figure 4.21: V-shape, mean d-axis flux linkage  $17.7mWb_{peak}$ , mean q-axis flux linkage  $133.3mWb_{peak}$

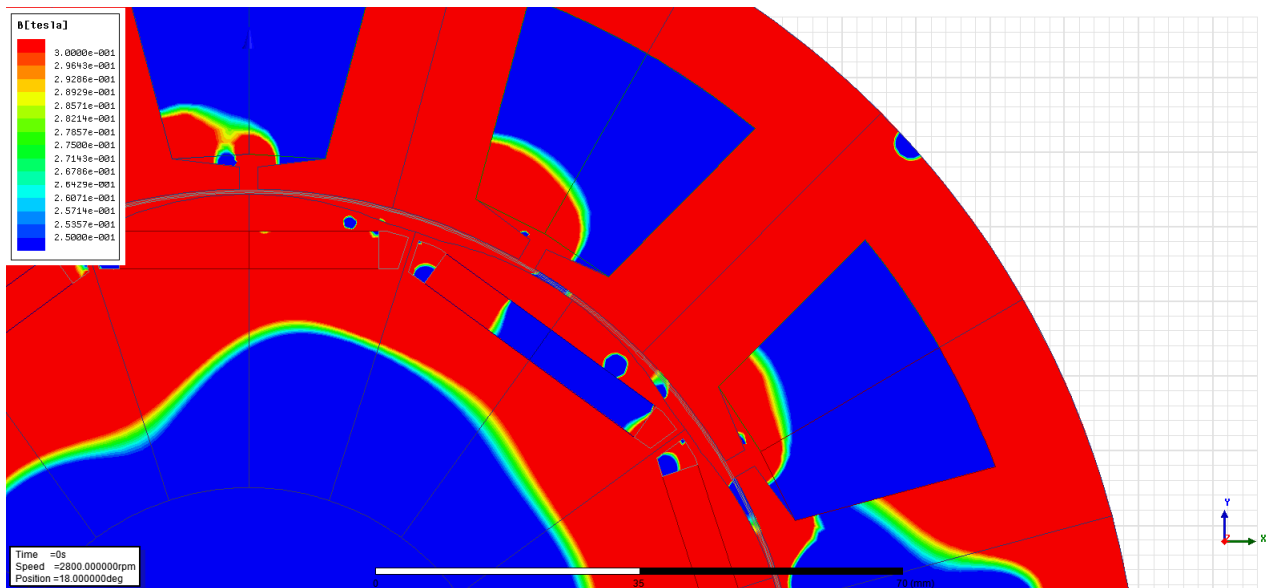


Figure 4.22: Detail of demagnetization in I-shape magnets: the magnet in the center of the picture is irreversible demagnetized for most of it.

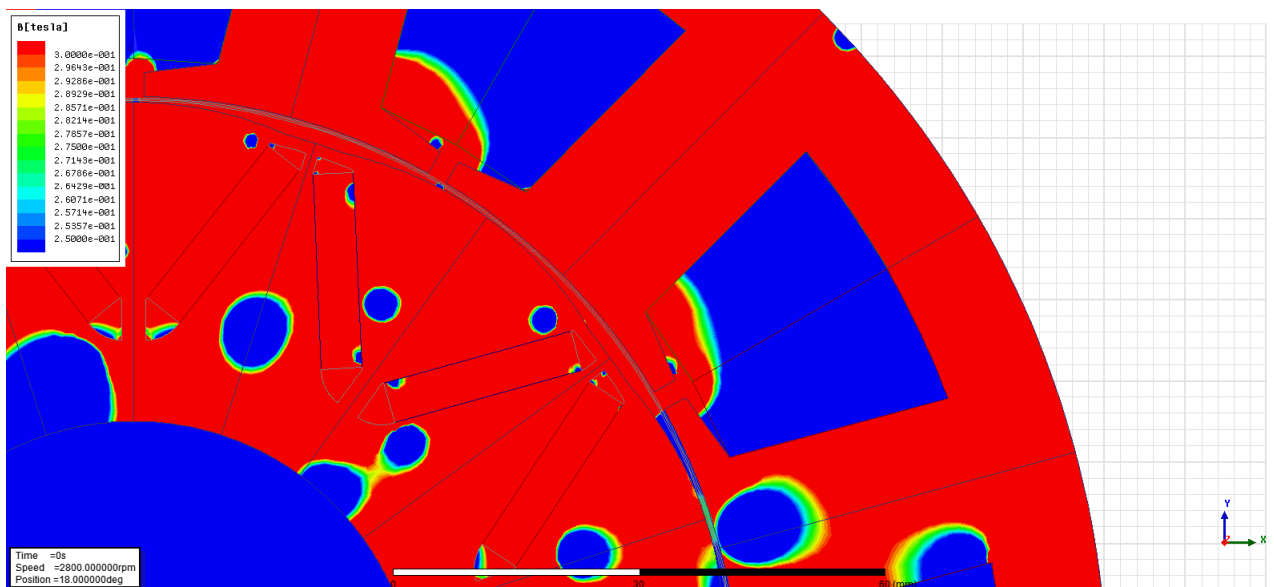


Figure 4.23: Detail of demagnetization in V-shape magnet: there are some demagnetized circular areas in the magnet in the center of the picture.

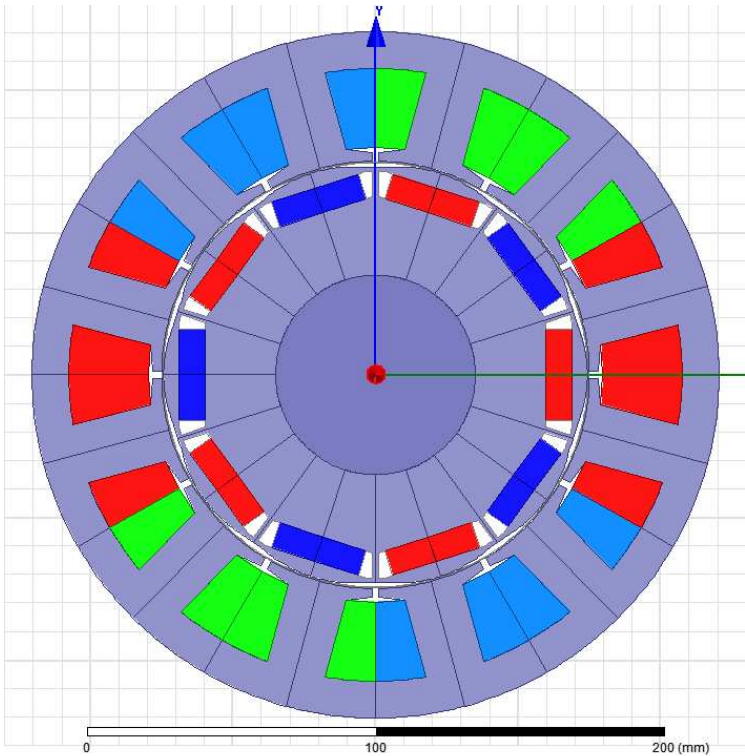


Figure 4.24: I-shape final design.

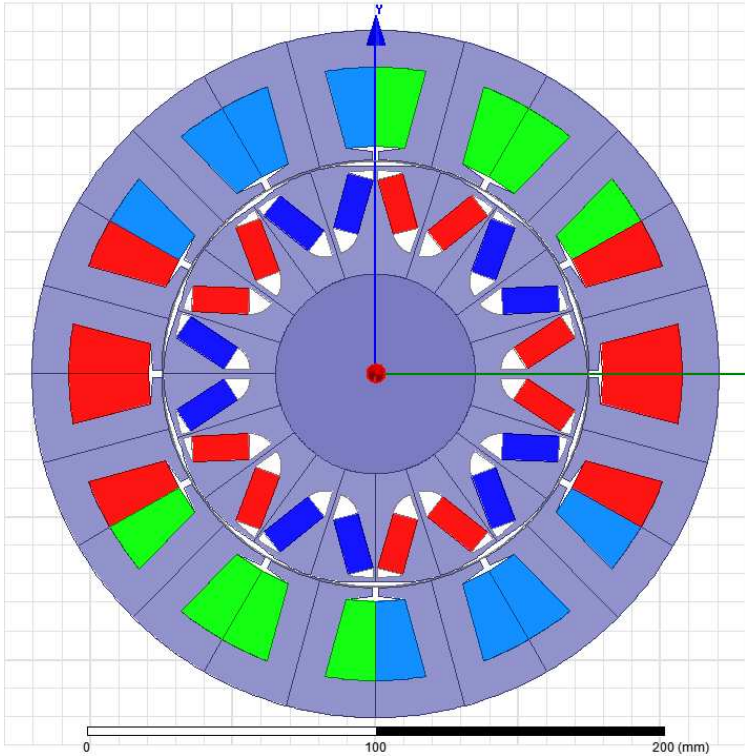


Figure 4.25: V-shape final design.

### 4.3. No load simulation

The no load simulation is performed rotating the machine at base speed with open circuit.

As reported in flux density maps of fig. 4.26, 4.27, bridges are to an adequate

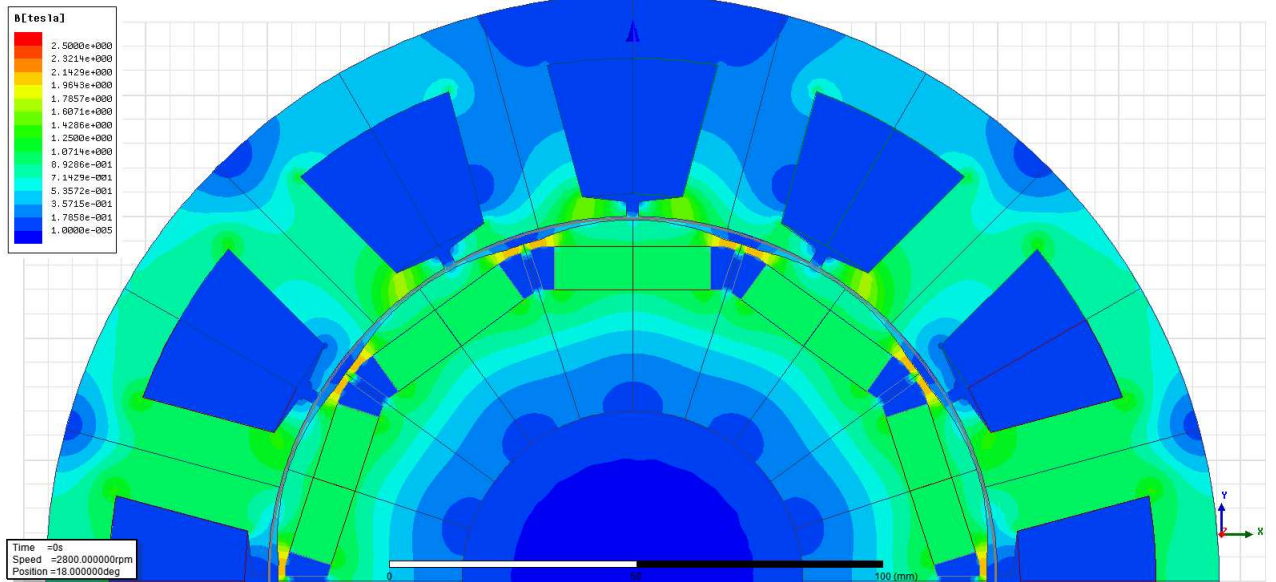


Figure 4.26: I-shape no load flux density map.

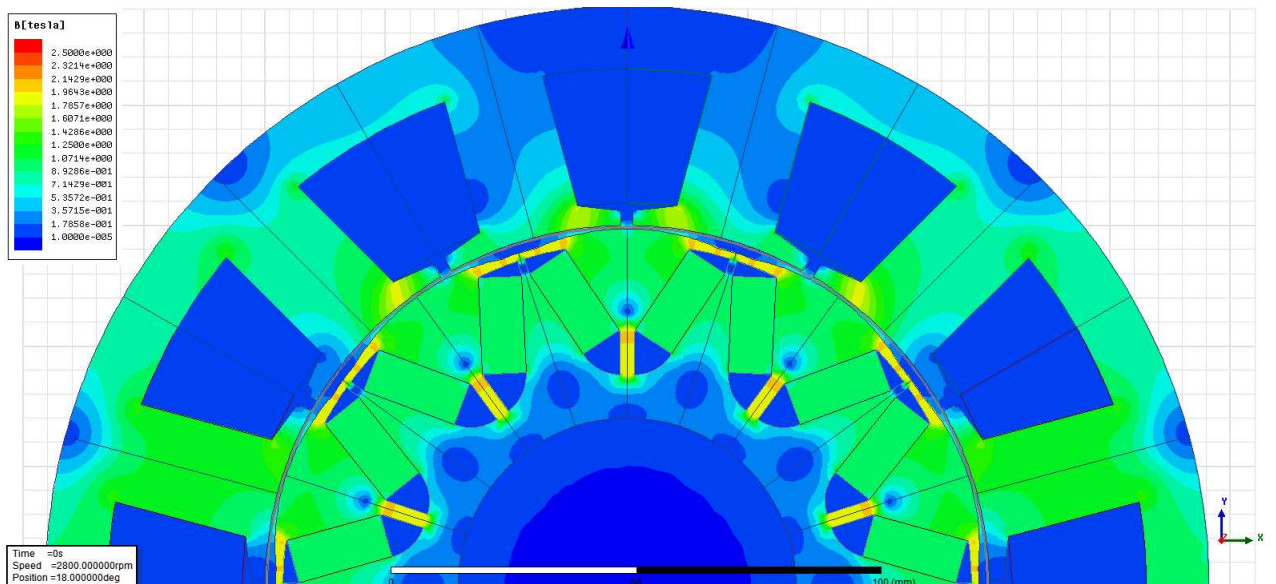


Figure 4.27: V-shape no load flux density map.

level of saturation, in order to prevent flux leakages.

V-shape design, due to the increase of magnets per pole, has got a peak value slightly higher (10%), than I-shape rotor. Both trends are however similar.

According to the previous flux density consideration, the V-shape design exhibit

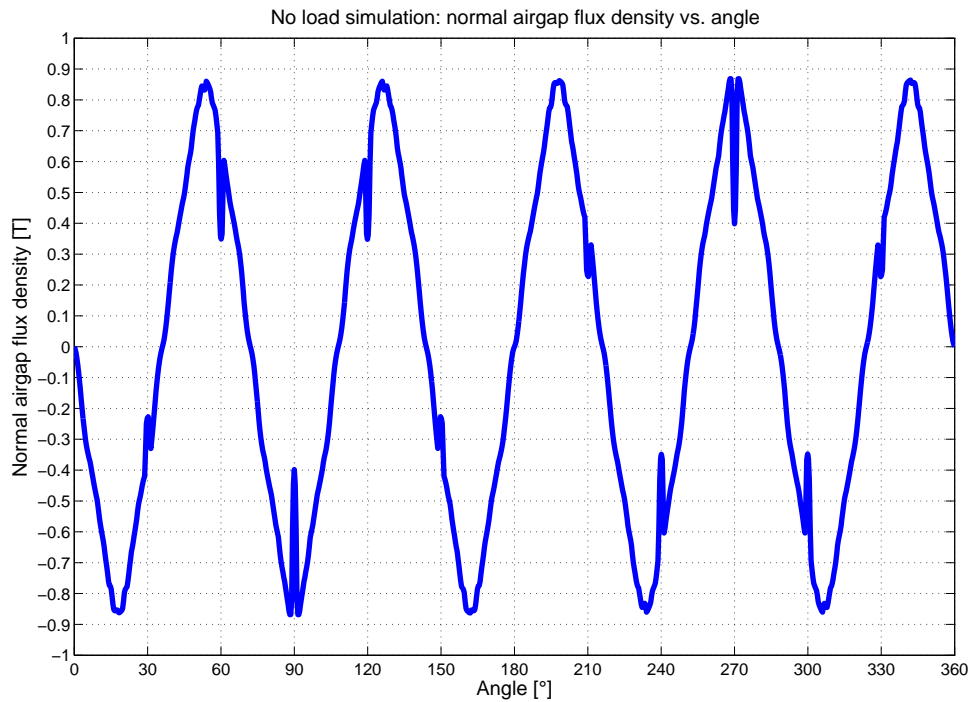


Figure 4.28: I-shape.

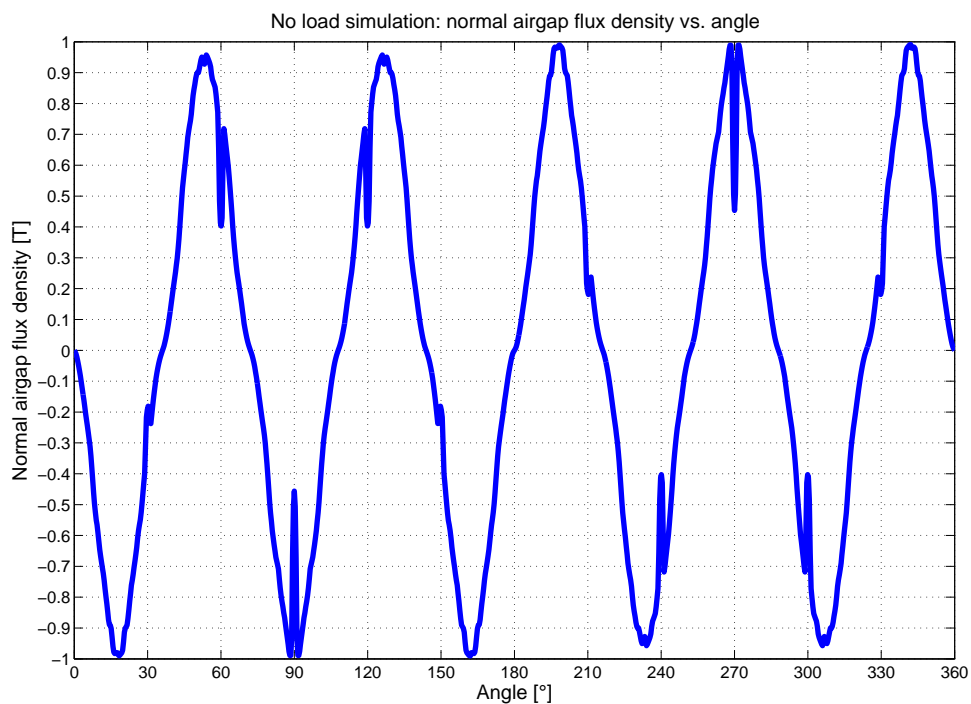


Figure 4.29: V-shape.

a  $PM$  flux linkage about 10% higher,  $\Lambda_{PM} = 65.1mWb_{peak}$  comparing to  $\Lambda_{PM} = 59.2mWb_{peak}$  of I-shape machine. Consequently, using eq. 13, the line to line back  $EMF$  is  $V_0 = 827V$  for V-shape while  $V_0 = 752V$  for I-shape, both values higher than the requested *FreedomCAR* limit  $600V_{peak}$ .

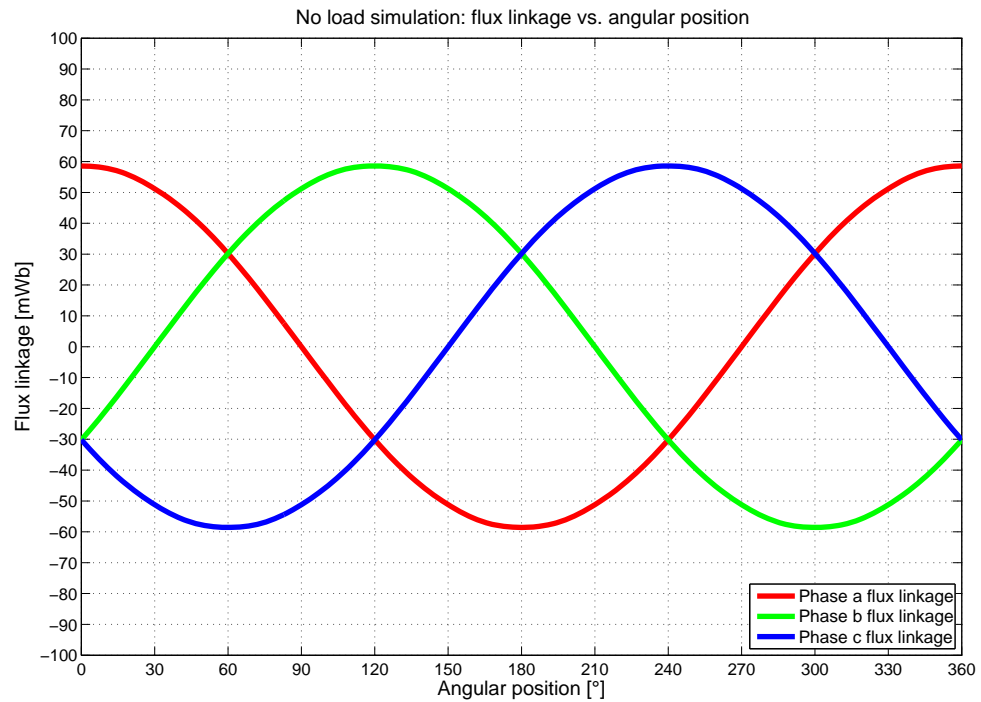


Figure 4.30: I-shape.

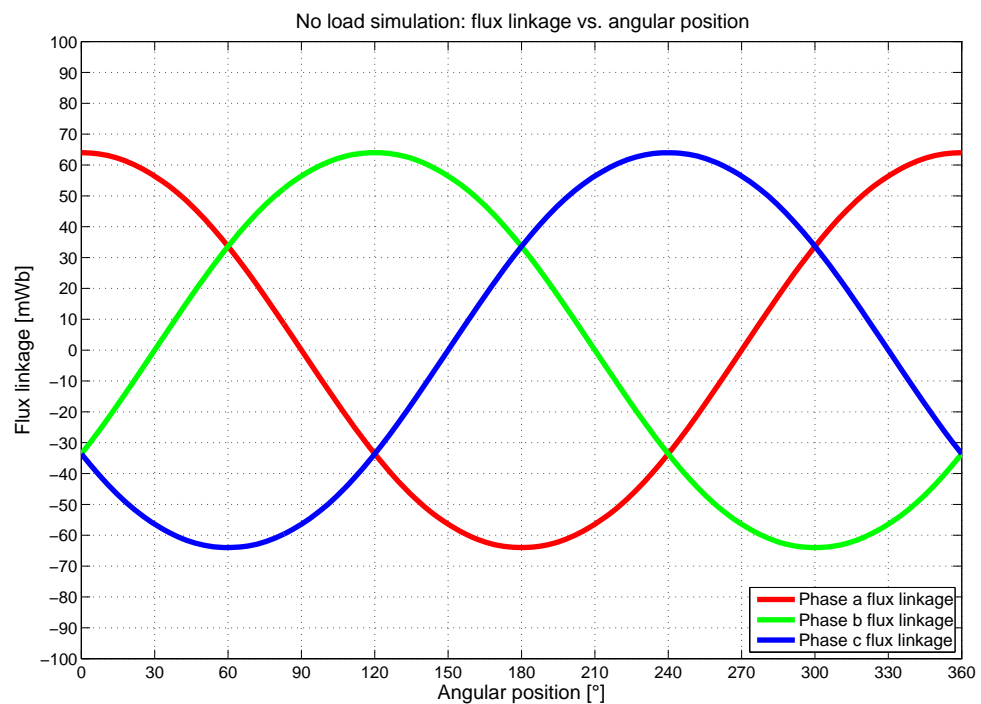


Figure 4.31: V-shape.

According to fig. 4.36, 4.37, comparing to I-shape design, V-shape design shows a cogging torque level about 400% higher than I-shape,  $119\text{mNm}$  vs.  $29.3\text{mNm}$  and this is caused by an higher variation of the permanence in the airgap due to V disposition of magnets.

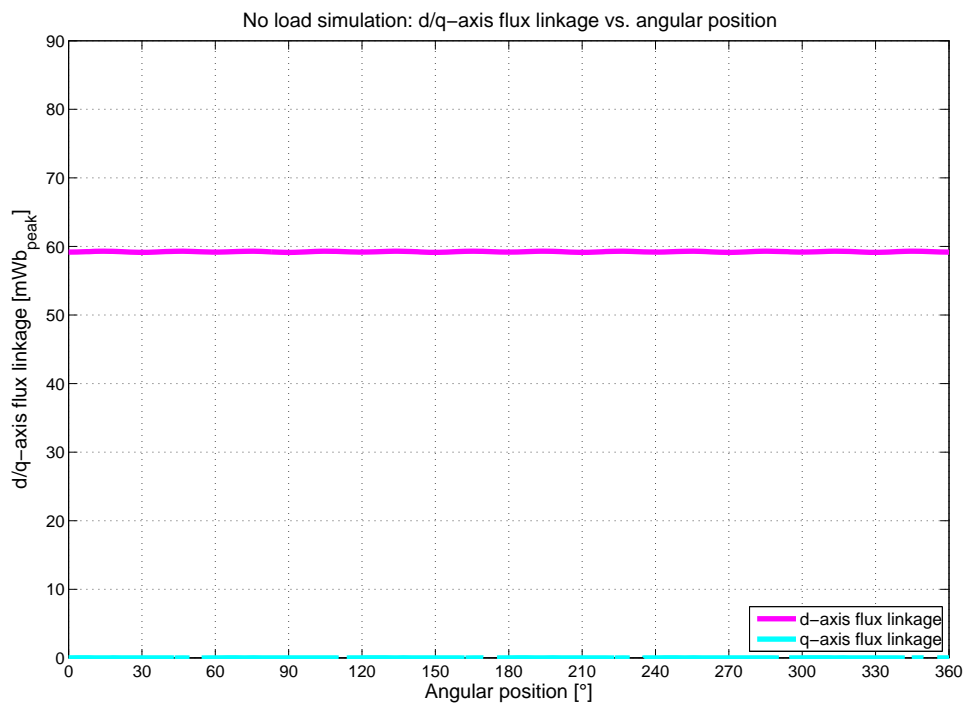


Figure 4.32: I-shape.

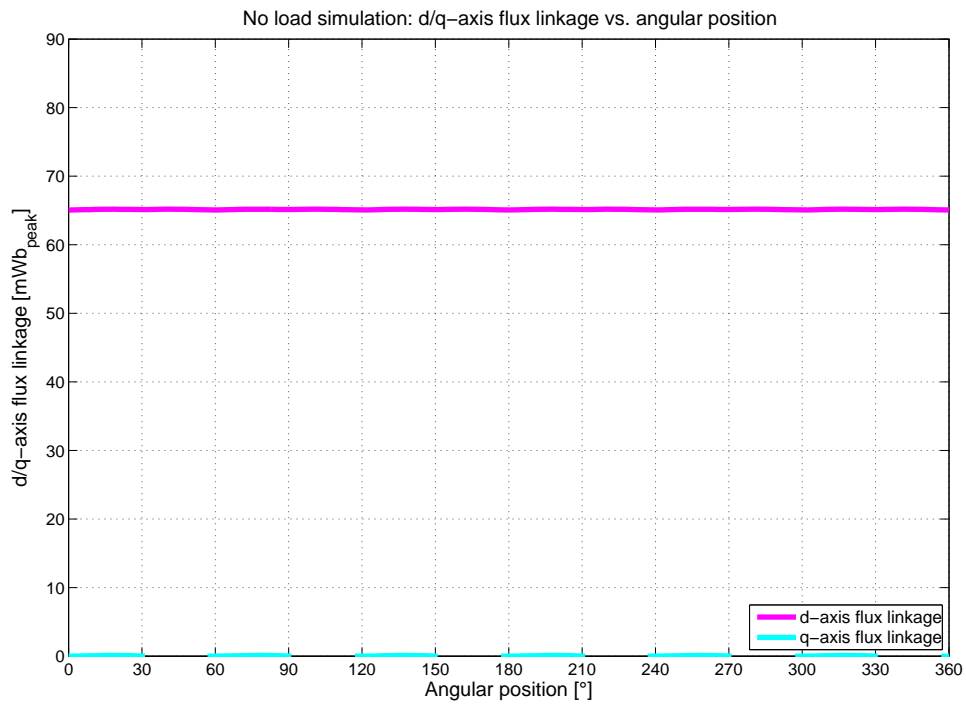


Figure 4.33: V-shape.



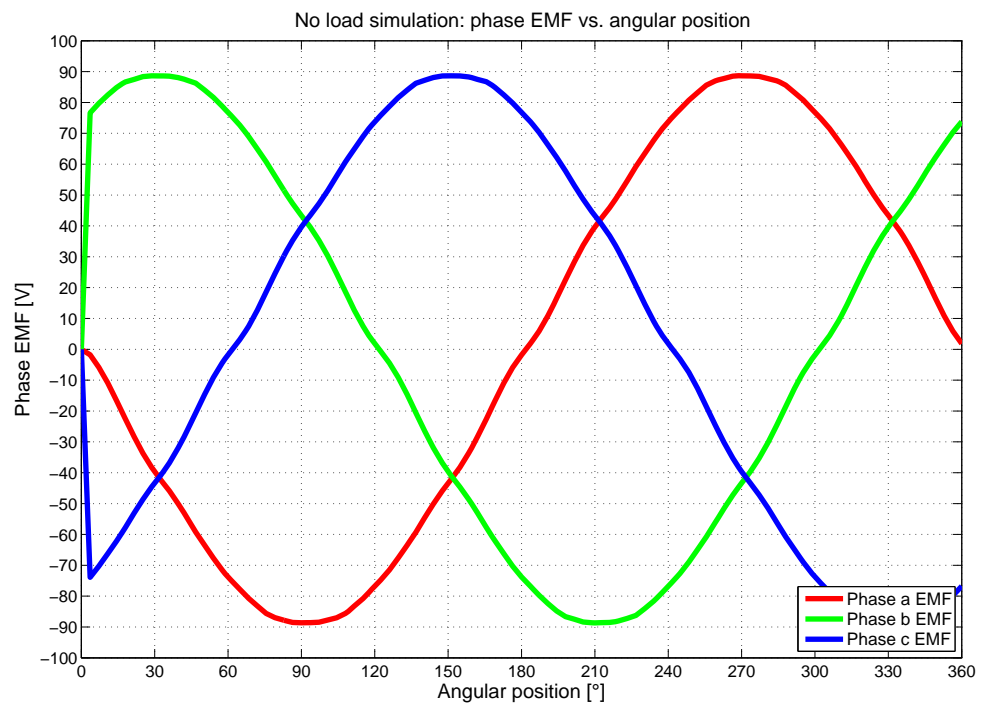


Figure 4.34: I-shape.

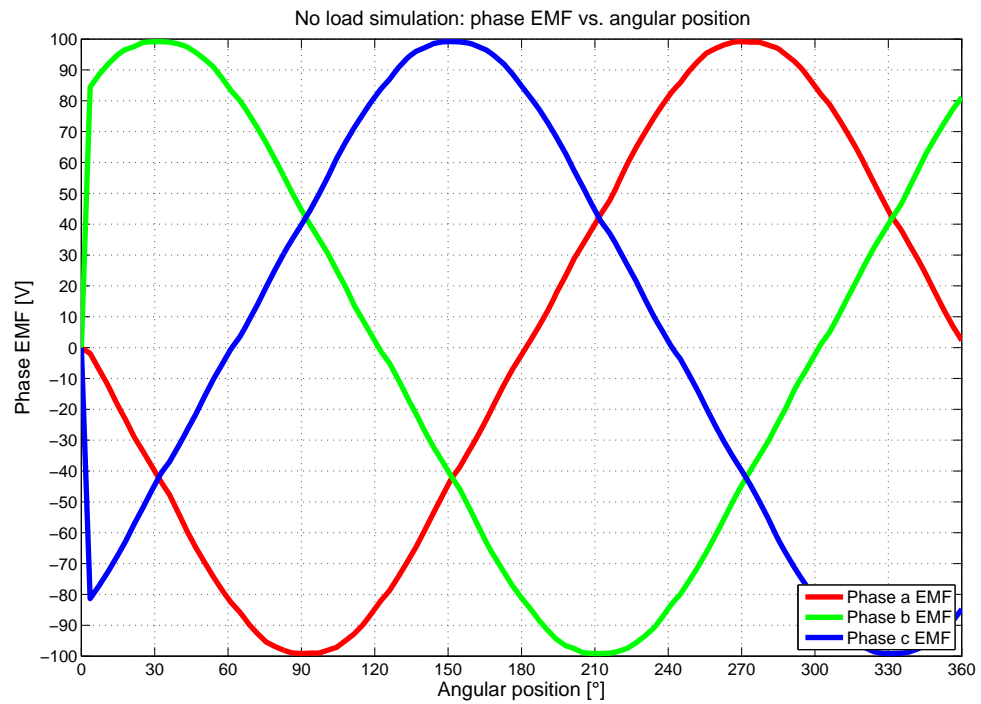


Figure 4.35: V-shape.

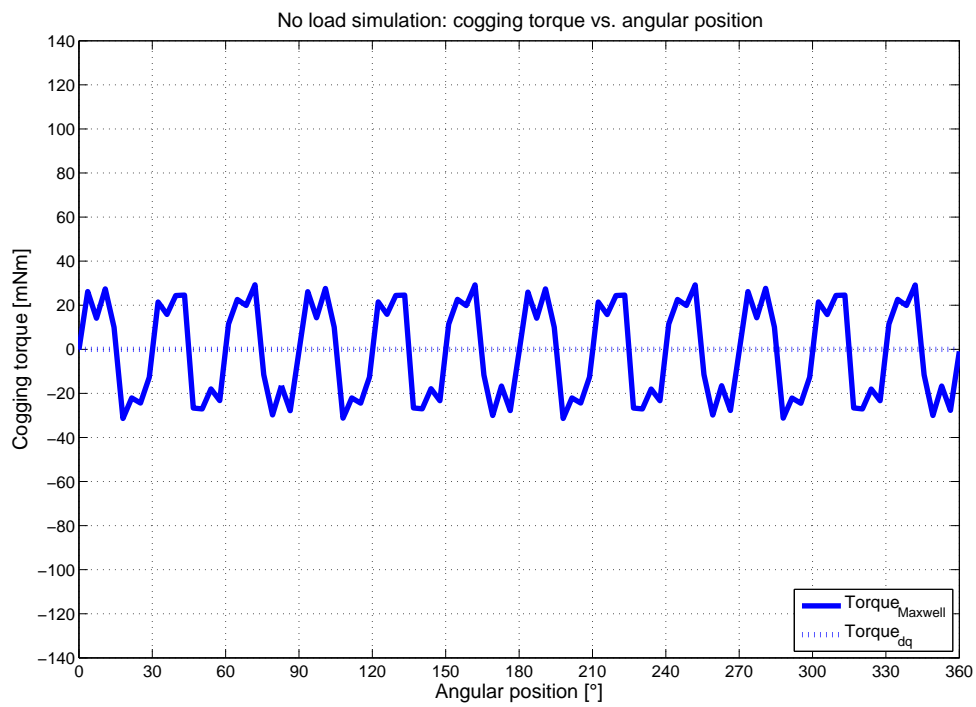


Figure 4.36: I-shape.

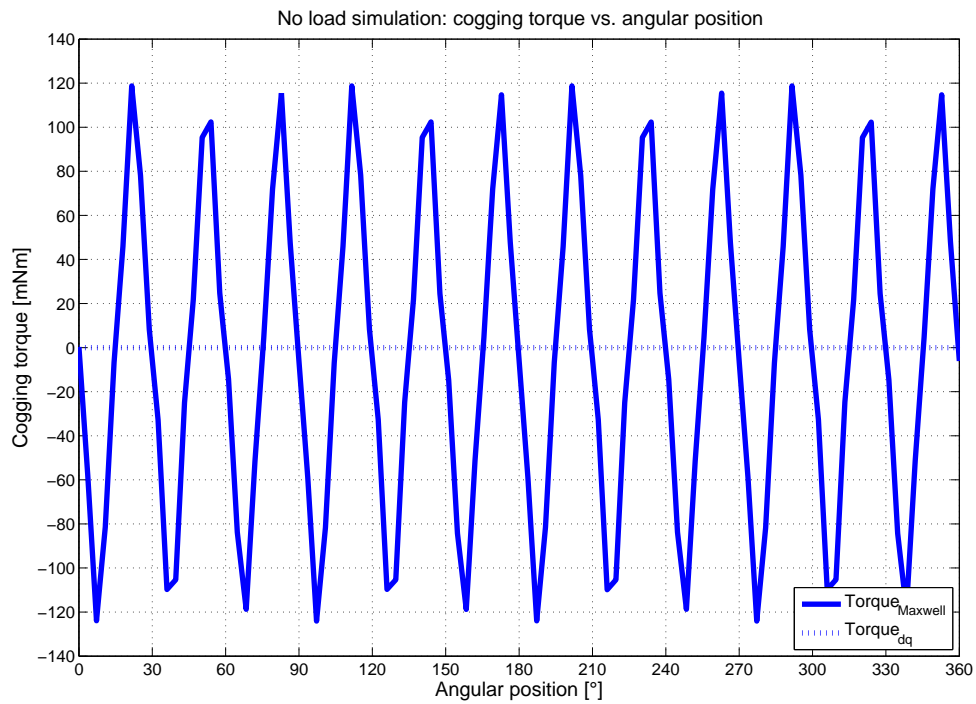


Figure 4.37: V-shape.

#### 4.4. Load simulation

Load simulation allows us to study the performance of the machine at rated conditions, in which it's developed the rated power at base speed. It's performed feeding the machines with the rated phase current that prove to be:

$$I_d = -47.8A_{RMS}, I_q = 152.0A_{RMS} \Rightarrow I = 159.3A_{RMS} \text{ for I-shape;}$$

$$I_d = -36.2A_{RMS}, I_q = 149.8A_{RMS} \Rightarrow I = 154.1A_{RMS} \text{ for V-shape.}$$

We can notice the appropriate level of flux density, according to analytical syn-

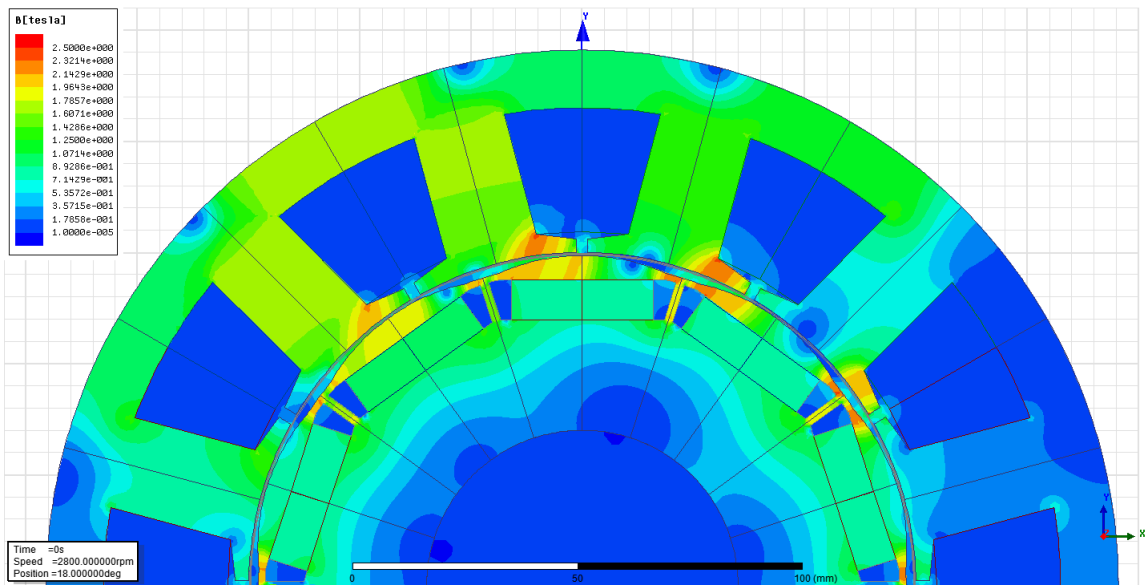


Figure 4.38: I-shape load simulation flux density map.

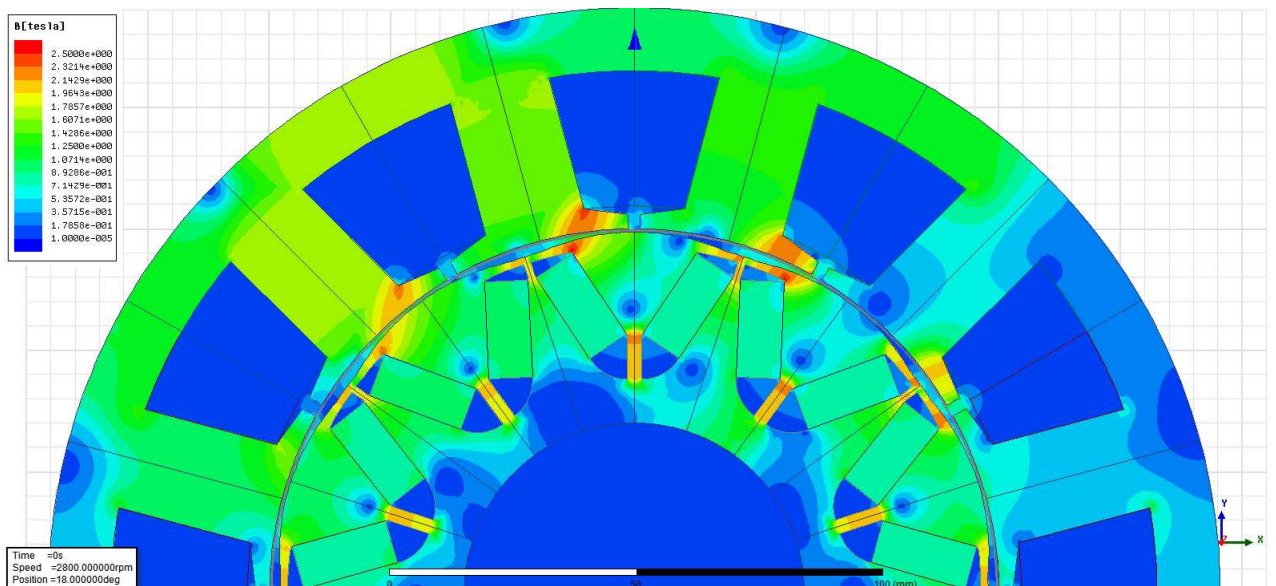


Figure 4.39: V-shape load simulation flux density map.

thesis, in the teeth iron  $B_t = 1.6 \div 2T$  and back iron  $B_{bi} = 1.3 \div 1.7T$ .

As highlighted in fig. 4.48, 4.49, for both the machines, in rated load,

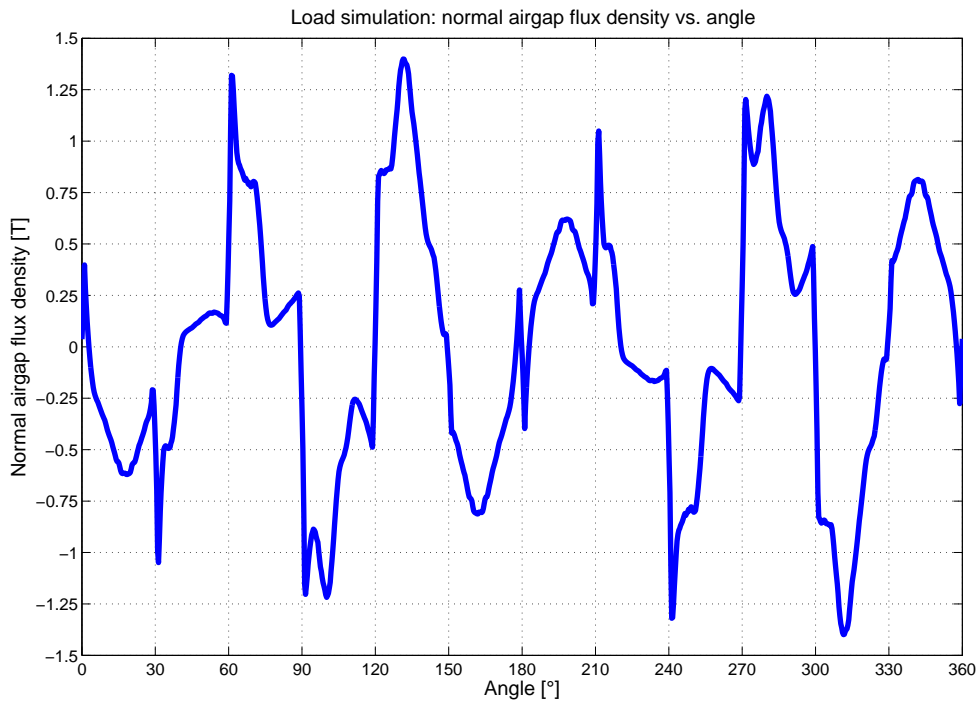


Figure 4.40: I-shape.

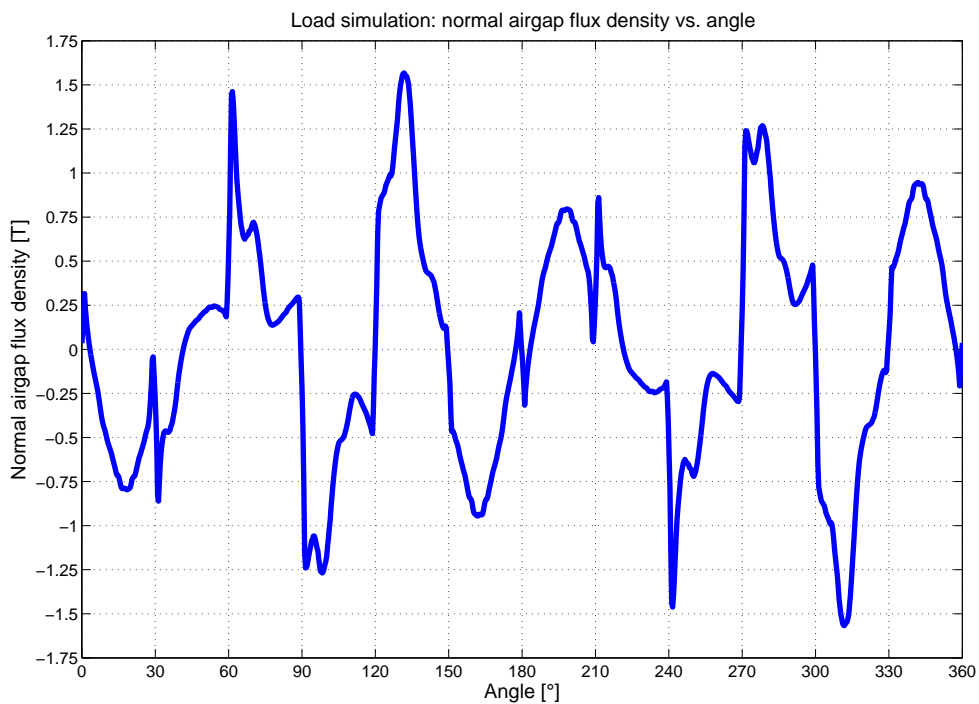


Figure 4.41: V-shape.

the torque ripple is lower than 5% target, equal to 2.2% for I-shape and 2.4%. In I-shape design, we can notice the presence of a significant value of the 12<sup>th</sup>

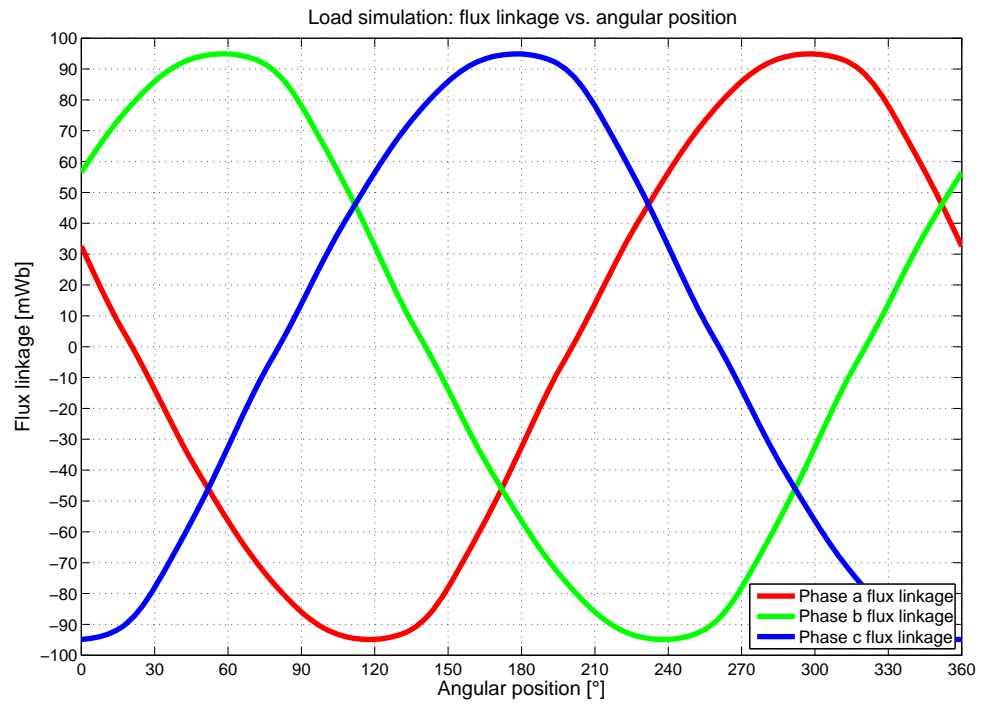


Figure 4.42: I-shape.

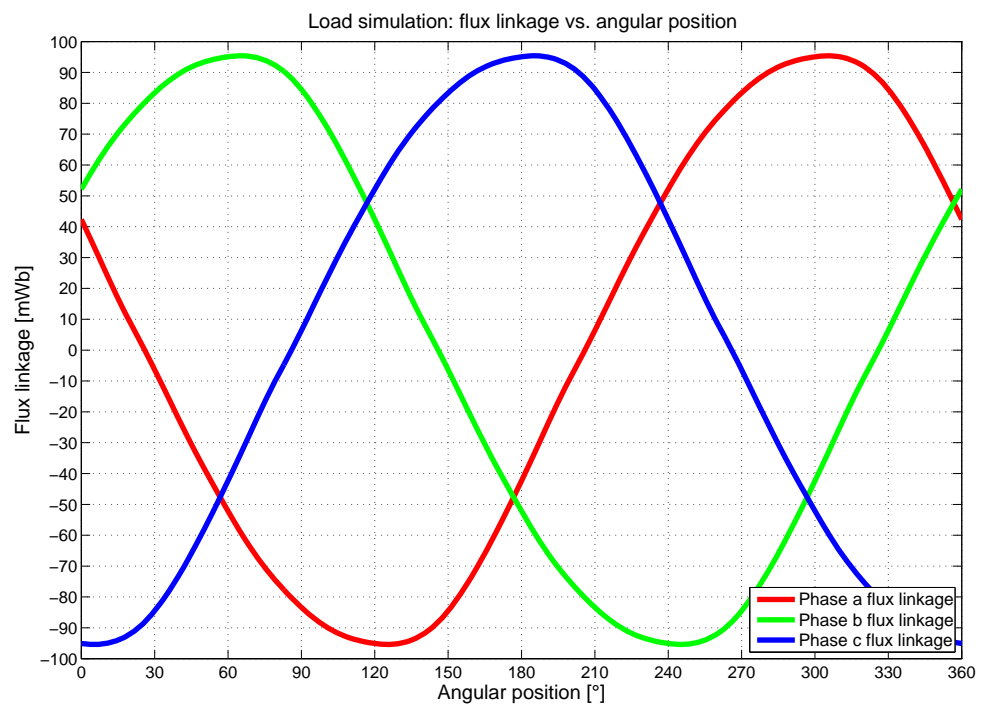


Figure 4.43: V-shape.

harmonic order.

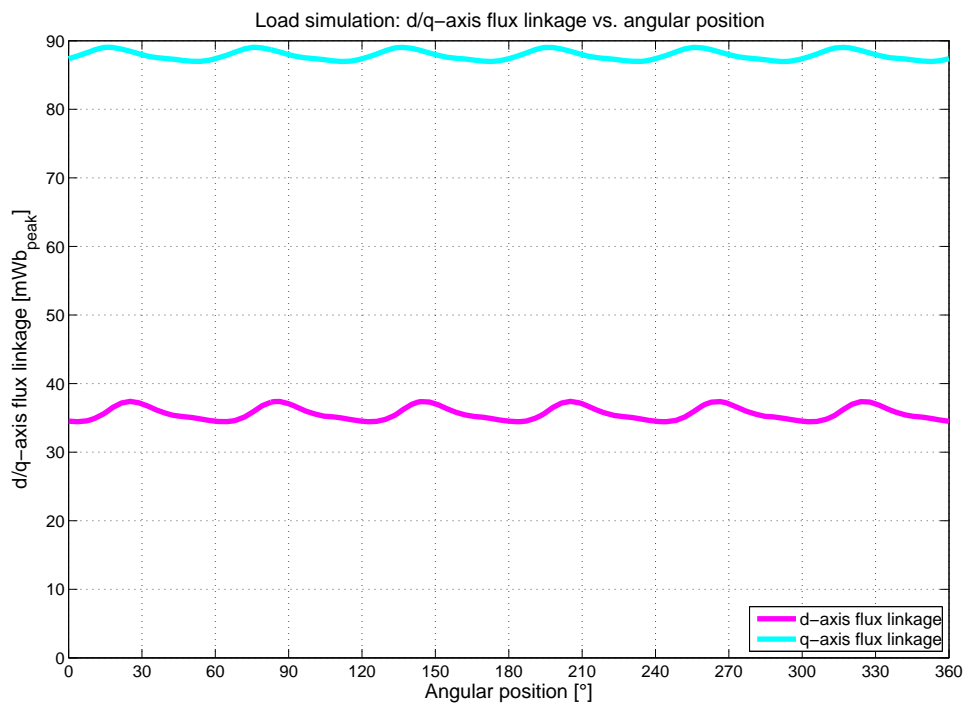


Figure 4.44: I-shape.

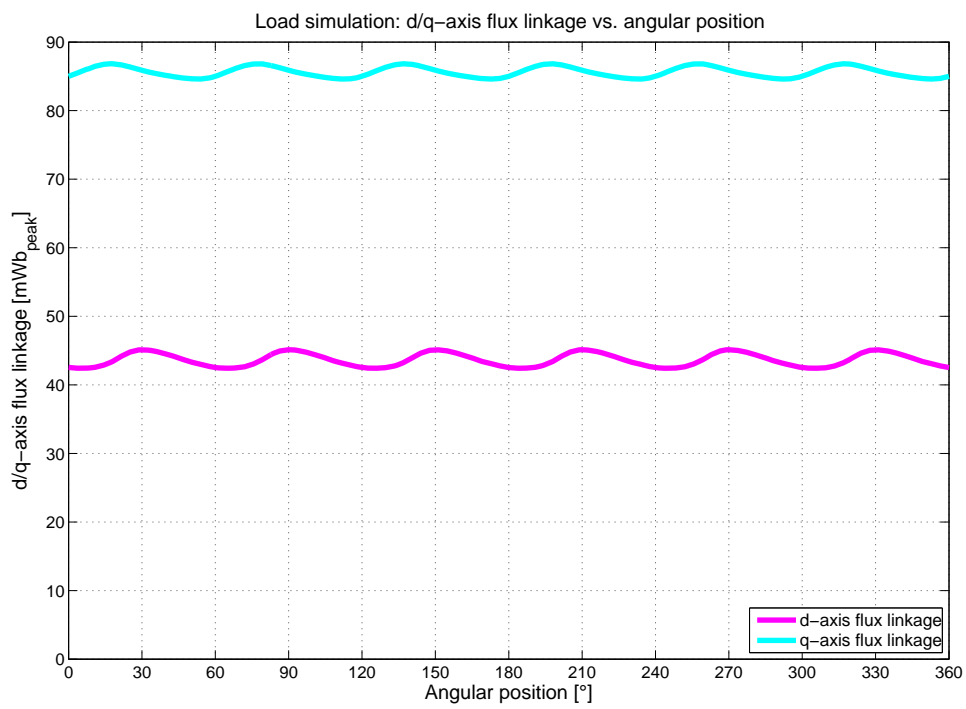


Figure 4.45: V-shape.

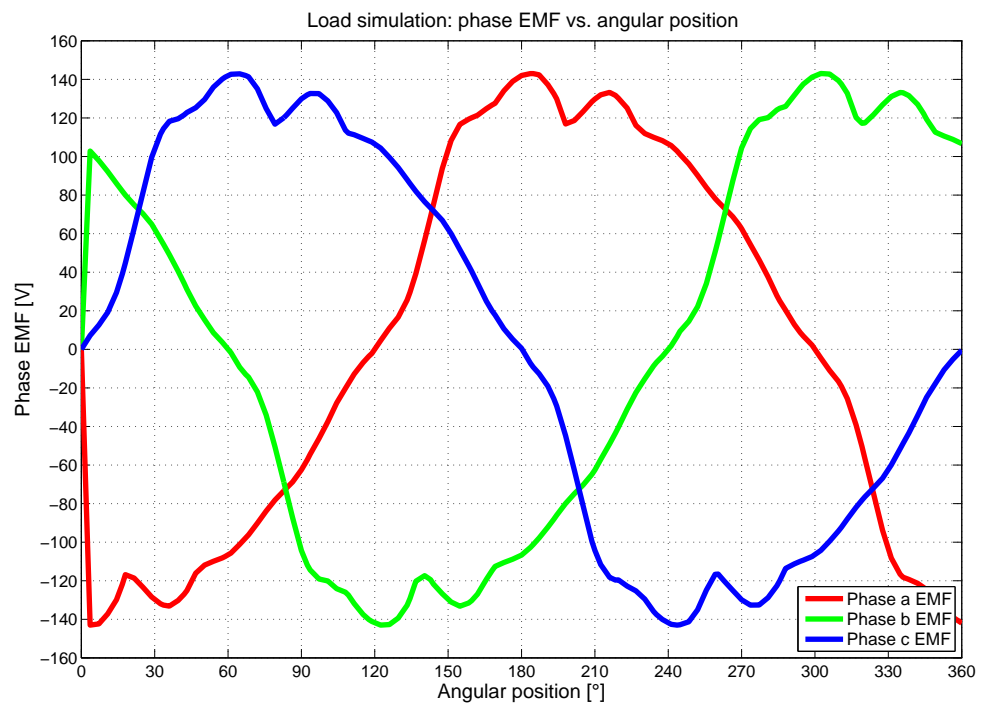


Figure 4.46: I-shape.

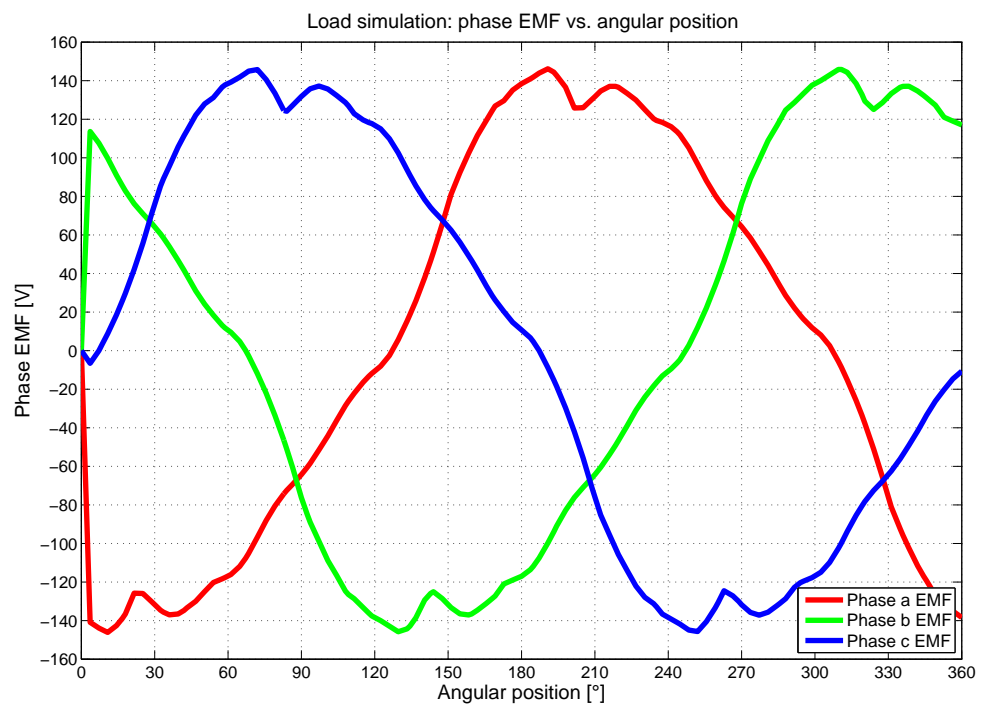


Figure 4.47: V-shape.

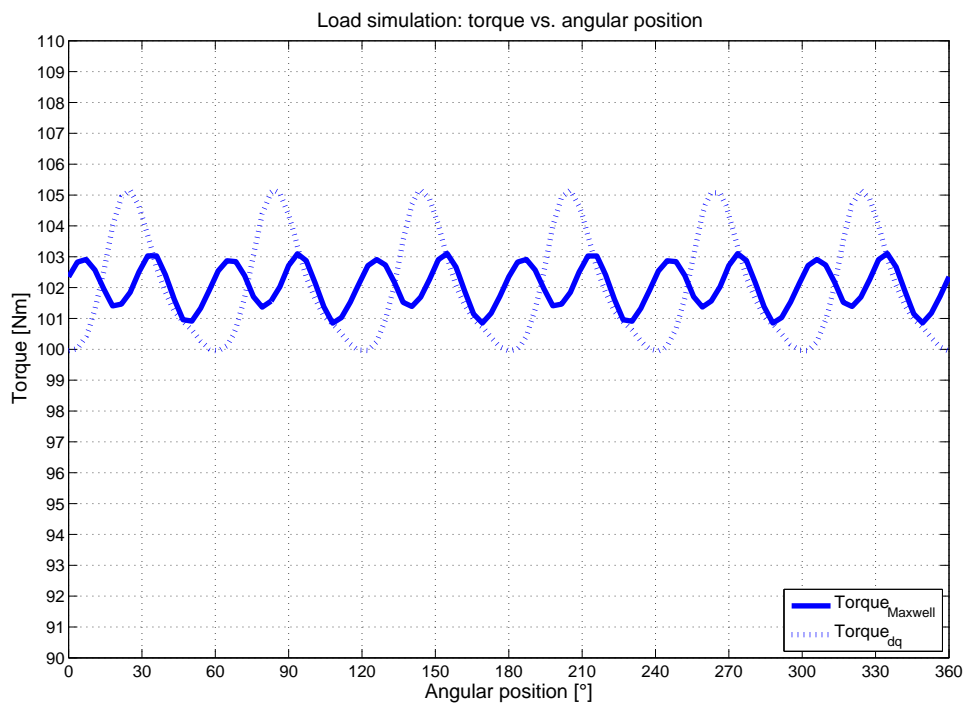


Figure 4.48: I-shape.

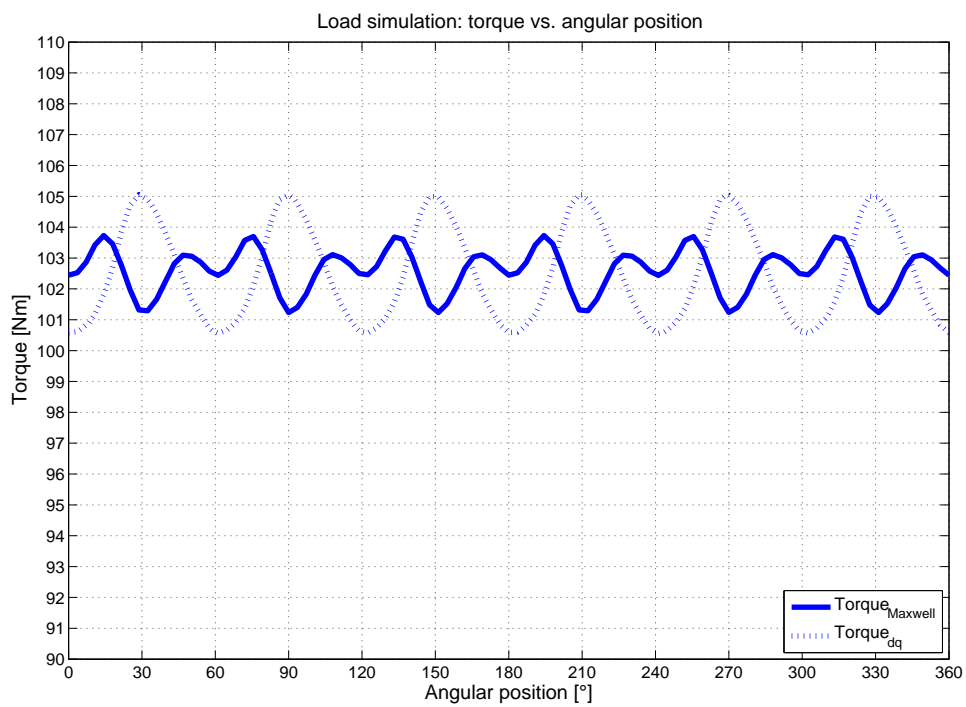


Figure 4.49: V-shape.



## 4.5. Overload simulation and demagnetization check

Overload simulation allows us to study the performance of the machines while they develop the maximum power at base speed. It's performed feeding the machines with the maximum phase current that prove to be:

$$I_d = -102.5A_{RMS}, I_q = 357.6A_{RMS} \Rightarrow I = 372.0A_{RMS} \text{ for I-shape;}$$

$$I_d = -100.0A_{RMS}, I_q = 354.0A_{RMS} \Rightarrow I = 367.9A_{RMS} \text{ for V-shape.}$$

The iron works, especially the teeth, work in moderate saturation level (about

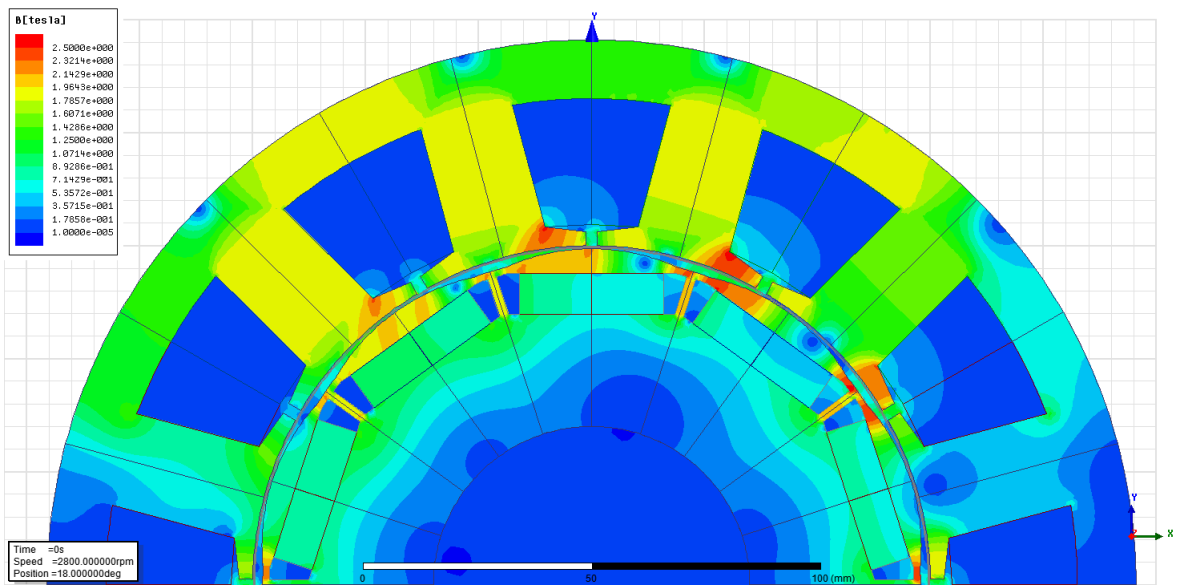


Figure 4.50: I-shape overload simulation flux density map.

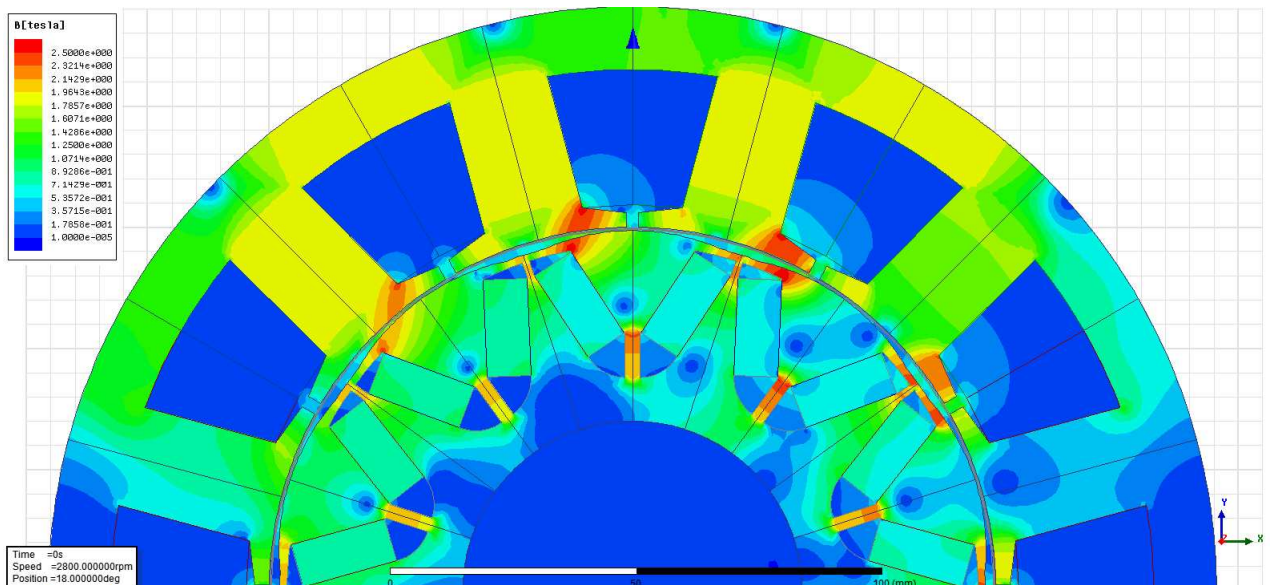


Figure 4.51: V-shape overload simulation flux density map.

$2T$ ), while the areas with highest flux density are concentrated in the vicinity of

slot opening.

All the *PMs* work with a flux density higher than knee point ( $0.15T @ 180^\circ$ ).

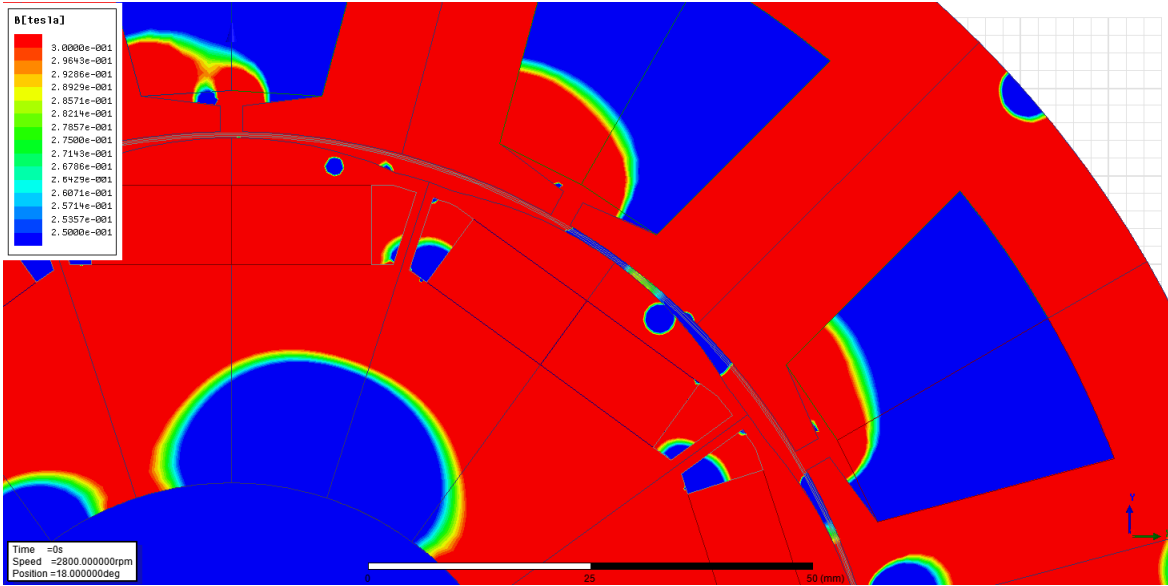


Figure 4.52: I-shape overload simulation demagnetization check.

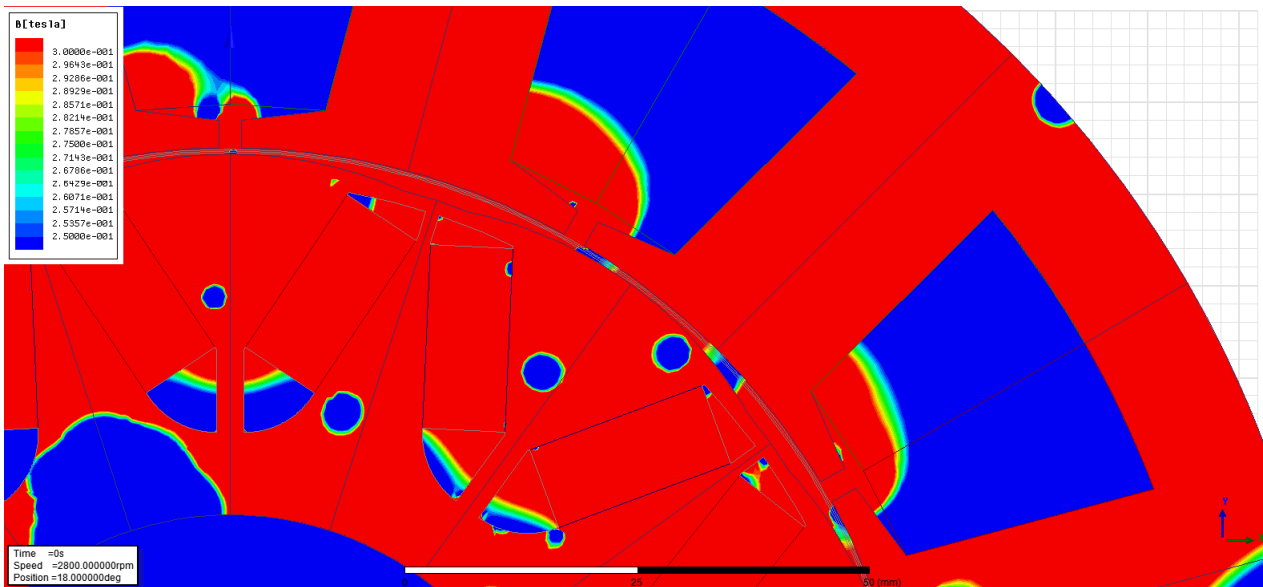


Figure 4.53: V-shape overload simulation demagnetization check.

However, we can see some critical point in which the demagnetization could start, especially in correspondence of vertices of magnets.

The presence of saturation is highlighted by the flat flux linkage trend (fig. 4.56, 4.57): consequently the induced *EMF* (equal to the minus of the time derived of the aforementioned flux linkage) shows an high deformation, as reported in fig. 4.60, 4.61.

In overload operation torque ripple remains however lower than 5% specifica-

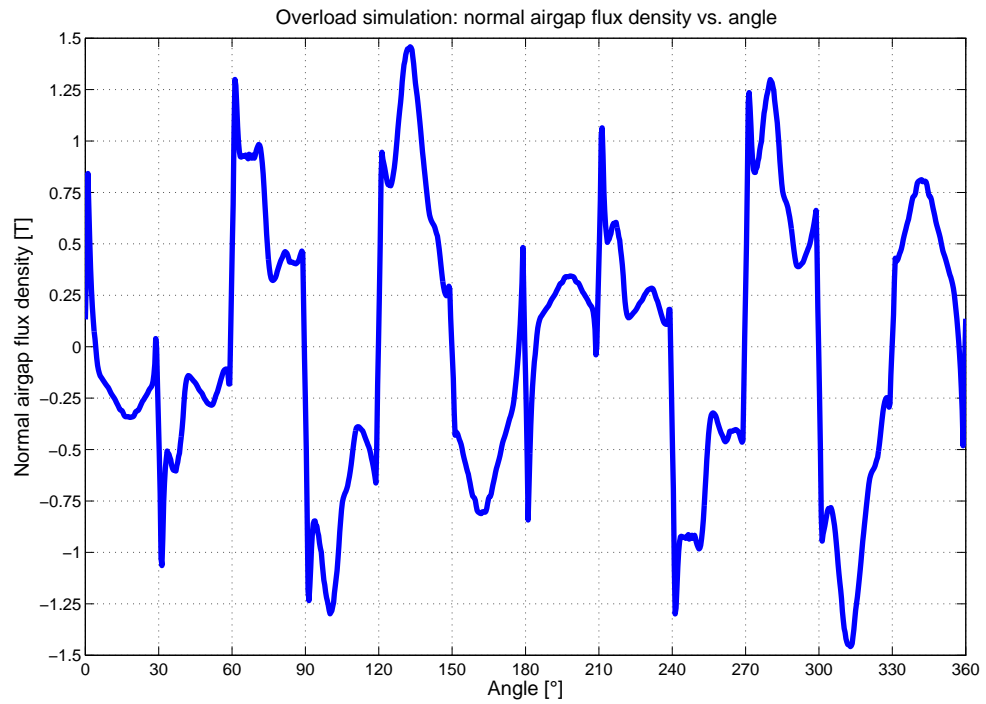


Figure 4.54: I-shape.

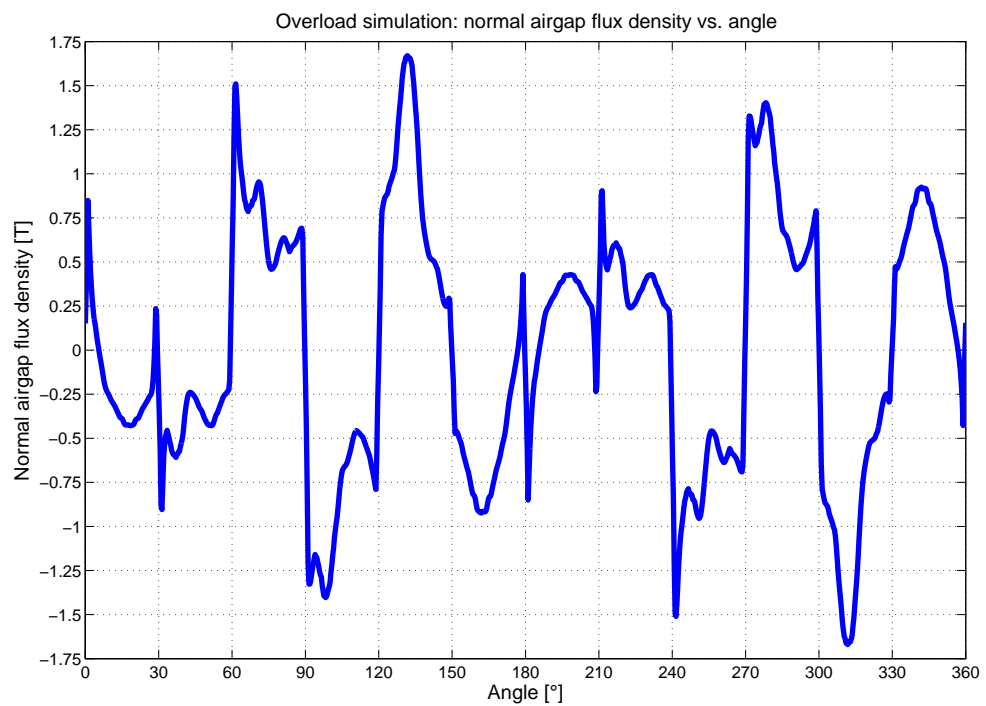


Figure 4.55: V-shape.

tion. For I-shape is a bit higher than V-shape, equal to 4.8% vs. 2.5%.

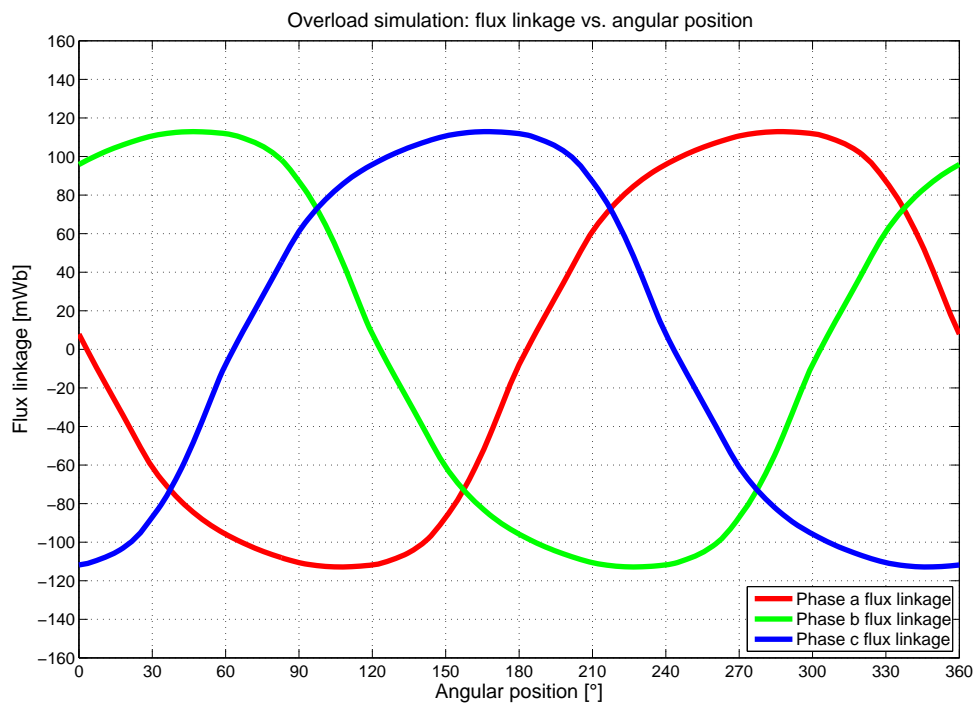


Figure 4.56: I-shape.

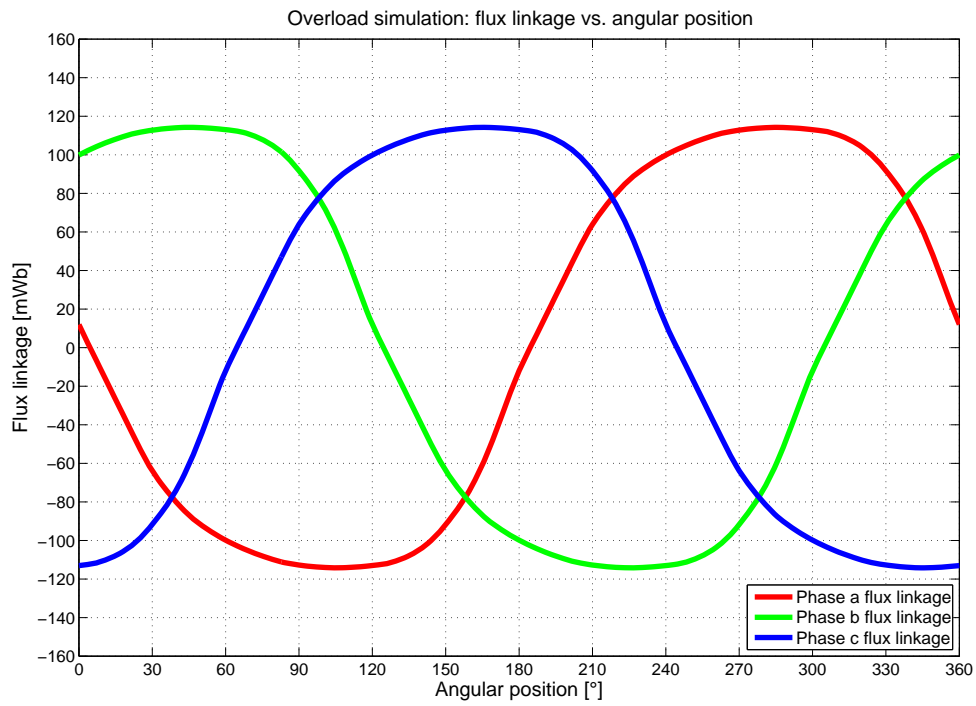


Figure 4.57: V-shape.

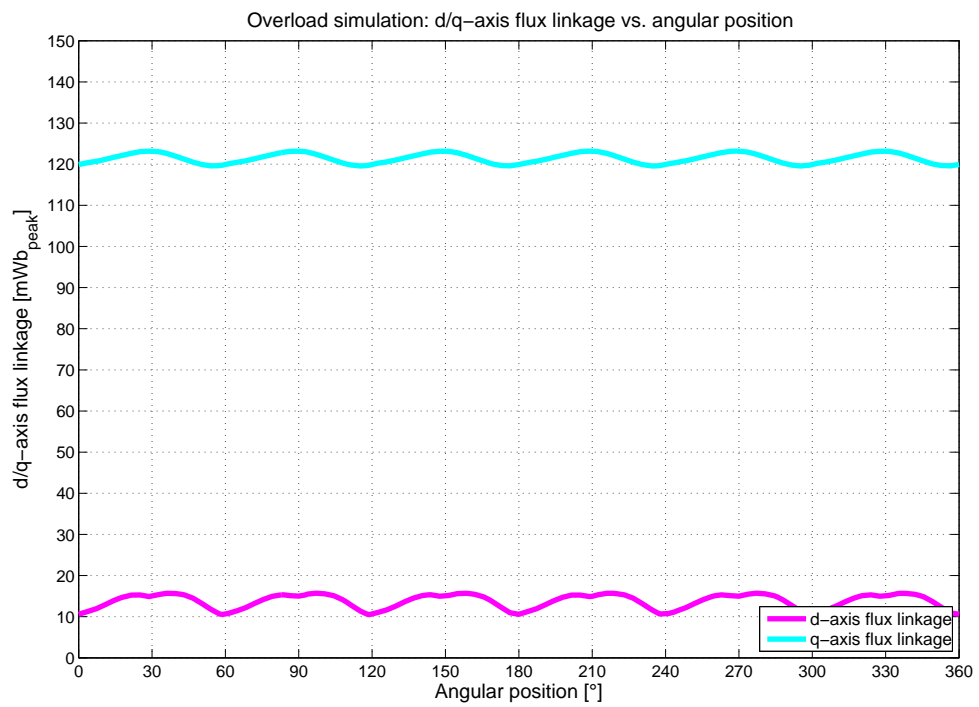


Figure 4.58: I-shape.

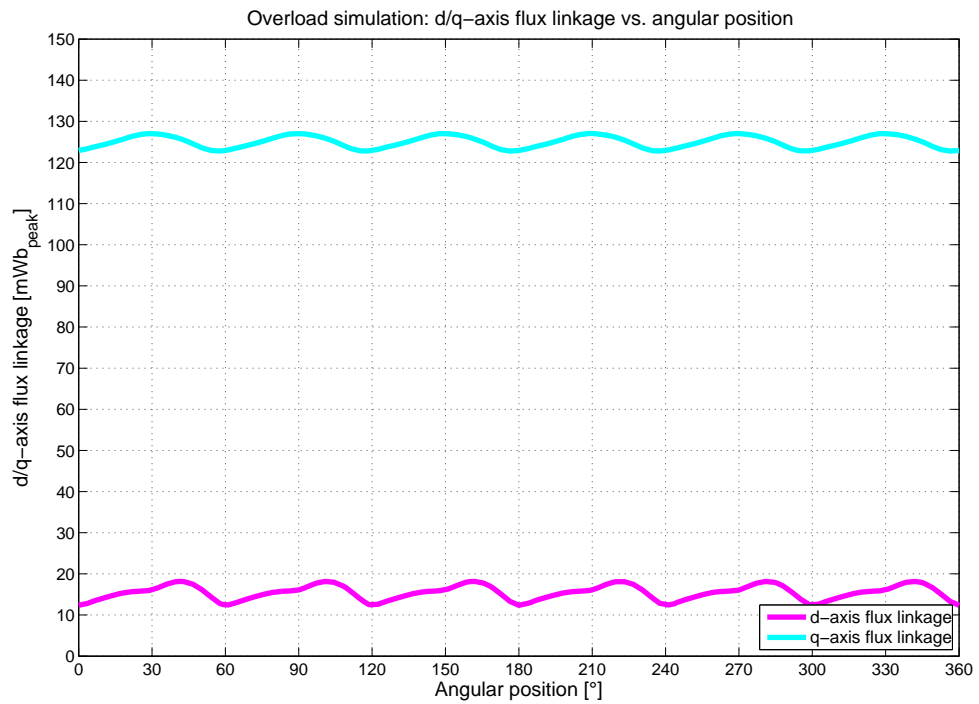


Figure 4.59: V-shape.

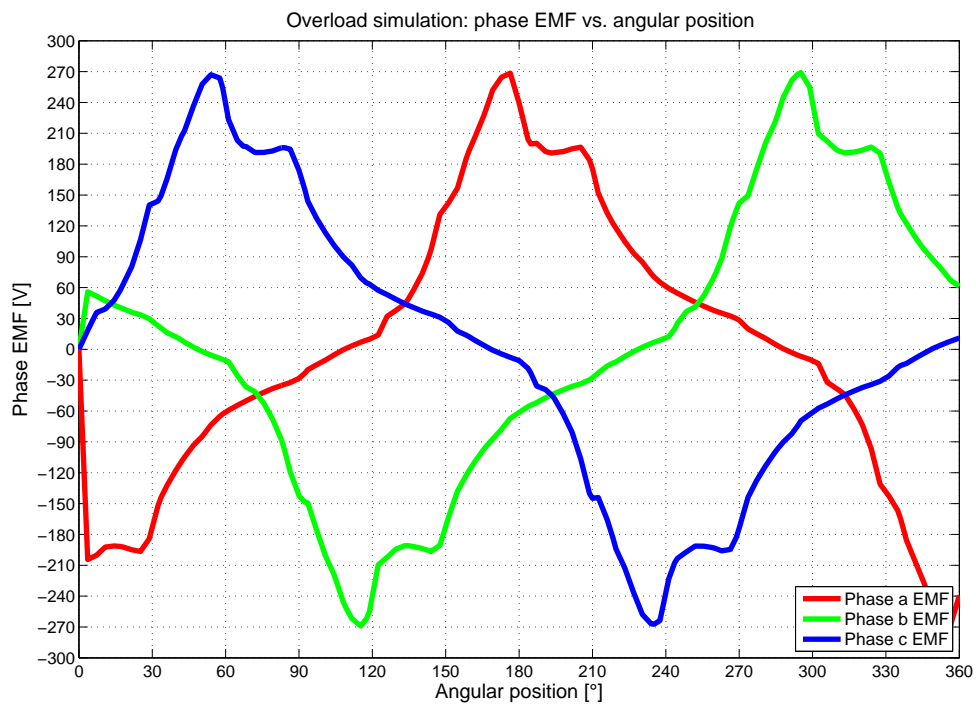


Figure 4.60: I-shape.

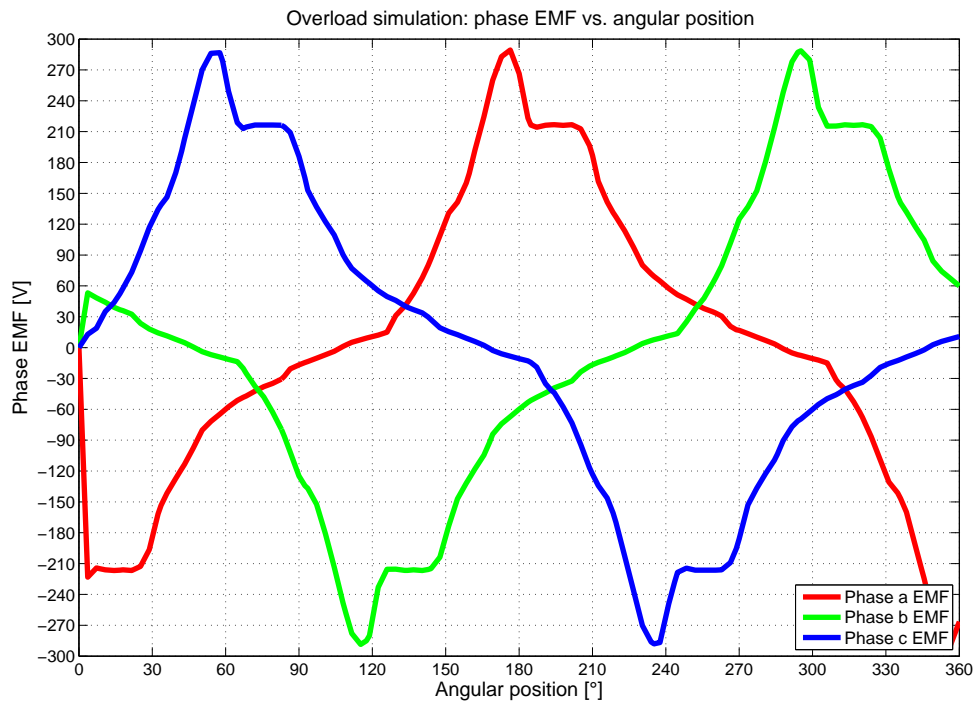


Figure 4.61: V-shape.

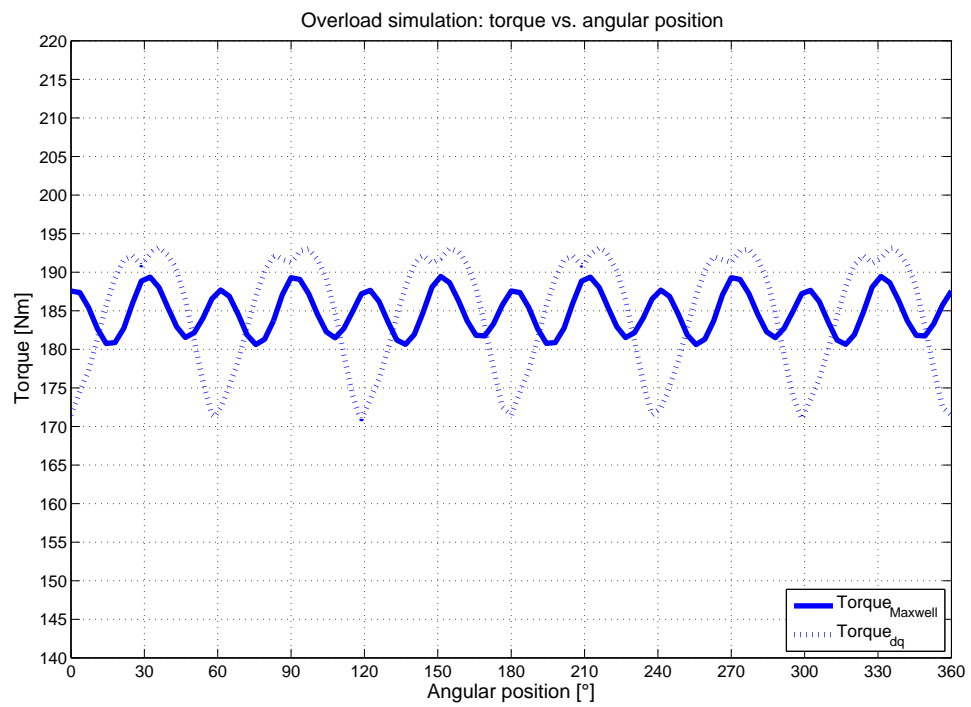


Figure 4.62: I-shape.

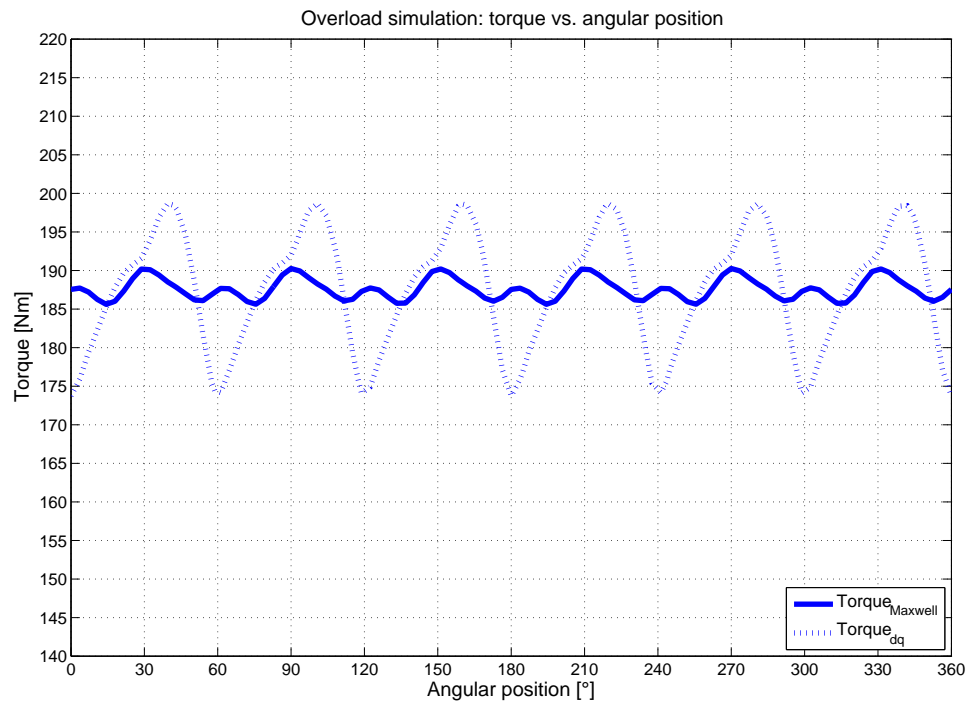


Figure 4.63: V-shape.

## 4.6. Current parametric simulation

The current parametric simulation aims to compute the electromechanical performances of the machines like, torque, phase current and phase voltage. The current information is especially useful to subsequently compute iron and *PM* eddy current losses and to properly design the control system. For this analysis, we neglect this losses, make referencing to the d/q-axis reference frame simplified circuits of fig. 4.64.

The inputs of our simulation are d/q-axis current arrays:

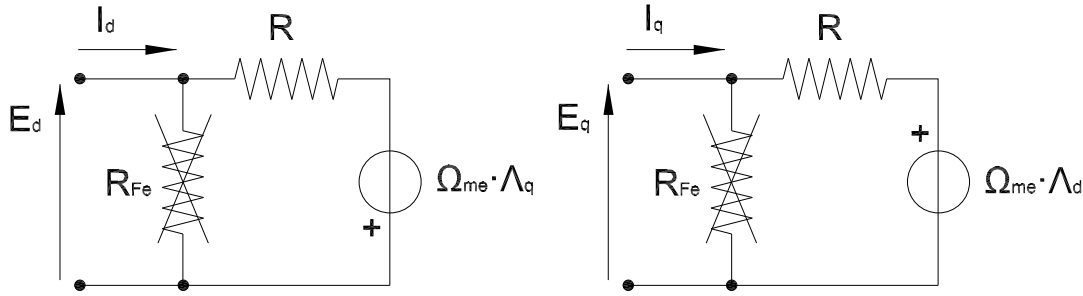


Figure 4.64: d/q-axis reference frame circuits: for the current parametric simulation we neglect the iron losses ( $R_{Fe} = \infty$ ).

- $\{I_d\} = \{-160, -140, \dots -20, 0, 20, \dots 140, 160\} A_{RMS}$
- $\{I_q\} = \{0, 20, \dots 380, 400\} A_{RMS}$

For computation simplicity, we define the following current matrix,

$$[I_d] = \begin{bmatrix} \{I_d\} \\ \dots \\ \{I_d\} \end{bmatrix} \quad (4.6)$$

$$[I_q] = \begin{bmatrix} \{I_q\}^T & \dots & \{I_q\}^T \end{bmatrix} \quad (4.7)$$

The outputs are a torque  $T$  and a d/q-axis flux linkage  $Lambda_d$ ,  $Lambda_q$  matrix, both computed in the first time step, neglecting the ripple in order to reduce the computation cost (one simulation last about  $10h$ ). For having a more accurate result, it would be necessary to evaluate the mean values in an full electric cycle, but with a great loss in working speed. We performed the parametric simulation at base speed, although obviously it doesn't influence the results because the



outputs aren't speed dependent.

$$[T] = \begin{bmatrix} T_{-160,0} & T_{-140,0} & \dots & T_{0,0} & \dots & T_{-160,140} & T_{160,0} \\ T_{-160,20} & T_{-140,20} & \dots & T_{0,20} & \dots & T_{-160,1420} & T_{160,20} \\ \dots & \dots & \dots & \dots & \dots & \dots & \dots \\ T_{-160,380} & T_{-140,380} & \dots & T_{0,380} & \dots & T_{-160,380} & T_{160,380} \\ T_{-160,400} & T_{-140,400} & \dots & T_{0,400} & \dots & T_{-160,400} & T_{160,400} \end{bmatrix} \quad (4.8)$$

$$[\Lambda_d] = \begin{bmatrix} \Lambda_{d,-160,0} & \Lambda_{d,-140,0} & \dots & \Lambda_{d,0,0} & \dots & \Lambda_{d,-160,140} & \Lambda_{d,160,0} \\ \Lambda_{d,-160,20} & \Lambda_{d,-140,20} & \dots & \Lambda_{d,0,20} & \dots & \Lambda_{d,-160,1420} & \Lambda_{d,160,20} \\ \dots & \dots & \dots & \dots & \dots & \dots & \dots \\ \Lambda_{d,-160,380} & \Lambda_{d,-140,380} & \dots & \Lambda_{d,0,380} & \dots & \Lambda_{d,-160,380} & \Lambda_{d,160,380} \\ \Lambda_{d,-160,400} & \Lambda_{d,-140,400} & \dots & \Lambda_{d,0,400} & \dots & \Lambda_{d,-160,400} & \Lambda_{d,160,400} \end{bmatrix} \quad (4.9)$$

$$[\Lambda_q] = \begin{bmatrix} \Lambda_{q,-160,0} & \Lambda_{q,-140,0} & \dots & \Lambda_{q,0,0} & \dots & \Lambda_{q,-160,140} & \Lambda_{q,160,0} \\ \Lambda_{q,-160,20} & \Lambda_{q,-140,20} & \dots & \Lambda_{q,0,20} & \dots & \Lambda_{q,-160,1420} & \Lambda_{q,160,20} \\ \dots & \dots & \dots & \dots & \dots & \dots & \dots \\ \Lambda_{q,-160,380} & \Lambda_{q,-140,380} & \dots & \Lambda_{q,0,380} & \dots & \Lambda_{q,-160,380} & \Lambda_{q,160,380} \\ \Lambda_{q,-160,400} & \Lambda_{q,-140,400} & \dots & \Lambda_{q,0,400} & \dots & \Lambda_{q,-160,400} & \Lambda_{q,160,400} \end{bmatrix} \quad (4.10)$$

We implemented a 2D interpolation for the previous matrices: we can define the electromagnetical characteristics of the machines, as follows.

#### 4.6.1. d/q-axis flux linkages

For having a first information about the trends of d/q-axis synchronous inductance and the value of the characteristic current, we refer to a particular operating condition in which the machine works with non cross saturation, that means evaluate the d-axis flux linkage with no q-axis current  $\{\Lambda_d(:,0)\}$  and the q-axis flux linkage with d-axis current equal to zero  $\{\Lambda_q(0,:)\}$ . The *PM* flux linkage array is  $\{\Lambda_{PM}\} = \{\Lambda_d(0,:)\}$ .

We calculate the d/q-axis synchronous inductances array  $\{L_d\}$ ,  $\{L_q\}$  according to the equations,

$$\begin{cases} \{L_d\} = \frac{\{\Lambda_d(:,0)\} - \{\Lambda_{PM}\}}{\{I_d\}} \\ \{L_q\} = \frac{\{\Lambda_q(0,:)\}}{\{I_q\}} \end{cases} \quad (4.11)$$

From the fig. 4.65, 4.66, we can evaluate the value of the characteristic current, that is  $I_{ch} = 89A_{RMS}$  for I-shape while  $I_{ch} = 101A_{RMS}$  for V-shape: we expect I-shape design exhibit a better behavior being closer to the rated current. For

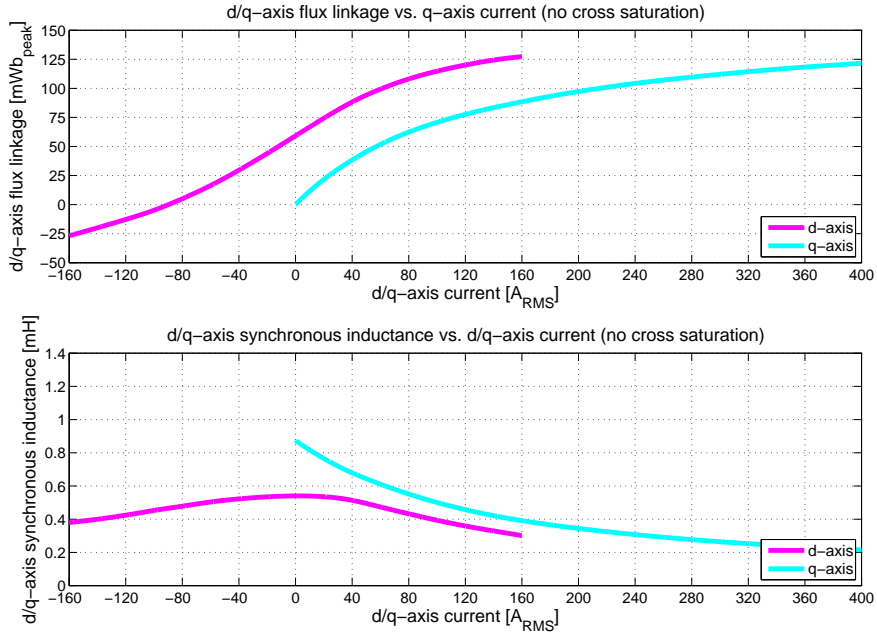


Figure 4.65: I-shape.

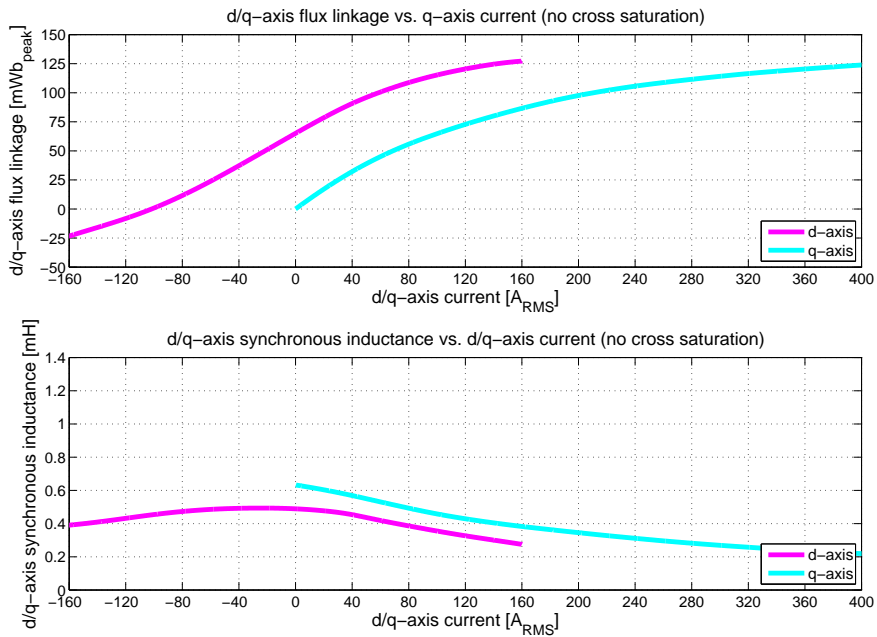


Figure 4.66: V-shape.

both cases the d-axis synchronous inductance has got approximately the same trend while the q-axis synchronous inductance, for I-shape, is slightly higher: so, in conclusion, we expect for I-shape a better anisotropy than V-shape.

Finally let's define the *PM* flux linkage matrix  $[\Lambda_{PM}]$ , as follows,

$$[\Lambda_{PM}] = \begin{bmatrix} \{\Lambda_{Pm}\} & \dots & \{\Lambda_{PM}\} \end{bmatrix} \quad (4.12)$$

### 4.6.2. Current space vector trajectory

Let's evaluate the current space vector trajectory, defining the following loca.

- **MTPA locus**

Let's calculate the phase current matrix  $[I]$ , as follows,

$$[I] = \sqrt{[I_d]^2 + [I_q]^2} \quad (4.13)$$

The "." symbol indicates that the operation is executed for each element of matrix.

The *MTPA* locus is defined by the  $(I_d, I_q)$  combination that produces the maximum torque per unit of current. We evaluate this maximum for each column, as follows,

$$\{T_{MTPA}\} = \max \left( \frac{[T]}{[I]} \right) \quad (4.14)$$

The *MTPA* locus is represented by the red line reported in fig. 4.67, 4.68, 4.69, 4.70.

- **MTPV locus**

Let's evaluate the flux linkage matrix  $[\Lambda]$ , equal to,

$$[\Lambda] = \sqrt{[\Lambda_d]^2 + [\Lambda_q]^2} \quad (4.15)$$

The *MTPV* locus is defined by the  $(I_d, I_q)$  combination that produces the maximum torque per unit of voltage, or in other words, per unit of flux linkage. We evaluate this maximum for each column, as follows,

$$\{T_{MTPV}\} = \max \left( \frac{[T]}{[\Lambda]} \right) \quad (4.16)$$

The *MTPV* locus is represented by the green line reported in fig. 4.67, 4.68, 4.69, 4.70.

- **Voltage limit locus**

From eq. 4.13, 4.14, we can write,

$$[E]^2 = [E_d]^2 + [E_q]^2 = (R \cdot [I_d] - \Omega_{me} \cdot [\Lambda_q])^2 + (R \cdot [I_q] + \Omega_{me} \cdot [\Lambda_d])^2 \quad (4.17)$$

Processing the previous equation, we reach the follows quadratic equation in the unknown speed.

$$[a] \cdot [\Omega_{me}]^2 + [b] \cdot [\Omega_{me}] + [c] = 0 \quad (4.18)$$

Where:

$$\begin{aligned} [a] &= [\Lambda]^2 \\ [b] &= 2 \cdot R \cdot \sqrt{2} \cdot ([\Lambda_d] \cdot [I_q] - [\Lambda_q] \cdot [I_d]) \\ [c] &= 2 \cdot (R^2 \cdot [I]^2 - [E]^2) \end{aligned}$$

The voltage limit is relate to the rated voltage, so each element of matrix  $[E]$  is  $E_n \cong 132V_{RMS}$ . The maximum speed matrix  $[n]$  is given by the equation,

$$[n] = \frac{60}{2 \cdot \pi \cdot p} \cdot \frac{\left( -[b] + \sqrt{[b].^2 - 4 \cdot [a] \cdot [c]} \right)}{2 \cdot [a]}. \quad (4.19)$$

Let's evaluate the matrix of the power developed  $[P]$ , ensuring the voltage limit, as follows,

$$[P] = \frac{2 \cdot \pi \cdot [n]}{60} \cdot [T] \quad (4.20)$$

From the previous data we can define the current space vector trajectory.

#### 1. Maximum torque point

The maximum torque  $T_{MAX} \cong 188Nm$  is developed working the machine in the big magenta star at base speed  $n_B = 2800rpm$ . In both designs, this point is inside the rated voltage limit with a fair degree.

#### 2. Constant available torque region in *MTPA*

From speed  $n = 0 \div 2800rpm$  the machines can work in *MTPA* till the base point, represented by the small magenta star, developing the rated torque  $T_n \cong 102Nm$ .

#### 3. Decrease available torque region in *MTPA*

From speed  $n = 2800 \div 4253rpm$  for I-shape and  $n = 2800 \div 4190rpm$  for V-shape both the machines work in *MTPA*, but in the sense of decreasing currents till intercepting the rated  $30kW$  isopower line (see fig. 4.69, 4.70). In this region the voltage increase without control till the rated value, while current is controlled in order to achieve an hyperbolic trend of torque , working in constant rated power.

#### 4. Decrease available torque region in *FW*

From speed  $n = 4253 \div 14000rpm$  for I-shape and  $n = 4190 \div 14000rpm$  for V-shape, both machines work in *FW* along the rated isopower line till maximum speed, increasing in negative sense the d-axis current and decreasing the q-axis current till intercepting the  $14000rpm$  rated voltage limit. In this region the machines are feeded at rated voltage working in constant rated power. It's interesting to note this last trajectory is approximately a straight line with zero in the characteristic current point, easily implemented in the control system.

The trajectory is described by d/q-axis current  $\{I_{dtraj}\}$ ,  $\{I_{qtraj}\}$ , flux linkages  $\{\Lambda_{dtraj}\}$ ,  $\{\Lambda_{qtraj}\}$  and speed  $\{n_{traj}\}$  arrays: current and speed were been used to perform a torque ripple and losses simulation, as described hereafter.

Let's calculate the d/q-axis synchronous inductances matrices  $[L_d]$ ,  $[L_q]$ , as

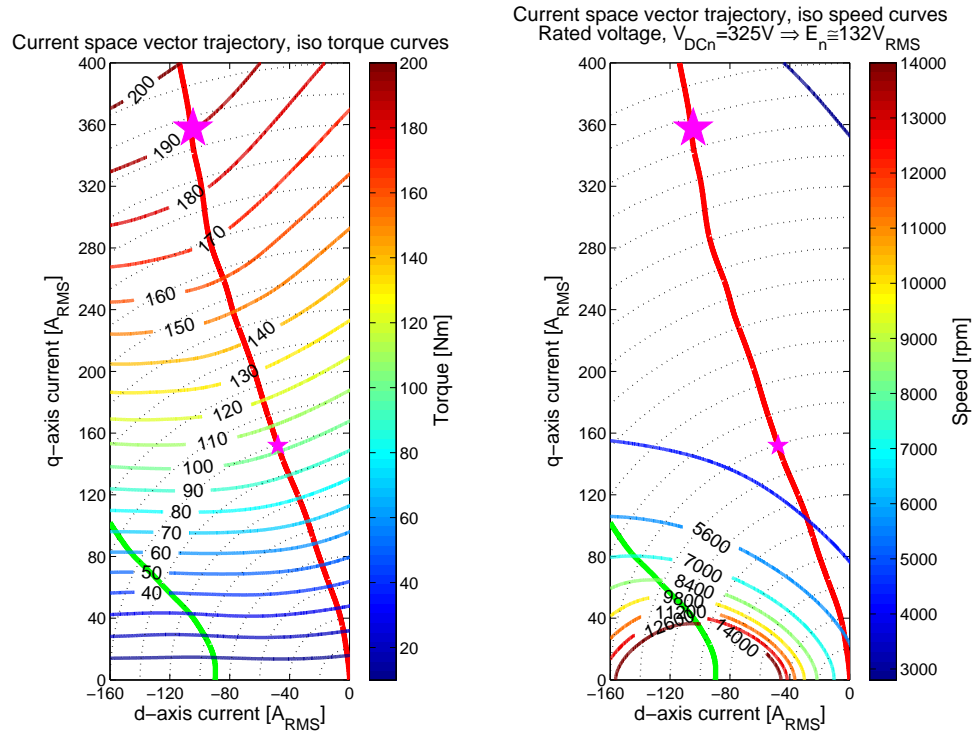


Figure 4.67: I-shape.

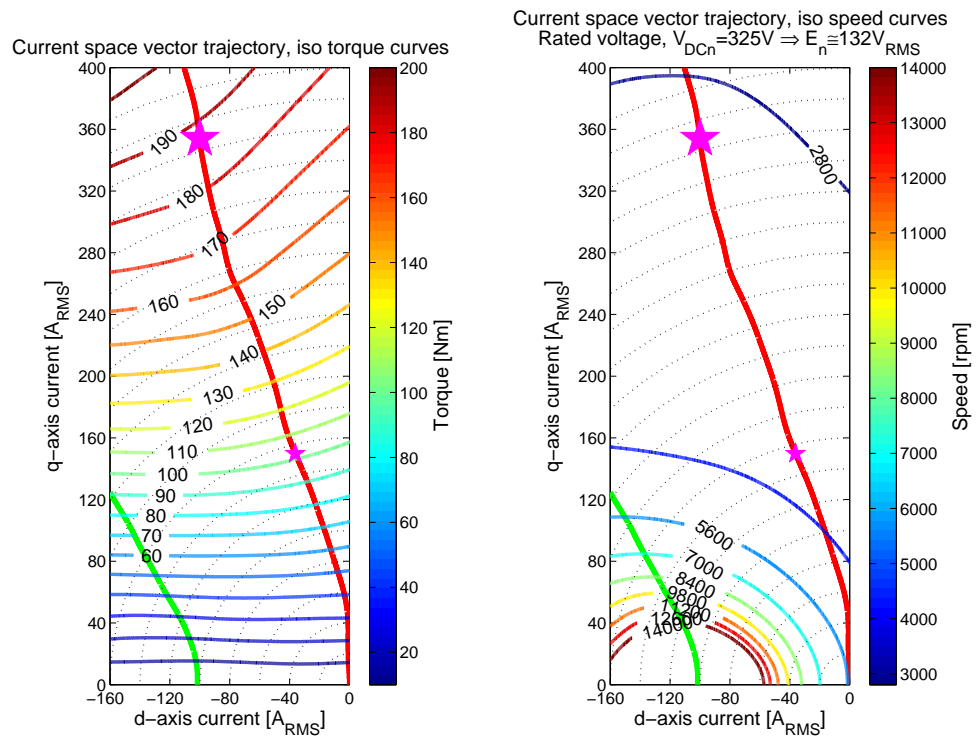


Figure 4.68: V-shape.

follows,

$$\begin{cases} [L_d] = \frac{[\Lambda_d] - [\Lambda_{PM}]}{[I_d]} \\ [L_q] = \frac{[\Lambda_q]}{[I_q]} \end{cases} \quad (4.21)$$

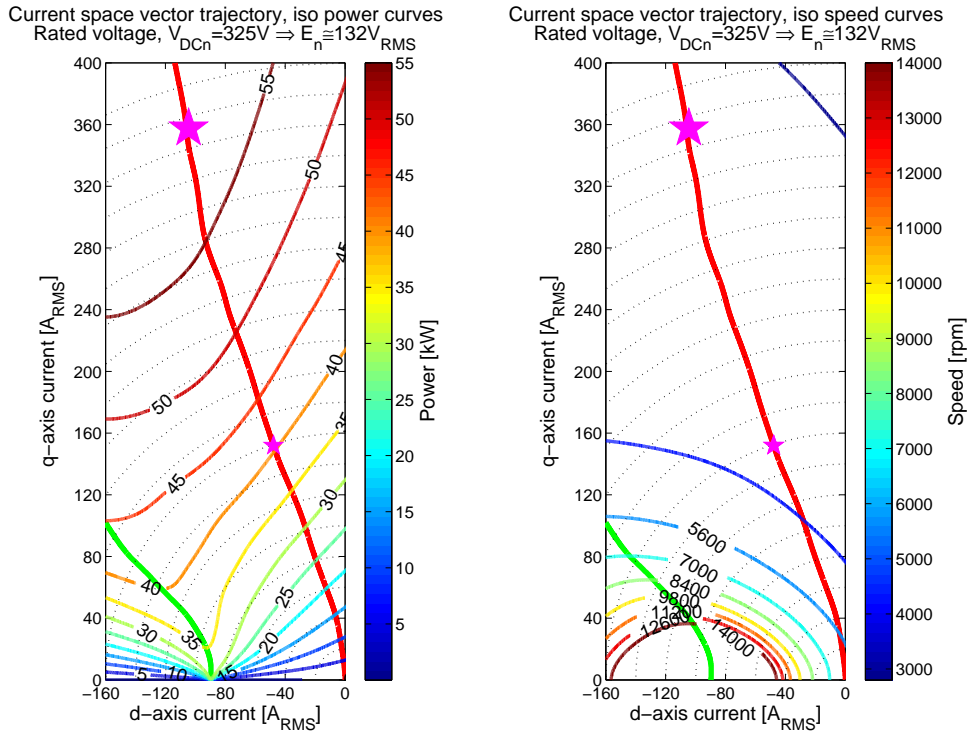


Figure 4.69: I-shape.

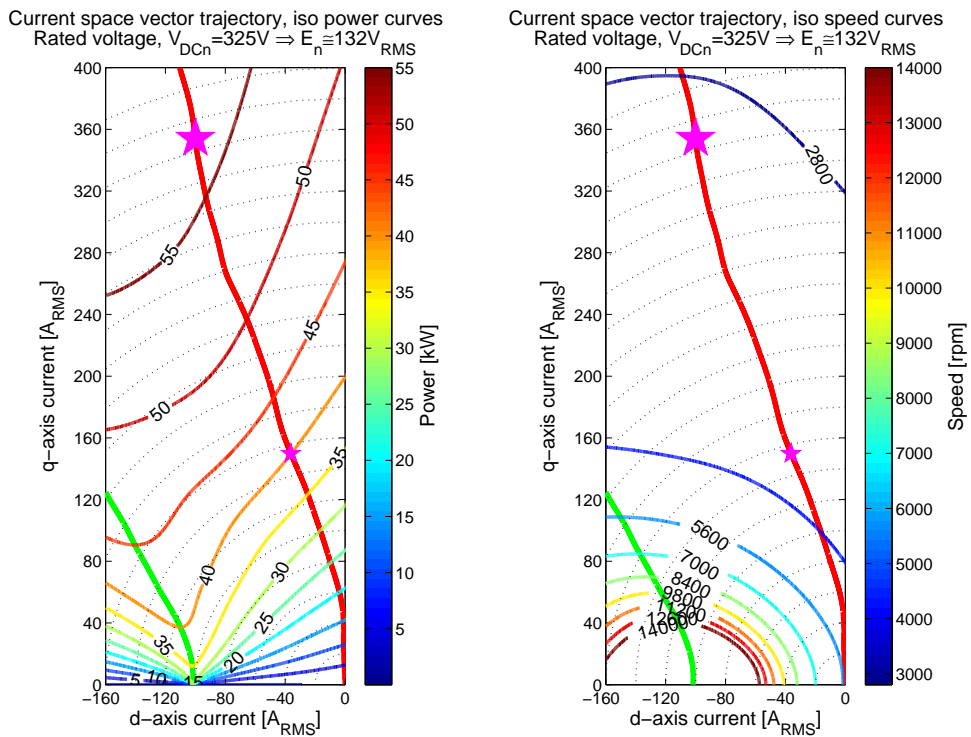


Figure 4.70: V-shape.

Consequently, the saliency ratio matrix  $[\xi]$ , is,

$$[\xi] = \frac{[L_q]}{[L_d]} \tag{4.22}$$

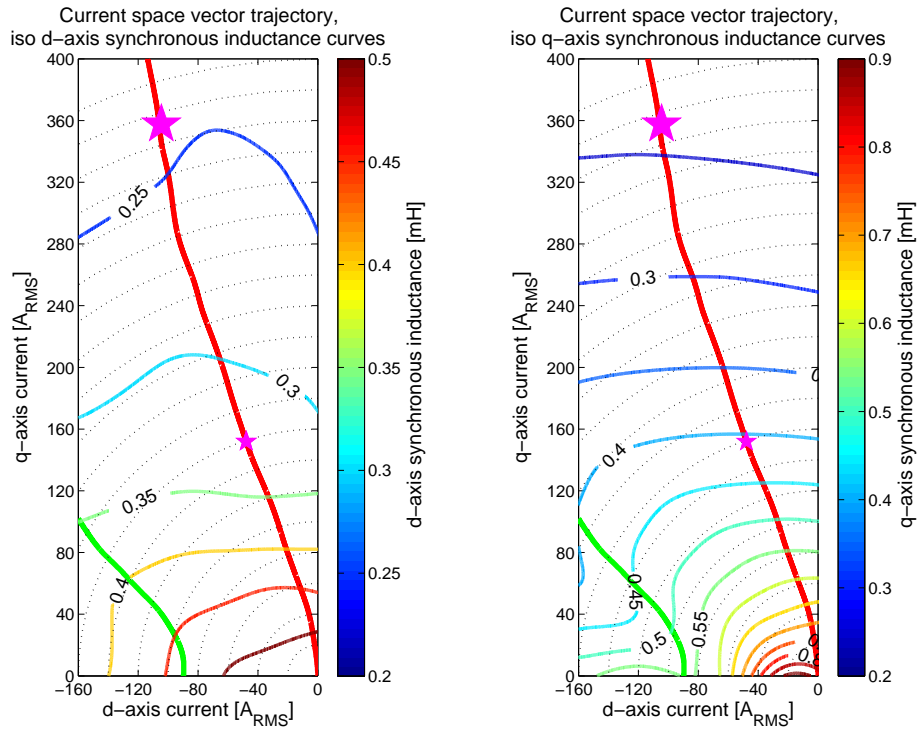


Figure 4.71: I-shape.

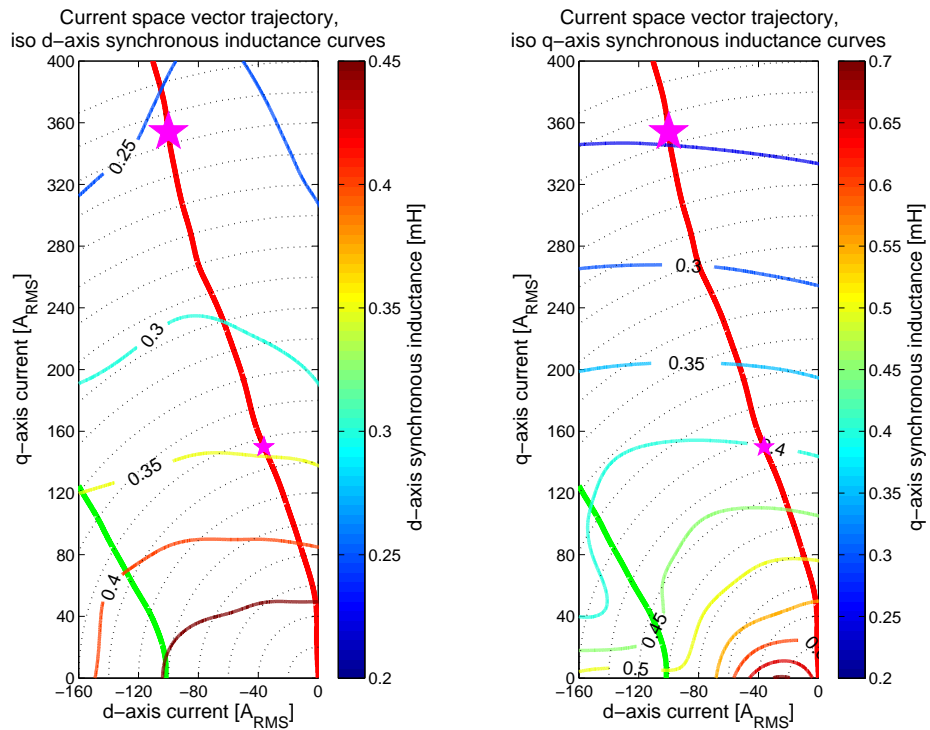


Figure 4.72: V-shape.

As mentioned in the previous paragraph, the last plots show the better anisotropy behavior of I-shape design than V-shape. Although, due to saturation it's not

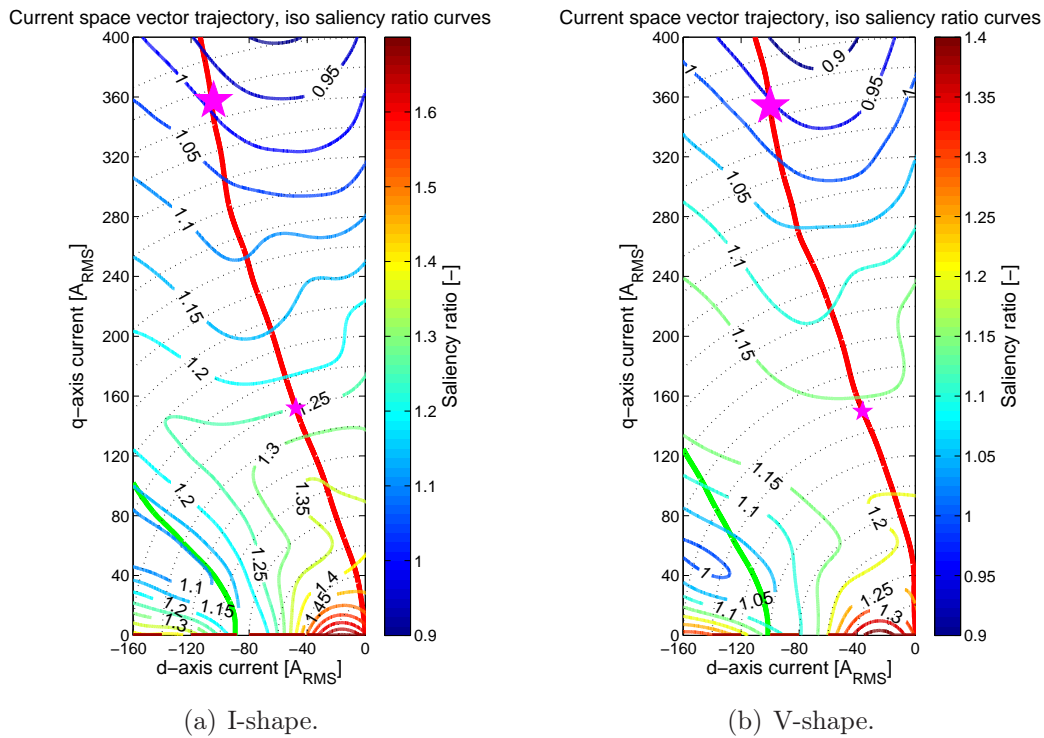


Figure 4.73:

possible to define a unique value of d/q-axis synchronous inductances, the mean value of the saliency ratio is estimable, being about  $\langle \xi \rangle = 1.3$  for I-shape and  $\langle \xi \rangle = 1.15$ , about  $-11\%$  lower: this result may depend on the flux barrier geometry of V-shape design because the q-axis shows an higher saturation level.



### 4.6.3. Torque

The machines met the requested torque-speed curves, both partial than rated load. Due to the chosen current space trajectory, we get perfect  $CPSR$  of 5:1.

From the torque equation is immediate to calculate the two contributions, the cylindrical  $[T_{cil}]$  and reluctance torque  $[T_{rel}]$  matrix, as follows,

$$[T_{cil}] = \frac{[T(I_d, I_q)] + [T(-I_d, I_q)]}{2} \quad (4.23)$$

$$[T_{rel}] = -\frac{[T(I_d, I_q)] - [T(-I_d, I_q)]}{2} \quad (4.24)$$

As reported in fig. 4.75, 4.76, 4.77, 4.78, according to the higher anisotropy of I-shape design, the reluctance torque is slightly higher than in V-shape, while this last design develops, due to an higher value of  $PM$  flux linkage, an higher cylindrical torque. For partial load the both the machine works in  $MTPA$  locus till about  $5000rpm$  in which the torque components change their trends.

In order to understand the saturation level is useful to plot the  $MTPA$  torque vs. the phase current, as reported in fig. 4.79, fig. 4.80: the trend in is linear till about the rated torque at base point, according to the load simulation that prove the appropriate values of flux density in the iron.

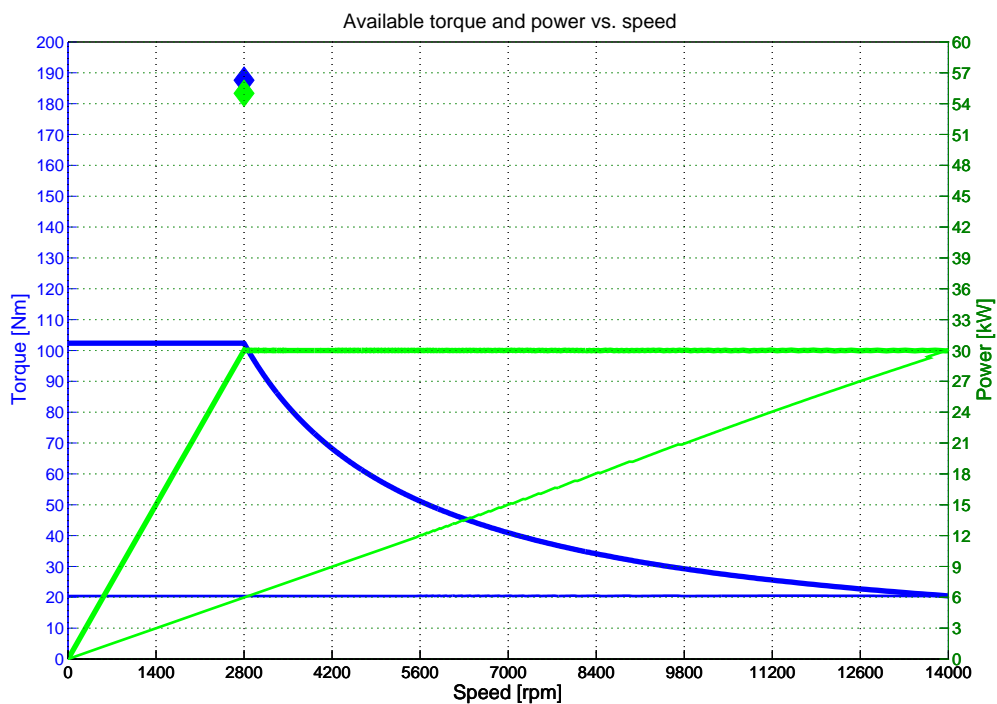


Figure 4.74: The thin line is relate to the partial load.

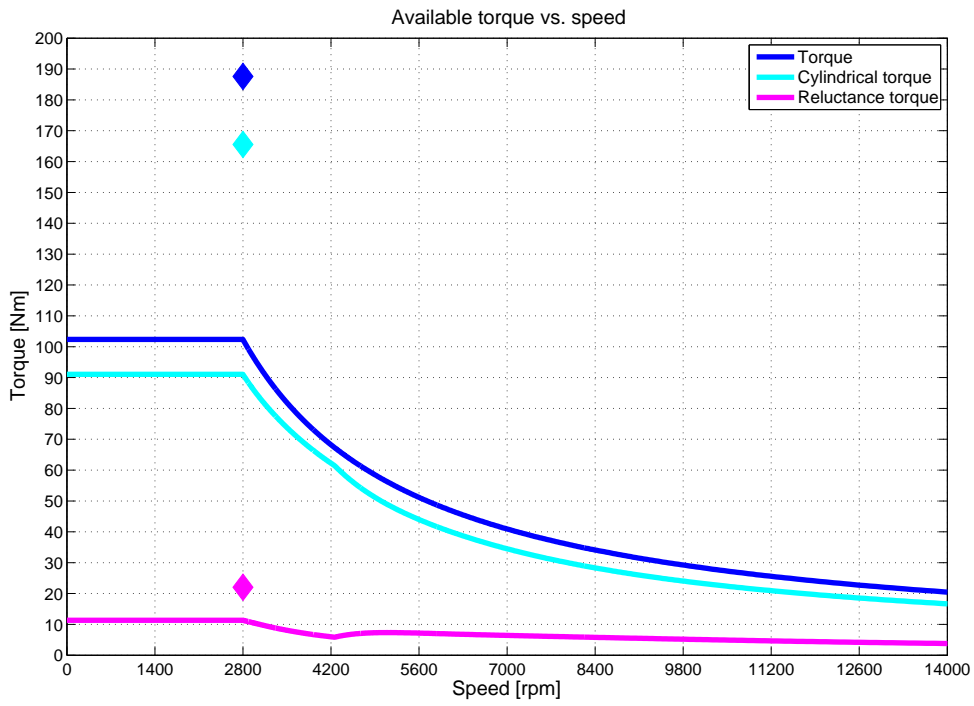


Figure 4.75: I-shape.

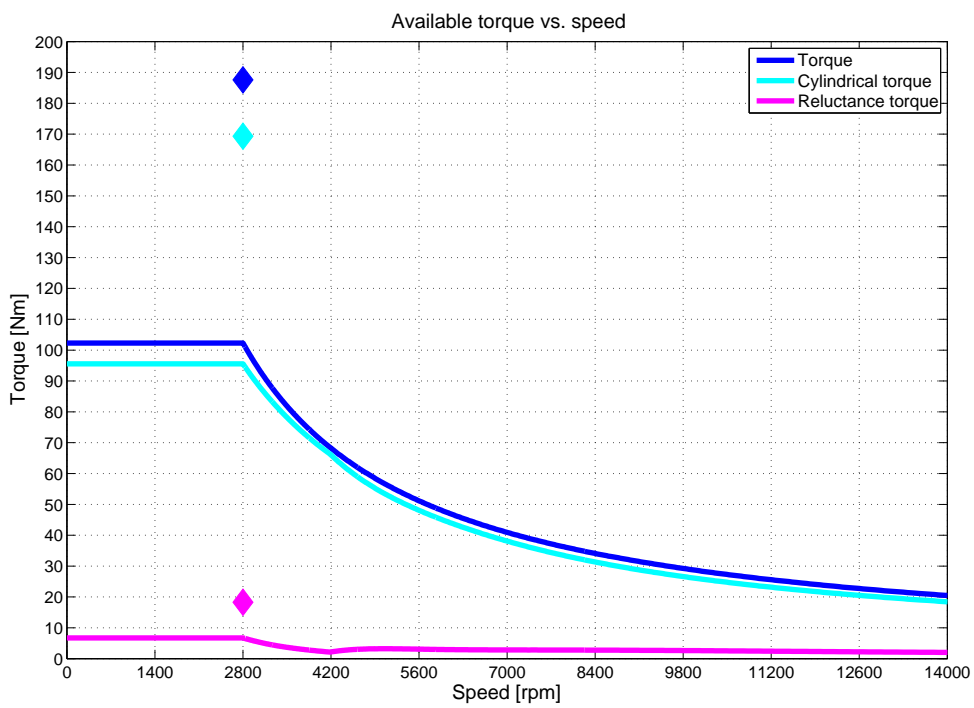


Figure 4.76: V-shape.

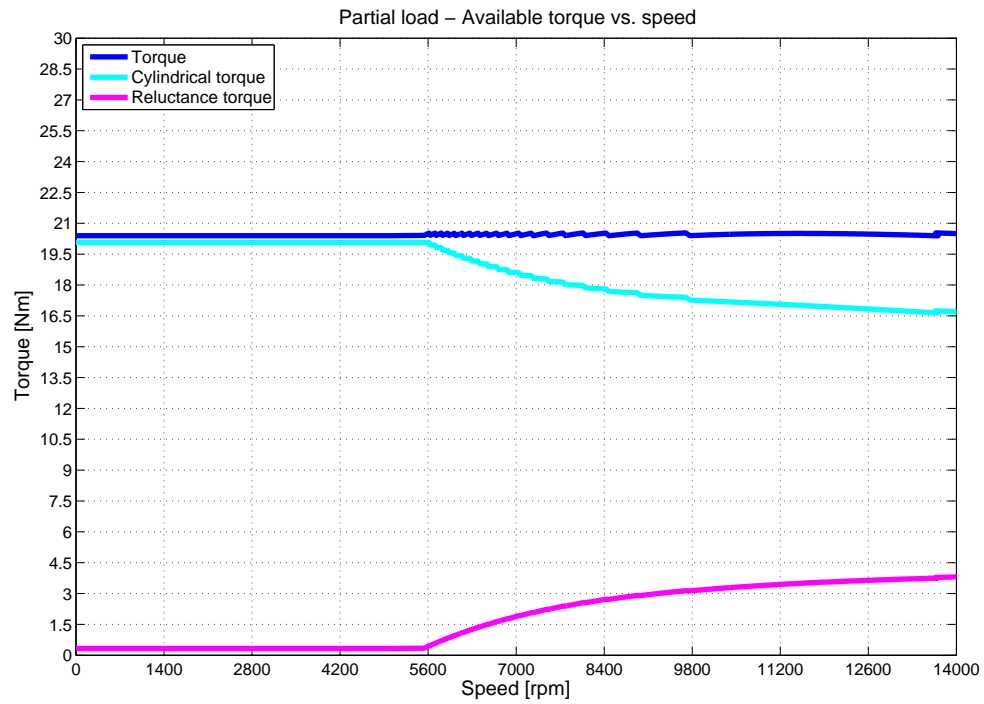


Figure 4.77: I-shape.

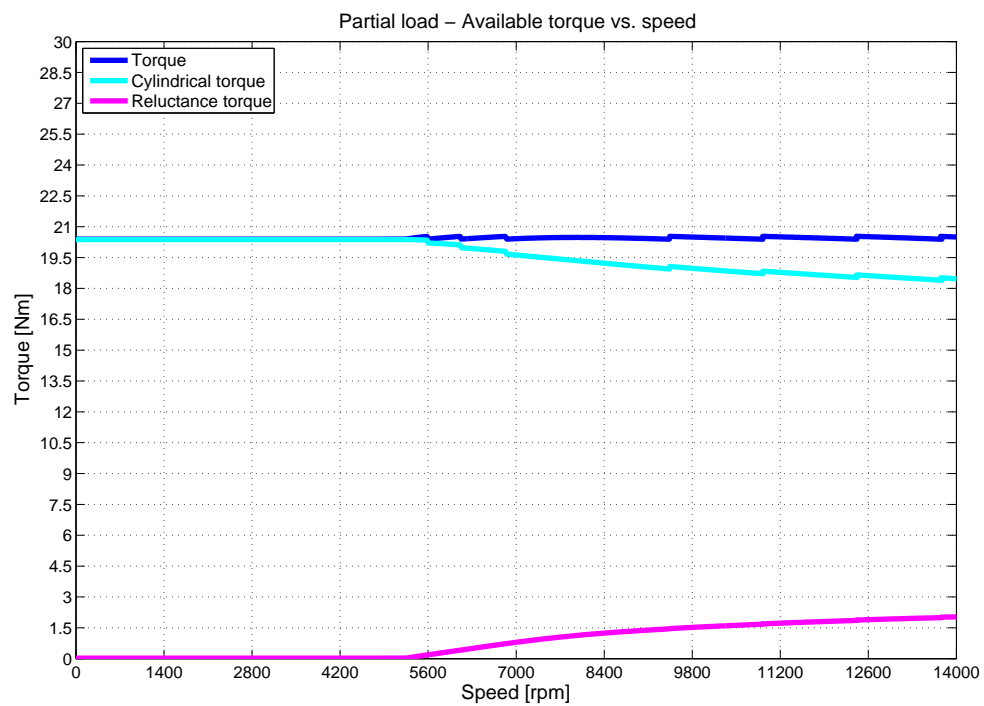


Figure 4.78: V-shape.

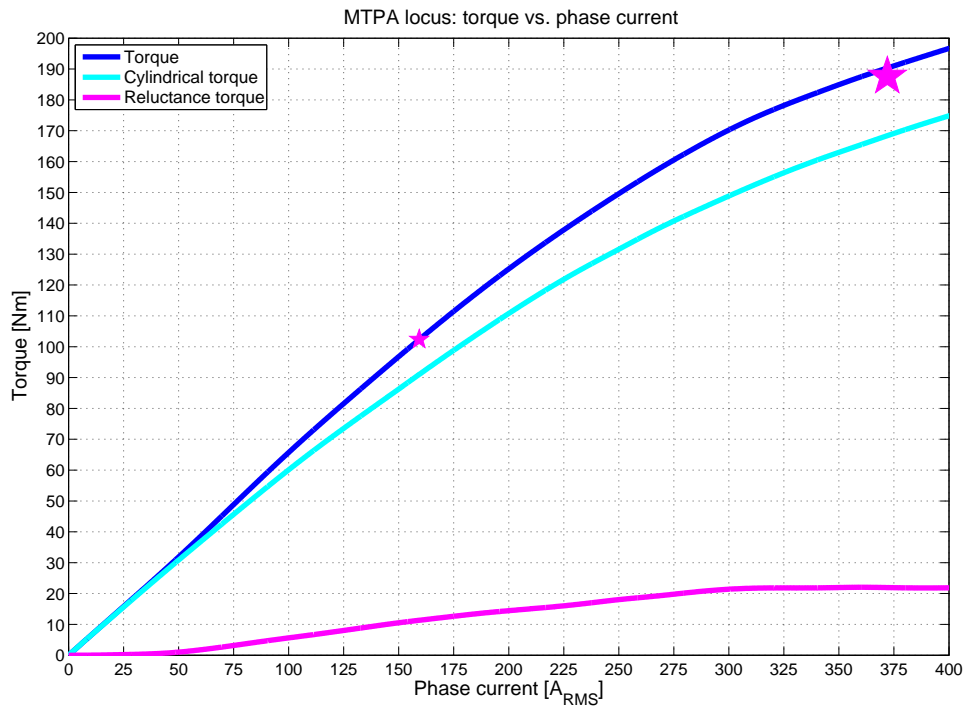


Figure 4.79: I-shape.

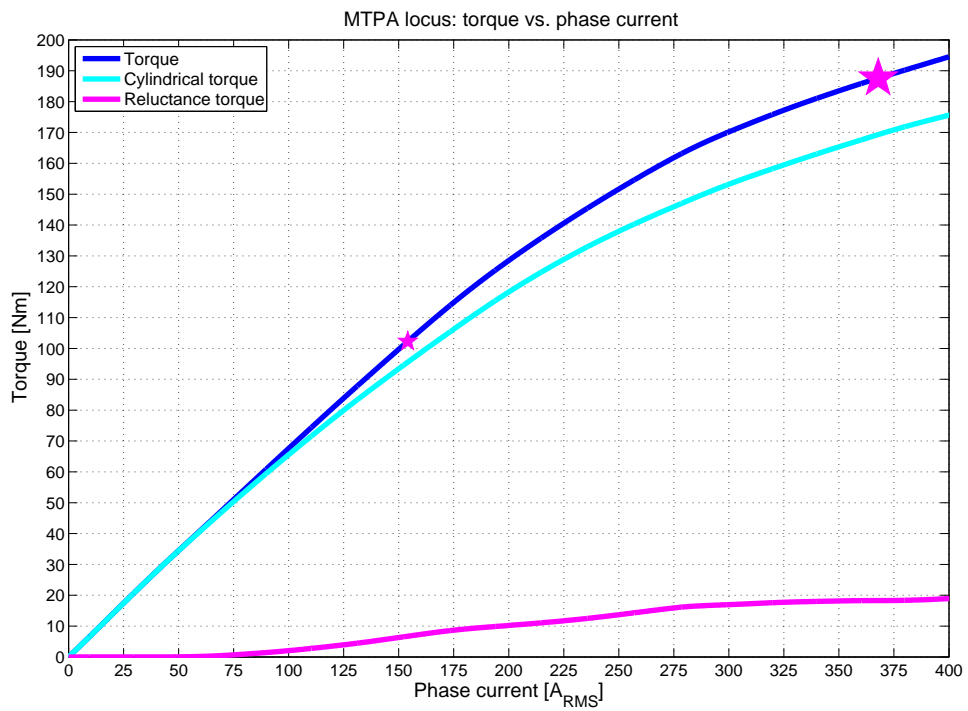


Figure 4.80: V-shape.

## 4.6.4. Torque ripple

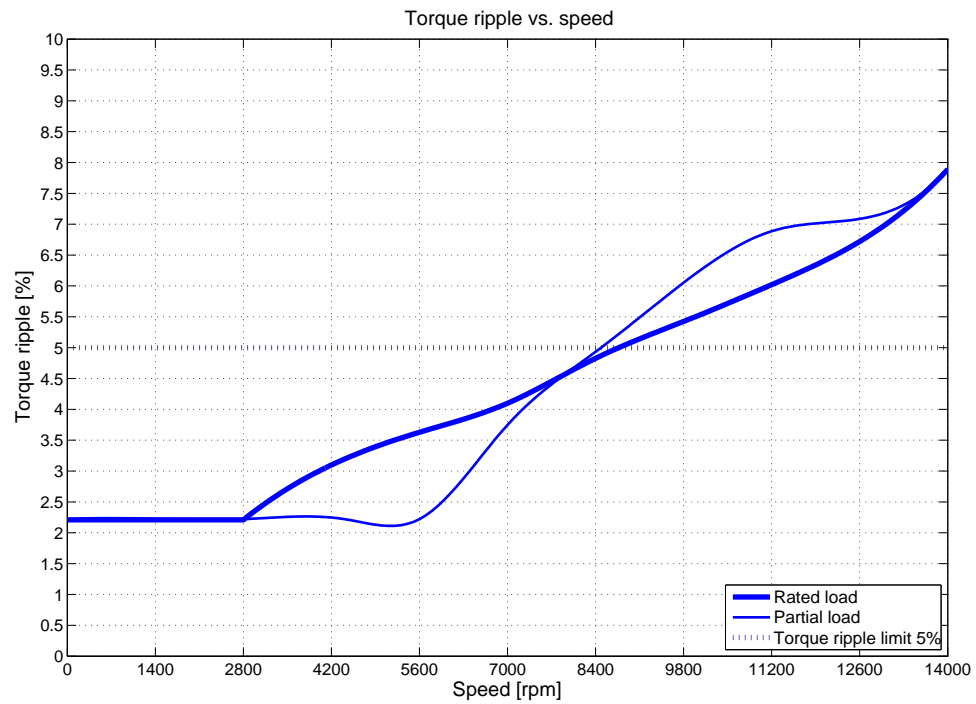


Figure 4.81: I-shape.

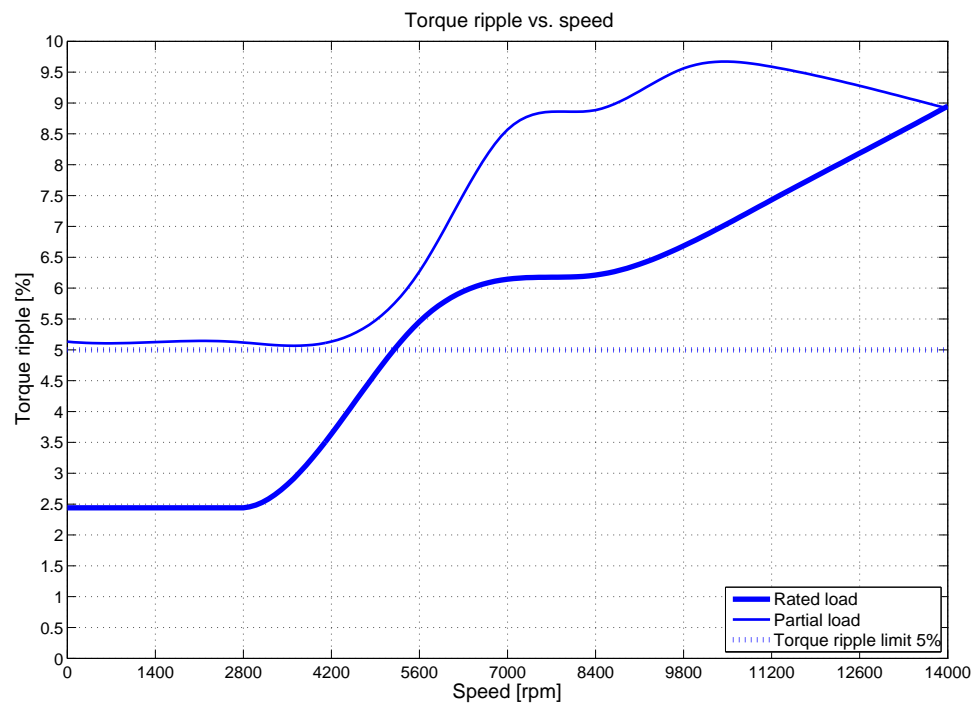


Figure 4.82: V-shape.

The torque ripple simulation was performed executing, for each point of current space vector trajectory (speed is obviously irrelevant), a transient simulation

that last one electric cycle in order to evaluate the mean torque and the torque ripple. As reported in fig. 4.81,4.82, the I-shape design shows better performance, both partial and rated load, while V-shape works good only at high loads. Both the designs don't achieve, in the full speed range, the requested 5% achieving maximum torque ripple value at high speed range, about 8% for I-shape and 9% for V-shape.

#### 4.6.5. Phase current and phase voltage

Let's calculate the phase voltage array  $\{E_{traj}\}$ , as follows,

$$\{E_{traj}\} = \sqrt{\{E_{dtraj}\}^2 + \{E_{qtraj}\}^2} \quad (4.25)$$

Where:

$$\begin{cases} \{E_{dtraj}\} = R \cdot \{I_{dtraj}\} - \frac{2 \cdot \pi \cdot p}{60} \cdot \{n_{traj}\} \cdot \{\Lambda_{qtraj}\} \\ \{E_{qtraj}\} = R \cdot \{I_{qtraj}\} + \frac{2 \cdot \pi \cdot p}{60} \cdot \{n_{traj}\} \cdot \{\Lambda_{dtraj}\} \end{cases} \quad (4.26)$$

As highlighted in fig. 4.83, 4.84 the motors work inside the rated voltage limit,  $E_n \cong 132V_{RMS}$ . The peak torque is reached with current and especially voltage slightly lower than the limit, emphasizing the possibility of further overloading.

The d/q-axis currents, rated load, are reported in fig. 4.85, 4.86.

V-shape design need, along *MTPA* locus, a current slightly lower than I-shape due to an higher *PM* flux linkage and so cylindrical torque. Viceversa, the analysis suggest that I-shape performance in flux-weakening are slightly better than V-shape for the higher reluctance torque contribution, especially at partial load. In order to check the thermal design, we evaluate the current density array  $\{J\}$ , as follows,

$$\{J_{traj}\} = \frac{\{I_{traj}\}}{S_{ceq}} \quad (4.27)$$

For both machines the rated current density is  $J \cong 7.5A/mm^2$ , slightly higher than the design value of  $J = 6A/mm^2$ , highlighting the goodness of the reached design. The maximum torque is achieved with a current density of  $J \cong 17.5A/mm^2$ . Finally, we calculate the power factor  $\{\cos \varphi\}$ , equal to the cosine of the displacement between phase voltage and phase current, so,

$$\{\cos \varphi\} = \cos \left( \arctan \left( \frac{\{E_{qtraj}\}}{\{E_{dtraj}\}} \right) - \arctan \left( \frac{\{I_{qtraj}\}}{\{I_{dtraj}\}} \right) \right) \quad (4.28)$$

As a consequence of the the value of characteristic current that, for I-shape, is closer to the predicted rated current  $88A_{RMS}$ , the power factor is maintained to a slightly higher value, near to unity, at high speed range than V-shape, both at rated and partial load.

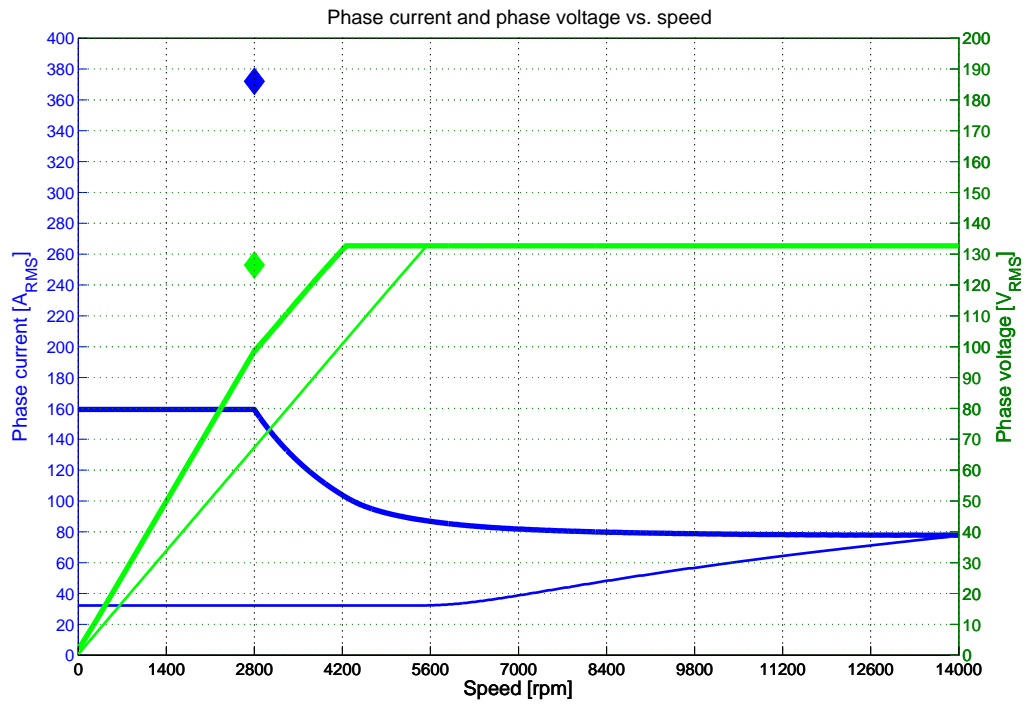


Figure 4.83: I-shape. The thin line is relate to the partial load.

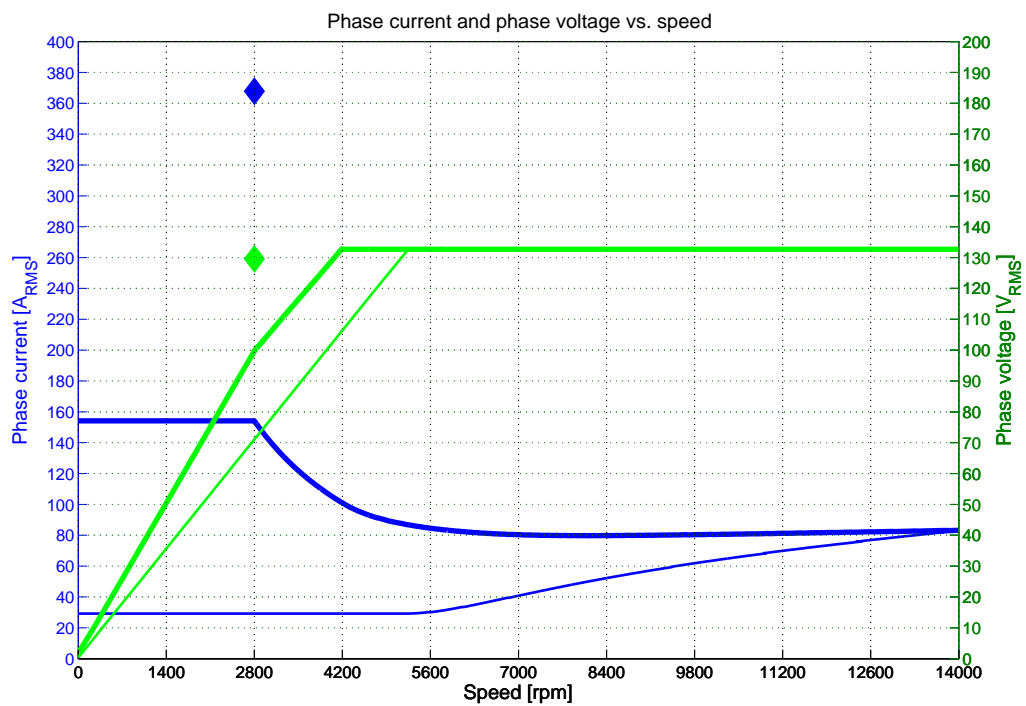


Figure 4.84: V-shape. The thin line is relate to the partial load.

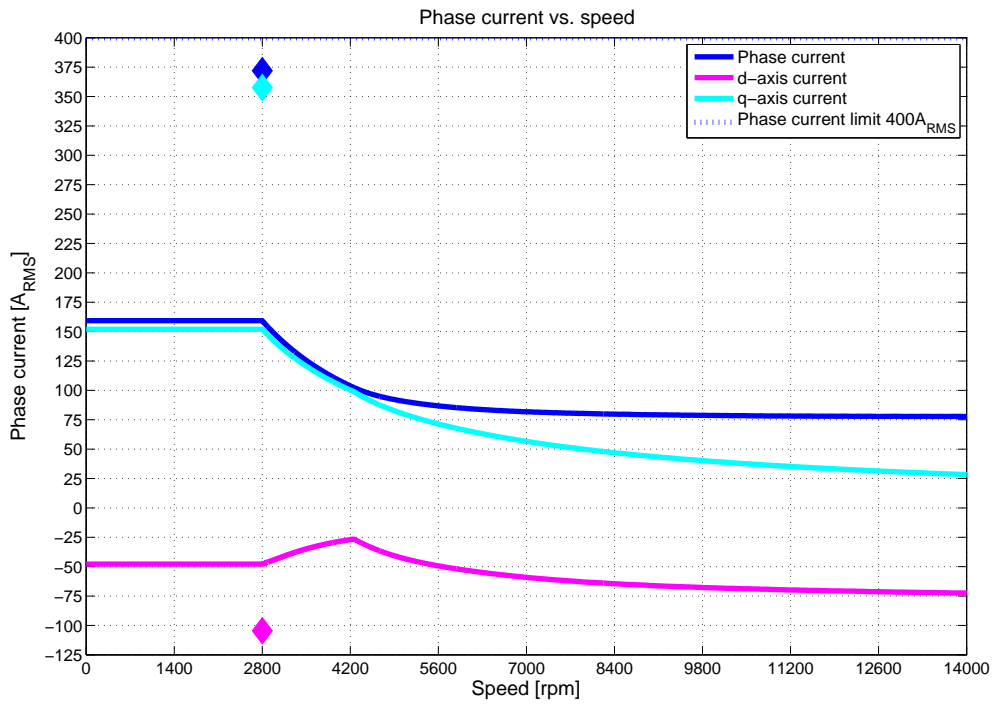


Figure 4.85: I-shape.

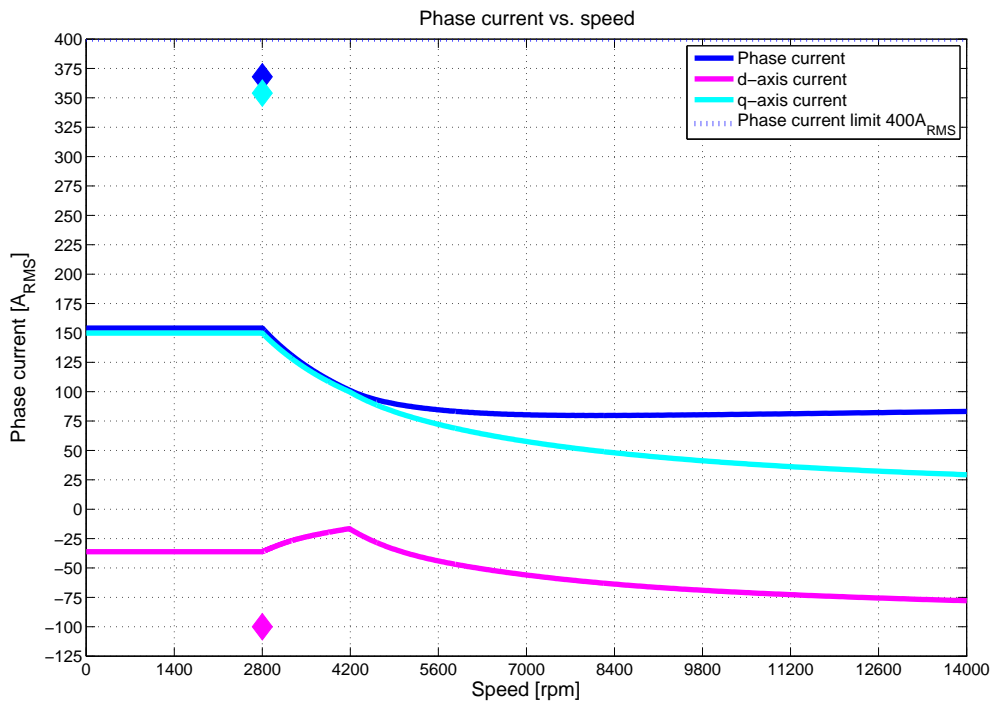


Figure 4.86: V-shape.



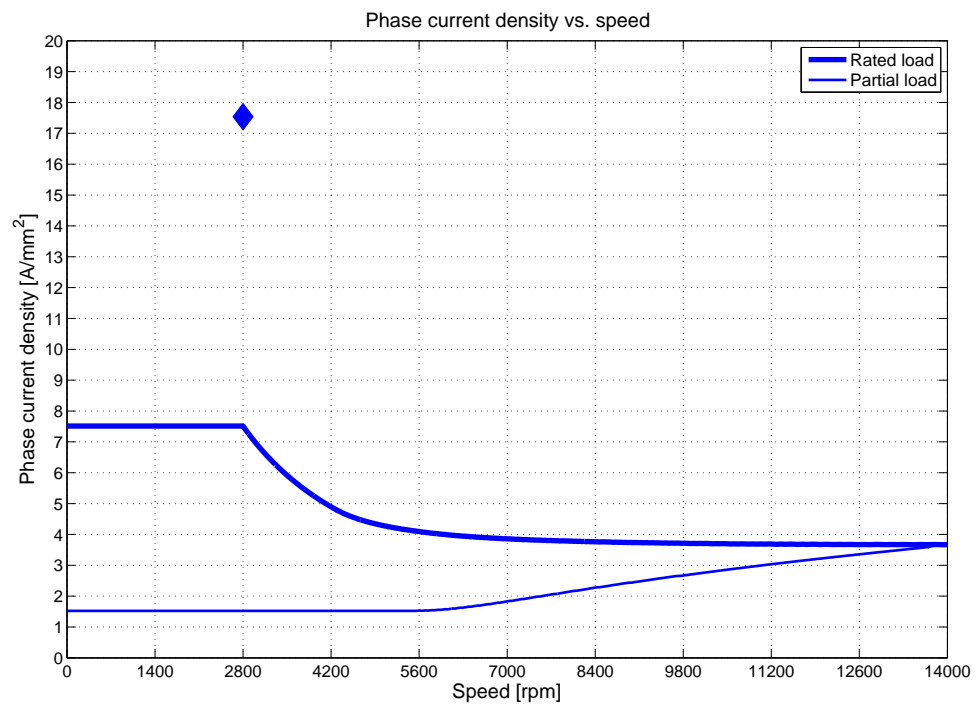


Figure 4.87: I-shape. The thin line is relate to the partial load.

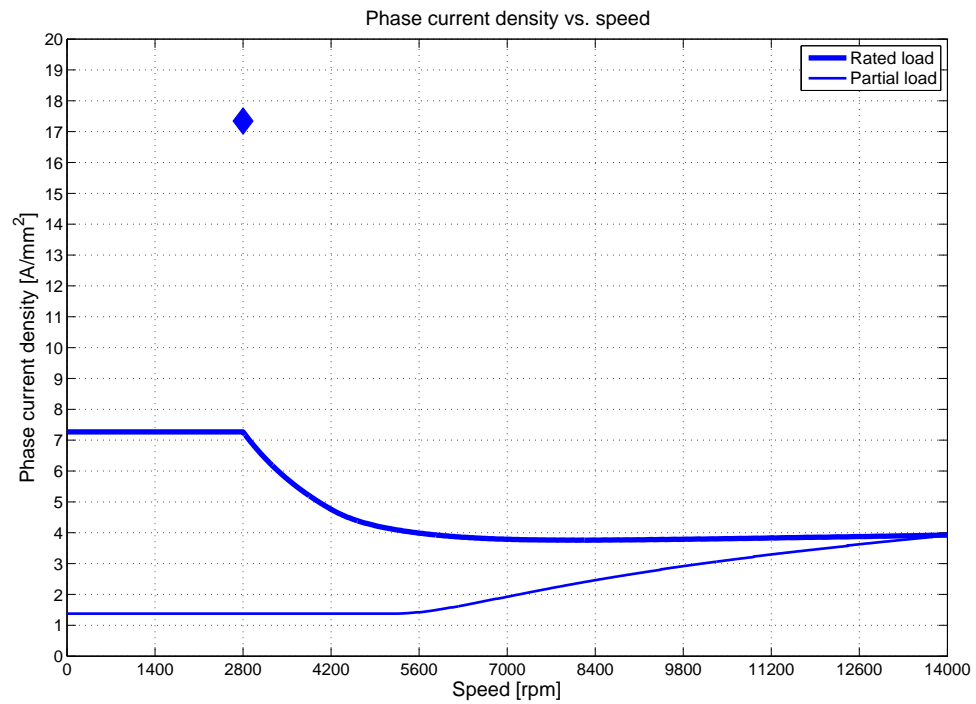


Figure 4.88: V-shape. The thin line is relate to the partial load.

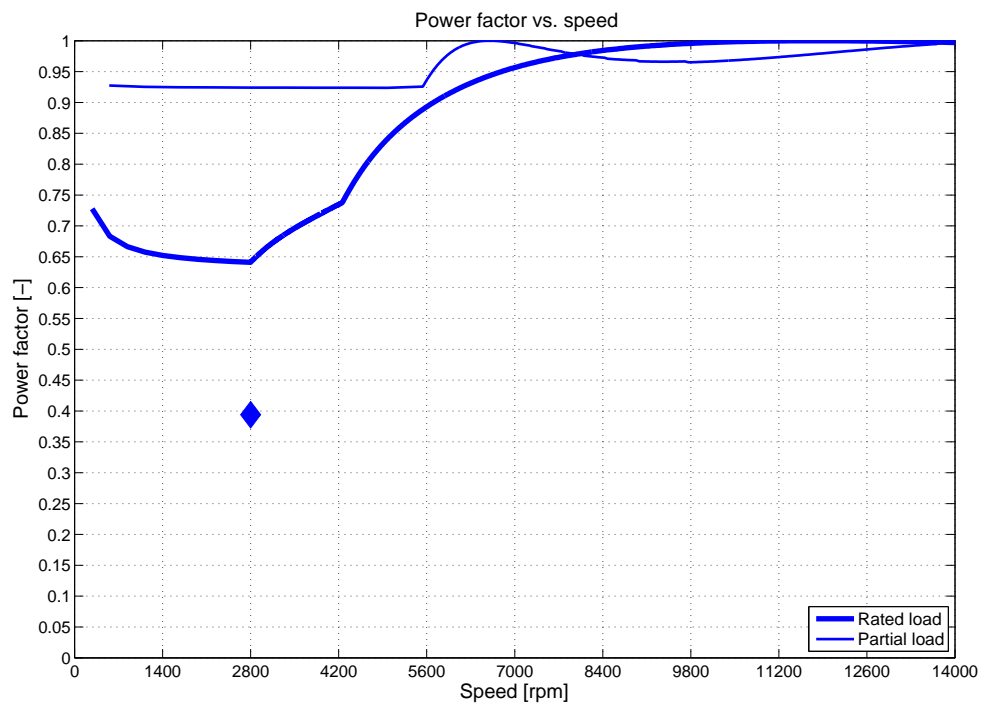


Figure 4.89: I-shape. The thin line is relate to the partial load.

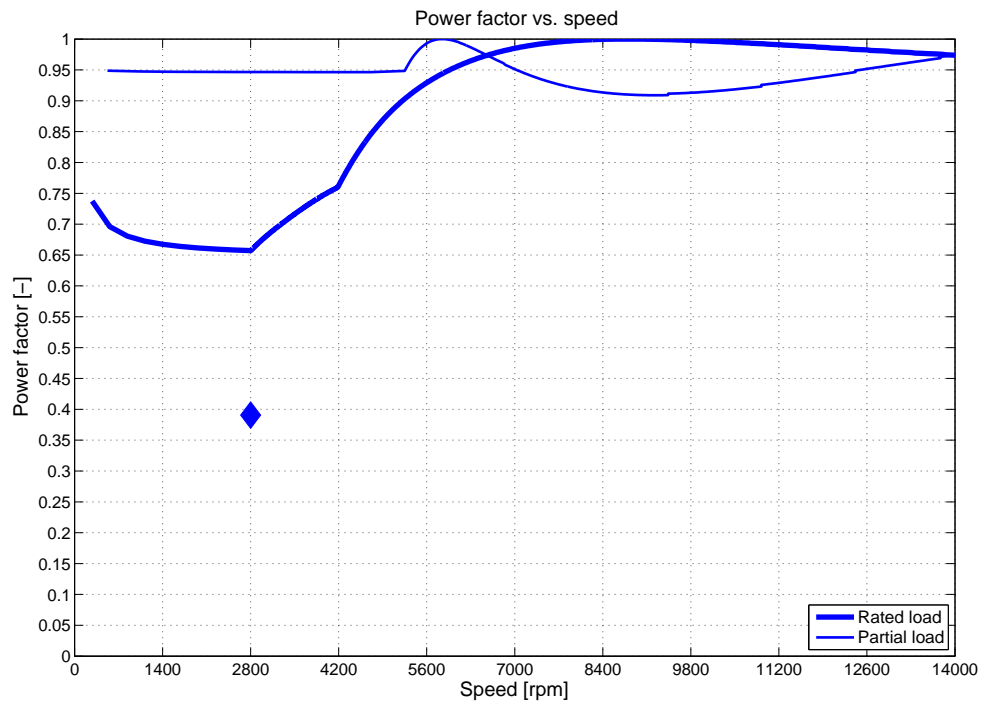


Figure 4.90: V-shape. The thin line is relate to the partial load.

## 4.7. Losses simulation

The losses simulation was performed evaluating:

- **Copper losses**

The copper losses are easily evaluated, assuming an uniform distribution of the current in the conductor: this is reasonable because, as mentioned above, due to the chosen conductor diameter, the skin effect is always negligible.

The copper losses array  $\{P_{C_{tra}j}\}$  is given by,

$$\{P_{C_{tra}j}\} = 3 \cdot R \cdot \{I_{tra}j\}^2 \quad (4.29)$$

- **Iron and *PM* eddy current losses**

We performed a transient simulation for each combination of d/q-axis current and speed (and so frequency) at rated and partial load. For each simulation we computed the stator, rotor iron losses and *PM* losses due to eddy current effect. Being a transient simulation, we must wait till the losses reach a steady state, as reported, for e.g. in fig. 4.91; we prove that it's achieved after about one electric cycle, so our simulations were prudentially performed till 1.5 electric cycle, and then we calculated the mean value in the last losses period.

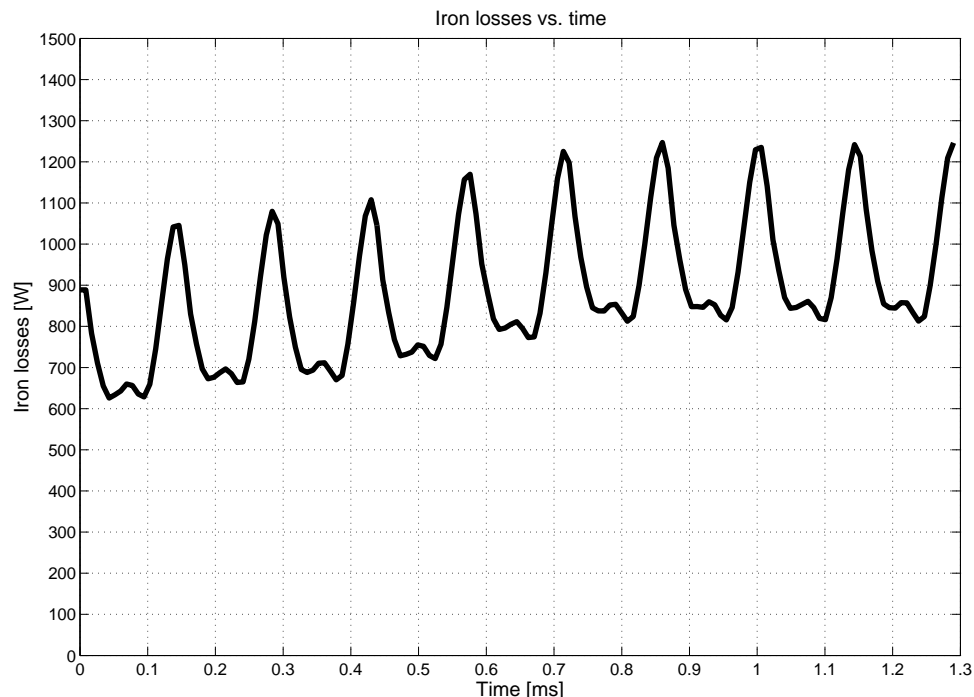


Figure 4.91: I-shape. Iron losses transient at 13955rpm; at this speed the period is 0.86ms.

A 1D interpolation was used in order to describe accurately the losses trends.

### 4.7.1. Copper losses

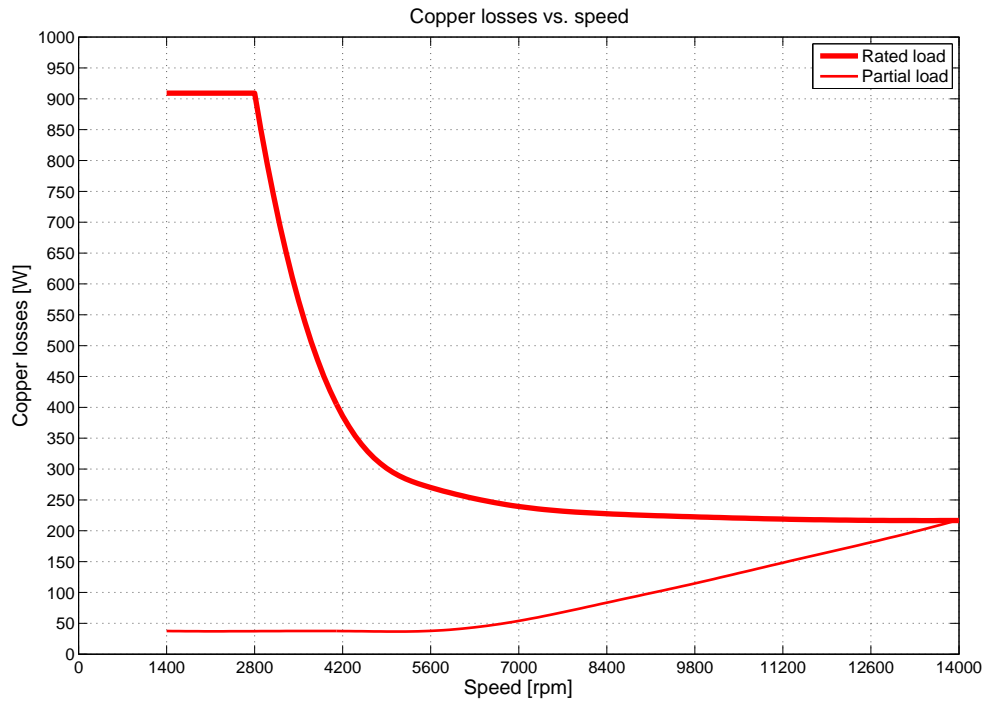


Figure 4.92: I-shape.

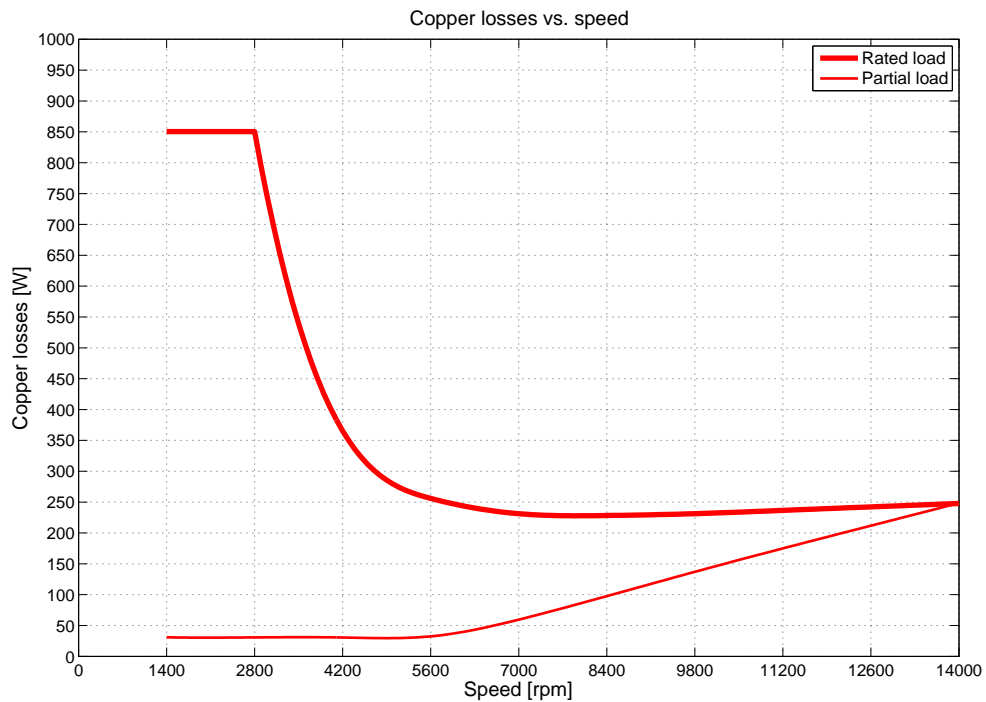


Figure 4.93: V-shape.

The trends of copper losses follows the current, it follows that V-shape shows, due to the higher cylindrical torque, a slightly lower copper losses at low speed.

Table 4.6: *PMs* eddy current and iron losses comparison at maximum speed  $14000rpm$  among different *FreedomCAR* designs.

<i>FreedomCAR</i> design	<i>PMs</i>	Rotor	Stator
	[W]	[W]	[W]
I-shape	120	230	730
V-shape	220	210	610
2011 P.B. Reddy <i>et al</i> , <i>IPM</i> [5]	~ 250	~ 900	~ 1250
2011 J.K. Tangudu <i>et al</i> , <i>IPM</i> [7]	~ 250	~ 700	~ 1000
2011 P.B. Reddy <i>et al</i> , <i>SPM</i> [5]	~ 1250	~ 20	~ 750

#### 4.7.2. Iron and *PMs* eddy current losses

As highlighted in par. 1.3.1, the *PMs* eddy current losses aren't negligible at high speed range. The segmentation of magnets is a popular technique for reducing this losses, so it was adopted a circumferential segmentation of the magnet, that it's the only possible to be simulated in 2D; In order to simulate the current flowing orthogonally to the problem plane, it was necessary to divide in turn the segment into two pieces and set between them a so called "end connection" that force the total current through the segment surface to be zero, as in real life. The width of each segments (made, in the model, of two pieces side by side) is almost the same for both the machines:  $5.3mm$  (6 segments) for I-shape and  $5mm$  (4 segments) for V-shape.

The result in terms of reduction of induced current density is considerable and this is highlighted in the following plots, although there are still areas in which the current density is more uneven, especially for V-shape design. As reported in fig. 4.99, ??, at maximum speed, for V-shape, the *PM* losses without segmentation are about 27% higher than those in I-shape, although the specific losses are almost the same value. The segmentation shows considerable effectiveness and it's mandatory because the eddy current losses in magnets would confirm, otherwise, the main cause of reduction of efficiency leading also to dangerous overheating. The reduction of losses is evaluated in the order of  $-90\%$  for I-shape design while  $-85\%$  for V-shape.

Regarding the iron losses, the results prove the impossibility of neglecting the rotor losses that contribute, at maximum speed, till about  $1/4$  of the total iron losses. Analyzing the value of at high speed range, we notice that the achieved value is lower than other *FreedomCAR* designs, as summarized in tab. 4.7.

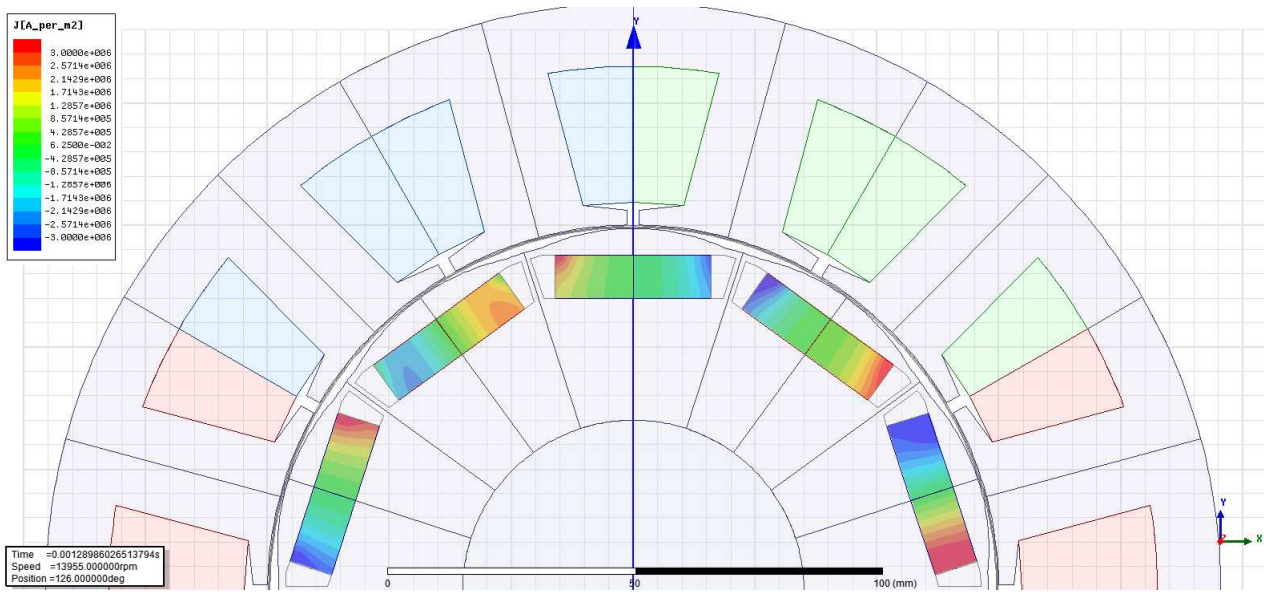


Figure 4.94: I-shape. Induced current density map in *PMs* at maximum speed.

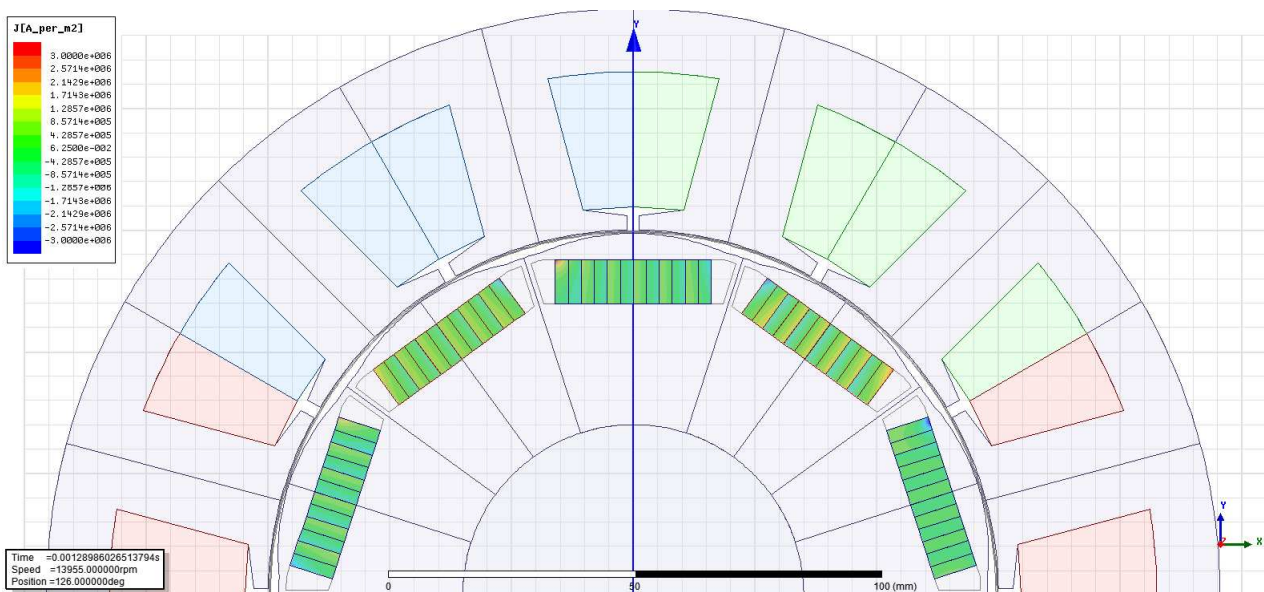


Figure 4.95: I-shape with segmented *PMs*. Induced current density map in *PMs* at maximum speed.

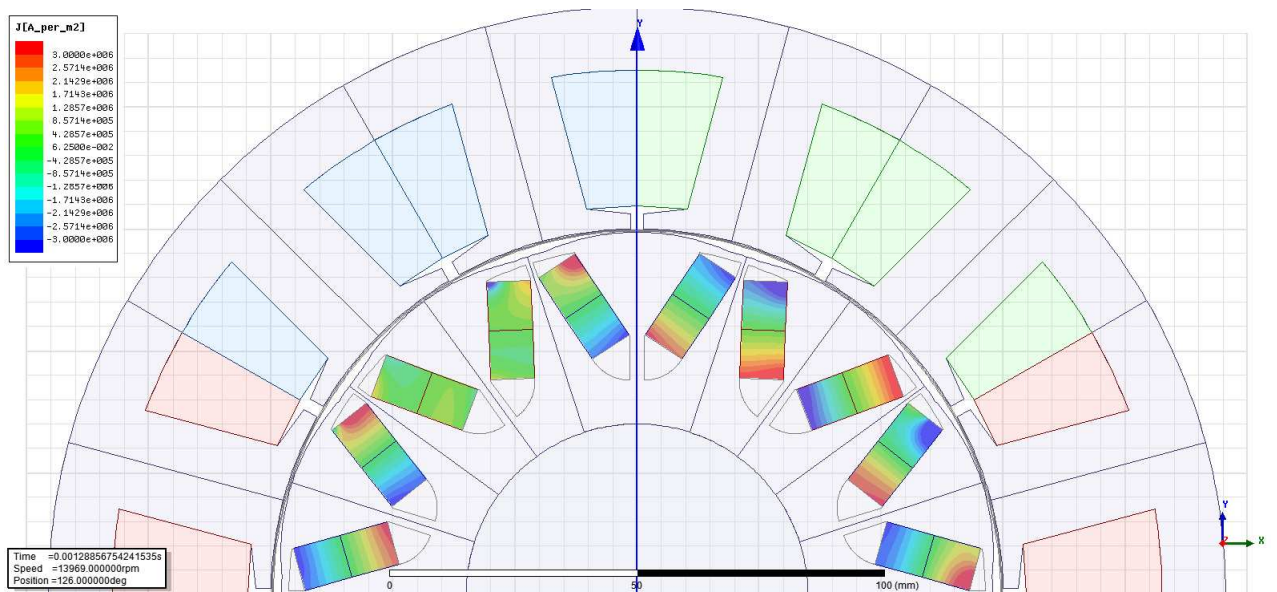


Figure 4.96: V-shape. Induced current density map in *PMs* at maximum speed.

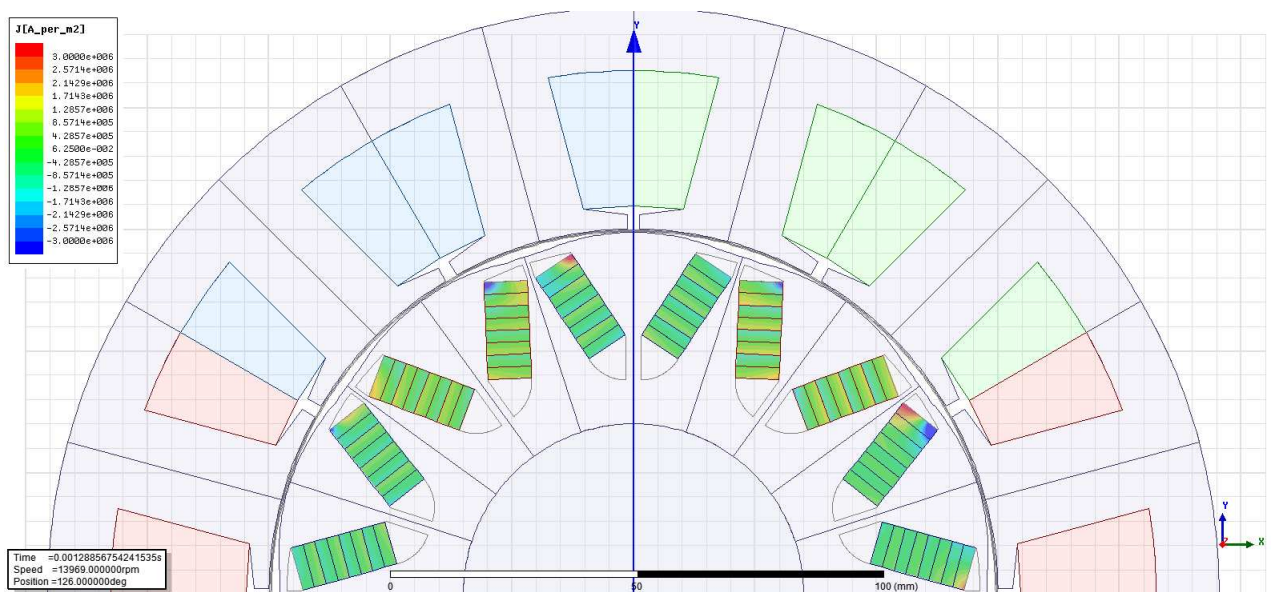


Figure 4.97: V-shape with segmented *PMs*. Induced current density map in *PMs* at maximum speed.

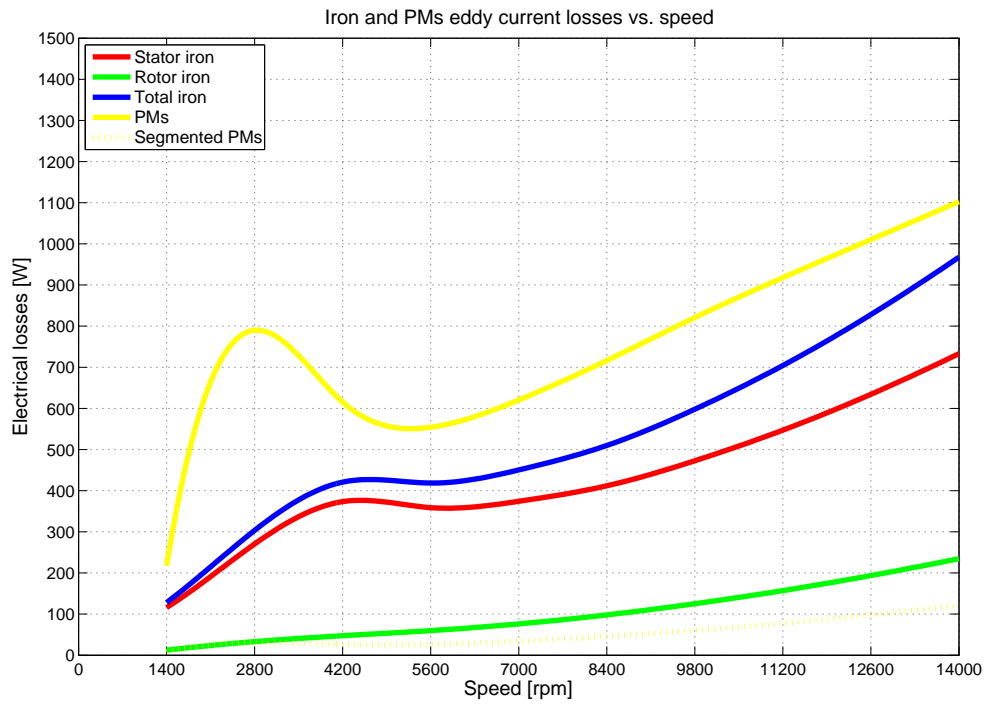


Figure 4.98: I-shape.

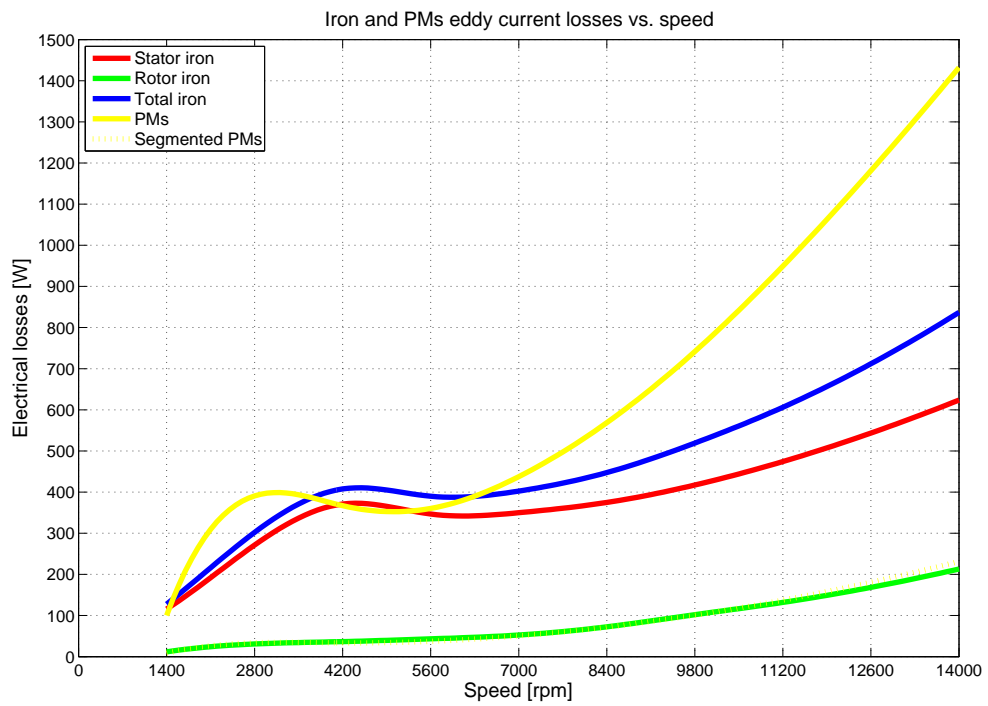


Figure 4.99: V-shape.



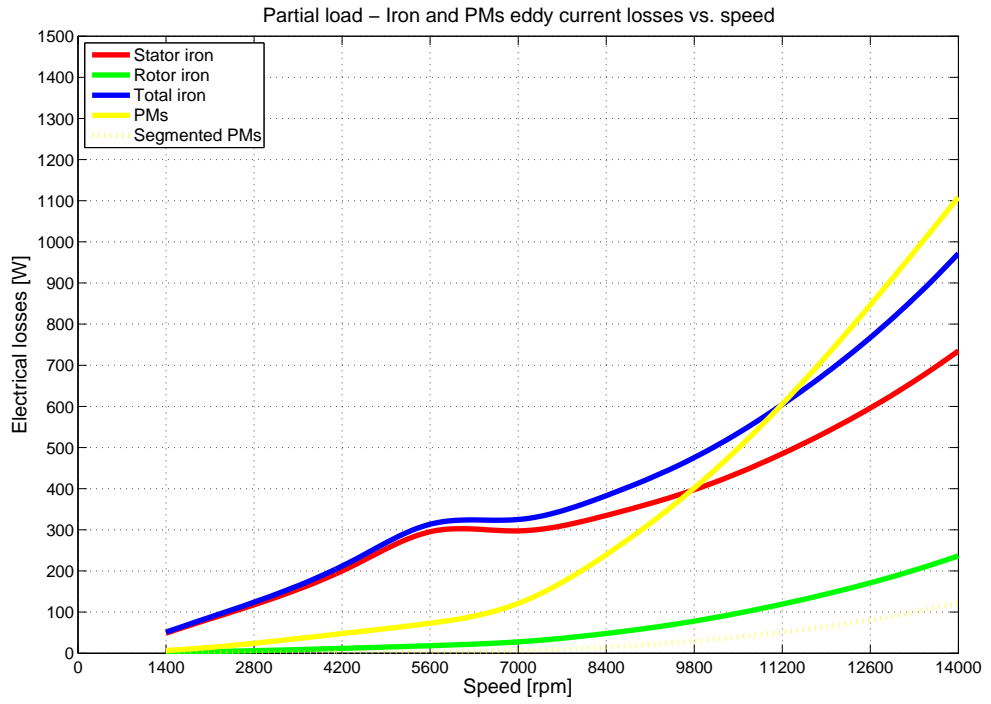


Figure 4.100: I-shape.

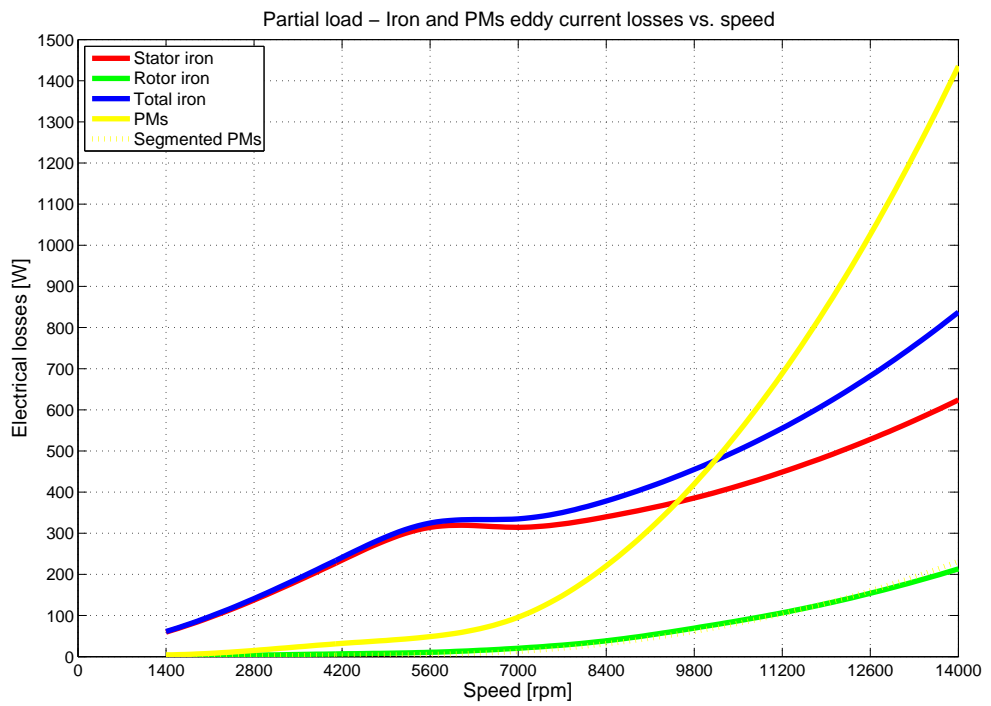


Figure 4.101: V-shape.

### 4.7.3. Efficiency vs. speed

Let's evaluate the electrical efficiency array  $\{\eta_{etraj}\}$  as follows,

$$\{\eta_{etraj}\} = \frac{\{P_{traj}\}}{\{P_{traj}\} + \{P_{Cutraj}\} + \{P_{PMtraj}\} + \{P_{Fetraj}\}}. \quad (4.30)$$

Where:

$\{P_{traj}\} = \{T_{traj}\} \cdot \frac{2 \cdot \pi}{60} \cdot \{n_{traj}\}$  is the developed power;

$\{P_{PMtraj}\}$  is the *PMs* eddy current losses;

$\{P_{Fetraj}\}$  is the iron losses losses.

Because we haven't got any information about mechanical losses, we estimated them, making reference to an experimental analysis performed on a similar *FreedomCAR* design, as reported in [5] and illustrated in fig. 4.102.

The total efficiency array  $\{\eta_{traj}\}$  is calculated assuming negligible the impact of

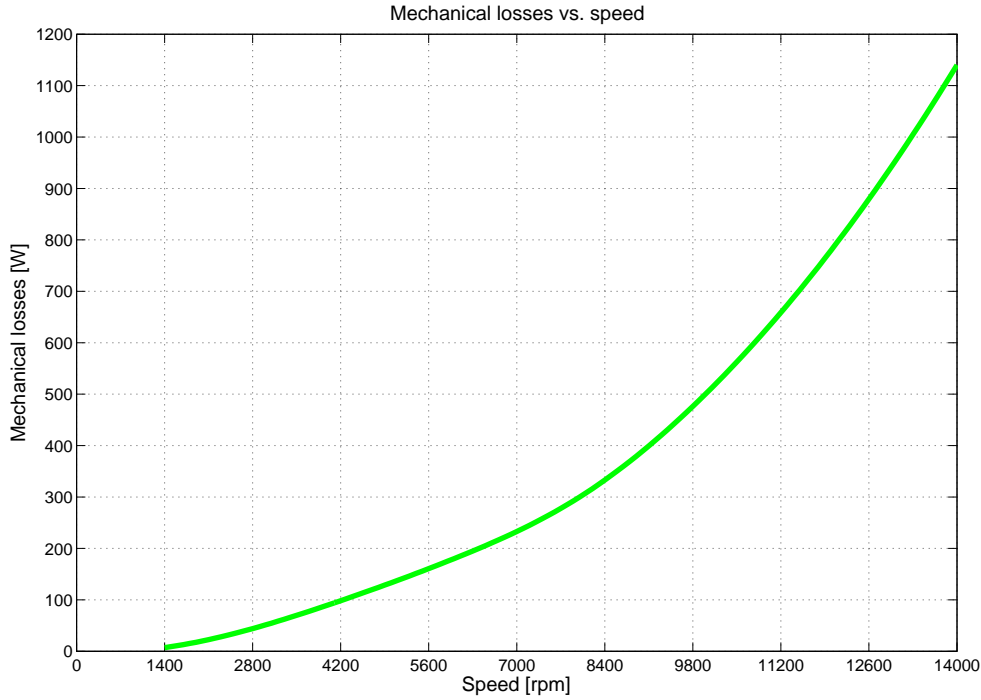


Figure 4.102: Predicted mechanical losses.

the resistance torque to the developed torque: in other words, we suppose that the output power is equal to the electromechanical power.

$$\{\eta_{traj}\} \cong \frac{\{P_{traj}\}}{\{P_{traj}\} + \{P_{Cutraj}\} + \{P_{PMtraj}\} + \{P_{Fetraj}\} + \{P_{mltraj}\}} \quad (4.31)$$

Where  $\{P_{mltraj}\}$  is the mechanical losses array described by the fig. 4.102.

Due to the low value achieved with iron and *PMs* eddy current losses, the efficiency results, with segmented *PMs* are very good: comparing to other *FreedomCAR* designs (see [5] - [6] - [7] - [8]), we can ensure, for the first time, an

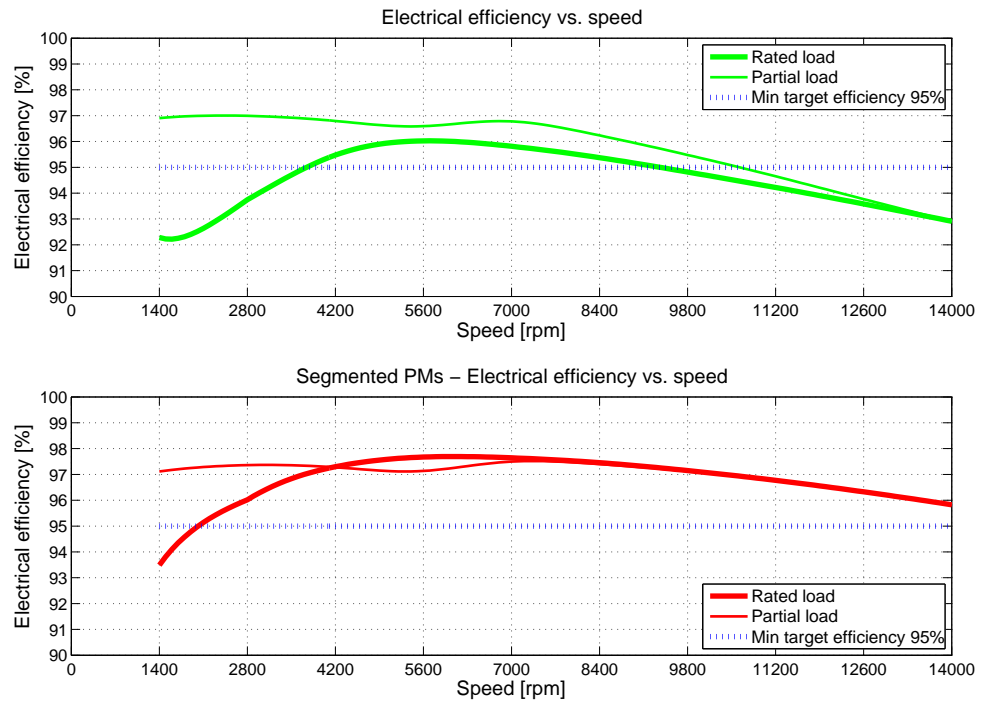


Figure 4.103: I-shape.

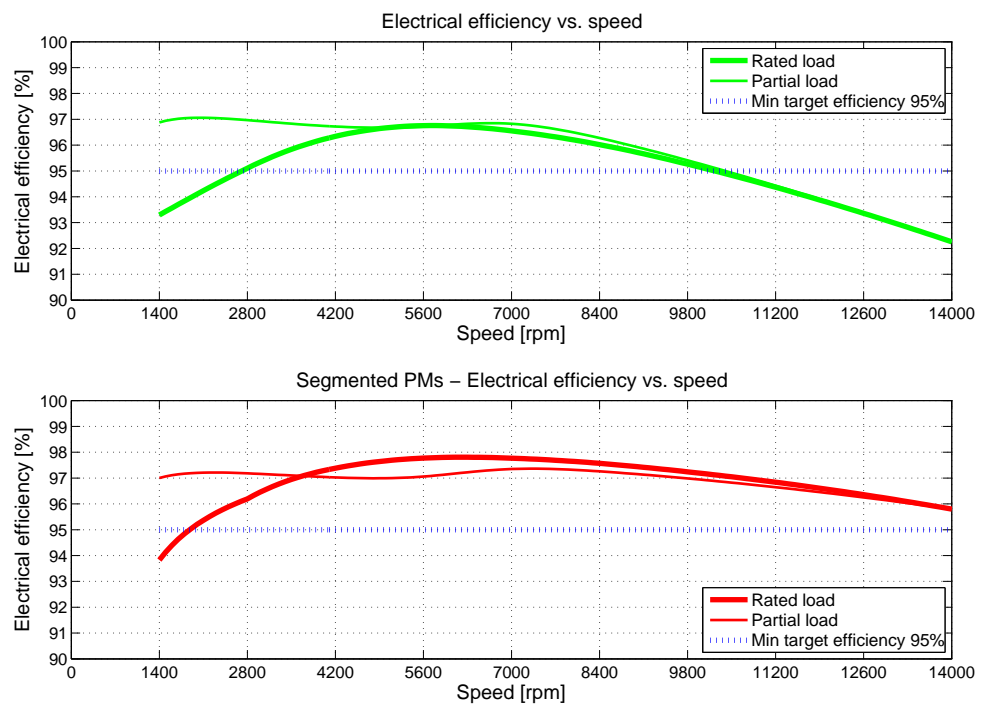


Figure 4.104: V-shape.

electrical efficiency higher than 95% till maximum speed. Both the machine offer, in this field, similar performance, working, at maximum speed with an electrical efficiency  $\eta_e = 95.7\%$ . The peak value is achieved between 5600rpm and 7000rpm, at  $\eta_e = 97.8\%$ .

Finally, regarding the total efficiency, none of the designs meet the requested

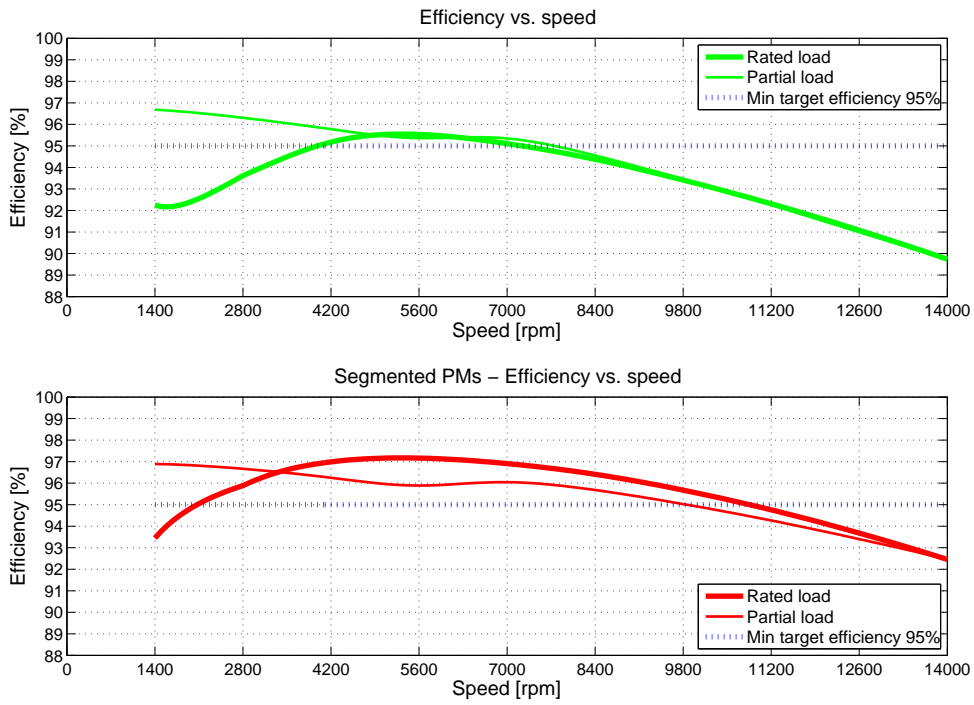


Figure 4.105: I-shape.

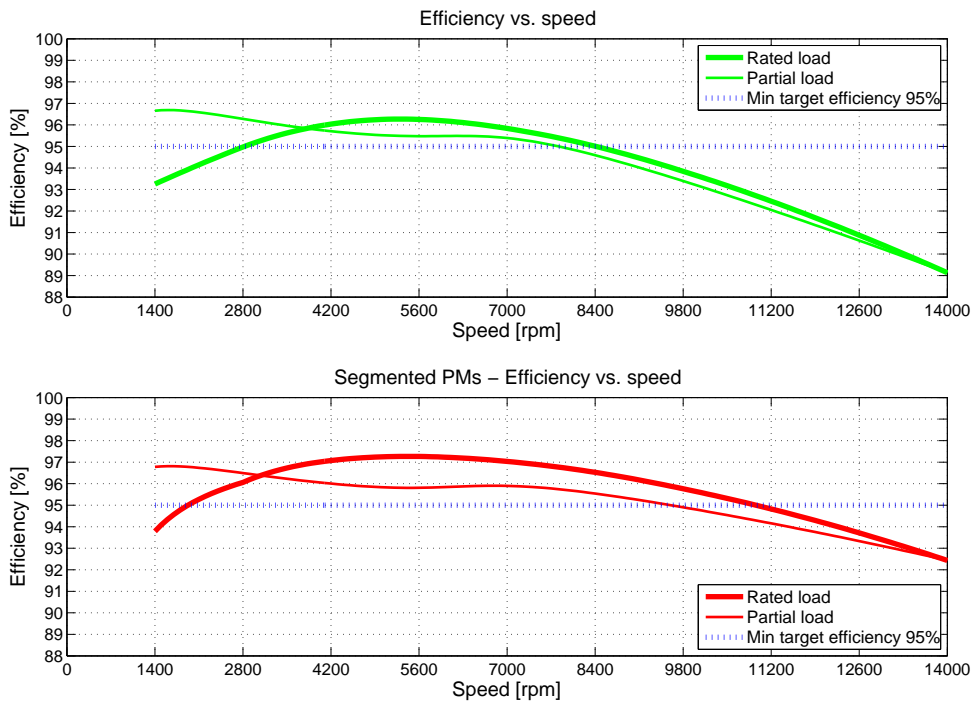


Figure 4.106: V-shape.

target of 95%. Due to the low value achieved with iron and *PMs* eddy current losses, this result mainly depends to the mechanical losses trend, and should be

Table 4.7: Efficiency comparison at maximum speed  $14000rpm$  among different *FreedomCAR* designs.

<i>FreedomCAR</i> design	Electrical efficiency	Efficiency
	[%]	[%]
I-shape	95.7	92.5
V-shape	95.7	92.5
2011 P.B. Reddy <i>et al</i> , <i>IPM</i> [5]	91	86.5
2011 J.K. Tangudu <i>et al</i> , <i>IPM</i> [7]	92	—
2011 P.B. Reddy <i>et al</i> , <i>SPM</i> [5]	92.1	—

possible, as highlighted in [5], reduce them at maximum speed of about 35%, using *lower loss bearings, lower loss seals and reducing churning losses due to the rotor inner bore*. However, for both designs, at partial load, it's ensured an efficiency higher than the limit, till  $9800rpm$  and the minimum value, achieved at maximum speed, is  $\eta = 92.5\%$ .

## 4.8. Comparison to a conventional rotor

In order to better understand the causes that led to this good excellent efficiency result, in particular if they're relate to the steel quality or to the unique rotor design, we performed a detailed simulation considering an I-shape *IPM* conventional round shape rotor (round shape height  $\Delta_r = 0mm$ ).

### 4.8.1. Load simulation

A load simulation was performed ( $I_d = -45.2A_{RMS}$ ,  $I_q = 140.6A_{RMS} \Rightarrow I = 147.7A_{RMS}$ ) in order to evaluate especially the torque ripple; as reported in fig. 4.110, is 11.5%, 6 times the same quantity evaluated in our *FreedomCAR* I-shape design. Moreover, contrary to what happens in round shape rotor, the peak-peak magnitude of the d/q torque is lower than the correspondent value of Maxwell torque.

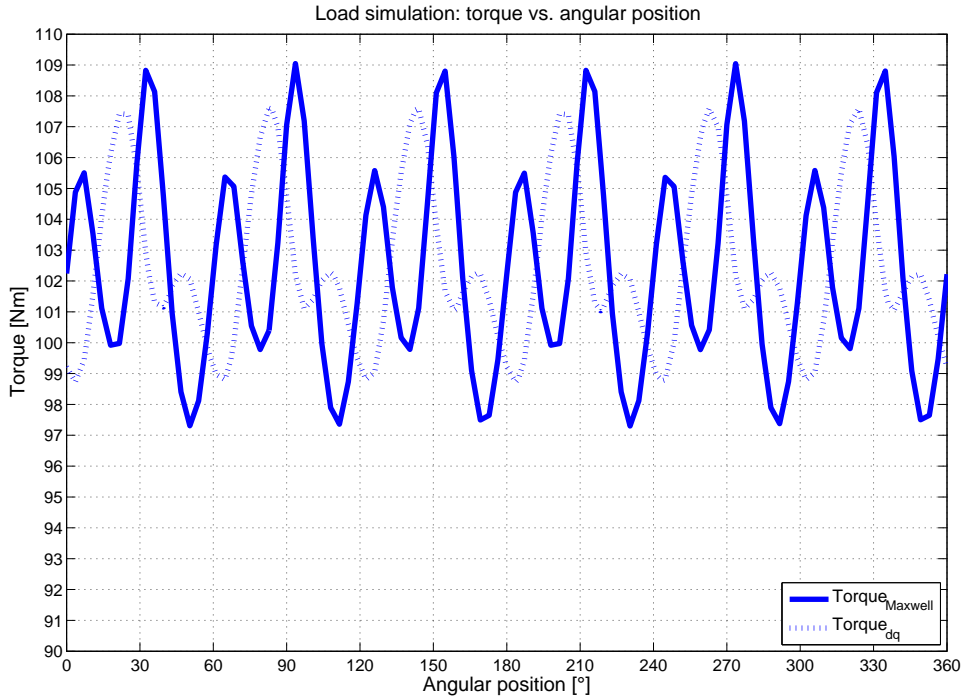


Figure 4.107:

#### 4.8.2. Current parametric simulation

Similarly to what was done previously, a current parametric simulation was performed changing the d/q-axis current  $I_d = -160 \div 160 A_{RMS}$   $I_q = 0 \div 400 A_{RMS}$  with step of  $20 A_{RMS}$ . Analyzing the d/q-axis flux linkages and synchronous inductances neglecting cross saturation, as reported in fig. 4.108, we notice, due to the reduction of q-axis airgap, at low currents, an higher value of q-axis synchronous inductances, evaluated in about 44% more than that of *FreedomCAR* I-shape design; also the d-axis synchronous inductances increase almost in the same way so the, so an expected increase of saliency ratio is however limited: its mean value is  $\langle \xi \rangle = 1.45$ .

#### 4.8.3. Torque ripple

The torque ripple trend, reported in fig. 4.113 with conventional rotor, describe immediately the great result reached, in terms of torque ripple reduction, using a round shape polar islands: neither at rated nor at partial load, the conventional rotor shape machine exhibit a value lower than the 5% limit. At maximum speed the it reaches almost 40%, while our *FreedomCAR* design works at 8%, 5 times lower.

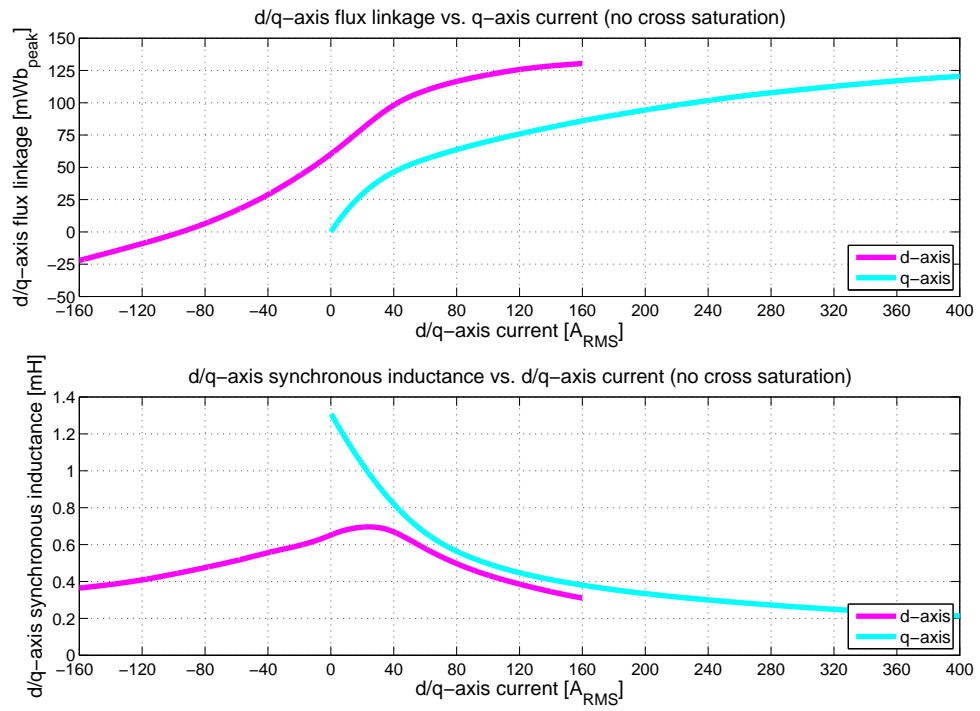


Figure 4.108:

Current space vector trajectory, iso saliency ratio curves

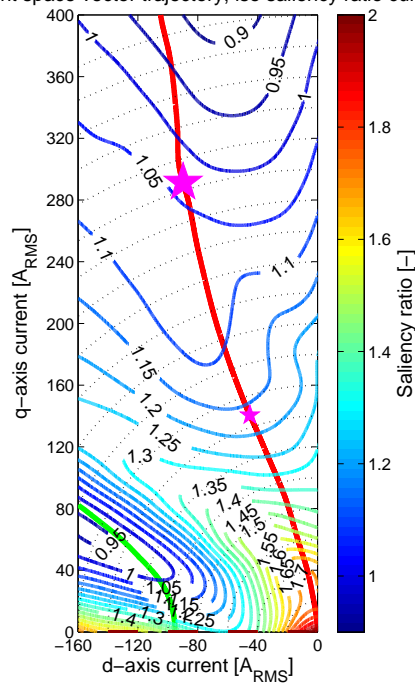


Figure 4.109:

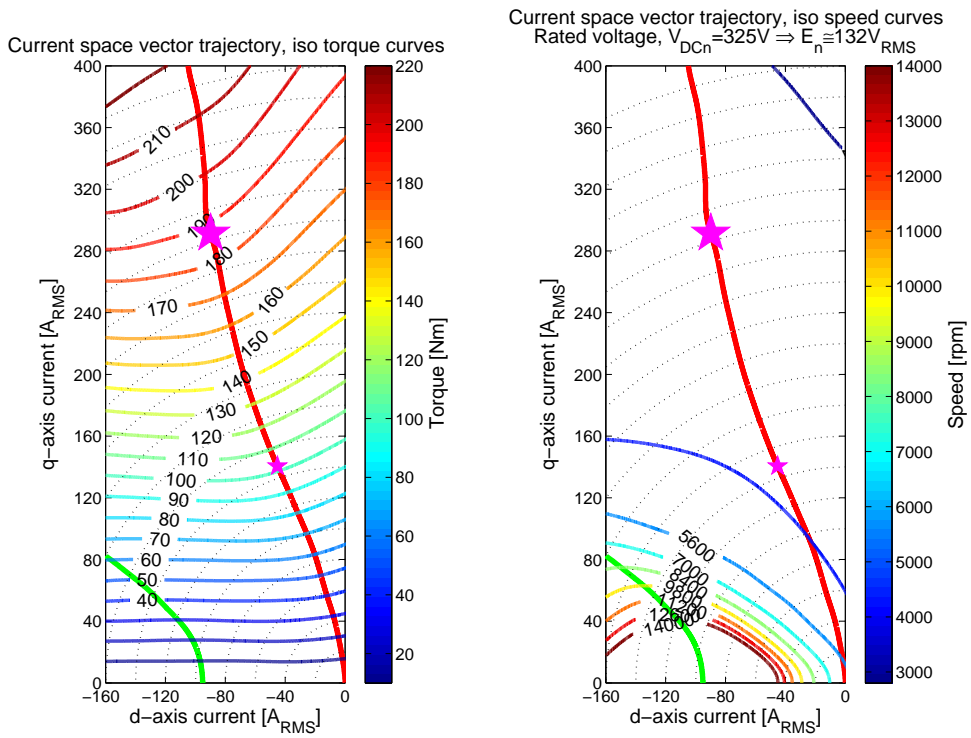


Figure 4.110:

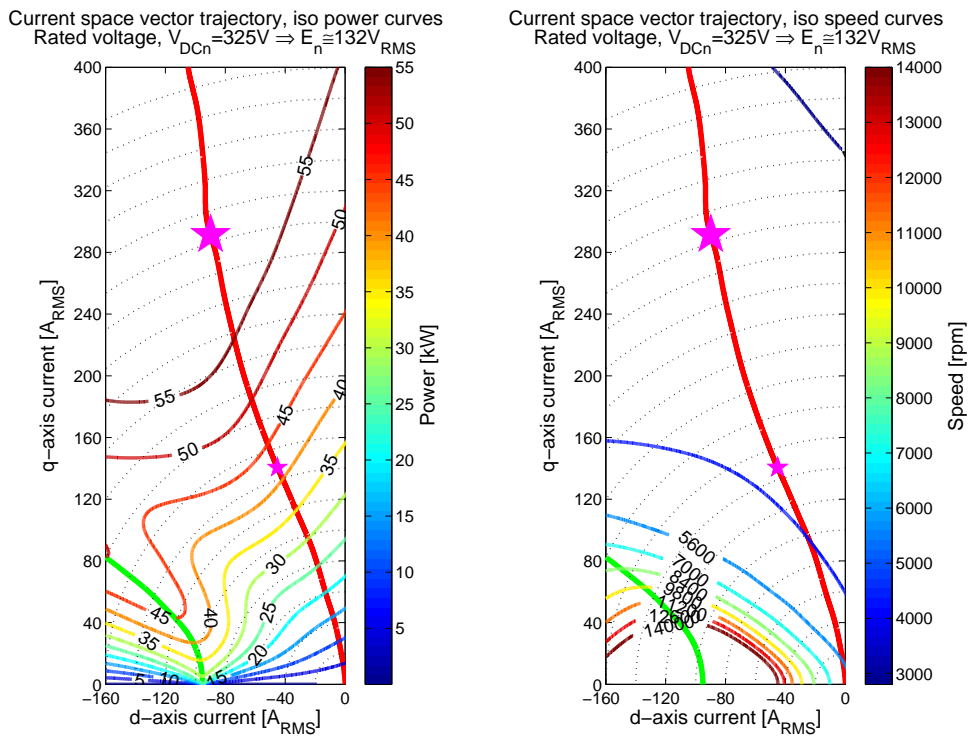


Figure 4.111:



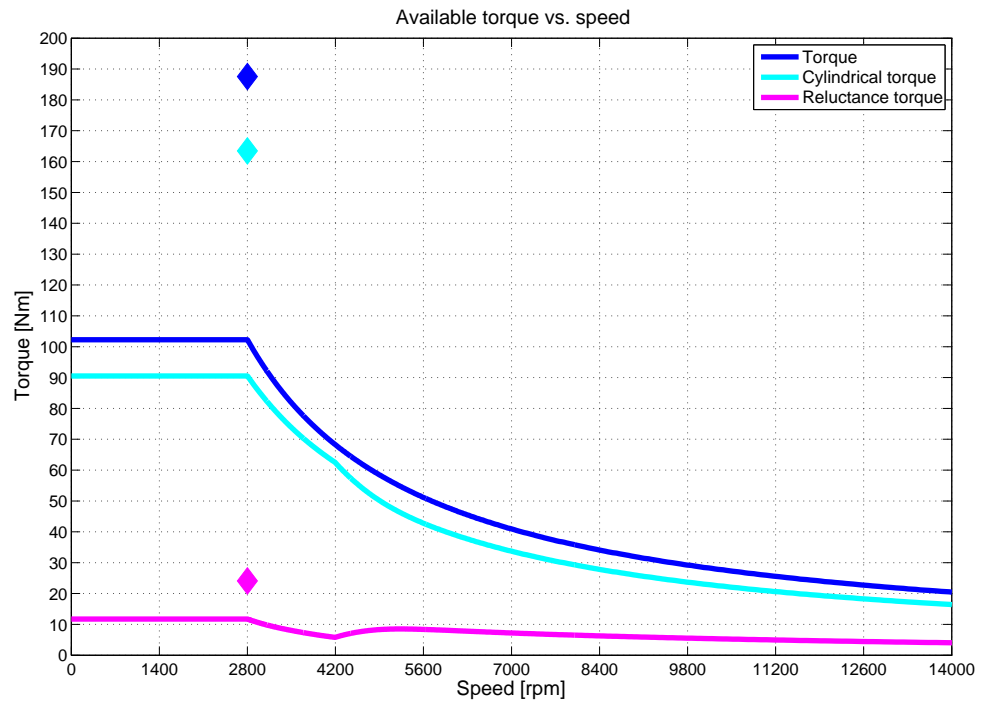


Figure 4.112:

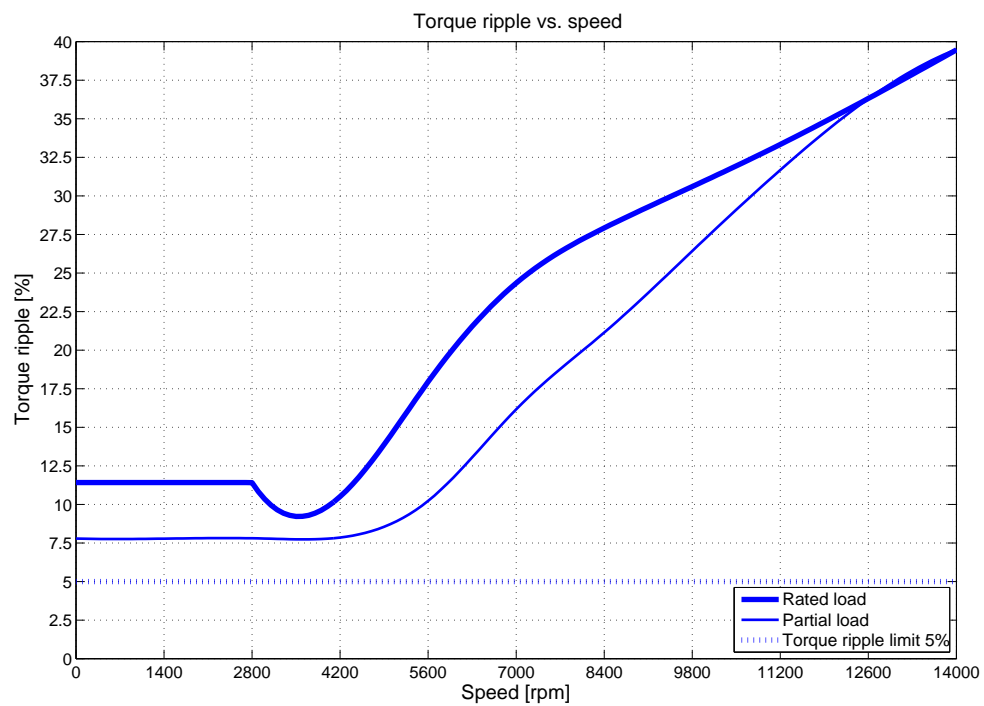


Figure 4.113:

Table 4.8: Losses and efficiency comparison at maximum speed 14000rpm between different designs.

Design	I-shape, <i>FreedomCAR</i>	I-shape, conventional
<i>PMs</i> eddy current losses	120	200
Rotor iron losses [W]	230	600
Stator iron losses [W]	730	1410
Electrical efficiency [%]	95.7	92.5

#### 4.8.4. Iron, *PMs* eddy current losses and electrical efficiency

The losses simulation performed in the conventional I-shape motor, shows a drastic increase of iron losses that gradually starts when the machine enter in *FW* area, both stator and iron: they're measurable, at maximum speed, in about twice of those evaluated in our *FreedomCAR* design. So we can conclude that the the excellent efficiency result achieved with the unconventional rotor comes from the particular shape adopted for polar islands.

In order to understand where are located these losses, we report the map

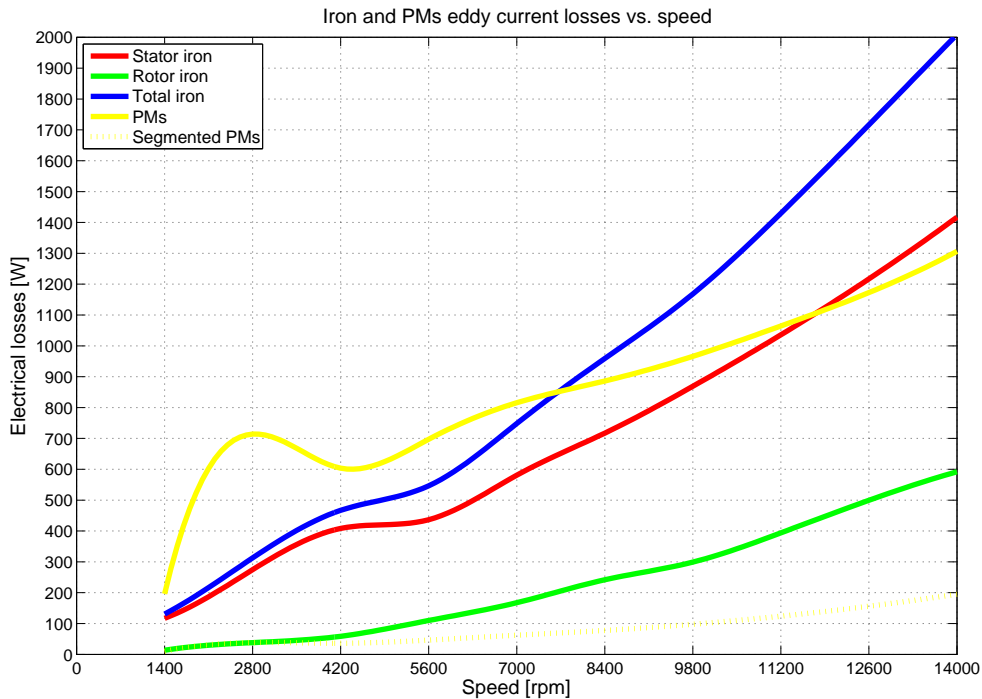


Figure 4.114:

of the iron losses density as illustrated in fig. 4.117, 4.119: the mainly sources of losses are locate in correspondance of the slot opening and and bridges, where the flux density drastically increase and, for the stator, is also characterized by brushes of flow. For conventional rotor, the losses in that areas prove to be higher

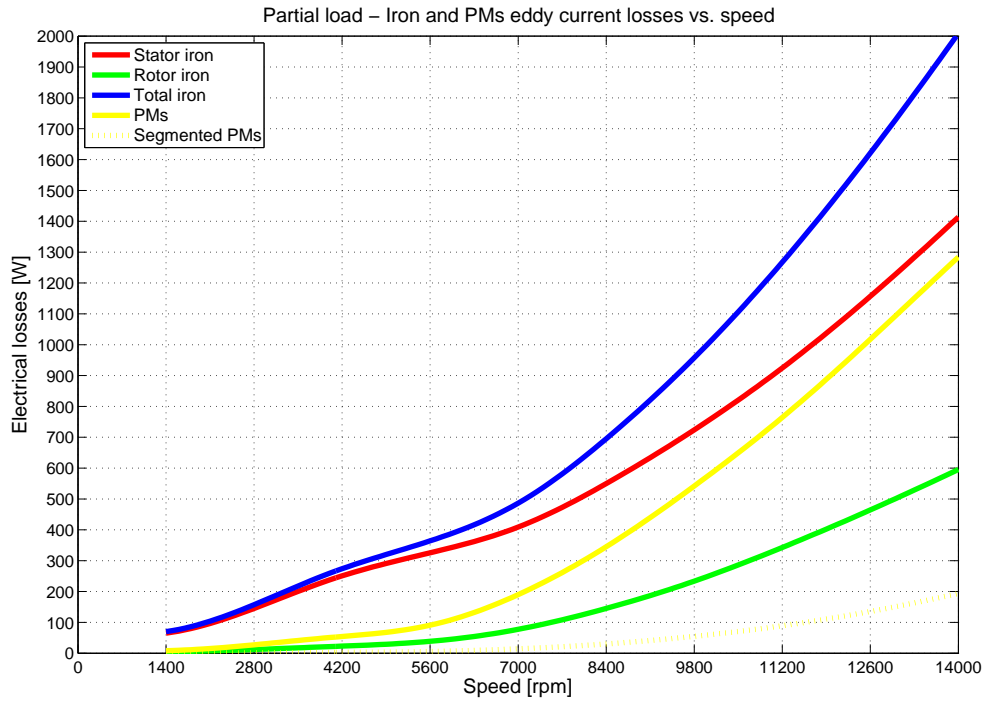


Figure 4.115:

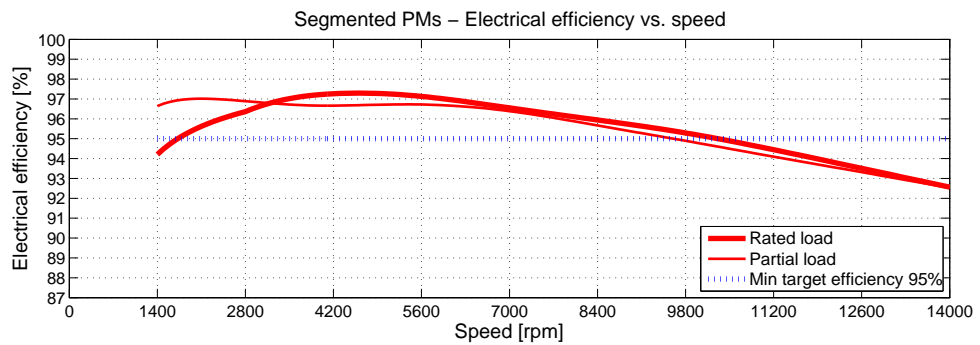
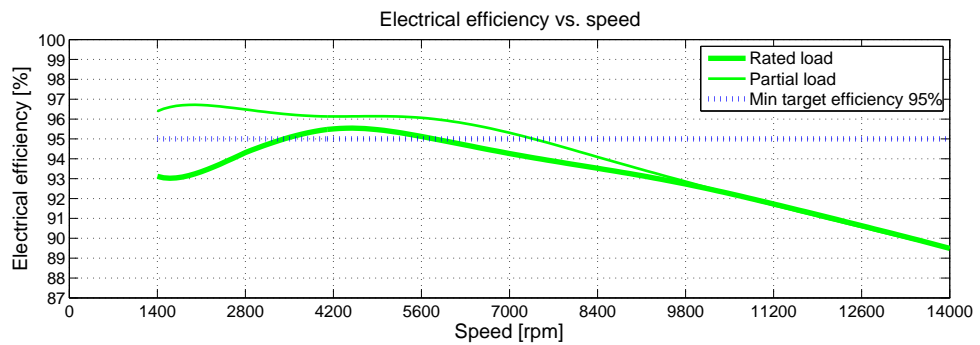


Figure 4.116:

and it could be relate to a lower *MMF* harmonic contents and better shape of the airgap flux density for the round shape design, as reported in fig.4.118, 4.120.

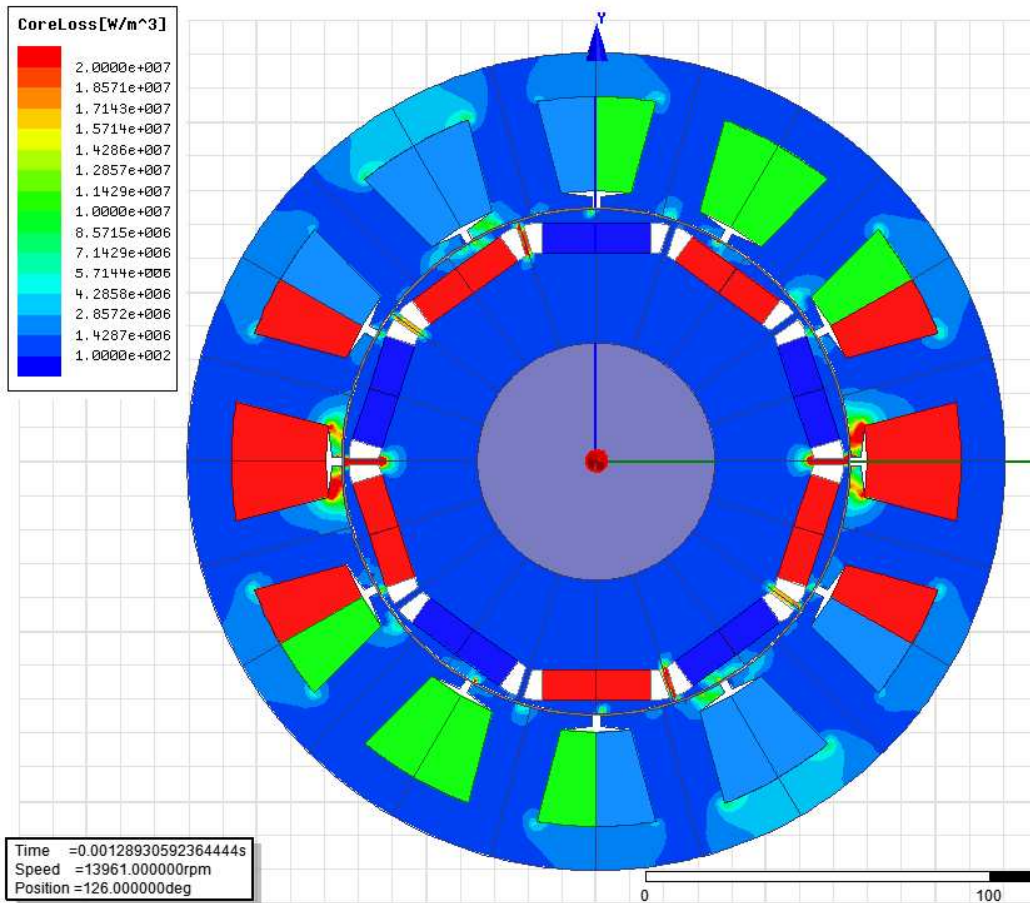


Figure 4.117: I-shape, conventional rotor. Iron losses density map at 14000rpm.

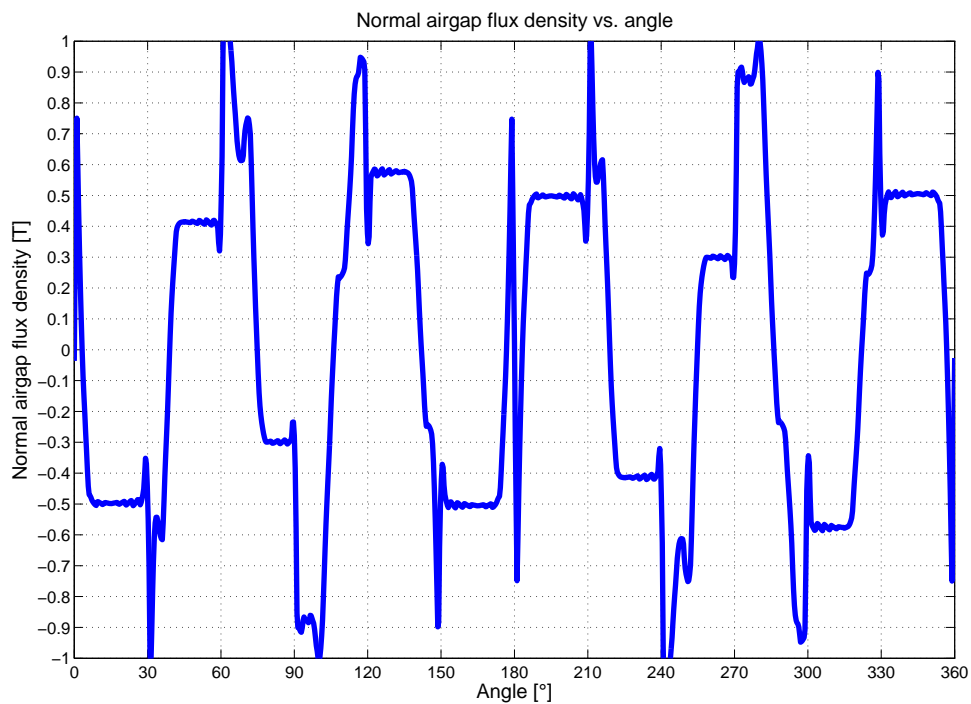


Figure 4.118: I-shape, conventional rotor. Normal airgap flux density at 14000rpm.

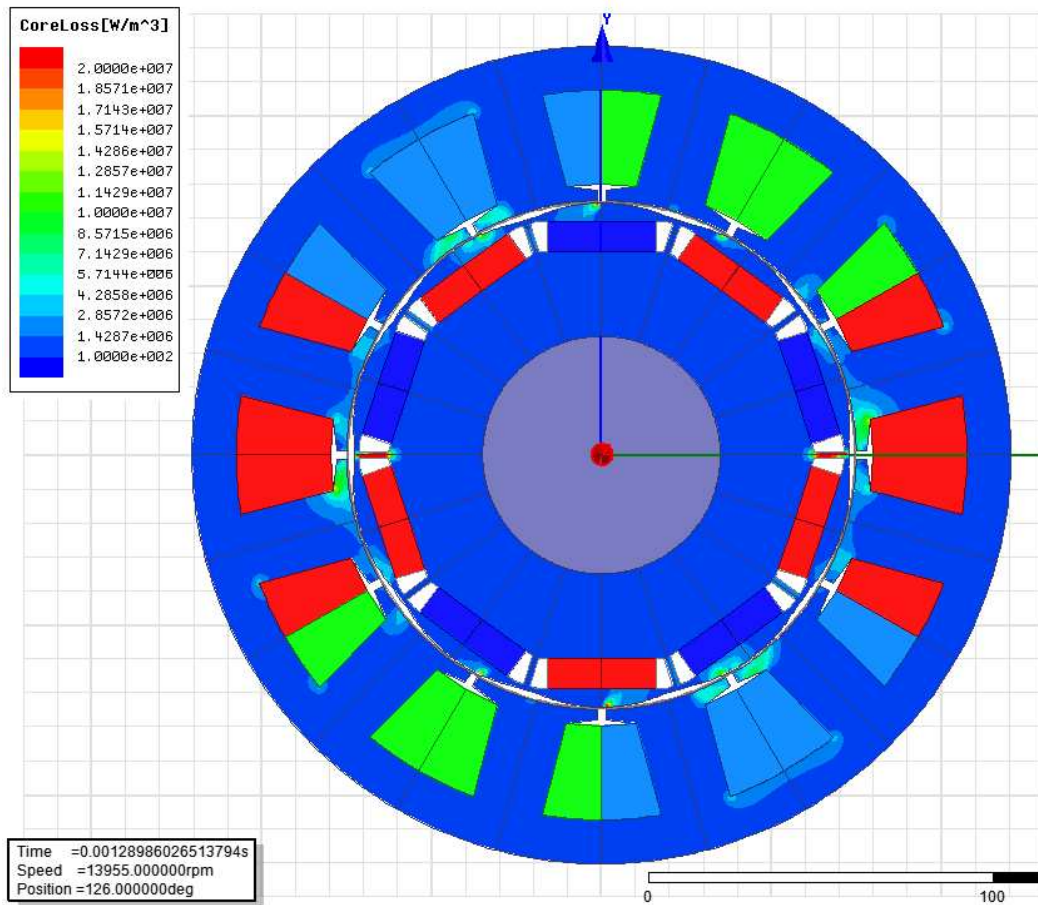


Figure 4.119: I-shape, *FreedomCAR* design. Iron losses density map at 14000rpm.

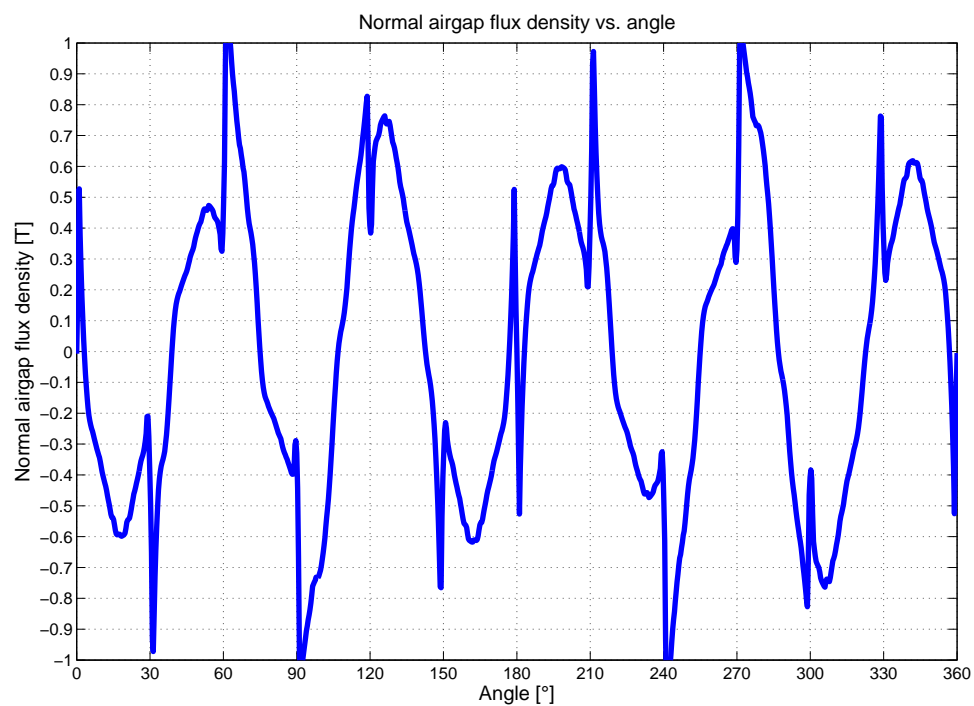


Figure 4.120: I-shape, *FreedomCAR* design. Normal airgap flux density at 14000rpm.

More investigation could be useful to understand the causes of this phenomena, but we can make some consideration concerning the stator iron losses, as follows. Assuming linear the iron, using the principle of superposition, we can image to evaluate the contribute of stator iron losses due the rotor flux density:

- in a conventional rotor shape, the rotor flux density trend is approximated to a square wave, so the stator seen the fundamental and the odd harmonic orders respectively at the main frequency and odd multiples of it. The losses are consequently induced by the total harmonics contribution.
- in a rotor with round shape polar islands, the rotor flux density trend is approximated to a sine wave, so the stator mainly seen the fundamental. The losses are consequently induced mainly only by the fundamental harmonic.

# CONCLUSIONS

In this report has been mainly studied the feasibility of the realization of an high performance *IPM* synchronous motor according to the latest *FreedomCAR* targets, using a round shape rotor and two different *PMs* configuration, I-shape (radial magnetization) and V-shape. At the end of this analysis we can say that **both designs meet most of the electromechanical desired requirements**. The key points to which this research has been directed, are summarized as follows.

- **Round shape of the rotor polar islands**

The most striking characteristic is the chosen round design for rotor polar islands. Although a meaningful loss in torque developed due to the higher airgap and the reduction of the saliency ratio, the benefits in terms of reduction of ripple and cogging torque are important. With a conventional rotor seems difficult to meet the same last performances, without additional measure (for. e.g. skewing, appropriately choice of flux barrier number and their geometry). The great result of the round shape design is in the high reduction of the rotor and stator iron losses, especially at high speed range, evaluated in about an half, compared to a conventional rotor: this lead both the machines to achieve the most difficult target of *FreedomCAR* specification, the electrical efficiency of 95% till 14000rpm.

So we can affirm that the round shape design of the polar island is a good technique in order to reduce cogging torque, torque ripple, and iron losses.

- **Electromechanical performances, I-shape/V-shape comparison**

As highlighted int tab. 5.1, both the machines are good candidate for *FreedomCAR* specifications, although the I-shape configuration seems, in general, better then V-shape for the following reasons:

1. Lower *PM* mass,  $-20\%$ .
2. Lower back *EMF* line-to-line voltage,  $-10\%$ .
3. In general a slightly higher saliency ratio, although isn't, as mentioned in chap. 2, the key characteristic in *FSCW* motors.

The first two point are correlate and extremely important in view of costs reduction, in which *PMs* has become in recent years the main term. Regarding the back *EMF* line-to-line at max speed, this study reaffirms the difficult to get the  $600V_{peak}$  voltage specification.

The third conclusion isn't a general rule for this kind of machine: at the beginning, we expect a better behavior for the V-shape design, especially an higher saliency ratio, and so reluctance torque component but this may depends on the V-shape geometry and relative flux barrier: we choose to maximize the cylindrical torque, reducing the bridge height as possible, ensuring the structural strength to centrifugal stress. However, due the high speed achieved by the motors, a detailed mechanical analysis to centrifugal stress (both steady state and transient) using *FEA* should be mandatory in order to check and get the best optimization of the dimensions of the rotor bridges. Regarding the constraint of torque ripple, the evaluated designs can meet the  $5\%$  only in a low speed ranges and this suggest additional measures are needed, for e.g. an appropriate skewing.

The losses results, as mentioned above, are the most interesting data achieved in this research: for the first time both designs reach, at least, the requested electrical efficiency of  $95\%$  till  $14000rpm$  and improvements aimed at reducing mechanical losses, should lead also to meet the total efficiency specifications. However *PMs* segmentation, at least circumferential, prove to be mandatory being, otherwise, the main source of losses at max speed.

Next steps should be addressed to an accurate optimization of both the machines: a reduction of stack length in order to set the max torque exactly in correspondence of the voltage limit and especially a mechanical and thermal analysis at maximum speed.

Finally we can make some considerations about the procedures used for the design of the motors.

The analytical synthesis method relate to the "*SPM* equivalent motor", described in this report, prove to have a good accuracy for the stator sizing while for the rotor show its limits: in fact the *PM* dimensions comes out test in *FEA*, although the analytical procedure give us some information of the order of magnitude of the *PM* thickness.

All the *FEA* simulation, executed in this research using the transient formulation, could be performed by a magnetostatic formulation, working in d-q/reference frame, for the evaluation of the current spatial trajectory; a time harmonic formulation is instead necessary for a rough calculation of the iron and eddy current losses, using a particular procedure called "current points method" [?]. In this way, is possible to use simple freeware *FEA* softwares, like *FEMM*, and make verification of the results, especially as regards the iron rotor losses.



Table 5.1: Key machine parameters summary

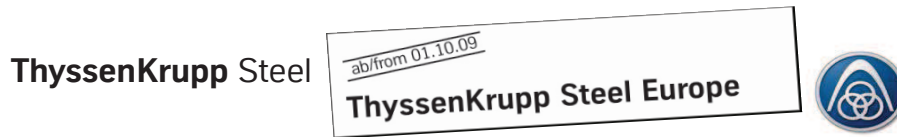
<b>Rotor configuration:</b>	<b>I-shape</b>	<b>V-shape</b>	<b><i>FreedomCAR</i></b>
Number of slots	12		
Number of poles	10		
Airgap diameter	150mm		
Stack length	87mm		
Stator outer diameter	241mm		
Airgap height	0.7mm		
Round shape rotor height	1.5mm		
# of conduc. per phase, series config.	64		
# of conduc. per slot, series config.	16		
Conductor area, series config.	21.21mm <sup>2</sup>		
<i>PM</i> dimensions (per pole)	9 × 32mm	2 × (9 × 20)mm	
Rated power	30kW		30kW
Max power	55kW		55kW
Rated current	159A <sub>RMS</sub>	154A <sub>RMS</sub>	
Max current	372A <sub>RMS</sub>	367A <sub>RMS</sub>	400A <sub>RMS</sub>
Characteristic current	89A <sub>RMS</sub>	101A <sub>RMS</sub>	< 400A <sub>RMS</sub>
Back <i>EMF</i> line-to-line @ 14000rpm	751V <sub>peak</sub>	826V <sub>peak</sub>	≤ 600V <sub>peak</sub>
<i>PMs</i> mass	1.90kg	2.38kg	
Copper mass	4.88kg		
Iron mass	17.52kg	16.75kg	
Total mass	24.30kg	24.01kg	≤ 35kg
Total volume	3.97ℓ		≤ 9.7ℓ
Estimated machine cost	346EUR	411EUR	
Iron M235-35A, 1.90EUR/kg			
<i>PM</i> NdFeB, 140EUR/kg (highly variable with time, quantity, etc.)			
Copper, 9.5EUR/kg			



CHAPTER 6

ADDENDUM

## 6.1. Iron datasheet: ThyssenKrupp® M235-35A



### Power Core® M235-35A Elektroband NO / NGO electrical Steel

#### Anwendungsgebiete

##### Application range

Die nicht kornorientierte Elektrobandsorte M235-35A der ThyssenKrupp Steel AG ist Ideal geeignet für hocheffiziente und energiesparende Anwendungen in Großmaschinen, Sondermaschinen und Schrittmotoren.

*The non grain oriented electrical steel grade M235-35A of the ThyssenKrupp Steel AG is suitable for highly energy efficient utilisations and economical applications as in large scale machines, special purpose motors and stepper motors.*

#### Magnetische Eigenschaften

##### Magnetic properties

	Garantiewerte nach DIN EN 10106 <i>Guaranteed values according to DIN EN 10106</i>	Sortentypische Mittelwerte ThyssenKrupp Steel AG <i>Typical mean values ThyssenKrupp Steel AG</i>
<b>Ummagnetisierungsverlust bei 50Hz</b> <i>Core loss at 50Hz</i>		
1,0* T	0,95 W/kg	0,96 W/kg
1,5 T	2,35 W/kg	2,24 W/kg
<b>Magnetische Polarisation bei</b> <i>Magnetic polarization at</i>		
2500 A/m	1,49 T	1,54 T
5000 A/m	1,60 T	1,64 T
10000 A/m	1,70 T	1,77 T

\* Die Größe des Ummagnetisierungsverlustes bei 1,0 T ist ein Anhaltswert und dient zur Information

*\* The core loss value at 1.0 T is a reference value and is for information purposes only*

Figure 6.1:

ThyssenKrupp Steel

ab/from 01.10.09

ThyssenKrupp Steel Europe



### Liefermöglichkeiten

#### Product range

Die Sorte M235-35A kann in Bandbreiten von 20 mm bis 1250 mm geliefert werden. Die Lieferung erfolgt im schlussgeglühten Zustand nach DIN EN 10106.

Für diese Sorte sind folgende Isolationsarten verfügbar:

*The grade M235-35A is available from 20 mm up to 1250 mm width. The material is fully finished according DIN EN 10106.*

*For this grade the following insulations are available:*

Isolationsarten Insulation types	
IEC 60404-1-1/04	ThyssenKrupp Steel AG
EC - 3	Stabolit 10
EC - 5	Stabolit 20
	Stabolit 30
	Stabolit 60
EC - 6	Stabolit 40
Backlack *	Stabolit 70
	Kombi-Isolierung Combined-Insulation

\* nicht im IEC geführt  
\* not conducted in IEC

Genauere Angaben zu den Isolationen entnehmen Sie bitte dem Isolationsdatenblatt oder unserem Produktkatalog.

*Additional information can be found in the insulating data sheets or our product brochure.*

Figure 6.2:

ThyssenKrupp Steel

ab/from 01.10.09

ThyssenKrupp Steel Europe



### Mechanische und technologische Eigenschaften

#### *Mechanical and technological properties*

Festigkeit in Walzrichtung <i>Strength in rolling direction</i>	Sortentypische Mittelwerte* <i>Typical mean values*</i>
<b>Streckgrenze Re</b> <i>Yield strength</i>	421 N/mm <sup>2</sup>
<b>Zugfestigkeit Rm</b> <i>Tensile strength</i>	532 N/mm <sup>2</sup>
<b>Bruchdehnung in WR in %</b> <i>Elongation in %</i>	15
<b>Mikrohärte HV5</b> <i>Hardness HV5</i>	218

\* nur zur Information  
\* for information purposes only

### Dickentoleranzen

#### *Thickness tolerances*

Dickentoleranzen <i>Thickness tolerances</i>	
<b>Max. Abweichung von der Nenndicke</b> <i>Max. deviation from nominal thickness</i>	± 8 %
<b>Max. Dickenunterschied parallel zur Walzrichtung auf einer Messlänge von 2 m</b> <i>Max. thickness variation parallel to rolling direction within one sheet or strip with a length of 2 m</i>	6 %
<b>Max. Dickenunterschied senkrecht zur Walzrichtung gemessen mindestens 30 mm vom Rand für Breiten &gt; 150 mm*</b> <i>Max. variation of thickness transverse to rolling direction measured at least 30 mm from the edge with a width &gt; 150 mm*</i>	0,02 mm

\* Für Schmalband (< 150 mm) dürfen bei der Anfrage und Bestellung andere Vereinbarungen getroffen werden  
\* For narrow strip (< 150 mm), other agreements may be made at the time of enquiry and order

Figure 6.3:

ThyssenKrupp Steel

ab/from 01.10.09

ThyssenKrupp Steel Europe



PS vs. J

Spezifischer Ummagnetisierungsverlust über magnetische Polarisierung

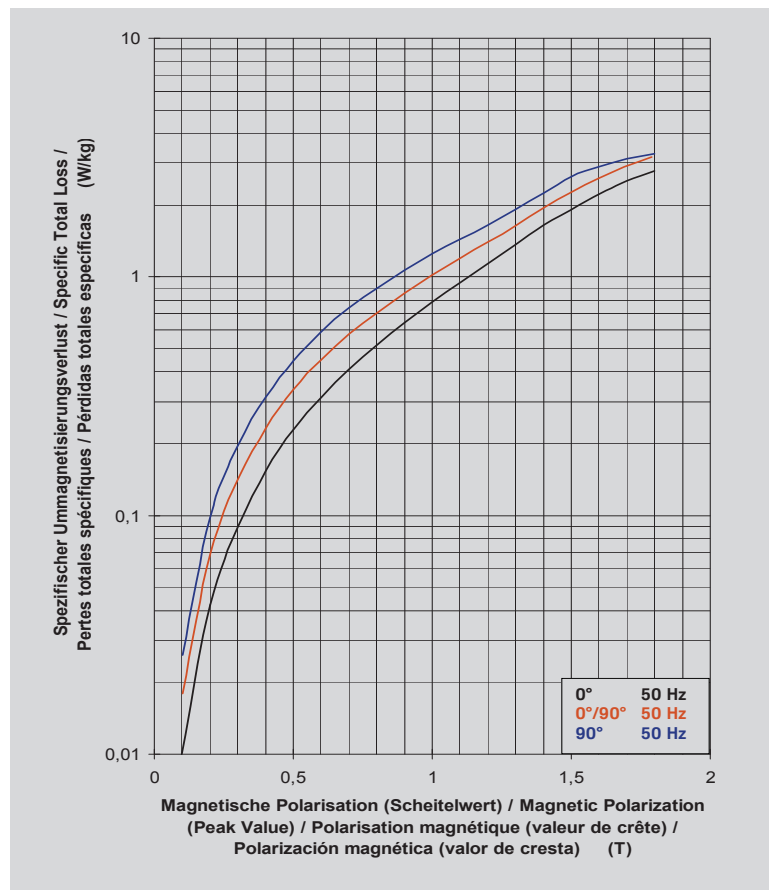
*Specific core loss vs. magnetic polarisation*

Figure 6.4:

ThyssenKrupp Steel

ab/from 01.10.09

ThyssenKrupp Steel Europe



J vs. H

Magnetische Polarisation über magnetische Feldstärke

Magnetic polarisation vs. magnetic field strength

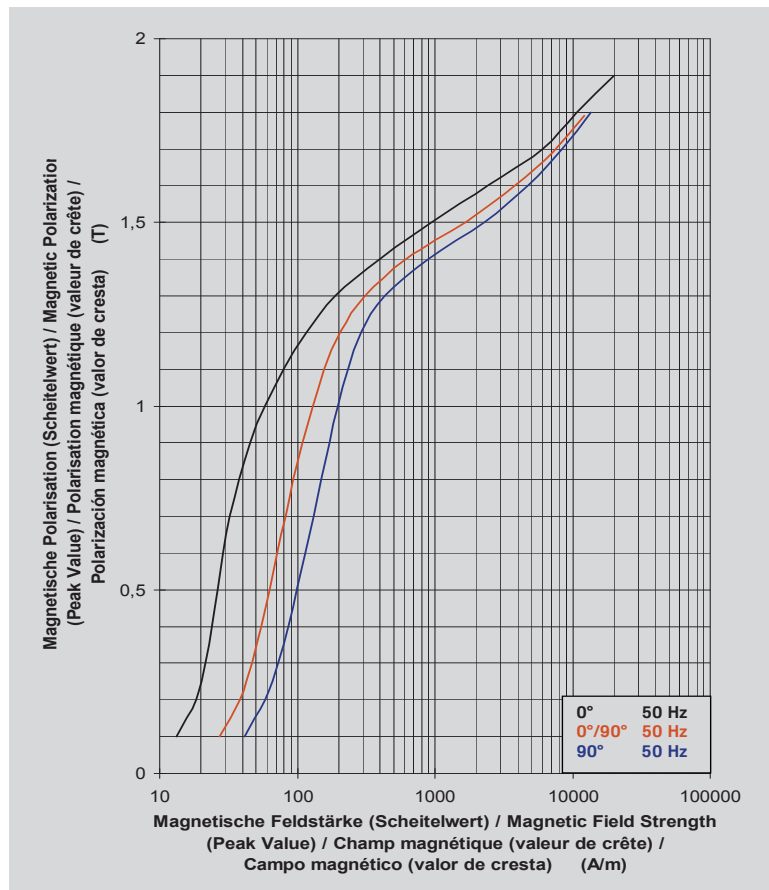


Figure 6.5:



ThyssenKrupp Steel

ab/from 01.10.09

ThyssenKrupp Steel Europe



Frequenzabhängige Kennwerte bei mittleren Frequenzen  
*Frequency dependent properties at middle frequencies*

f = 50Hz								
J T	H A/m			$\mu_s$ 0°/90°	P <sub>s</sub> W/kg			S <sub>s</sub> VA/kg 0°/90°
	0°	90°	0°/90°		0°	90°	0°/90°	
0,5	26	99	63	6343	0,23	0,44	0,33	0,65
0,6	29	114	72	6674	0,31	0,59	0,45	0,87
0,7	32	131	82	6826	0,41	0,74	0,57	1,13
0,8	37	149	94	6802	0,52	0,90	0,71	1,45
0,9	45	171	109	6600	0,64	1,07	0,85	1,82
<b>1,0</b>	<b>58</b>	<b>198</b>	<b>128</b>	<b>6197</b>	<b>0,78</b>	<b>1,25</b>	<b>1,02</b>	<b>2,31</b>
1,1	79	234	157	5578	0,94	1,44	1,19	2,94
1,2	115	293	204	4688	1,14	1,65	1,40	3,87
1,3	189	428	310	3343	1,36	1,91	1,64	5,63
1,4	400	895	619	1800	1,65	2,25	1,95	10,30
<b>1,5</b>	<b>953</b>	<b>2284</b>	<b>1683</b>	<b>710</b>	<b>1,93</b>	<b>2,63</b>	<b>2,27</b>	<b>28,14</b>
1,6	2403	4738	3835	333	2,22	2,89	2,59	71,91
1,7	5983	8305	7523	181	2,52	3,13	2,92	159,98
1,8	10726	13555	12590	115				
1,9	20186	23152	21890	70				

f = 100Hz					f = 200Hz				
J T	H A/m		P <sub>s</sub> W/kg 0°/90°	S <sub>s</sub> VA/kg 0°/90°	J T	H A/m		P <sub>s</sub> W/kg 0°/90°	S <sub>s</sub> VA/kg 0°/90°
	0°/90°	0°/90°				0°/90°	0°/90°		
0,5	65	6147	0,77	1,36	0,5	70	5665	1,88	3,00
0,6	73	6515	1,04	1,83	0,6	79	6041	2,55	4,03
0,7	83	6718	1,34	2,38	0,7	88	6305	3,30	5,21
0,8	94	6743	1,66	3,02	0,8	99	6439	4,13	6,60
0,9	109	6575	2,01	3,80	0,9	112	6399	5,03	8,21
<b>1,0</b>	<b>128</b>	<b>6201</b>	<b>2,39</b>	<b>4,76</b>	<b>1,0</b>	<b>130</b>	<b>6121</b>	<b>6,03</b>	<b>10,22</b>
1,1	157	5594	2,81	6,03	1,1	157	5567	7,13	12,83
1,2	204	4687	3,30	7,92	1,2	203	4695	8,39	16,61
1,3	304	3405	3,88	11,31	1,3	302	3424	9,88	23,40
1,4	621	1795	4,61	20,84	1,4	620	1798	11,93	42,85
<b>1,5</b>	<b>1694</b>	<b>706</b>	<b>5,36</b>	<b>57,05</b>	<b>1,5</b>	<b>1671</b>	<b>715</b>	<b>14,14</b>	<b>116,66</b>
1,6	3877	329	6,22	146,93	1,6				
1,7					1,7				
1,8					1,8				
1,9					1,9				

Figure 6.6:

ThyssenKrupp Steel

ab/from 01.10.09

ThyssenKrupp Steel Europe



**Frequenzabhängige Kennwerte bei hohen Frequenzen**  
*Frequency dependent properties at high frequencies*

f = 400Hz					f = 500Hz				
J T	H A/m 0°/90°	$\mu_a$ 0°/90°	$P_s$ W/kg 0°/90°	$S_s$ VA/kg 0°/90°	J T	H A/m 0°/90°	$\mu_a$ 0°/90°	$P_s$ W/kg 0°/90°	$S_s$ VA/kg 0°/90°
0,2	47	3374	0,93	1,61	0,2	49	3226	1,27	2,10
0,3	60	3990	1,96	3,08	0,3	63	3786	2,68	4,04
0,4	71	4491	3,27	4,86	0,4	75	4245	4,47	6,41
0,5	81	4894	4,82	6,96	0,5	86	4610	6,60	9,21
0,6	92	5208	6,61	9,38	0,6	98	4888	9,08	12,47
0,7	102	5438	8,64	12,18	0,7	110	5087	11,91	16,23
0,8	114	5591	10,92	15,40	0,8	122	5215	15,12	20,59
0,9	128	5598	13,71	19,44	0,9	137	5214	19,06	26,00
<b>1,0</b>	<b>143</b>	<b>5560</b>	<b>16,64</b>	<b>24,04</b>	<b>1,0</b>	<b>153</b>	<b>5202</b>	<b>23,28</b>	<b>32,18</b>
1,1	165	5296	19,95	29,88	1,1	174	5023	28,07	39,90
1,2	208	4597	23,69	38,09	1,2	211	4520	33,47	50,52
1,3	303	3420	28,04	52,34	1,3	306	3383	39,80	68,81
1,4					1,4				
<b>1,5</b>					<b>1,5</b>				
1,6					1,6				

f = 1000Hz					f = 2000Hz				
J T	H A/m 0°/90°	$\mu_a$ 0°/90°	$P_s$ W/kg 0°/90°	$S_s$ VA/kg 0°/90°	J T	H A/m 0°/90°	$\mu_a$ 0°/90°	$P_s$ W/kg 0°/90°	$S_s$ VA/kg 0°/90°
0,2	60	2668	3,54	5,09	0,2	77	1033	10,09	13,13
0,3	78	3079	7,39	9,94	0,3	102	1567	20,75	25,78
0,4	94	3401	12,32	15,97	0,4	127	1883	35,71	42,95
0,5	110	3629	18,28	23,18	0,5	152	2092	53,53	63,64
0,6	128	3722	25,91	32,30	0,6	181	2203	76,01	89,65
0,7	147	3795	34,57	42,83	0,7	212	2249	102,74	120,86
0,8	167	3816	44,61	55,12	0,8				
0,9	189	3798	56,26	69,60	0,9				
<b>1,0</b>	<b>212</b>	<b>3747</b>	<b>69,76</b>	<b>86,75</b>	<b>1,0</b>				
1,1	239	3663	85,30	107,30	1,1				
1,2	269	3553	103,44	133,85	1,2				
1,3	324	3192	124,26	174,41	1,3				
1,4					1,4				
<b>1,5</b>					<b>1,5</b>				
1,6					1,6				

Figure 6.7:

ThyssenKrupp Steel

ab/from 01.10.09

ThyssenKrupp Steel Europe



#### Erläuterungen zu den Datenblättern

*Comments on Data Sheets / Commentaires pour les fiches techniques /  
Aclaraciones a las hojas de datos*

$f$	=	Frequenz / Frequency / Fréquence / Frecuencia
$J$	=	Magnetische Polarisation (Scheitelwert) / Magnetic Polarization (Peak Value) / Polarisation magnétique (valeur de crête) / Polarización magnética (valor de cresta)
$H$	=	Magnetische Feldstärke (Scheitelwert) / Magnetic Field Strength (Peak Value) / Champ magnétique (valeur de crête) / Intensidad de campo magnético (valor de cresta)
$P_s$	=	Spezifischer Ummagnetisierungsverlust / Specific Total Loss / Pertes totales spécifiques/ Pérdidas totales específicas
$S_s$	=	Spezifische Scheinleistung / Specific Apparent Power / Puissance apparente spécifique/ Potencia aparente específica
$T$	=	Anisotropiefaktor / Anisotropy Factor / Facteur d'anisotropie / Factor anisotrópico
$P_h$	=	Hystereseverlust / Hysteresis Loss / Pertes par hystérésis / Pérdidas por histéresis
$P_e$	=	Wirbelstromverlust / Eddy Current Loss / Pertes par courants de Foucault / Pérdidas por corrientes parásitas
$H_c$	=	Koerzitivfeldstärke / Coercive Field Strength / Champ coercitif / Intensidad de campo coercitivo
$B_r$	=	Remanente magnetische Polarisation / Remanent Magnetic Polarization / Polarisation magnétique rémanente / Polarización magnética remanente
$\mu_a$	=	Amplitudenpermeabilität / Amplitude Permeability / Perméabilité d'amplitude / Permeabilidad de amplitud
$0^\circ, 90^\circ$ $0^\circ/90^\circ$	=	Winkel zur Walzrichtung / Angle to Rolling Direction / Angle par rapport au sens du laminage / Ángulo relativo al sentido de laminación

Figure 6.8:

## 6.2. NdFeB PM datasheet: Neomax® NMX-36EH

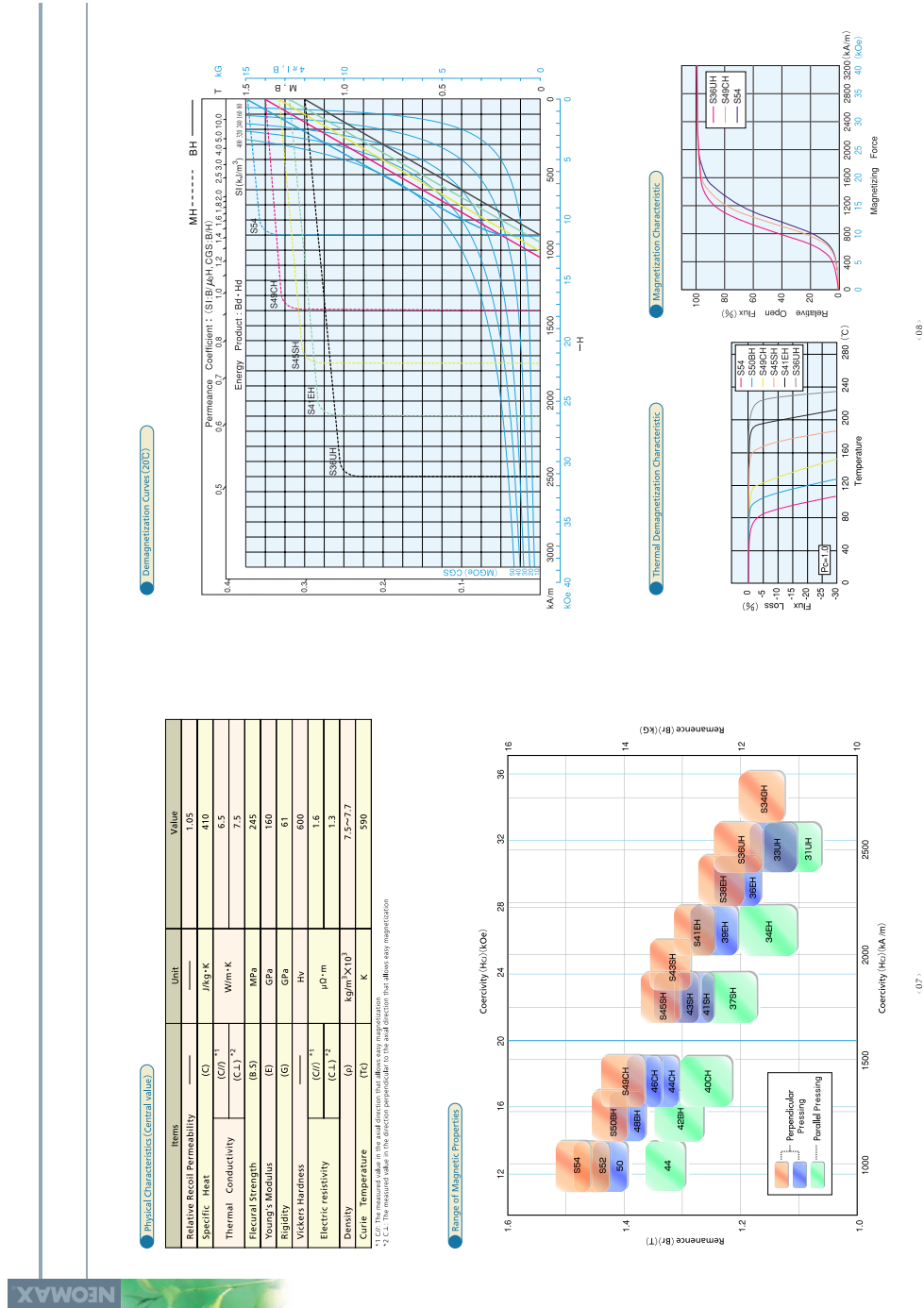
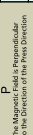
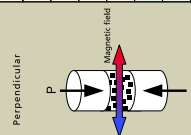


Figure 6.9:

**Magnetic Characteristics of NEOMAX®**

**Magnetic Characteristics**

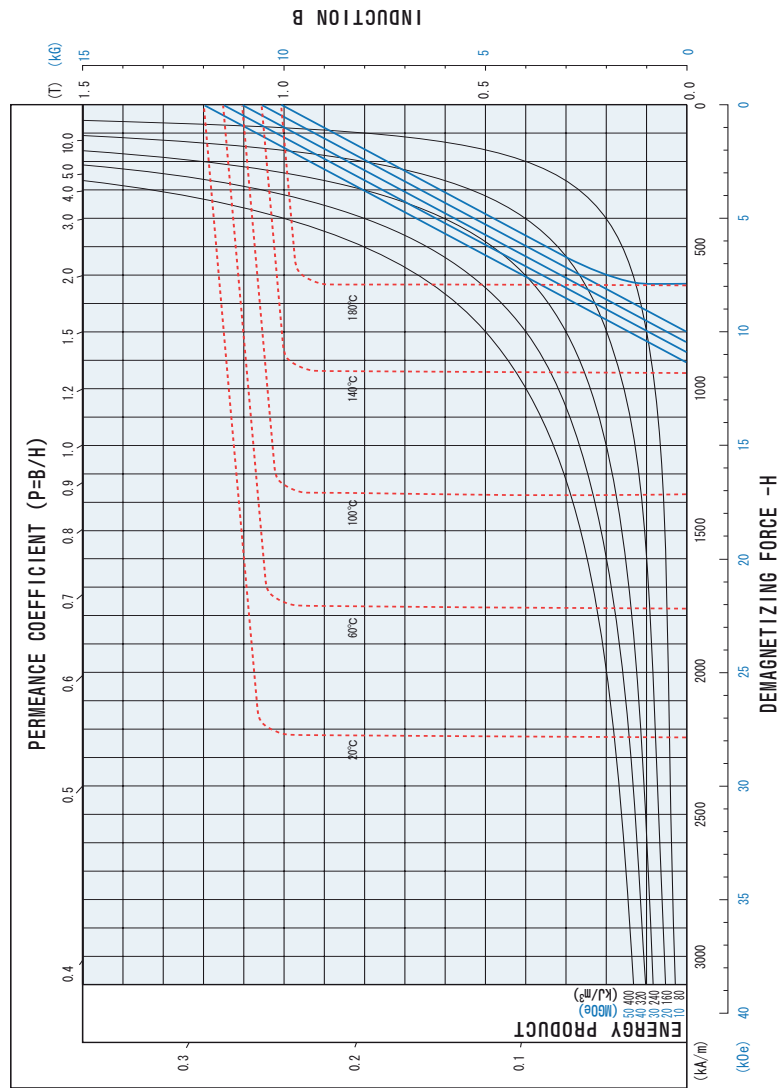
Pressing Method	Material Code	Remanence Br		Coercivity				Max. BH Product (BH) max.	Temp. Coeff. Of Br	Temp. Coeff. Of HcJ	Thermal Expansion Coeff	
		T	KG	HcH	HcK	HcJ	1/K				1/K	
Perpendicular	NMX-S54	1.45~1.51	14.5~15.1	939~1153	≥875	≥11	405~437	51~55	-0.60	6.3	-1.5	
	NMX-S82	1.42~1.48	14.2~14.8	838~984	≥875	≥11	389~421	49~53	-0.59			
	NMX-S50BH	1.39~1.45	13.9~14.5	1042~1122	≥1114	≥14	374~405	47~51	-0.58			
	NMX-S49CH	1.36~1.43	13.6~14.3	1019~1106	≥1273	≥16	368~397	46~50	-0.55			
	NMX-S45SH	1.30~1.37	13.0~13.7	970~1058	≥1671	≥21	326~366	41~46	-0.52			
	NMX-S43SH	1.28~1.35	12.8~13.5	862~1042	≥1830	≥23	310~380	39~44	-0.50			
	NMX-S41EH	1.24~1.31	12.4~13.1	923~1018	≥1990	≥25	294~334	37~42	-0.48			
	NMX-S38EH	1.19~1.27	11.9~12.7	863~978	≥2228	≥28	270~310	34~39	-0.47			
	NMX-S38UH	1.16~1.24	11.6~12.4	883~982	≥2387	≥30	254~294	32~37	-0.44			
	NMX-S34GH	1.12~1.20	11.2~12.0	859~939	≥2626	≥33	238~278	30~35	-0.44			
	NMX-50	1.39~1.45	13.9~14.5	835~1034	≥875	≥11	374~405	47~51	-0.60	6.3	-1.5	
	NMX-48BH	1.36~1.42	13.6~14.2	1018~1098	≥1114	≥14	358~389	45~49	-0.59			
	NMX-46CH	1.33~1.39	13.3~13.9	994~1074	≥1273	≥16	342~374	43~47	-0.57			
	NMX-44CH	1.30~1.36	13.0~13.6	978~1058	≥1313	≥16	326~368	41~45	-0.55			
	NMX-43SH	1.27~1.34	12.7~13.4	947~1026	≥1671	≥21	310~380	39~44	-0.55	6.4	-1.7	
	NMX-41SH	1.24~1.31	12.4~13.1	923~1002	≥1830	≥23	294~334	37~42	-0.50			
NMX-39EH	1.20~1.28	12.0~12.8	915~984	≥1990	≥25	278~318	35~40	-0.48				
NMX-38EH	1.16~1.24	11.6~12.4	883~982	≥2228	≥28	254~294	32~37	-0.46				
NMX-33UH	1.10~1.18	11.0~11.8	838~915	≥2387	≥30	230~270	29~34	-0.46	6.5	-1.9		
Parallel	NMX-44	1.29~1.36	12.9~13.6	858~1018	≥875	≥11	318~388	40~45	-0.60	6.3	-1.5	
	NMX-42BH	1.26~1.34	12.6~13.4	831~1026	≥1114	≥14	302~342	38~43	-0.59			
	NMX-40CH	1.21~1.30	12.1~13.0	915~1010	≥1273	≥16	278~326	35~41	-0.57			
	NMX-37SH	1.17~1.26	11.7~12.6	878~978	≥1671	≥21	282~310	33~39	-0.55	6.4	-1.7	
	NMX-36EH	1.10~1.20	11.0~12.0	827~931	≥1990	≥25	250~278	29~35	-0.48			
	NMX-31UH	1.06~1.16	10.6~11.6	795~899	≥2387	≥30	206~254	26~32	-0.46	6.5	-1.9	



The characteristics given above may vary depending on shape and size of the magnet, guaranteed characteristics will be sorted by individual consultation.  
 \* HcJ: The measured value in the axial direction that allows easy magnetization. \* C.T.C.: The measured value in the direction perpendicular to the axial direction that allows easy magnetization.

Figure 6.10:

ID: NMX-36EH



注) この磁気特性曲線は代表値になります。

Figure 6.11:

### 6.3. Conductors datasheet: CEI-UNEL 01723-72

0,180	0,200	0,224	0,250	0,280	0,315	0,355	0,400	0,450	0,500	0,560	0,630	0,710	0,800	0,850	0,900	0,950	1,000	1,060	1,120	1,180	1,250	1,320	1,400	1,500	1,600	1,700	1,800	1,900	2,000	2,120	2,240	2,360	2,500	2,650	2,800	3,000	3,150	3,350	3,550	3,750	4,000	4,200	4,500	4,750	5,000			
0,003	0,003	0,003	0,004	0,004	0,004	0,004	0,005	0,005	0,005	0,006	0,006	0,007	0,008	0,009	0,009	0,010	0,010	0,011	0,011	0,012	0,013	0,013	0,014	0,015	0,016	0,017	0,018	0,019	0,020	0,021	0,022	0,024	0,025	0,027	0,028	0,030	0,032	0,034	0,036	0,038	0,040	0,043	0,045	0,048	0,050			
0,6499	0,5281	0,4224	0,3373	0,2698	0,2139	0,1689	0,1327	0,1051	0,08534	0,06794	0,05381	0,04234	0,03788	0,03334	0,02950	0,02634	0,02362	0,02134																														
0,7068	0,5706	0,4534	0,3659	0,2907	0,2289	0,1797	0,1419	0,1118	0,09037	0,07215	0,05687	0,04481	0,04022	0,03530	0,03131	0,02789	0,02506	0,02259																														
0,222	0,245	0,272	0,301	0,334	0,371	0,414	0,462	0,516	0,569	0,632	0,706	0,790	0,885	0,937	0,990	1,041	1,093	1,153	1,217	1,279	1,351	1,423	1,506	1,608	1,711	1,813	1,916	2,018	2,120	2,243	2,366	2,488	2,631	2,784	2,938	3,142	3,294	3,498	3,702	3,905	4,160	4,414	4,668	4,923	5,177			
0,2262	0,2793	0,3501	0,4364	0,5474	0,6938	0,8800	1,117	1,414	1,746	2,189	2,771	3,520	4,469	5,045	5,656	6,301	6,982	7,845	8,758	9,722	10,91	12,16	13,68	15,79	17,87	20,18	22,62	25,21	27,93	31,38	35,03	38,88	43,64	49,03	54,74	62,84	65,28	78,36	87,99	98,18	111,7	126,1	141,1	157,5				
0,6775	0,5488	0,4375	0,3512	0,2800	0,2212	0,1742	0,1372	0,1084	0,08781	0,07000	0,05531	0,04355	0,03903	0,03430	0,03038	0,02710	0,02432	0,02195	0,01953	0,01750	0,01576	0,01405	0,01259	0,009757	0,008575	0,007596	0,006755	0,006081	0,005488	0,004884	0,004375	0,003941	0,003512	0,003126	0,002800	0,002439	0,002212	0,001956	0,001742	0,001561	0,001372	0,001212	0,001084	0,0009730	0,0008781			

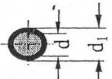
Fili di rame rotondi smaltati con bispessoro doppio CNR-CEI (UNEL 01723-72)							
La presente unificazione è conforme alle raccomandazioni IEC 182-1 e 182-2 Ed. 1964, nonché alle raccomandazioni IEC della serie 317 ED. 1970							
							
Dimensioni in mm.							
1	2	3	4	5	6	7	8
Condotore di rame		Bispessoro e smalto min		Diametro sullo smalto d2 max.		Massa filo rame g/m	
Diam. Nomin. d	Tolleranz a diametro ±	Resistenza elettrica a 20°C				Resist. elettrica media teorica Ω/m	
		Minima Ω /m	Massima Ω /m				
0,020	0,003	46,65	65,31	0,004	0,027	0,00279	54,88
0,025	0,003	30,56	41,09	0,005	0,034	0,00436	35,12
0,032	0,003	18,87	24,44	0,007	0,043	0,007150	21,44
0,040	0,003	12,21	15,37	0,008	0,054	0,01117	13,72
0,050	0,003	7,903	9,659	0,010	0,068	0,01745	8,781
0,063	0,003	5,033	6,029	0,012	0,085	0,02771	5,531
0,071	0,003	3,985	4,725	0,014	0,095	0,03520	4,355
0,080	0,003	3,156	3,704	0,016	0,105	0,04468	3,430
0,090	0,003	2,507	2,913	0,017	0,117	0,05655	2,710
0,100	0,003	2,042	2,349	0,018	0,129	0,06982	2,195
0,112	0,003	1,646	1,864	0,019	0,143	0,08758	1,750
0,125	0,003	1,328	1,488	0,020	0,159	0,1090	1,405
0,140	0,003	1,064	1,180	0,022	0,176	0,1368	1,120
0,160	0,003	0,8192	0,8983	0,025	0,199	0,1788	0,8575

Figure 6.12:

## 6.4. Program codes

In this *CD-ROM* are stored the following program codes:

- Analytical synthesis codes (MathWorks Matlab®)
- Process codes (Ansoft Maxwell® VB scripts)
- Postprocess codes (MathWorks Matlab®)







## Bibliography

- [1] *US DoE, International Energy Outlook 2011*, <http://www.eia.gov/forecasts/ieo/world.cfm>
- [2] Mehrdad Ehsani, Yimin Gao, Ali Emadi, *Modern Electric, Hybrid Electric, and Fuel Cell Vehicles - Fundamentals, Theory and Design*, CRC Press, 2010; p. 10.
- [3] Pietro Menga, *Battery and Hybrid Electric Vehicles*, Seminar - University of Padova, 09/06/2010
- [4] G. Ombach, J. Junak, *Comparative study of IPM motor with different airgap flux distribution*, IEEE, -
- [5] *US DoE, FreedomCAR, Partnership plan*, 05/09/2002
- [6] *US DoE, FY 2011 Annual Progress Report for Advanced Power Electronics and Electric Motors*, 2012
- [7] *US DoE, 2010 FreedomCAR and Fuel Partnership - Highlights of Technical Accomplishments*, 2011
- [8] *US DoE, Evaluation of the 2007 Toyota Camry Hybrid Sinergy Drive System*, 04/2008
- [9] *US DoE, FY 2011 Final Report on Assessment of Motor Technologies for Traction Drives of Hybrid and Electric Vehicles*, IEEE, 2012
- [10] P. B. Reddy, A. M. El-Refaie, K. Huh, J. K. Tangudu, T. M. Jahns, *Comparison of Interior and Surface PM Machines Equipped with Fractional-Slot Concentrated Winding for Hybrid Traction Applications*, IEEE, 2011
- [11] W. L. Soong, T. J. E. Miller, *Field-weakening performance of brushless synchronous AC motor drives*, IEEE, 1994

- 
- [12] A. Vagati, G. Pellegrino, P. Guglielmi, *Comparison between SPM and IPM motor drives for EV applications*, IEEE, 2010
- [13] P.B. Reddy, T. M. Jahns, P. J. McClever, T. P. Bohn, *Design, Analysis and Fabrication of an High-Performance Fractional-Slot Concentrated Winding Surface PM Machines*, IEEE, 2011.
- [14] J. K. Tangudu, T. M. Jahns, T. P. Bohn, *Design, Analysis and Loss Minimization of a Fractional-Slot Concentrated Winding IPM Machine for traction Applications*, IEEE, 2011.
- [15] J. K. Tangudu, T. M. Jahns, *Comparison of Interior PM Machines with Concentrated and Distributed Stator Windings for Traction Applications*, IEEE, 2011.
- [16] W. L. Soong, P. B. Reddy, A. M. El-Refajaie, T. M. Jahns, N. Ertugrul, *Surface PM Machine Parameter Selection for Wide Field-Weakening Applications*, IEEE, 2007
- [17] E. Fornasiero, N. Bianchi, S. Bolognani, *Slot Harmonic Impact on Rotor Losses in Fractional-Slot Permanent Magnet Machines*, IEEE, 2011
- [18] N. Bianchi, E. Fornasiero, *Index of rotor losses in three-phase fractional slot permanent magnet machines*, IEEE, 2009
- [19] N. Bianchi, *Permanent Magnet Synchronous Motors*, 2009
- [20] P. Salminen, J. Pyrhönen, F. Libert, J. Soulard, *Torque ripple of permanent magnet machines with concentrated windings*, ISEF, 2005
- [21] A. M. El-Refajaie, T. M. Jahns, *Optimal flux weakening in surface PM machines using fractional-slot concentrated windings*, IEEE, 2005
- [22] F. Magnussen, C. Sadaragani, *Winding factors and Joule losses of permanent magnet machines with concentrated winding*, IEEE, 2003
- [23] L. Chong, M. F. Rahman, *Saliency ratio derivation and optimisation for interior permanent magnet machine with concentrated windings using finite-element-analysis*, IEEE, 2010.
- [24] J. K. Tangudu, T. M. Jahns, A. M. El-Refajaie, *Unsaturated and saturated saliency trends in fractional slot concentrated winding interior permanent magnet machines*, IEEE, 2010.